2

ORNL/Sub/86-95901/02

INVESTIGATION OF THE EFFECTS OF MICROALLOY CONSTITUENTS SURFACE TREATMENTS AND OXIDATION CONDITIONS ON THE DEVELOPMENT AND BREAKDOWN OF PROTECTIVE OXIDE SCALES

OCTOBER 1990

Report Prepared by

V. SRINIVASAN
PRINCIPAL INVESTIGATOR
UES, INC.
4401 DAYTON-XENIA ROAD
DAYTON, OH 45432

under

SUBCONTRACT NO. 86X-95901C

for

OAK RIDGE NATIONAL LABORATORY
OAK RIDGE, TN 37831
operated by
MARTIN MARIETTA ENERGY SYSTEMS, INC.
for the
U.S. DEPARTMENT OF ENERGY
Under Contract No. DE-AC05-84OR21400

ORNL/Sub--86-95901/02

DE91 004521

INVESTIGATION OF THE EFFECTS OF MICROALLOY CONSTITUENTS SURFACE TREATMENTS AND OXIDATION CONDITIONS ON THE DEVELOPMENT AND BREAKDOWN OF PROTECTIVE OXIDE SCALES

OCTOBER 1990

Research sponsored by the U.S. Department of Energy,
Fossil Energy
Advanced Research and Technology Development Materials Program

Report Prepared by

V. SRINIVASAN
PRINCIPAL INVESTIGATOR
UES, INC.
4401 DAYTON-XENIA ROAD
DAYTON, OH 45432

under

SUBCONTRACT NO. 86X-95901C

for

OAK RIDGE NATIONAL LABORATORY
OAK RIDGE, TN 37831
operated by
MARTIN MARIETTA ENERGY SYSTEMS, INC.
for the
U.S. DEPARTMENT OF ENERGY
Under Contract No. DE-AC05-84OR21400

FOREWORD

This report represents an account of work performed under subcontract 86X-95901C from September 4, 1986 to August 31, 1990, for Martin Marietta Energy Systems, Inc. which operates Oak Ridge National Laboratory, Oak Ridge, TN for DOE. This program was administered by Advanced Research and Technology Division under Fossil Energy Materials Program with Dr. R.R. Judkins as Program Manager. This report was prepared by Dr. V. Srinivasan, principal investigator and program manager.

The research was conducted at the Materials Research Division of Universal Energy Systems, Inc., Dayton, OH under the direction of Dr. V. Srinivasan with the support of Dr. Peter P. Pronko, the Division Director. The team consisted of participants not only from UES, but from other institutions as listed below: (UES): D.E. Goodman (June 1988-), A.R. Kraus, Dr. S.C. Kung (Feb. 89-Oct. 89), Dr. R.S. Bhattacharya, Dr. A.K. Rai and A.W. McCormick; (Ames Lab): L.L. Jones; (UDRI): D. Wolf, T. Whittberg and J. Hoenigman; (PNL): D. Baer; (STEM): R. Ayer; (HTML/ORNL): Dr. M. Ferber, J.V. Cathcart, Dr. A. Choudhary, R. Padgett and L. Harris. Professor G.H. Meier of the University of Pittsburgh was a consultant. Facilities at the Material Analysis User Center of HTML/ORNL were used with the permission of Dr. V.J. Tennary, Director. The report was typed by Ms. Dee Dee Donley.

The following papers are based on work carried out under this contract and have been published in scientific journals or presented in scientific conferences.

Journals and Proceedings

Oxidation and Sulfidation of Implanted and Unimplanted AISI 446 Steel, V. Srinivasan, A.W. McCormick and A.K. Rai, Oxid. Met., 34 (1990), 401

The Effect of Yttrium on the Scale Formation and Breakdown in Fe-Cr-Al Alloy in Mixed Gas, Si-Cheng Kung and V. Srinivasan, Oxid. Met., 33, (1990), 481

Analysis of Oxidation Kinetics in Xe-implanted AISI Steel, V. Srinivasan, Scripta Met. 24, 739 (1990)

Effects of Ion Implantation on the Mixed Gas Corrosion of a Chromia Former, V. Srinivasan, D.E. Goodman and A.R. Kraus, Mater. Sci. Engg., 121/122, 525 (1989)

Corrosion of Fe-25Cr Alloy with Microconstituent Additions of Hf and Pt, V. Srinivasan, NACE Paper #522 (1989)

Effects of Rare-Earth Additions on the Breakdown of Protective Oxide Scales in the Presence of Sulfur, V Srinivasan and D.E. Goodman, Proc. Symposium on "Corrosion & Particle Erosion at High Temperatures," Eds. V. Srinivasan and K. Vedula, TMS, Warrendale, PA, pp. 179 (1989)

Oxidation/Corrosion of Surface-modified Alloys, V. Srinivasan, in "High Temperature Coatings," Eds. M. Khobaib and R.C. Krutenat, TMS, Warrendale, PA, pp. 153 (1987)

Reports

A Review on the Effects of Microalloying, Surface Treatment and Oxidation Conditions on the Formation and Breakdown of Protective Oxide Scales on Fossil Energy Materials, V. Srinivasan, ORNL/Sub/86-95901/01 (1989)

Conference Presentations

Effect of Y and Hf on the Corrosion Behavior of an Alumina Former, V. Srinivasan and Si-Cheng Kung, 119th Annual Meeting of TMS, Anaheim, CA, Feb. 18-22 (1990)

Characteristics of Oxide Scales in Ce-doped Fe-25Cr Binary Alloy, R. Ayer and V. Srinivasan, 119th Annual Meeting of TMS, Anaheim, CA, Feb. 18-22 (1990)

Effects of Ion Implantation on Mixed Gas Corrosion of a Chromia Former, V. Srinivasan, D.E. Goodman and A.R. Kraus, 2nd Int. Symposium on "High Temperature Corrosion" Les Embiez, France, May 22-26 (1989). (Invited paper)

Corrosion of an Fe-25Cr Alloy with Microconstituent Additions of Hf and Pt, V. Srinivasan, "Corrosion$_{89}$", NACE, New Orleans, LA, April 17-21 (1989)

Effects of Rare-earth Additions on the Breakdown of Protective Oxide Scales in the Presence of Sulfur, V. Srinivasan and D.E. Goodman, 118th Annual Meeting of TMS, Las Vegas, NV, Feb. 27-Mar. 3 (1989)

Analysis of Oxide/Corrosion Scales by Ion Beam Techniques, V. Srinivasan and R.S. Bhattacharya, in Symposium on "Environmental Degradation of Ion and Laser Beam-treated Surfaces" TMS Fall Meeting, Chicago, IL (1988)

Oxidation-Sulfidation of Ion Implanted Fe-25 wt.% Cr (AISI 446), V. Srinivasan, G.H. Meier, G.K. Kim and R.S. Bhattacharya, 117th Annual Meeting of TMS, Phoenix, AZ (1988)

High Temperature Corrosion of Ion Implanted Fe-25Cr-20Ni Alloy, V. Srinivasan, TMS Fall Meeting, Cincinnati, OH (1987)

Oxidation/Corrosion of Surface-modified Alloys, V. Srinivasan, in Symposium on "High Temperature Coatings," TMS Fall Meeting, Orlando, FL (1986)

TABLE OF CONTENTS

TABLE OF CONTENTS (CONT'D.)

1.0 SUMMARY

The research reported here explores the scientific principles behind improving the corrosion resistance of traditional ferritic and austenitic steels that are used extensively in fossil energy systems. The objective of this program is to understand and gain control over factors that improve and extend significantly the protectiveness of chromia and alumina scales. For this purpose, investigations were carried out to understand the effects of minor alloying additions, the methods of their incorporation, surface treatments and oxidizing conditions on the formation and breakdown of protective oxide scales. High purity Fe-25Cr, Fe-25Cr-20Ni and Fe-25Cr-6Al were chosen as base alloys. The additives were Ce, Hf, La, O, Pt, Si, Y and α-Al_2O_3 dispersoids. In-got metallurgy (I/M) and powder metallurgy (P/M) routes and ion implantation procedures were used to incorporate them. Cold rolling (50%) was included as a surface pretreatment. Coupons of these alloys were exposed isothermally and cyclically to gas mixtures of $H_2/H_2O/H_2S/Ar$ with oxygen and sulfur activities simulating coal derived atmospheres. The test temperatures were between 700° and 500°C, and exposure times were up to 500 h. In addition, isothermal and cyclic oxidation runs in O_2 at 1 atm or low pO_2, and preoxidation followed by multioxidant exposures were made. For kinetics studies, TGA apparatus was used. Scales at different stages of formation and breakdown, and the substrates were examined using a variety of conventional and advanced surface analytical tools to find the initial and final location and chemical status of additives and scale-forming species.

Under the conditions examined, the most effective additions to chromia formers were elemental Si and α-Al_2O_3 dispersoids. The reactive elements and Pt were least effective.

Scale breakdown begins by forming (FeCr) sulfides at several places locally on the gas/scale interface of Fe-25Cr and Fe-25Cr-20Ni when the local concentrations of Fe and Cr reach critical values by diffusing through the oxide scale. In the case of Fe-25Cr-20Ni, (FeNi) sulfides nucleate over (FeCr) sulfides. These sulfides break through the protective oxides and form sulfide channels leading to internal sulfidation. The positive influence of Si and α-Al_2O_3 dispersoid addition is tentatively explained by postulating the formation of a thin barrier (SiO_2) layer and/or defects modification in oxides by doping to account for reduced outward Fe and Cr flux.

Fe-25Cr-6Al has exhibited excellent corrosion resistance, and sulfidation was not observed under the conditions examined here. Addition of reactive elements at 0.3 and 1.0% levels led to local sulfidation of oxide scale particularly along the substrate grain boundaries where a significant amount of the additives was present initially in the form of intermetallics. Pt is not a reactive element, and its addition did not result in grain boundary segregation and sulfidation. Addition of reactive elements at levels around or below their solubility range may not lead to such premature localized sulfidation.

Ion implantation and cold rolling do not alter the scale formation and breakdown process. At low temperature and high ratio of sulfur to oxygen potential, sulfidation is faster and oxide formation is more difficult. Only sulfide rich scales form.

"Research sponsored by the U.S. Department of Energy, Fossil Energy AR&TD Materials Program, DOE/FE AA 15 10 10 0, Work Breakdown Structure Element UES-3"

2.0 INTRODUCTION

2.1 DEFINITION OF THE PROBLEM

The ferritic and austenitic iron base alloys are of primary interest for applications in several fossil energy systems as superheaters, reheaters, syngas coolers and other heat exchangers or recovery systems. They have adequate long term mechanical properties such as creep strength and ductility and fracture resistance at service temperatures, and can be easily fabricated and joined in required shapes. However, they do not have sufficient resistance to corrosion in coal derived atmospheres characterized by mixture of several gases such as CO, CO_2, CH_4, NH_3, N_2, H_2S, H_2O, H_2, SO_2 and NO_x and mineral ash. Corrosion generally proceeds by sulfidation, deposit-induced corrosion, and halogenation and may be assisted by erosion. In coal combustion and coal gasification, sulfidation is by far the dominant process of material degradation. The sulfides, carbides or other reaction products are not protective in the sense that they do not form a barrier to reactants in the substrate and the mixed gas atmosphere.

The only way alloys and coatings are protected against sulfidation and corrosion at high temperatures is by forming and maintaining protective oxide scales. Once the protective oxide scales form, they act as a barrier for the transport of reactants between the substrate and the environment, thereby providing resistance to further degradation because of very slow diffusion of reactant anions and cations in them. Chromia (Cr_2O_3) and alumina (Al_2O_3) are widely studied protective oxide scales. They form on alloys and coatings with sufficient amounts of Cr and/or Al at high temperatures by selective oxidation. The method of protection of alloys and coatings against high temperature oxidation/corrosion is thus, in principle, similar to the biological process of autoimmunization.

Coal gasification and fluidized bed combustion processes generate gaseous mixtures that have low oxygen activity and significantly high activity of sulfur. Applications of principal interest involve temperatures in the range of 700°-500°C. Under these conditions protective Cr_2O_3 or α-Al_2O_3 scales are either difficult to form on materials with sufficient amounts of Cr and/or Al, or destroyed sooner or later by sulfidation. Even the most oxidation resistant alloys succumb to sulfidation attack, and the reasons for this are not well understood. The above temperature regime, 700°-500°C is, further, different from that generally reported in literature where alloys are exposed to temperatures well above 800°C and evaluated for their corrosion behavior. The reason for the emphasis on temperatures above 800°C is the impetus given by aircraft engine manufacturers to get alloys and coatings with higher and higher temperature capability for engine application. Most of our present understanding may not be thus helpful to gain an insight into the factors that will promote the formation and maintenance of protective scales with extended durability and to the design of corrosion resistant alloys for application at 700°C and below because of possible changes in the competing reactions and the rate-controlling process.

In this report several aspects of the problem of sulfidation of ferritic and austenitic steels in coal derived atmospheres are addressed. The research described herein has led to a better understanding of the effects of several variables, and some positive recommendations for improving sulfidation resistance and development of sulfidation resistant alloys.

2.2 TECHNICAL BACKGROUND

The theme of several investigations in the area of gaseous corrosion has been to understand the factors that make the protective oxides retain or lose their protectiveness in the presence of a second oxidant such as sulfur [1-4]. Oxides, sulfides or other reaction products which are in thermodynamic equilibrium with the atmosphere form on exposing an alloy for a long time to a gas mixture to minimize the Gibbs free energy of the metal-gas system, and the driving force for scaling is thus thermodynamic in origin. It is possible to predict thermodynamically the nature of the steady state scaling. Wagner [5,6] has shown that for the formation of protective oxides, Cr_2O_3 or Al_2O_3 externally by selective oxidation, the solute concentration, N_x of x (= Cr or Al),

$$N_x = \left[\frac{\pi g^*}{2} \frac{N_o D_o V_m}{D_x V_{ox}} \right]^{1/2} \quad (1)$$

and that for maintenance of the growth of the protective oxide scale,

$$N_x = \frac{V_m}{16 Z_x} \left(\frac{\pi k_p}{D_x} \right)^{1/2} \quad (2)$$

Here $N_o D_o$ is the oxygen permeability in the substrate alloy, D_x is the diffusivity of the solute, x (Cr or Al), V_m and V_{ox} are the molar volumes of alloy and the protective oxide, k_p is the parabolic rate constant for the growth of protective oxide, Z_x is the valence of Cr or Al, π is a constant, and g* is a factor $\simeq$0.3, dependent on the volume fraction of oxide required for the transition from internal to external oxidation. The protective oxide scale must be more stable than the lowest oxide of any component of the base alloy. The above equations define the conditions that the concentration of x (Cr or Al) must be large enough to provide and maintain necessary solute flux at the reaction site. Systems take long times, particularly at intermediate and low temperatures, to establish steady state oxidation or the formation of equilibrium scales. The nature and characteristics of the protective scales has been discussed elsewhere [7].

Metallurgical and environmental factors affect the development of protective oxides. The factors include alloy chemistry, surface pretreatment, grain size, and the partial pressure of oxygen in the environment [7]. Addition of Cr to Fe brings down the parabolic rate constant significantly reaching a minimum at about 30% Cr (all compositions are in wt.% unless otherwise defined) at 900°C in 1 atm air [8]. The ternary addition of Cr to Fe-Ni also reduces the kinetics of oxidation up to 20% Cr [9]. Alloying influences the kinetics by modifying the scale morphology and changing the steady state scale composition to produce a more protective scale. Alloy grain size, surface conditions, and surface pretreatments affect the nucleation and growth process and hence the nature of oxides formed [10-14]. A thin

protective Cr_2O_3 layer is formed easily on fine grained 304 stainless steel at 800°C in air, but not on coarse grained steel [13]. In vacuum annealed 304 with large grains relatively thick iron oxides formed over the grains and thin Cr rich oxides on the grain boundaries [13]. Initial cold working reduced the extent and the amount of transient oxides and accelerated the formation of steady state protective oxides in continuous layers. A large number of fast diffusion paths in the form of grain boundaries and dislocations in fine grained and cold worked alloys respectively, provide sufficient flux of Cr at the surface to form a large number of oxide nuclei resulting in a continuous oxide layer. An increase in the diffusion rate of Cr, according to Eq. 1 should decrease the concentration, N_x, for the transition from internal to external oxidation. Indeed cold working has resulted in the formation of Cr_2O_3 scale in alloys that are otherwise marginally lean in Cr. The method of initiating the oxidation reaction also has an influence on the scale morphology, composition and the kinetics during the steady state oxidation [15]. At sufficiently low oxygen activities the nonprotective transient oxides such as NiO, Fe_2O_3, and CoO do not form. The defect structure and ionic conductivity of the oxides depend on the oxygen partial pressure, and hence the diffusion rates of cations and oxygen. In the case of chromia formers no strong dependence of parabolic rate constant on oxygen activity was observed [16].

High temperature alloys and coatings are based on Fe, Ni and Co matrices. They require high levels of Al to form protective alumina. At these levels they exhibit brittleness and poor mechanical properties. However, ternary addition of Cr, acting as oxygen getter brings down the required level of Al and promotes the alumina formation [17]. A well known example is the Kanthal-type Fe-25Cr-4Al. For binary alloys Cr must be more than 20% and for ternary Fe-Cr-Al and Ni-Cr-Al, Cr and Al must be above about 15 and 5% respectively.

The protective oxide scales lose their protectiveness when they start spalling and cracking. Degradation is severe under thermal cycles. In the absence of any mechanical abrasion or particle impact (erosion) the major cause of scale breakdown is the growth and thermal stresses. Scales form initially epitaxially. The lattice mismatch between the substrate and the scale induces stresses. As the scale thickens, growth stresses are generated because of the difference in the molar volumes of metal ion and its oxide [18]. The ratio of the oxide:metal volume (Pilling-Bedworth ratio) is greater than 1 for Cr_2O_3 and Al_2O_3. When the oxidation reaction occurs within the scale [19], more compressive stresses are developed. The situation is worse at the edges and the reentrant corners. In addition, thermal stresses are generated during thermal cycles because of the difference in the thermal expansion coefficients between the oxide scale and the alloy. When metal ions are converted into oxides, vacancies are generated and get condensed at the scale/metal interface in the form of pores and cavities [20]. They, in turn, weaken the scale adhesion. At temperatures above 1000°C Cr_2O_3 undergoes an oxidative reaction to form volatile CrO_3 particularly in fast flowing oxygen and in the presence of atomic oxygen and water vapor [16]. Protection offered by Cr_2O_3 above 1000°C is thus limited by frequent spallation or cracking and chemical reactions. Reformation of protective oxide scales depletes Cr or Al in the substrate, and this leads to the formation of nonprotective base metal oxides. To retain the protectiveness of Cr_2O_3 or α-Al_2O_3 the scales should have good fracture toughness and matching creep and thermophysical properties.

It has been known for more than 50 years that a remarkable improvement in scale performance in purely oxidizing conditions can be achieved by small additions of reactive elements or stable oxide dispersoids [21]. The reactive elements have a great affinity for oxygen and include rare earths also. Ce, Dy, Gd, Hf, La, Sc and Y at levels less than about 1 at.% or inert oxides of rare earths, Al, Cr and Si at 1 or 2 vol.% are added in bulk to Fe-, Ni-, and Co-base alloys. A spectacular improvement in the oxide scale adherence by the addition of the above constituents is commonly observed in both the chromia and alumina formers [16,21]. However, the specific effects of oxygen active elements or stable oxide dispersoids are different for chromia and alumina formers. In the first case, the presence of these additions reduces the Cr level (Eq. 1) required for the formation of protective chromia scales, the amount of transient oxides and the extent of transient oxidation. In this respect, they act as oxygen getter. They slow down the oxidation kinetics at temperatures above 850°C or so, and modify the dominant scale growth process from that of cation diffusion controlled to one of anion diffusion controlled. In the case of alumina formers, the reactive elements or their oxides do not have apparently any major influence either on the minimum level of aluminum required to form external alumina scale or on the transient oxidation and the oxidation kinetics. However, these additions do improve scale adherence.

The reactive element (or the oxide dispersoid) effect can be chemical, physical, mechanical, or a combination thereof in nature. The most popular explanations are: (a) oxide pegging: the internally oxidized reactive element containing phases or the oxide dispersoids that lie across the scale-substrate interface keying the scale to the substrate [16,21]; (b) vacancy sink: incoherent interfaces of internally oxidized reactive element containing phases or the oxide dispersoids with the matrix acting as vacancy sinks for the vacancies generated during oxidation reaction and preventing them from condensing at the scale-metal interface into pores and cavities [20-22]; (c) doping of the Cr_2O_3 or α-Al_2O_3 by the reactive elements modifying the scale defect structure and thereby leading to reduced kinetics, growth stresses and increased plasticity [16,21,23,24]; (d) chemical bonding [21,25,26]; and (e) sulfur effect: binding S which otherwise segregates to scale-metal interface weakening the scale adhesion [27,28]. More than one postulate is required often to explain the observed reactive element effects, and there are observations that contradict any one of the above postulates. Observation of Briant and Luthra [29] that Y addition does not reduce the surface S segregation goes against the explanation based on "sulfur gettering". Although the reactive element effect is real and has been exploited in aircraft industry to develop the most oxidation resistant alloys/coatings, explanations of this effect are still a subject of conjecture and controversy. This is one of the areas where technology is ahead of scientific understanding of the phenomenon. Almost the entire data base on reactive element effects comes from observations at temperatures above 800°C.

Careful experiments have been done to understand the effect of reactive elements/dispersoids on the scale morphology and their initial and final location and chemical status [19,23,24,30-34]. (I/M) and (P/M) alloys and ion implanted alloys were used. Scales formed at 1200°C on Fe-27Cr-4Al have small oxide grains near the metal/scale interface and elongated grains near the scale/gas interface. Further, it is postulated that the oxidation reaction takes place within the scale between the inward diffusing oxygen down the oxide grain boundaries and the outward diffusing Al through the oxide grains. Smaller oxide grains are seen at the gas/scale interface on similarly exposed Fe-27Cr-4Al-0.82Y, and the oxide

grains are larger well below the gas/scale interface. A change in the scale growth mechanism is deduced involving oxidation reaction at the metal/scale interface. Y in a similar Fe-25Cr-4Al-0.5Y alloy is present in different shapes and sizes as intermetallic $(FeCr)_4(AlY)$ before thermal exposure [23]. As a result of exposure to oxygen at 1100°-1200°C, α-Al_2O_3 scale with columnar fine grains forms on the alloy by the inward diffusion of oxygen. As the scale front advances, it engulfs the intermetallics $(FeCr)_4(AlY)$. The latter are converted to $Y_3Al_5O_{12}$ thereby doping the scale with Y and releasing Fe and Cr into the matrix. The enhanced scale adhesion is a result of Y doping which promotes fine oxide grains and relief of growth stress by plastic flow. Further, Y prevents Al transport in the oxide grain inhibiting the oxidation reaction within the scale. Y segregation to oxide grain boundaries has been reported in Y implanted Co-25Cr and Fe-20Cr-25Ni/Nb oxidized in O_2 at 1000°C and CO_2 at 825°C respectively [30-32]. In Ce implanted Ni-30Cr alloy exposed to CO/CO_2 gas mixture in the range 900°-1100°C, the Cr_2O_3 growth rate is lower by a factor of 8 than in the unimplanted alloy and Ce rich oxide grain boundaries and random $CeCrO_3$ phases in the oxide scale are reported [24]. The reduction in the parabolic rate constant is attributed to the consumption of Cr interstitials in Cr_2O_3 scale through doping of the scale by Ce in the oxide grain and at oxide grain boundaries.

The presence of a second oxidant such as sulfur can significantly change the oxidation behavior of Cr_2O_3 and Al_2O_3 formers, particularly at low oxygen partial pressures. Under this situation, environmental factors become important, and the effect of minor additions of reactive or other alloying elements is not clearly understood. Thermodynamic stability diagrams for metal-oxygen-sulfur systems constructed from thermodynamic data define the stability regions for various corrosion products as a function of activities of the two gas components. Sulfide formation has been reported in Fe-, Ni- and Co-base alloys in the chromium oxide stability region at oxygen chemical potentials higher than the thermodynamic MS/MO boundaries. The experimental MS/MO boundary, called kinetic boundary for obvious reasons, depends on the levels of Cr or Al and any experimental parameters that promote the protective oxide formation. As the partial pressure of oxygen is increased at given sulfur activity, longer times are required for the protective oxides to be broken down by sulfides. This clearly indicates some parallel diffusion process that involves Fe, Ni, Co and/or Cr. Superposition of thermochemical stability diagrams of each alloying element will not give a true representation of stability regions of reaction products for the alloy because the activities of each component differ from unity in the alloy, and the formation of spinel, thio-spinel, solid solutions, and oxy-sulfides is not considered. The observation of a kinetic boundary clearly indicates the possible changes in the formation of protective oxide scales and the importance of chemical breakdown of these scales in the presence of second oxidant, sulfur. Attempts have been made to construct thermochemical stability diagrams for binary alloys incorporating the variation in metal activities [35,36]. Equilibrium single phase and two phase regions involving mixed sulfides, oxide-sulfide mixtures and spinels have been identified.

On exposure to a substoichiometric low oxygen activity sulfur bearing gas mixture, scale formation can occur in more than one way. Simultaneously, oxide and sulfide nuclei can form and grow at their characteristic rates. If the nucleation rate of sulfides is considerably slower than the corresponding rate of oxide, protective oxide scale will soon form uniformly over the substrate submerging the isolated sulfide nuclei. This happens when

H_2O/H_2S is increased [37]. Further, growth of these initially formed sulfides requires S transport through the protective scale. In the absence of such S transport they do not grow. With a large number of sulfide nuclei the development of protective oxide scale is not possible at lower H_2O/H_2S ratio because the parabolic rate constants for sulfide formation at a given temperature are several orders of magnitude higher than that for oxidation. Global sulfidation will occur.

Cr containing Fe-, Ni- and Co-base alloys which form protective oxide scales exhibit significant variation in their resistance to sulfidation in low oxygen and high sulfur potentials. This emphasizes the importance of the substrate chemistry and the doping of the scale by the base metal ions. Excellent reviews are available on the corrosion behavior of high temperature alloys in coal conversion environments [38,39]. Natesan and his collaborators have examined several Fe base alloys to understand the corrosion behavior in coal derived atmospheres. Regardless of sulfur potential, protective oxide scales form at oxygen partial pressures that are 3 orders of magnitude higher than that of "CrS"/Cr_2O_3 equilibrium values in the temperature range 750°-1000°C. Sulfur penetration through the scale is postulated to initiate sulfidation at the scale/metal interface which leads to internal sulfidation and outward sulfide growth. The scale consists of (NiFe) sulfide at the gas/scale interface and (FeCr) sulfide below this layer. In more oxidizing situation Cr_2O_3 is observed at the metal/scale interface. Perkins and Vonk [40] investigated the corrosion behavior of several model high purity Fe-Cr, Fe-Cr-Ni, Fe-Cr-Al, Ni-Cr, Ni-Cr-Al, and Co-25Cr in the temperature range 600°-1100°C. The oxygen and sulfur potentials covered a wide range: $pS_2=3x10^{-6}$ to 10^{-8} and $pO_2=3x10^{-16}$ to $3x10^{-18}$ atm. Fe-25Cr-20Ni has the least corrosion resistance. Fe-25Cr-5Al and Ni-46Cr form respectively Al_2O_3 and Cr_2O_3 protective scales and have comparable corrosion resistance. Fe is incorporated in oxide scales on Fe-25Cr-20Ni, and not in scales on Fe-25Cr. Fe_3O_4 is not present in chromic oxide scale formed on Fe-25Cr-20Ni in H_2/H_2O mixture. Breakdown of chromic oxide scale is observed to occur at the gas/scale interface by the formation of (FeNi) sulfides. According to Perkins and Vonk [40] the presence of sulfur in the environment assists the outward diffusion of Fe and Ni.

Cr_2O_3 scale with Fe_2O_3 as a minor component forms on Fe-17-30% Cr in $H_2/H_2O/H_2S$ at temperatures 800°-1000°C above the critical oxygen activity. At lower oxygen activity (CrFe) S forms over the Cr_2O_3. Cracks in the Cr_2O_3 scale lead to internal sulfidation and oxidation [36].

Baxter and Natesan studied the effect of Nb and Zr additions on the corrosion behavior of Fe-25Cr and Fe-25Cr-20Ni exposed to oxygen-sulfur environment [2,41,42]. The Cr-oxide scales were more adherent in Nb- or Zr-bearing alloys and scale breakdown was considerably delayed. A barrier layer of refractory metal oxide, Nb_2O_5, below Cr_2O_3 forms in the substrate and reduces the outward diffusion of Fe and Ni. In Nb-implanted Fe-25Cr and Fe-25Cr-20Ni scale breakdown is initiated by the formation of CrS, and (FeCr) and (FeNi) sulfides respectively. Stott et al. exposed Y containing Fe-27Cr and Fe-27Cr-4Al to gas mixtures with $pO_2=3x10^{-23}$ and $pS_2=3x10^{-8}$ atms at 750°C with and without preformed oxide scales [43]. Preoxidation was performed at 900°C in H_2/H_2O for 20 h. All the alloys without any preoxidation develop external sulfides on exposure to mixed gas. Breakdown of preformed Al_2O_3 and Cr_2O_3 scale occurs by sulfur penetration through the scale, formation at the metal/scale interface of base metal sulfides and the establishment of sulfide "ducts". In

alumina forming Y free alloy these ducts are associated with cracks in the scale. Y-containing alloys exhibit a similar process of scale breakdown with the exception that the breakaway corrosion occurs after a longer period of protective oxidation behavior and that the sulfide ducts are not associated with scale cracks possibly because of improved scale plasticity and adhesion due to Y addition.

Huang et al. [44] and Kim and Meier [3] studied the effect of reactive elements on the scale formation and breakdown process in alumina formers at 900°-1100°C. Their experimental alloys were Fe-18Cr-6Al and Fe-18Cr-6Al-1Hf respectively. Both direct exposure and exposure after preoxidation to mixed gas (pO_2=$2x10^{-15}$ to $2x10^{-19}$ and pS_2=10^{-6} to 10^{-10} atm) were employed. Protective alumina scale forms at low pS_2, but at high pS_2 FeS is the major component of the scale. Preformed oxide scale on Hf free alloy breaks down as a result of S ingress through cracks in the scale, and subsequent formation of fast growing sulfides. Hf containing alloy resists the most after preoxidation, and preformed scale on it is also resistant to cracking as indicated by the acoustic emission measurement. According to Kim and Meier [3], on exposure to sulfur containing atmosphere, Fe and HfO_2 in the preformed scale react with S to form (FeS) and HfS_2 channels. These channels assist the diffusion of S and base metal ions, Fe and Cr in opposite directions to form external and internal sulfides.

Stroosnijder [45] considered Ce implantation and external application of CeO_2 to improve the corrosion resistance of Alloy 800H in atmospheres of low oxygen and high sulfur activities at 700°C. The weight gain of Ce implanted (10^{17} ions/sq. cm.) alloy is three times less than that of unimplanted one. The Ce implanted as well as preoxidized CeO_2 coated 800H exhibits scale breakdown starting at the gas/scale interface in the form of (FeCr) sulfide or Cr sulfide. However, ceria coated alloy after preoxidation is resistant to sulfidation for times up to 2000 h in S-O atmosphere at 700°C.

Reliance on Cr_2O_3 or α-Al_2O_3 for sulfidation resistance at high temperatures is thus considerable. These oxides have corundum structure with hexagonal close packing of oxygen ions and Al^{3+} or Cr^{3+} filling two-thirds of octahedral sites. The solubility of S and diffusivity of Fe, Cr, Ni, S and O in them are also considerably small. Such properties are not fully exhibited by the thermally grown Cr_2O_3 and α-Al_2O_3 in purely oxidizing or low oxygen activity gas mixtures. This clearly brings out the importance of doping by the substrate elements, defect structure, grain structure, size and orientation, oxide grain boundary structure, other phases present, and the scale continuity with the substrate of the thermally grown oxides. The reactive element effect in pure oxidation appears to be mostly associated with doping the scale, promoting fine grain oxides and improving creep and fracture properties [23,24,46]. These changes are important, and can provide substantial protection against sulfidation where mechanical scale failure and cracks play a major role in S and other reactant transports in scales on alloys without reactive element addition. Even in situations where the alloys without any reactive element develop compliant protective scale, the addition of reactive elements or dispersoids could play a major role in modifying the scale defect structure to reduce significantly the permeability of reactants such as S, Ni and Fe. Essentially any reactive element addition either in bulk or by surface modification, should reduce the activities of the above elements in the growing scale to delay the breakdown process. Simple reduction in the oxidation kinetics (smaller scale thickness) by the minor

additions alone without any effect on the transport of S and other reactants will not lead to protection against sulfidation, and, in fact, could cause early sulfidation because of shorter diffusion distance/thinner scale.

Effects of minor additions of oxygen active elements and others and surface pretreatments are reasonably established in purely oxidizing conditions at temperatures above 850°C. Extension of the above benefits to multioxidant situations needs to be explored. The role of the above variables in offering protection against corrosion in coal conversion environments at temperatures below 700°C is not well understood. The formation of protective oxides in the presence of second oxidant appears to be different. The processes that lead to the breakdown of protective oxide scales in the oxide stable region in the presence of a second oxidant such as S are not clear. An important step toward developing sulfidation resistant ferritic and austenitic alloys is to understand and discern the factors that govern the formation and maintenance of protective scales in the presence of S and the effect of minor alloying additions and other variables.

2.3 OBJECTIVES AND SCOPE

This program aims at developing a better understanding of corrosion behavior of materials in fossil energy environments and a technology base for new materials that would enhance plant efficiency and reliability. The objective is to achieve better control over the growth and maintenance of protective oxide scales in order to improve the long term durability of heat exchanger and heat recovery materials in low oxygen activity environments through metallurgical and processing innovations without making any compromise over mechanical property requirements. Focus under this objective is to investigate the effects of microalloy constituents, methods of their incorporation, surface treatments and oxidation conditions on the formation and eventual breakdown of protective scales on chromia and alumina forming alloys or coatings.

The program is designed to perform investigations on high purity iron base alloys that are representatives of chromia and alumina formers with and without microconstituents. Minor alloying additions are chosen from reactive elements and other conventional additives. Although originally only elemental additions are planned, near the end of this program the possible positive influence of alumina addition to chromia formers is recognized. Alloys with alumina dispersoids are also consequently examined, thereby expanding the scope of this program. I/M route and surface modification by direct ion implantation are the two methods of incorporation of alloying elements considered here. Corrosion response of the experimental alloys is studied isothermally and cyclically in typical simulated coal derived atmospheres to evaluate the effects of alloying additions, the method of incorporation, surface pretreatments and oxidizing conditions. The emphasis is in the temperature range from 500° to 700°C. In addition, pure oxidation runs are included to provide a basic understanding of the nature of the scale that forms in the absence of a second oxidant, S. Surface pretreatments include cold rolling by about 50%. A variety of advanced surface and other analytical tools are used to characterize the scale, and the initial and final location and chemical status of scale-forming species and the additives.

3.0 TECHNICAL APPROACH

3.1 EXPERIMENTAL MATERIALS

3.1.1 Base Alloys

The base alloys, Fe-25Cr, Fe-25Cr-20Ni and Fe-25Cr-6Al were prepared by Carpenter Technology Corporation for use by all the participants of this program. The master heats were approximately 60 kg. The alloys were produced by vacuum induction melting (VIM) and cast into 3 to 3.25 in. round ingots. They were then electroslag refined to reduce undesirable contaminants, and cast into round ingots of 5.8 in. in diameter. The alloys were hot forged in 2.25 in. squares after soaking the Fe-25Cr and Fe-25Cr-20Ni alloys at 1065°C and 1177°C for 2 h. The forged Fe-25Cr and Fe-25Cr-20Ni were hot cut, while Fe-25Cr-6Al was cold cut. The alloys were reheated to the soaking temperatures for 30 min., hot rolled into prismatic bars of 1 in. squares and slowly cooled in vermiculite.

The chemical compositional analyses of the base alloys in wt.% are given in Table 1.

Table 1. Wet Chemical analysis of base alloys, wt.%.

Alloy Designation	Fe-25Cr	Fe-25Cr-20Ni	Fe-25Cr-Al
Heat No.	T08007	T08008	T08009
Cr	24.68	24.8	24.73
Ni	<0.01	19.47	<0.01
Al	0.02	0.01	5.59
Si	0.03	0.02	0.04
C	0.02	0.02	0.02
S	0.002	0.003	0.002
P	0.027	0.027	0.028
Mn	<0.01	<0.01	<0.01
Ti	<0.01	<0.01	<0.01
O	0.035	0.056	0.0034
Fe	Bal	Bal	Bal

3.1.2 (I/M) Alloys with Minor Additions of Reactive and Other Constituents

Microconstituents that are chosen to modify the base alloys by bulk additions or by surface implantation are Ce, Hf, La, O, Pt, Si, Y and Al_2O_3.

Alloys with bulk additions of Ce, Hf, La, Pt, Si and Y were prepared by the Materials Preparation Center of Ames Laboratory, Iowa State University, Ames, IA through I/M route. For this purpose the base alloys of the compositions reported in Table 1 were provided to the above center. The base alloys were cleaned first removing the exterior oxide scale by abrasive grinding, then in cold HCl and rinsed in methanol. The alloying additions were cleaned using appropriate chemical regents followed by thorough rinsing in methanol. The base alloy and the addition element were weighed using an accuracy of ±0.1 mg. One weight percent level was chosen for each microconstituent addition.

Alloys were nonconsumably arc melted into button shaped ingots by first melting the base alloys and allowing the addition elements to be drawn into the molten base alloys. Each alloy button was remelted, flipped over and melted again, and this sequence was repeated to ensure homogeneity. The arc melted button was placed on a copper drop cast mold, arc-melted and allowed to drop cast. The total weight of each alloy was about 130 g. Since all the experimental I/M alloys were prepared following the same procedure, wet chemical analysis was not done on each alloy, but a few alloys were analyzed to estimate the level of impurities introduced by the process. Table 2 lists the experimental alloys with nominal chemical composition, and Table 3 gives the results of wet chemical analysis of a few alloys.

3.1.3 (I/M) Alloys for the Studies on the Effect of Surface Pretreatment

The above preparation procedure was followed to obtain Fe-25Cr and Fe-25Cr-6Al with 0.3 Hf or 0.3 Y for studies on the effect of surface pretreatment. Each alloy button was sealed inside a 316 stainless steel (SS) jacket in an argon filled glove box. The SS envelopes were then placed in a muffle furnace at 800°C and allowed to reach the furnace temperature. Each envelope was then individually removed from the furnace, and quickly rolled at a reduction of 0.015 to 0.02 in. per pass and returned to the furnace. Hot rolling was continued until all the alloys were reduced to approximately 2 mm in thickness. Alloys to be cold rolled were set aside for cooling to R.T. Hot rolling was continued as described above in the case of other alloys till a final thickness of about 1 mm was reached. The alloys that were set aside were cold rolled at a reduction rate of 0.01 in. per pass again to a final thickness of 1 mm (40-50% cold reduction). The SS envelopes were then opened, and the alloy sheets were removed. The nominal chemical compositions of the alloys are given in Table 2.

3.1.4 (P/M) Alloys with Al_2O_3 Dispersoids

Experimental alloys with alumina dispersions were prepared at the Battelle Columbus Division. The starting materials were elemental powders (Cerac, Inc.) of size $\leq$5 μm and alumina powder of submicron size prepared at UES by sol gel method.

Table 2. Designation and nominal chemical compositions of the experimental alloys, wt.%.

Designation	Nominal Composition	Route	Initial Condition
T08007	Fe-25Cr	I/M	A
AFX-5	Fe-25Cr-1Ce	I/M	A
AFW-60	Fe-25Cr-1Hf	I/M	A
AFX-8	Fe-25Cr-1La	I/M	A
AFW-64	Fe-25Cr-1Pt	I/M	A
AFW-299	Fe-25Cr-3Si	I/M	A
AFX-7	Fe-25Cr-1Y	I/M	A
AFY-116H	Fe-25Cr	I/M	HR
AFY-116C	Fe-25Cr	I/M	CR
AFY-117H	Fe-25Cr-0.3Hf	I/M	HR
AFY-117C	Fe-25Cr-0.3Hf	I/M	CR
AFY-120H	Fe-25Cr-0.3Y	I/M	HR
AFY-120C	Fe-25Cr-0.3Y	I/M	CR
UES-1	Fe-25Cr-1.5Al_2O_3	P/M	A
T08008	Fe-25Cr-20Ni	I/M	A
AFW-151	Fe-25Cr-20Ni-1Ce	I/M	A
AFW-69	Fe-25Cr-20Ni-1Hf	I/M	A
AFX-2	Fe-25Cr-20Ni-1La	I/M	A
AFW-144	Fe-25Cr-20Ni-1Pt	I/M	A
AFW-296	Fe-25Cr-20Ni-3Si	I/M	A
AFX-4	Fe-25Cr-20Ni-1Y	I/M	A
UES-2	Fe-25Cr-20Ni-1.5Al_2O_3	P/M	A
T08009	Fe-25Cr-6Al	I/M	A
AFX-10	Fe-25Cr-6Al-1Ce	I/M	A
AFX-15	Fe-25Cr-6A-1Hf	I/M	A
AFX-12	Fe-25Cr-6Al-1La	I/M	A
AFX-9	Fe-25Cr-6Al-1Pt	I/M	A
AFX-13	Fe-25Cr-6Al-3Si	I/M	A
AFX-11	Fe-25Cr-6Al-1Y	I/M	A
AFY-121H	Fe-25Cr-6Al	I/M	HR
AFY-121C	Fe-25Cr-6Al	I/M	CR
AFY-122H	Fe-25Cr-6Al-0.3Hf	I/M	HR
AFY-122C	Fe-25Cr-6Al-0.3Hf	I/M	CR
AFY-123H	Fe-25Cr-6Al-0.3Y	I/M	HR
AFY-123C	Fe-25Cr-6Al-0.3Y	I/M	CR

I/M = Ingot Metallurgy
P/M = Powder Metallurgy; Mechanical Alloying
A = Annealed or Homogenized
HR = Hot-rolled
CR = Cold-rolled

Table 3. Wet chemical analyses of a few selected experimental (I/M) alloys, in wt.%.

Elements	AFW-60	AFW-64	AFW-69	AFW-144	AFW-151
C	0.01	0.01	0.01	0.01	0.01
Mn	<0.01	<0.01	<0.01	<0.01	<0.01
P	0.008	0.008	0.013	0.009	0.009
S	0.005	0.01	0.005	0.005	0.005
Si	0.04	0.04	0.04	0.04	0.04
Ni	<0.01	0.02	18.86	18.86	19.2
Cr	24.71	24.7	24.32	24.66	24.6
Cu	<0.01	<0.01	<0.01	<0.01	<0.01
Al	0.02	0.019	0.02	0.019	0.02
Ti	<0.01	<0.01	<0.01	<0.01	<0.01
Hf	0.83	-	0.82	-	-
Pt	-	0.96	-	1.03	-
Ce	-	-	-	-	1.18
O	0.034	0.034	0.019	0.053	0.02
Fe	Bal	Bal	Bal	Bal	Bal

Milling was done in Spex Model 8000 mixer mill using a hardened steel mill cylinder, and stainless steel balls (reject bearings). All runs started with 500 g of balls; powder was turboblended for 30 min. before milling; after loading, the mill was purged with Ar before sealing, and then run at 190 rpm. The argon was used for its surfactant properties in the mechanical alloying process.

The alloy powders were cold pressed at 40 ksi in 1 in. OD, 1/8 in. wall, type 304SS tubes (plugged with 3/8 in. endcaps and seal welded at the bottom) vacuum outgassed overnight (at ~5 μ) at a temperature that was gradually increased to 1000°C, and then sealed off while hot. The sealed tubes were leak checked before and after consolidation by hot isostatic processing (HIP). HIP-ing was done at Battelle; the conditions were 300 ksi at 1200°C for 3 h. After consolidation, the 304SS can was removed by machining in each case. The nominal composition of the P/M alloys are given in Table 2.

3.1.5 Ion Implanted Alloys

Besides the P/M and the conventional I/M routes to incorporate the microconstituents, direct ion implantation process was selected to study the effect of method of incorporation of minor elements on the corrosion behavior in this program. The minor elements chosen for surface modifications were Ce, Hf, Y, Si, and O. All three base alloys were implanted with each of the selected ions.

Coupons of approximate dimensions 10 mm x 10 mm x 1 mm were cut from the supplied base alloy bars. They were polished both sides metallographically up to 1 μ diamond, ultrasonically cleaned, thoroughly washed with deionized water and dried. Direct ion implantation was carried out either in Tandetron, a high energy implanter or Extrion, a high beam current unit. The substrate alloys and the details of implantation are given in Table 4.

3.1.6 Initial Conditions of the Experimental Materials

Rectangular or circular coupons were cut from the supplied bars with approximate dimensions of 10 mm x 10 mm x 1 mm or diameter 12 mm x 1 mm. A hole with a millimeter in diameter was drilled in each coupon for suspension into the reaction chamber. Actual dimensions of each coupon were measured before exposure. These coupons were metallographically polished, finishing with 1 μ diamond paste. They were ultrasonically cleaned, thoroughly washed in deionized water and dried. No heat treatment was given to the supplied bars before or after cutting the coupons.

Table 4. Substrate alloys and the details of ion-implantation.

Substrate Alloy Composition	Species Implanted	Energy KeV	Nominal Dose, ions/cm^2
Fe-25Cr	Ce^+	180	$4x10^{16}$
Fe-25Cr-20Ni	Si^+	1000	$5x10^{16}$
	O^+	1000	10^{17}
	Pt^+	1000	10^{16}
	$Si^+ + O_2^+$	1000; 625	10^{16}; $2x10^{16}$
Fe-25Cr-6Al	Ce^+	160	$5x10^{16}$
	Si^+	1000	$5x10^{16}$
	Y^+	160	10^{16}

3.2 EXPERIMENTAL METHODS

3.2.1 Isothermal and Cyclic Oxidation

Oxidation characteristics of base alloys, alloys with bulk additions of microconstituents and ion implanted alloys were studied under isothermal and cyclic conditions at temperatures ranging from 700° to 900°C for times up to 500 h. For this purpose, Cahn microbalances were used. Samples were suspended from one arm of the balance into a quartz reaction tube, and a continuous positive flow of dry oxygen in reaction tube was maintained at about 100 cm^3/min and 1 atm. The preheated tubular furnace was raised to surround the sample to initiate the oxidation reaction. The sample reached the test temperature in about 20 min. Weight change was continuously recorded. The test temperature was maintained within ±2°C. The oxidation kinetics was so slow below 700°C that the isothermal tests at 500° and 600°C were not continued.

Cyclic tests were performed on selected alloys by raising and lowering the furnace at regular intervals pneumatically. Each thermal cycle was of 1 h duration. The sample was maintained at the test temperature for 50 min, and for the remaining 10 min the furnace was brought well below the sample. The lowest temperature that the sample experienced during each thermal cycle was about 50°C. A continuous flow of dry O_2 at 1 atm was maintained at 100 cm^3/min.

Coupons were weighed before and after exposure.

3.2.2 Isothermal and Cyclic Exposures to Gas Mixture $H_2/H_2O/H_2S/Ar$

Samples were exposed to gas mixtures of H_2, H_2O, H_2S and Ar. A premixed H_2-2% H_2S gas was used to obtain the required sulfur activity at the test temperatures, and a separate stream of Ar was bubbled through a water bath maintained at a constant temperature. Gas flows were controlled by commercial mass flow controllers and a central electronic feedback system. Samples were hung from quartz pins of a quartz extension rod inside a horizontal quartz reaction tube with their thinnest sides facing upstream. An auto honeycomb Pt catalyst was kept just ahead of the samples upstream at the same temperature as the samples to equilibrate the two gas mixtures. The reaction quartz tube with samples and the auto catalyst was surrounded by a tubular resistance furnace. The furnace temperature was controlled by a commercial temperature controller, and the specimen temperature was maintained within ±2°C of the test temperature. The test temperature and the other experimental parameters are given in Table 5.

Multiple specimens were exposed simultaneously to a given set of experimental conditions. Specimens were hung from quartz pins at one end of a quartz extension rod. The other end of the rod had an encapsulated iron piece. The extension rod with samples were concentrically enclosed inside the quartz reaction tube. Initially the samples were kept in cold part of the reaction tube. N_2 was first flowed to flush out air, and then switched to the experimental gas mixture. When the test temperature was reached in the test section of the quartz reaction tube, the extension rod with the samples was slowly and gently pushed in using an electromagnet, and the reaction was started. At the end of the exposure the

Table 5. Experimental parameters.
(Exposure time varied: 10 min to 192 h)

Temp °C	Flow Rate, sccm			Water Temp. °C	pO_2 atm.	pS_2 atm.	Gas Mixture Designation
	H_2	H_2/H_2S	Ar				
700	10	-	190	47	1.13×10^{-20}	-	A
	-	10	190	47	1.17×10^{-20}	1.22×10^{-8}	B
	-	30	170	47	1.30×10^{-21}	1.19×10^{-8}	C
	-	50	150	35	1.18×10^{-22}	1.19×10^{-8}	D
600	-	10	190	47	1.11×10^{-23}	9.43×10^{-10}	E
500	-	10	190	47	1.72×10^{-27}	3.78×10^{-11}	F
1000	10	-	190	47	1.97×10^{-14}	-	G

$\log pH_2O \text{ (atm)} = -\frac{2900}{T} - 4.65 \log T + 19.732$ [Ref. 47]

$H_2 + 1/2\ O_2 \rightarrow H_2O$; $\Delta G = -246000 + 54.8T$, J [Ref. 47]

$H_2 + 1/2\ S_2 \rightarrow H_2S$; $\Delta G = -90290 + 49.39T$, J [Ref. 47]

extension rod was again gently pulled out to the cold part of the tube using the electromagnet maintaining the flow of the experimental gas mixtures. The gas was switched to N_2 to drive away completely the experimental gas mixture when the samples cooled down to about 50°C. After turning off the N_2 gas the exposed samples were removed carefully from the quartz reaction tube.

Coupons were weighed before and after each exposure.

A few samples were periodically exposed to $H_2/H_2O/H_2S$/Ar mixture at 700°C to evaluate the propensity of the scale to fracture due to thermal cycles. The periodic exposure was achieved manually, and one block of thermal cycles is shown schematically in Figure 1. Each block was of 24 h duration, and samples were exposed to four such blocks, totalling 96 h.

For kinetics study a Cahn microbalance was used to record continuous weight change of the sample in the experimental gas mixture.

3.2.3 Isothermal Preoxidation and Mixed Gas Exposure

To study the scale breakdown processes/mechanisms, samples were preoxidized in $H_2/H_2O/Ar$ mixture at 700° and 1000°C for times up to 96 h. Before each preoxidation run, the reaction quartz tube was baked in flowing H_2 at a temperature higher than 700°C or at 1000°C for times up to 24 h to drive away any residual S from the previous sulfidation tests. Samples were introduced into and removed from the reaction chamber/quartz tube following the procedure described above. After preoxidation either samples were removed for the scale analysis or exposed to sulfidizing gas mixture ($H_2/H_2O/H_2S/Ar$). The samples were thus not subject to a thermal shock in the latter case, when the temperatures of preoxidation and subsequent sulfidation were the same. However, a mild thermal shock was experienced by samples that were preoxidized at 1000°C or 700°C and sulfidized later at 700°C or below respectively.

Exposure matrix is given in Table 6.

3.2.4 Characterization of Scales and the Substrates

To achieve the objectives of this program a variety of analytical tools were used, and they included optical and scanning electron microscopy (SEM), energy dispersive analysis by X-rays (EDAX), X-ray diffraction (XRD), scanning/transmission electron microscopy (STEM), sputter Auger electron spectroscopy (AES), scanning Auger microprobe (SAM), X-ray photo spectroscopy (XPS)/electron spectroscopy for chemical analysis (ESCA), secondary ion mass spectrometry (SIMS), Rutherford backscattering spectroscopy (RBS) and mechanical probe (Nanoindentor). The choice of the technique was made on the basis of the scale thickness and the information required to understand the scale formation/breakdown processes. Although oxygen was detected by EDAX, it was not included in the chemical analysis by EDAX. The estimated weight percent data are expressed in this report taking the total weights of metals and sulfur to be 100.

Special specimen preparation was required only for STEM studies. Coupons of experimental steels were metallographically polished down to a thickness of about 100 μ. Discs of 3 mm in diameter were punched out from these foils. After thorough washing and drying, they were exposed to various experimental environments for times up to 24 h. The exposed discs were electrolytically thinned using a single jet polishing unit and a solution consisting of 100 ml methanol, 200 ml butyl cellosolve, 12 g lithium chloride and 24 g magnesium perchlorate. The temperature and voltage were in the range of -50 to 60°C and 80 to 200 V. After perforation the samples were cleaned in running water, dried and ion-milled to improve the electron transparency using a Gatan ion-mill.

Table 6. Exposure matrix.

Alloy	Gas Mixture and T°C			Oxidation in Oxygen	Sulfidation in Gas Mixture of Preformed Oxide Scale
	B,700°	E,600°	F,500°		
Fe-25Cr	✓	✓	✓	✓ (I,C,L)	✓
Fe-25Cr-1Ce	✓	-	-	✓ (L)	✓
Fe-25Cr-1Hf	✓	✓	✓	✓ (I,C,L)	✓
Fe-25Cr-1La	✓	-	-	✓ (L)	✓
Fe-25Cr-1Pt	✓	-	-	✓ (I)	-
Fe-25Cr-3Si	✓	-	-	✓ (L)	✓
Fe-25Cr-1Y	✓	✓	✓	✓ (L)	✓
Fe-25Cr (HR)	-	-	-	-	✓
Fe-25Cr (CR)	-	-	-	-	✓
Fe-25Cr-0.3Hf (HR)	-	-	-	-	✓
Fe-25Cr-0.3Hf (CR)	-	-	-	-	✓
Fe-25Cr-0.3Y (HR)	-	-	-	-	✓
Fe-25Cr-0.3Y (CR)	-	-	-	-	✓
Fe-25Cr-1.5Al_2O_3	✓	-	-	✓ (I,C,L)	✓
Fe-25Cr-Ce (Imp)	✓	-	-	✓ (L)	✓
Fe-25Cr-20Ni	✓	✓	✓	✓ (I,C,L)	✓
Fe-25Cr-20Ni-1Ce	✓	-	-	✓ (L)	✓
Fe-25Cr-20Ni-1Hf	✓	✓	✓	✓ (I,C)	✓
Fe-25Cr-20Ni-1La	✓	-	-	✓ (L)	✓
Fe-25Cr-20Ni-1Pt	✓	-	-	✓ (I)	✓
Fe-25Cr-20Ni-3Si	✓	-	-	✓ (L)	✓
Fe-25Cr-20Ni-1Y	✓	✓	✓	✓ (L)	✓
Fe-25Cr-20Ni-1.5Al_2O_3	✓	-	-	✓ (I,C,L)	✓
Fe-25Cr-6Al	✓	✓	✓	✓ (L)	✓
Fe-25Cr-6Al-1Ce	✓	-	-	✓ (L)	✓
Fe-25Cr-6Al-1Hf	✓	✓	✓	✓ (L)	✓
Fe-25Cr-6Al-1La	✓	-	-	✓ (L)	✓
Fe25Cr-6Al-1Pt	✓	-	-	✓ (L)	✓
Fe-25Cr-6Al-3Si	✓	-	-	✓ (L)	✓
Fe-25Cr-6Al-1Y	✓	✓	✓	✓ (L)	✓
Fe-25Cr-6Al-Ce (Imp)	-	-	-	-	✓
Fe-25Cr-6Al-Y (Imp)	-	-	-	-	✓
Fe-25Cr-6Al (HR)	-	-	-	-	✓
Fe-25Cr-6Al (CR)	-	-	-	-	✓
Fe-25Cr-6Al-0.3Hf (HR)	-	-	-	-	✓
Fe-25Cr-6Al-0.3Hf (CR)	-	-	-	-	✓
Fe-25Cr-6Al-0.3Y (HR)	-	-	-	-	✓
Fe-25Cr-6Al-0.3Y (CR)	-	-	-	-	✓

I = Isothermal at 1 atm. O_2
C = cyclic at 1 atm. O_2
L = Low pO_2

HR = Hot-rolled
CR = Cold-rolled

4.0 EXPERIMENTAL RESULTS

4.1 PREEXPOSURE MICROSTRUCTURE OF EXPERIMENTAL ALLOYS

More than 35 alloys with and without bulk additions of microconstituents were investigated. Initial microstructures of a selected number of alloys are shown in Figure 2a-2n. Minor additions have very limited or zero solubility in the base alloys and significantly segregated to grain boundaries. However, the microstructure of (P/M) alloys is totally different and has fine grains. No attempt was made to obtain uniform grain sizes in all alloys.

4.2 ISOTHERMAL AND CYCLIC OXIDATION KINETICS

4.2.1 Base Alloys

Oxidation kinetics of base alloys Fe-25Cr and Fe-25Cr-20Ni alloys exhibited modest weight gains during isothermal oxidation in pure O_2 at 700°C. Figure 3 shows the relationship between specific weight gain (weight gain/unit area) and time for the above alloys. Their weight gains were comparable at any instant. However, the Fe-25Cr-6Al alloy gained negligible weight under identical exposure conditions, and, therefore, no meaningful kinetic plots could be made. Specific weight gains were plotted in log-log scale, (not shown). The slopes obtained from log-log plots may not, in general, represent the steady state kinetics because of significant contributions from the transient oxidation with faster kinetics.

During oxidation the total specific weight gain, Δm, at any instant is a sum of two components (48-49):

$$\Delta m = \Delta m_i + \Delta m_p \qquad (3)$$

Δm_i is the weight gain due to transient oxidation, and is a function of time, t until $t=t_i$, the end of transient period. At $t>t_i$, Δm_i is a constant. Δm_p represents the steady state weight gain assuming parabolic rate kinetics. It is difficult to deduce from the weight gain data whether the protective scale (chromia or alumina) formation with its characteristics parabolic rate kinetics is established at the initiation of oxidation reaction or at a latter time, $t>0$. Considering that parabolic rate kinetics is established at a finite time, $t_p>0$, the total specific weight gain, Δm at $t>t_i>t_p$ is, according to Pieraggi (48), given by

$$\Delta m = \Delta m_i + k_p^{1/2} (t-t_p)^{1/2} \qquad (4)$$

where Δm_i is a constant representing the total specific weight gain as a result of defunct transient oxidation and k_p is the true parabolic rate constant.

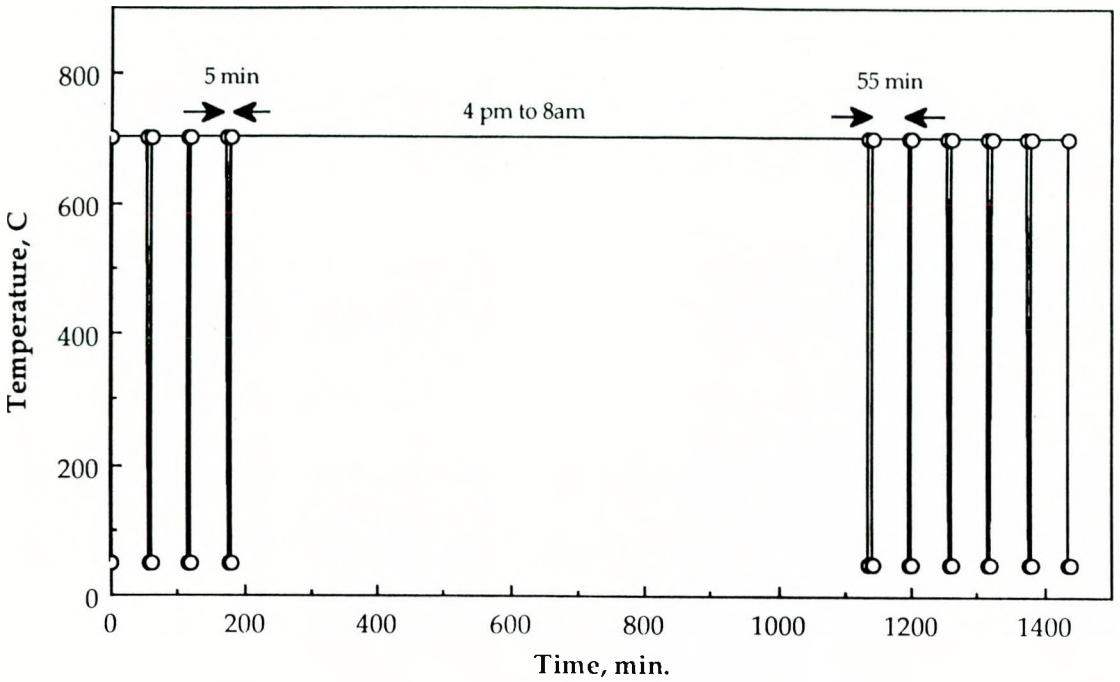

Fig. 1. One block of thermal cycles in gas mixture B.

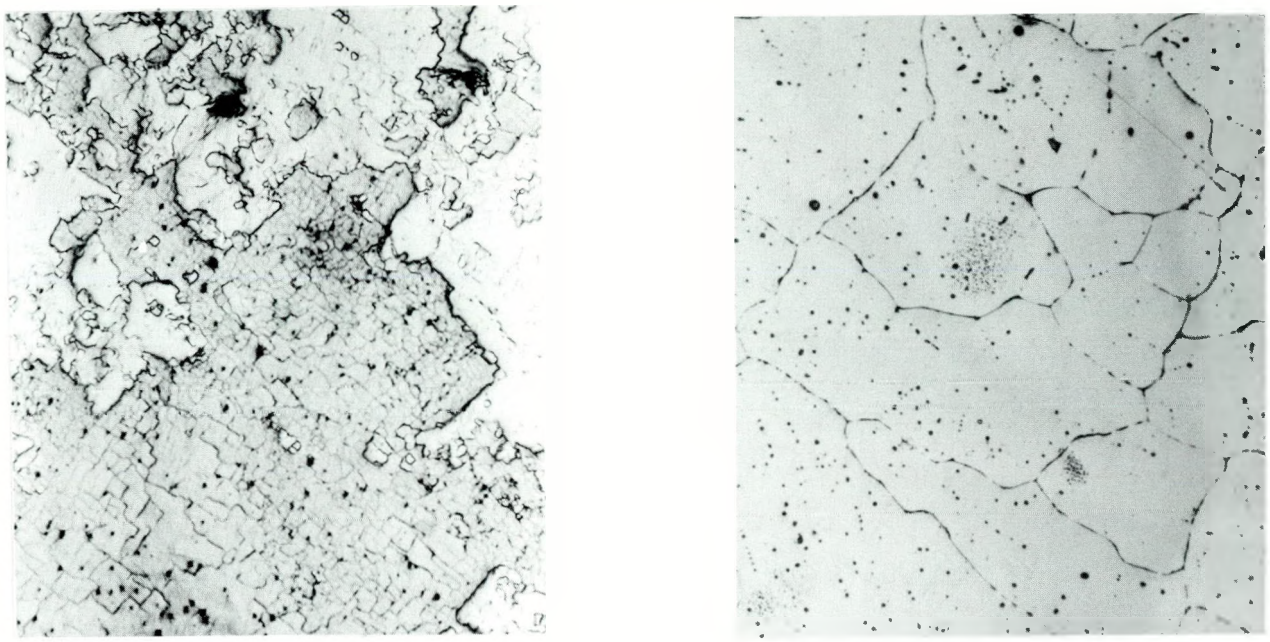

(a) Fe-25Cr, 87.5X

(b) Fe-25Cr-1Ce, 200X

Fig. 2. Initial microstructure of experimental alloys.

(c) Fe-25Cr-1Hf, 100X

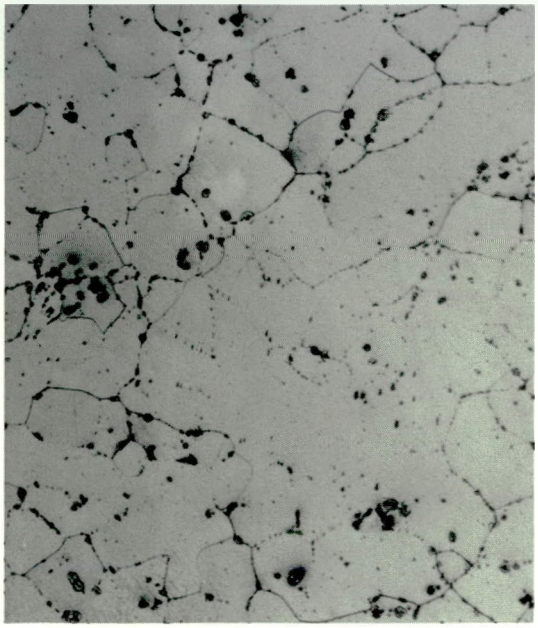

(d) Fe-25Cr-1La, 100X

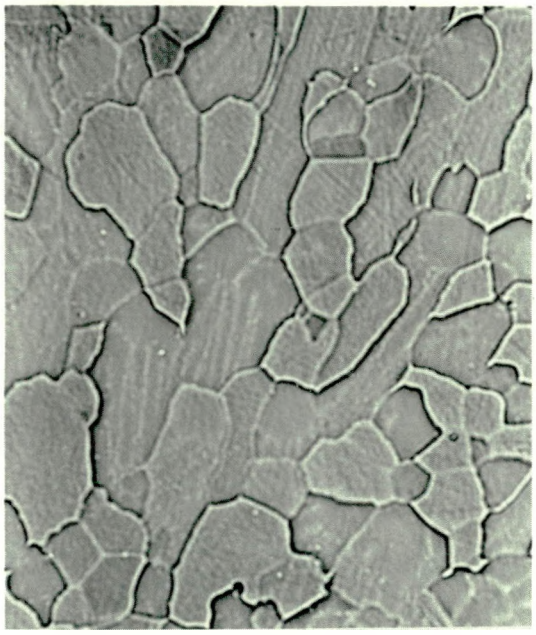

(e) Fe-25Cr-1Pt, 100X

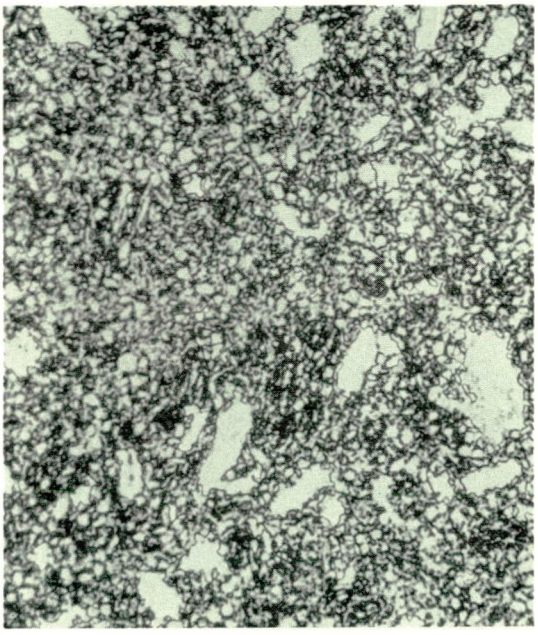

(f) Fe-25Cr-1.5Al_2O_3, 400X

Fig. 2 (cont'd.). Initial microstructure of experimental alloys.

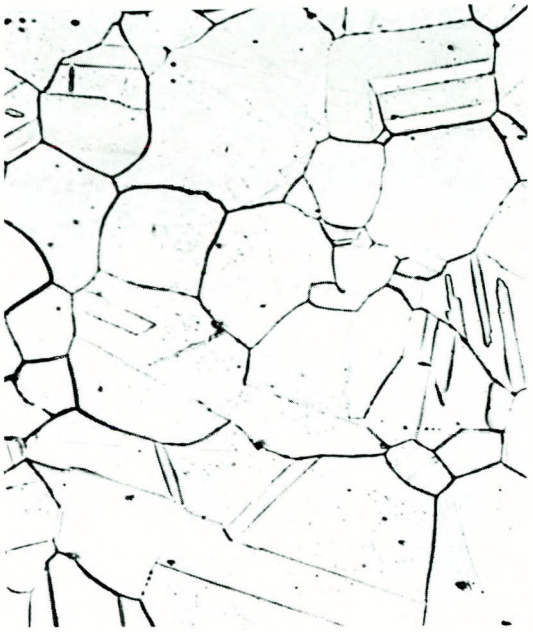

(g) Fe-25Cr-20Ni, 200X

(h) Fe-25Cr-20Ni-1Ce, 400X

(i) Fe-25Cr-20Ni-1Hf, 400X

(j) Fe-25Cr-20Ni-1La, 100X

Fig. 2 (cont'd.). Initial microstructure of experimental alloys.

(k) Fe-25Cr-20Ni-1Pt, 400X

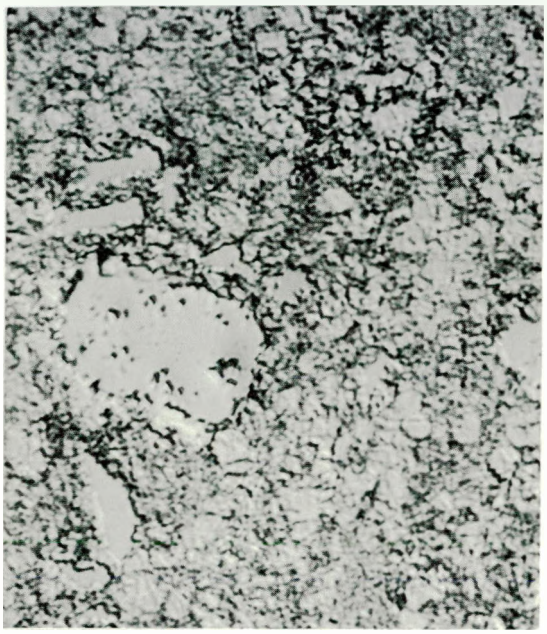

(ℓ) Fe-25Cr-20Ni-1.5Al_2O_3, 400X

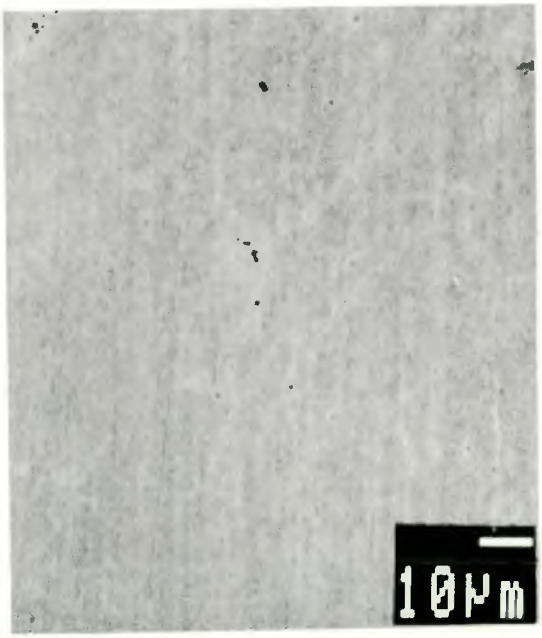

(m) Fe-25Cr-6Al

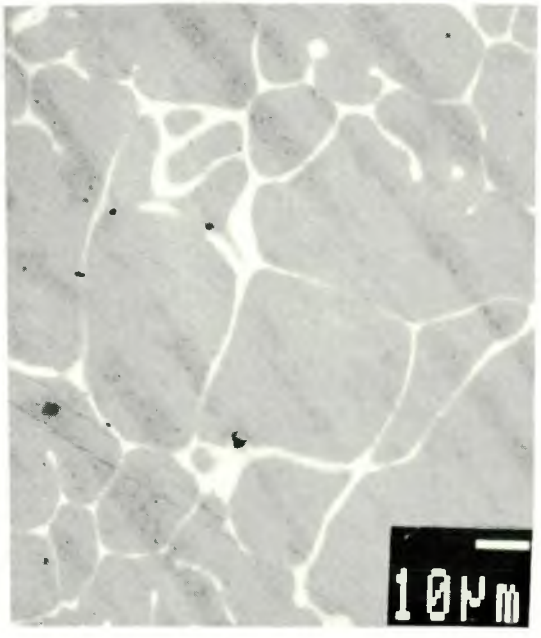

(n) Fe-25Cr-6Al-1Y, 100X

Fig. 2 (cont'd.). Initial microstructure of experimental alloys.

The values of k_p and t_p are not known a priori and have to be evaluated from the experimental values of the total specific weight gain, Δm. Typical plots of Δm vs $t^{1/2}$ are shown in Figures 4a-b for Fe-25Cr and Fe-25Cr-20Ni. The total weight gain, Δm at $t>t_i$ is given by

$$\Delta m = \Delta m_i' + k_p'^{1/2}\, t^{1/2} \tag{5}$$

Here $\Delta m_i'$ is the intercept on the Y axis and k_p is the apparent parabolic rate constant. Δm_i, $\Delta m_i'$,k_p and k_p' are related as shown below (48):

$$\frac{\Delta k_p}{k_p} = \frac{(k_p'-k_p)}{k_p} = \frac{t_p}{(t-t_p)} \tag{6}$$

$$\Delta m_i - \Delta m_i' = \frac{k_p^{1/2}\, t_p}{(t-t_p)^{1/2}} \tag{7}$$

The values of the Y intercept, $\Delta m_i'$ and the apparent parabolic rate constant, k_p' were obtained by fitting a line to the long term kinetic data using the least square approximation. The constant, Δm_i for each alloy was the maximum plateau value (Y intercept) at long times of the plot,

$$\Delta m_i = \Delta m - k_p^{1/2}\,(t-t_p) \simeq \Delta m - k_p^{1/2}\, t^{1/2} \tag{8}$$

since $k_p \simeq k_p'$ at $t>>t_p$. The values of Δm_i, $\Delta m_i'$, k_p, k_p' and t_p for the base alloys are given in Tables 7a-b.

The specific weight gains of Fe-25Cr and Fe-25Cr-20Ni under isothermal and cyclic conditions are given as a function of time and temperature in Figures 5a-b. The Arrhenius plots of isothermal true parabolic rate constants, k_p are shown in Figures 6a-b for the base alloys. The activation energies estimated from these plots for oxidation processes in Fe-25Cr and Fe-25Cr-20Ni are 40.56 and 32.52 Kcal/mole respectively, Table 8.

4.2.2 (I/M) Alloys with Minor Bulk Additions

The results of isothermal and cyclic oxidation tests of Fe-25Cr-20Ni-1Hf and Fe-25Cr-20Ni-1Pt are shown in Figures 7a-b in the form of specific weight gains vs time. Data appear to fall within the scatter band of specimen-to-specimen variation, and thus, there

Table 7(a) Experimental values of kinetics parameters for selected alloys.
(a) Fe-25Cr and its derivatives

Alloy	Temp °C	$x10^6 mg^2/cm^4$ min k_p' or $k_p^*=k_p(a)$	mg/cm^2		t_p, min
			Δm_i	$\Delta m_i'$	
Fe-25Cr	700	3.57 (I)	0.1170	0.1168	0
		3.39 (I)	0.06333	0.06344	0
		5.74 (I)	0	0	0
		1.25 (I)	0	0	0
		1.45 (I)	0.204	0.2038	0
	820	1.18 (I)	0	0	0
	900	55.78 (I)	0.0736	0.0735	0
		14.08 (C)	0.1798	0.1799	0
Fe-25Cr-1.5Al_2O_3	700	0.17 (I)	.001	0.0008	0
		0.53 (I)	0	0	0
		0.65 (C)	0.032	0.033	0
	800	4.46 (I)	0.0345	0.0348	0
		4.75 (C)	0	0	0
	900	11.58 (I)	0.153	0.1531	0
		12.67 (C)	0.08875	0.08875	0
Fe-25Cr-1Pt	700	3.0 (I)	0.032	0.032	0

I = Isothermal Oxidation, C = Cyclic Oxidation; Test Temp. ↔ 50°C; (a) because t_p=0, Eq. 6

Table 7(b) Experimental values of kinetics parameters for selected alloys.
(b) Fe-25Cr-20Ni and its derivatives

Alloy	Temp °C	$x10^6 mg^2/cm^4$ min k_p' or $k_p^*=k_p(a)$	mg/cm²		t_p, min
			Δm_i	$\Delta m_i'$	
Fe-25Cr-20Ni	700	2.67 (I)	0.1093	0.1093	0
		4.52 (I)	0.1123	0.1120	0
		3.74 (C)	0.2246	0.2254	0
		74.7 (I)	0	0	0
		12.89 (I)	0.1523	0.1523	0
	800	3.63 (I)	0.05033	0.0504	0
		5.15 (C)	0.1029	0.1038	0
	900	84.12 (I)	0	0	0
		19.82 (C)	0.2446	0.2445	0
Fe-25Cr-20Ni-1Hf	700	5.89 (I)	0.2718	0.2719	0
		8.46 (I)	0.0454	0.0422	0
		14.63 (C)	0.1647	0.1645	0
		10.47 (I)	0.151	0.1512	0
		1.75 (I)	0.076	0.0761	0
Fe-25Cr-20Ni-1Pt	700	2.05 (I)	0.0500	0.0521	0
		23.26 (I)	0	0	0
O-Imp. Fe-25Cr-20Ni	700	0.77 (I)	0.159	0.159	0
		2.32 (I)	0.1246	0.1247	0
		4.79 (C)	0.3785	0.3793	0
Si-Imp. Fe-25Cr-20Ni	700	0.63 (I)	0.1945	0.1943	0
		1.16 (I)	0.1324	0.1325	0
		0.17 (I)	0.146	0.1458	0
Si-O-Imp. Fe-25Cr-20Ni	700	4.56 (I)	0.1258	0.126	0
Fe-25Cr-20Ni-1.5Al_2O_3	700	0.58 (I)	0.021	0.0207	0
	800	1.81 (I)	0.0133	0.0135	0
		1.05 (C)	0.0187	0.0187	0
	900	17.56 (I)	0.1302	0.1302	0
		10.96 (C)	0.125	0.1252	0

I = Isothermal Oxidation, C = Cyclic Oxidation; Test Temp. ↔ 50°C; (a) because t_p=0, Eq. 6

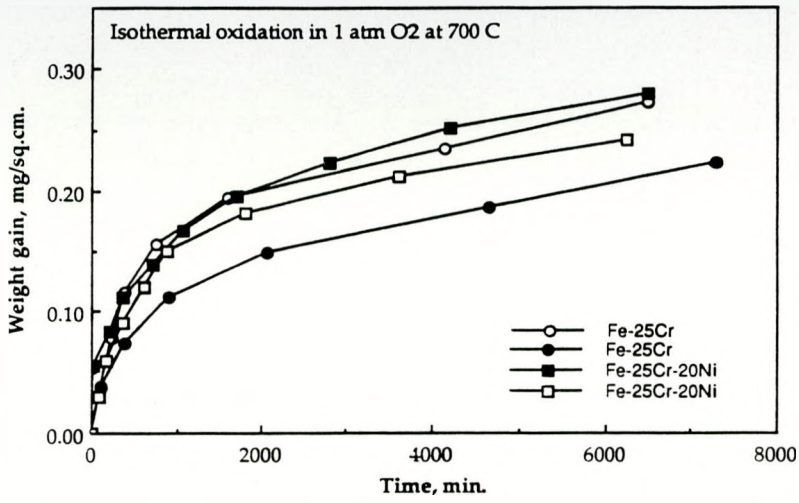

Fig. 3. Specific weight vs time.

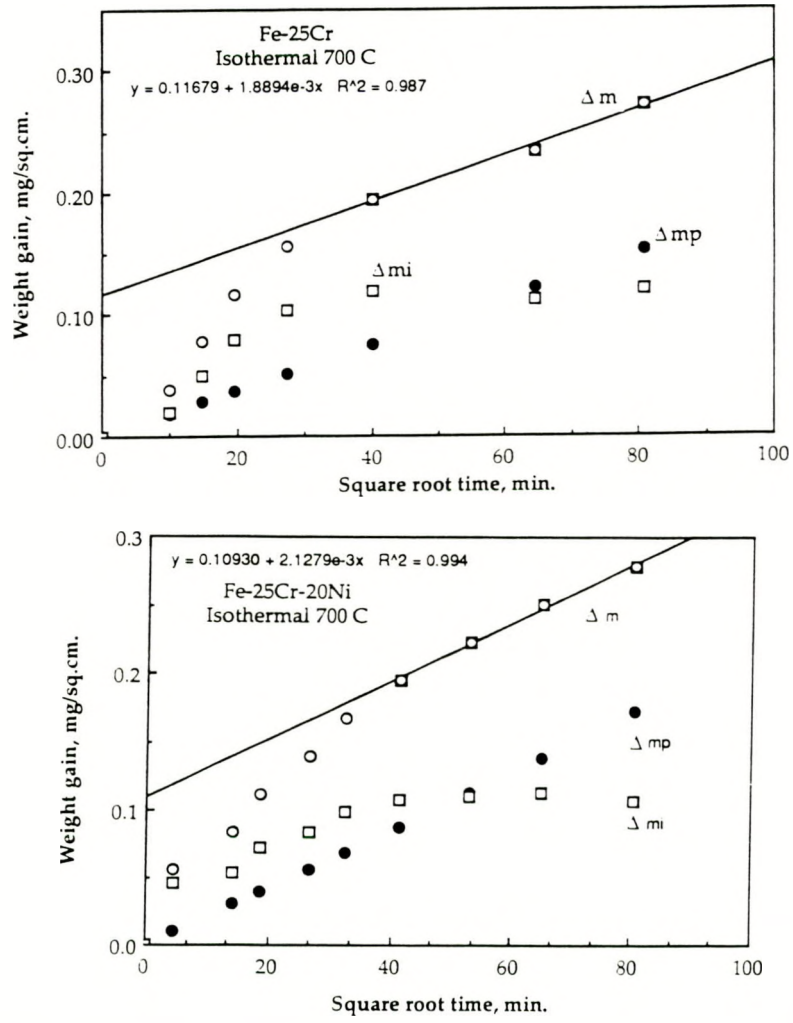

(a)

(b)

Fig. 4a-b. Variation of total weight gain, Δm, parabolic weight gain, Δm_p and transient weight gain, Δm_i with time.

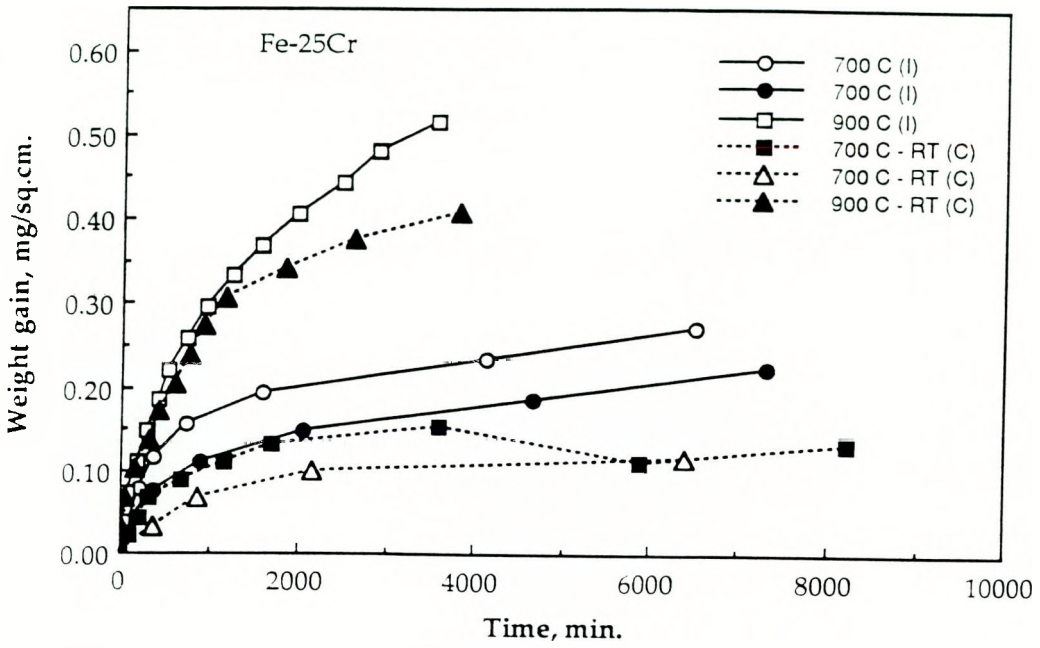

(a) Fe-25Cr

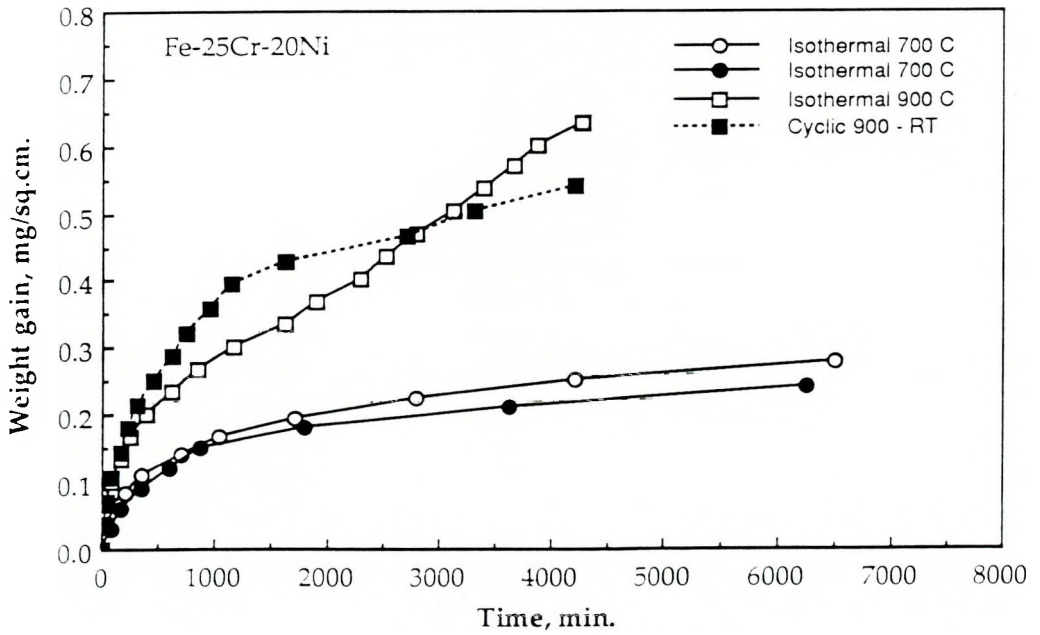

(b) Fe-25Cr-20Ni

Fig. 5. Kinetics curves.

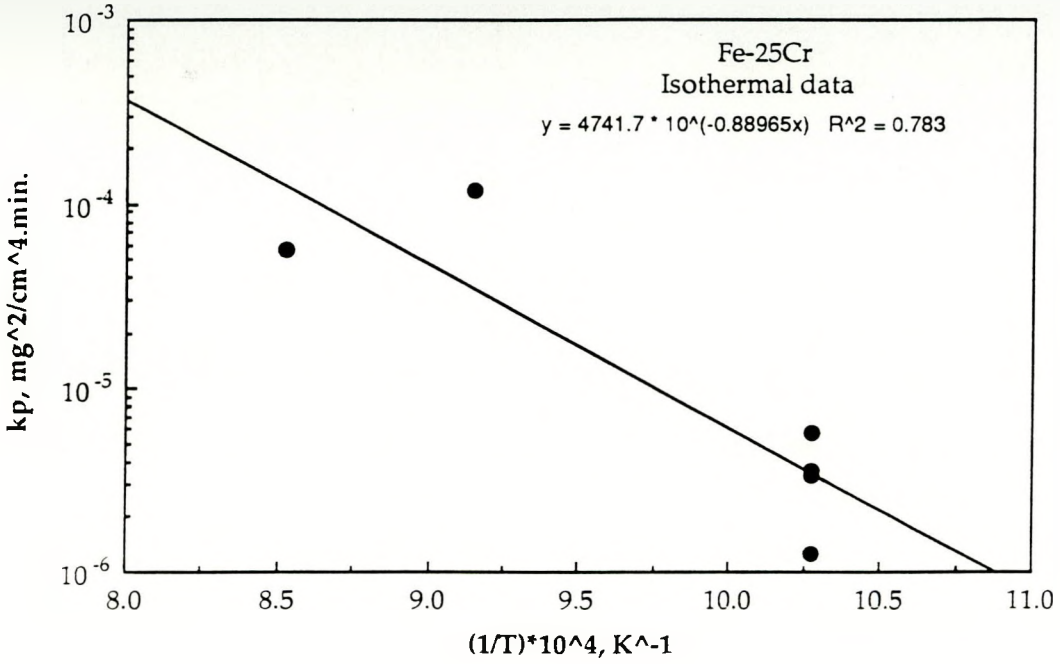

(a)

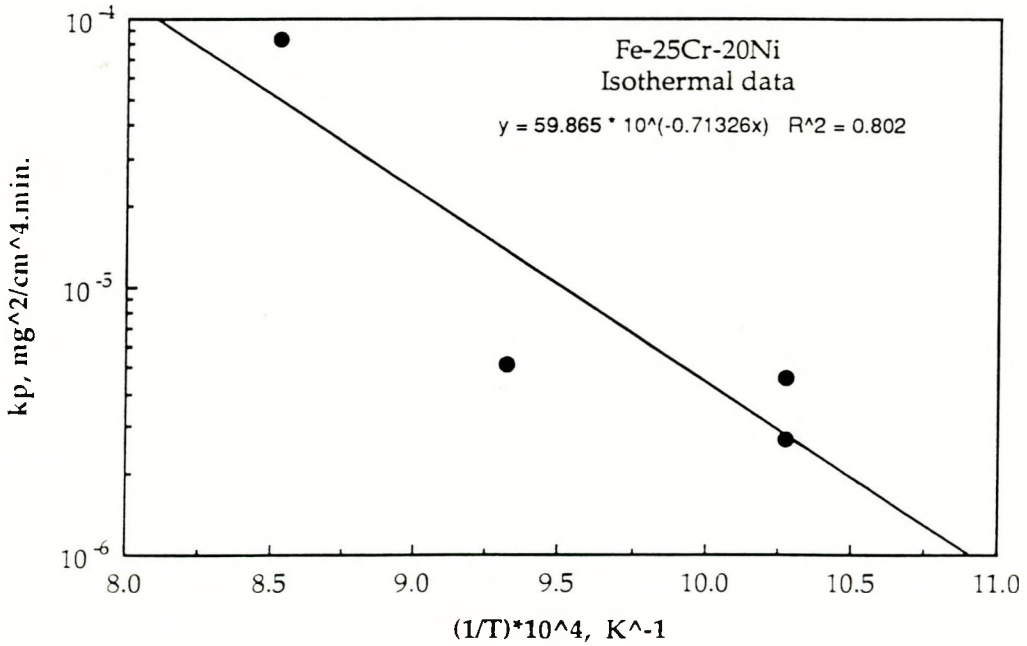

(b)

Fig. 6. Arrhenius plots.

Table 8. Activation energies for steady state oxidation.

Alloy	Q, Kcal/mole	Pre-exponential Factor, mg^2/cm^4 min.
Fe-25Cr	40.56 (I)	$4.741x10^3$ (I)
Fe-25Cr-1.5Al_2O_3	35.15 (I) 34.5 (I,C)	50.953 (I) 39.699 (I,C)
Fe-25Cr-20Ni	32.52 (I)	59.86 (I)
Fe-25Cr-20Ni-1.5Al_2O_3	37.94 (I) 37.86 (I,C)	$1.678x10^2$ (I) $1.26x10^2$ (I,C)

I = Isothermal, at 1 atm. O_2
C = Cyclic, at 1 atm. O_2

is no significant variation in the weight gains due to microalloying. The parabolic oxidation rates, k_p for the above alloys were evaluated linearizing the long term data, from the plot Δm vs $t^{1/2}$ described earlier, and are included in Table 7. A comparison of the parabolic rate constants of the above alloys with that of base alloys is shown in Figure 8. Considerable scatter is observed in k_p suggesting the absence of any oxygen active element effect under the reported condition.

4.2.3 (P/M) Alloys with Al_2O_3 Dispersoids

The specific weight gains experienced by Fe-25Cr-1.5 Al_2O_3 and Fe-25Cr-20Ni-1.5 Al_2O_3 during oxidation in O_2 are described in Figures 9a-b as a function of time. The parabolic kinetics rates for the above alloys were evaluated using the Pieraggi procedure and are included in Table 7. The oxidation responses of base alloys and Al_2O_3 dispersed alloys are compared in Figures 10a-b. The weight gain is less under cyclic condition than under isothermal conditions. The Arrhenius plots relating the true parabolic rate constants, k_p for Fe-25Cr-1.5 Al_2O_3 and Fe-25Cr-20Ni-1.5 Al_2O_3 and the reciprocal of test temperatures are illustrated in Figures 11a-b. The data used to construct these figures are from the isothermal tests. The activation energies estimated from the slopes of the Arrhenius plots are about 35-38 kcal/mole, Table 8. Use of cyclic data also gives similar values, Table 8.

4.2.4 Ion Implanted Alloys

The surfaces of base alloys were modified with Ce, Hf, O, Si, Pt or Y by direct implantation procedure. Oxidation tests were performed only on a selected number of implanted alloys because of absence of any significant positive effects. The weight gain data of several Si, O, and Si/O implanted Fe-25Cr-20Ni are compared with that of base alloy in Figure 12 in the form of kinetics plots. Si implanted alloy shows lower rate of weight gain at

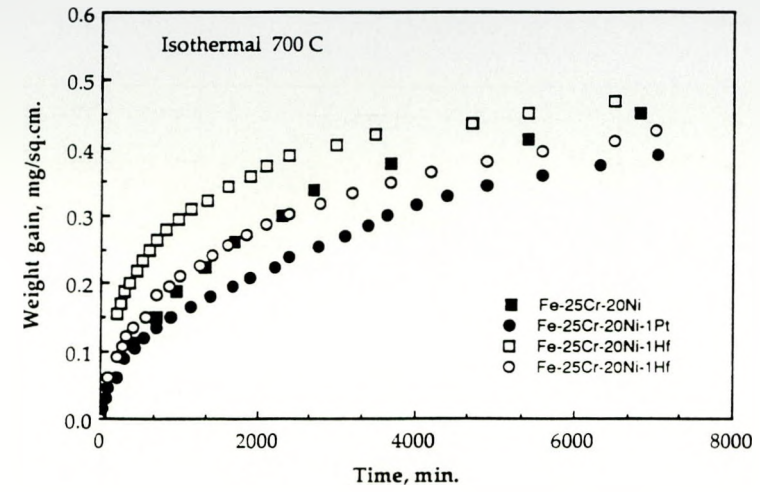

(a)

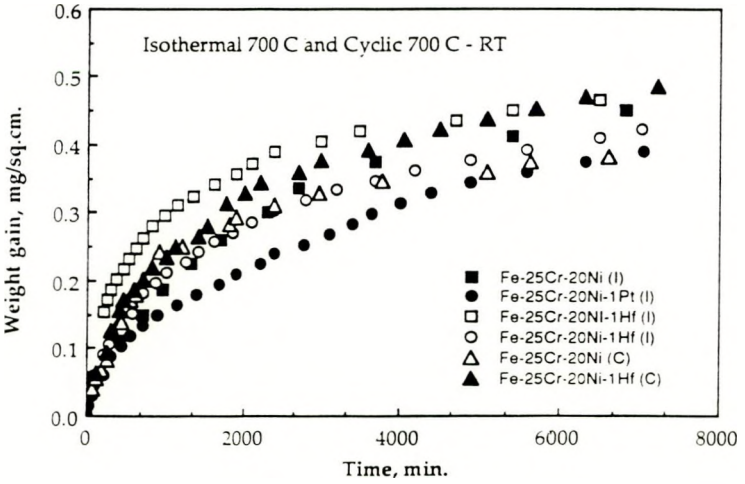

(b)

Fig. 7. Kinetics curves.

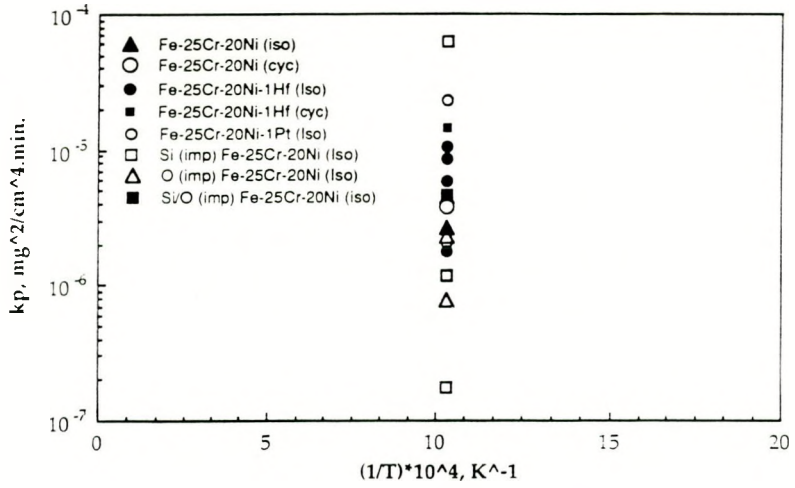

Fig. 8. A comparison of parabolic rate constants.

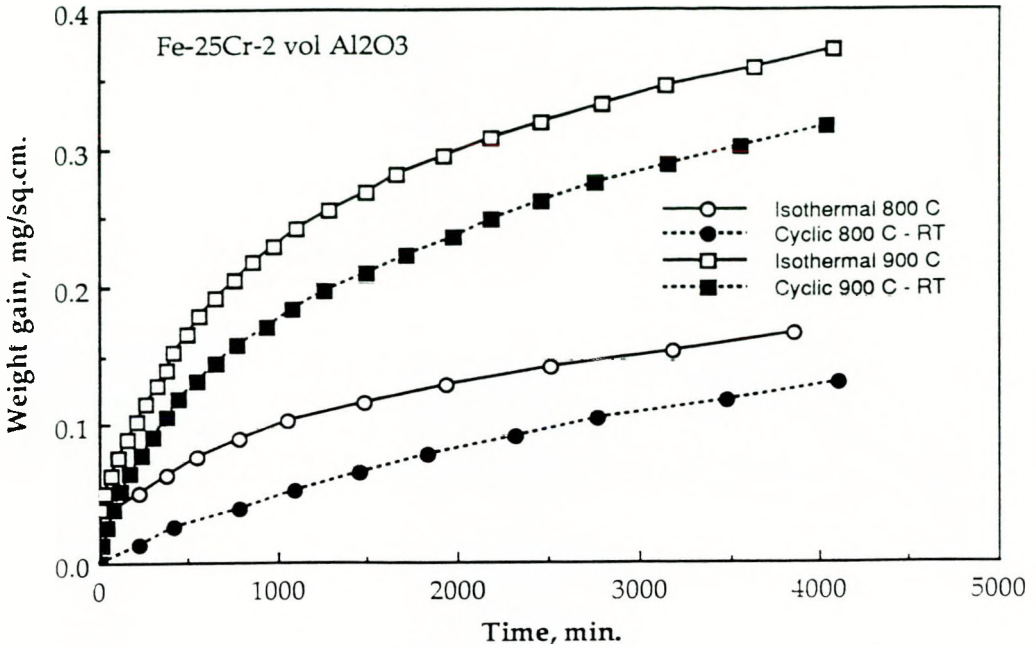

(a) Fe-25Cr-1.5Al_2O_3

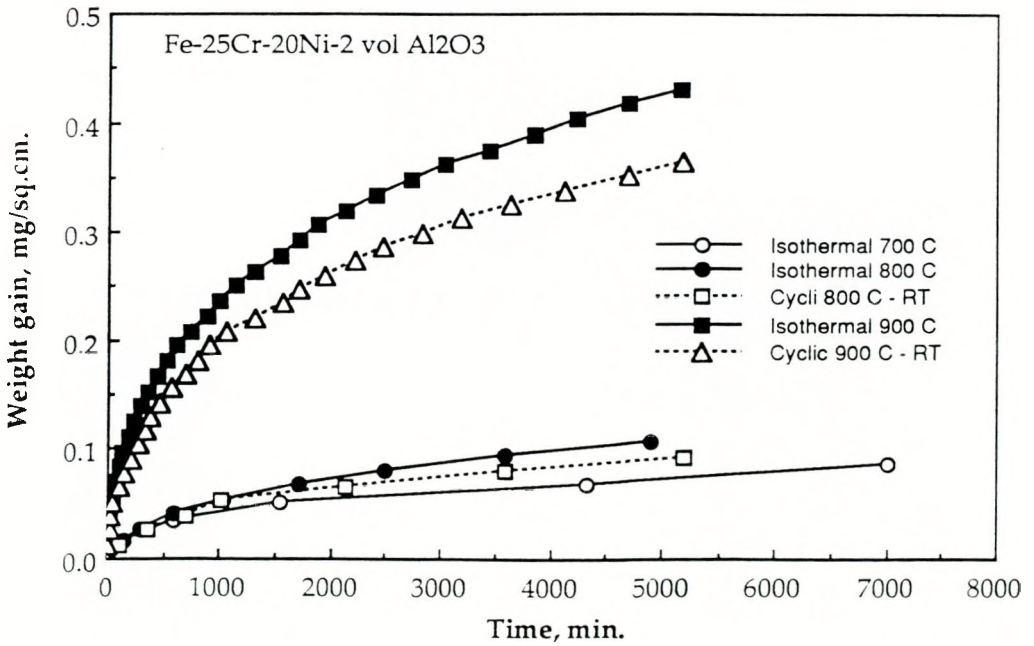

(b) Fe-25Cr-20Ni-1.5Al_2O_3

Fig. 9. Specific weight gain vs time.

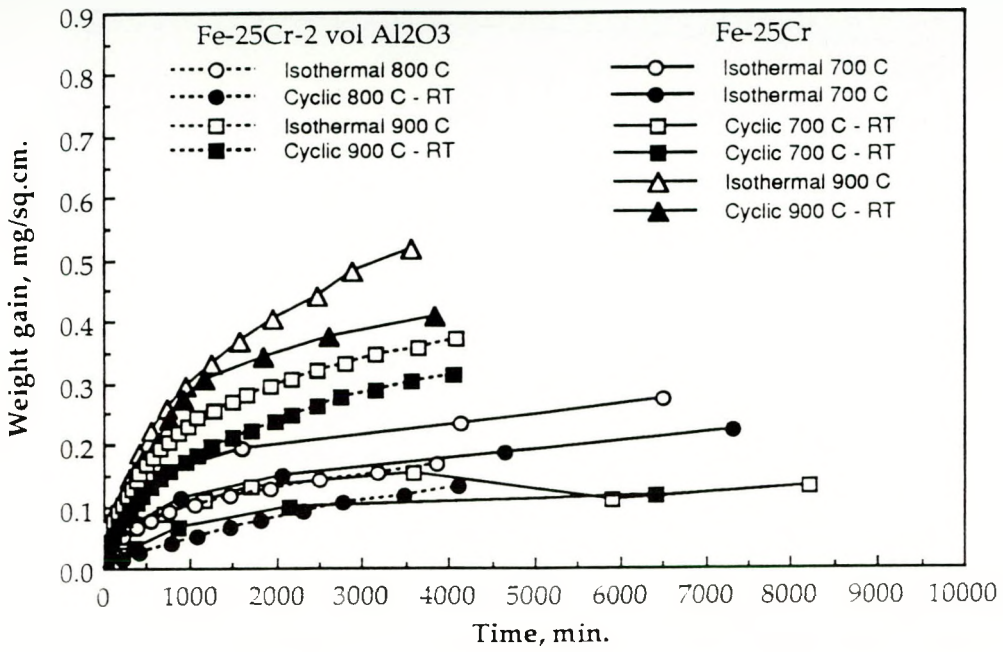

(a) Fe-25Cr and Fe-25Cr-1.5Al_2O_3

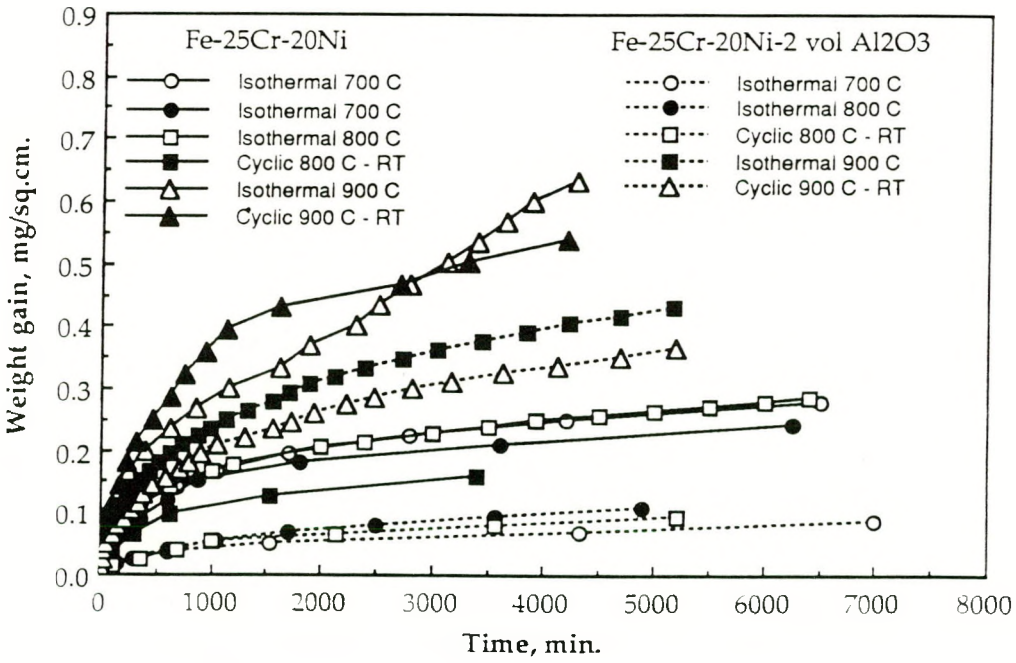

(b) Fe-25Cr-20Ni and Fe-25Cr-20Ni-1.5Al_2O_3

Fig. 10. Effect of Al_2O_3 addition on oxidation kinetics.

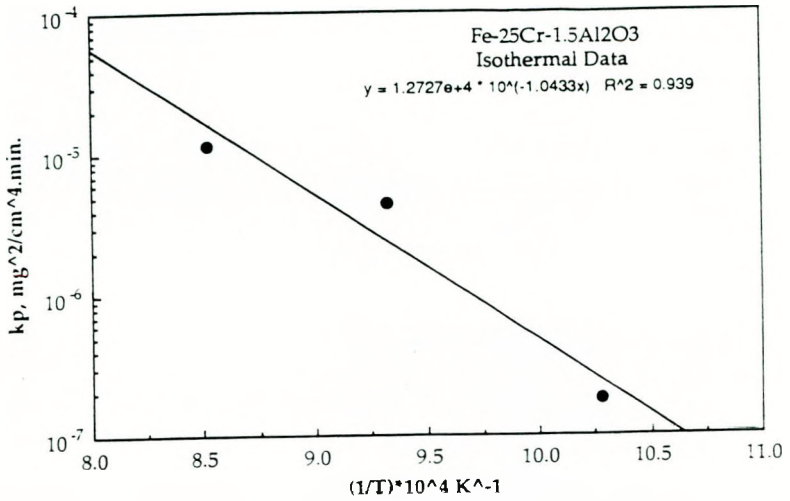

(a)

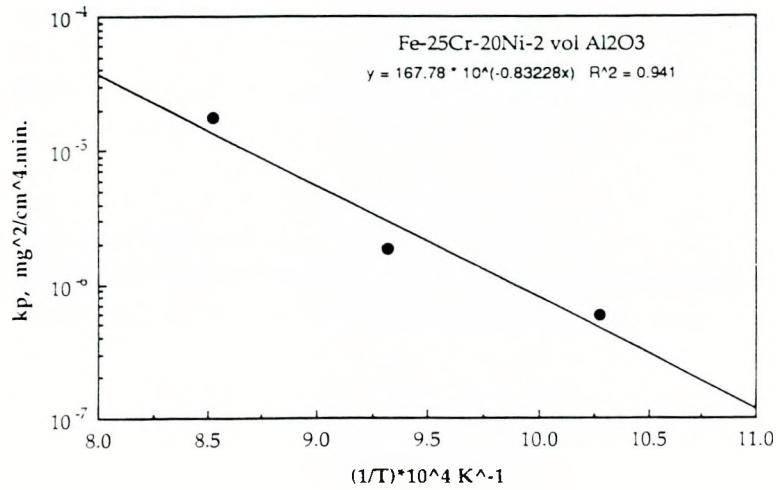

(b)

Fig. 11. Arrhenius plot.

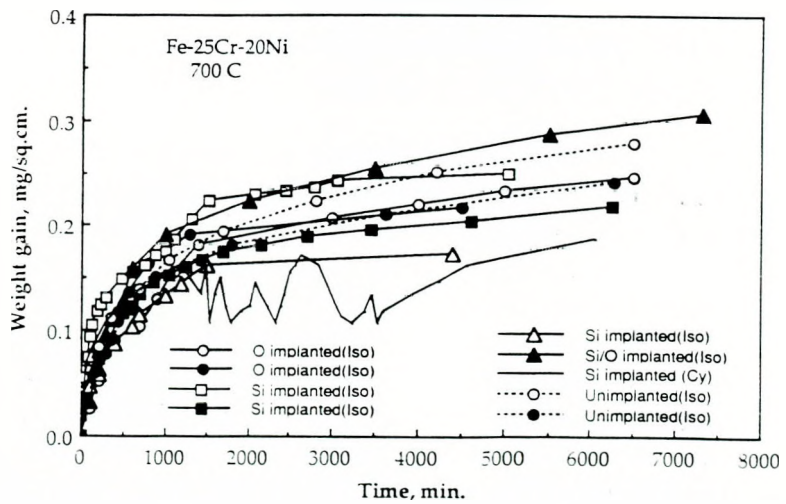

Fig. 12. Kinetics curves of Fe-25Cr-20Ni with and without implants.

longer times under isothermal conditions, but exhibits scale spallation during cyclic oxidation and also variability in isothermal weight gains.

The steady state parabolic oxidation rates, k_p determined from least square fitting of long term Δm vs $t^{1/2}$ plots for each of the implanted alloys are given in Table 7 and Figure 8.

4.3 CHARACTERISTICS OF OXIDE SCALES

4.3.1 (I/M) Fe-25Cr and Fe-25Cr-X Alloys

The surface and the cross section of the oxide scale on Fe-25Cr are shown in Figures 13a-c. The scales shown in these figures were the result of exposure to O_2, 1 atm at 700°C for about 120 h and are Cr rich (Table 9). XRD lines corresponded to that of Cr_2O_3 and BCC Fe-Cr matrix. Scale is granular, but uniform and faceted, and has a range of grain sizes varying from approximately 0.5 to 2 μ. The scale is adherent with no significant voiding at the metal/scale interface, Figure 13c which is a backscattered electron image (BEI). The scale appearance and composition is not uniform in the early stages of oxidation. Figure 13d is SEM of the oxide scale formed on Fe-25Cr after 2 h exposure to O_2 at 700°C. There are several spots or circular islands with a spectrum of diameters, and they appear to have spread laterally from their respective nuclei. These features are rich in Cr, (Table 9).

Scales formed in the early stages of pure oxidation in O_2 for 4 h at 700°C were analyzed by STEM. In the bright field TEM image of the scale/metal interface, Figure 14a, fine grain oxide is seen at the metal/scale interface while the oxide grains are coarser near the gas/scale interface. Figure 14b describes the interface between the coarse and fine grain oxides. The size of fine grained oxides varies between 50 and 80 nm, while that of coarse grained oxides is between 0.4 and 0.6 μ. Selected area diffraction ring pattern from fine grained oxides and convergent beam diffraction patterns from individual coarse oxide grains, shown in Figures 15 and 16a-b, suggest that the fine grained oxides are invariably the rhombohedral Cr_2O_3 and that the coarse grained oxides are mixed: some are Cr_2O_3 and others do not correspond to any known chromium oxide. Further, the Fe content of fine grain oxides is more than that of coarse grain oxides, (EDAX not shown). The overall Fe content of the scale progressively increases from the gas/scale interface to the scale/metal interface, as revealed by the Auger spectra from different depths, Figure 17a-c.

The bulk addition of microconstituents does not modify significantly the basic scale morphology and composition. Fine grain oxide is seen at the metal/scale interface of Fe-25Cr-1Ce as in the case of Fe-25Cr after oxidation in 1 atm O_2 at 700°C for 4 h, Figure 18a-b. Other similarities of scale characteristics between the base alloy and Fe-25Cr-1Ce include the presence of coarse oxide grains with grain sizes 0.4 to 0.6 μ away from the metal/scale interface, fine grains of size 50-80 nm at the scale/metal interfaces; fine grains and coarse grains that can be indexed as rhombohedral Cr_2O_3, and coarse grains that do not correspond to any known chromium oxide. A major difference in the scale composition is the presence of random dispersion of Ce rich phase with sizes ranging from 5 to 25 nm, Figure 19a. The EDAX spectrum from the fine grain region containing Ce rich phase indicates the presence of significant amount of Fe, Figure 19b.

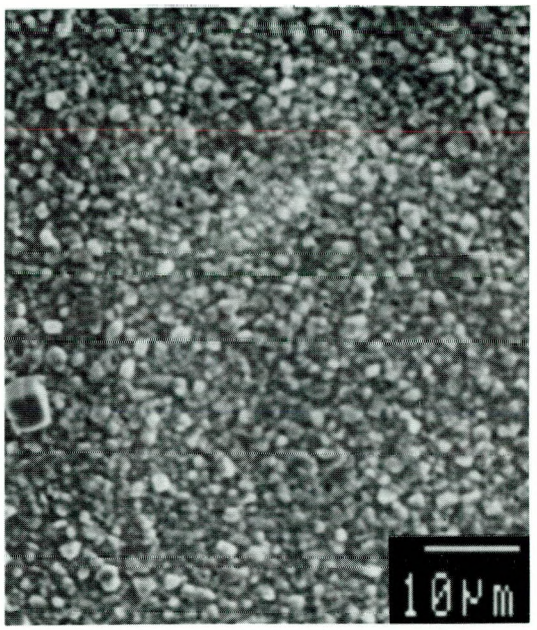

(a) 120h. Low mag

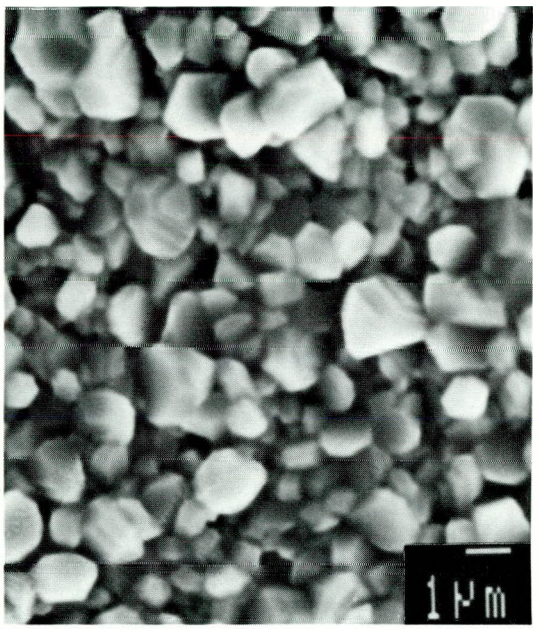

(b) 120h. High mag

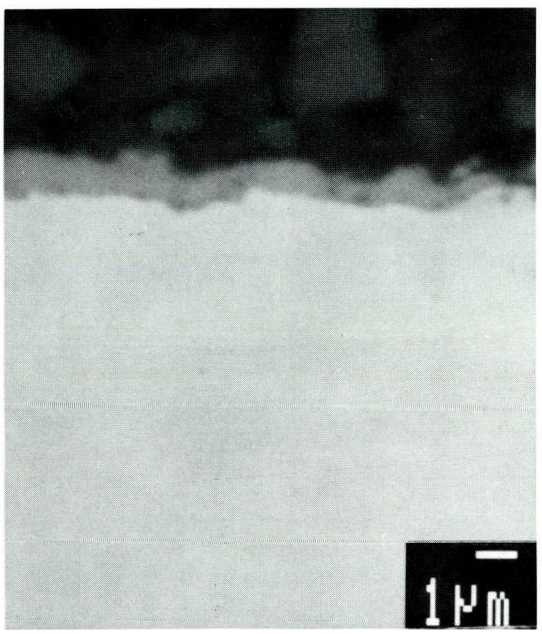

(c) 120h. X-section (BEI)

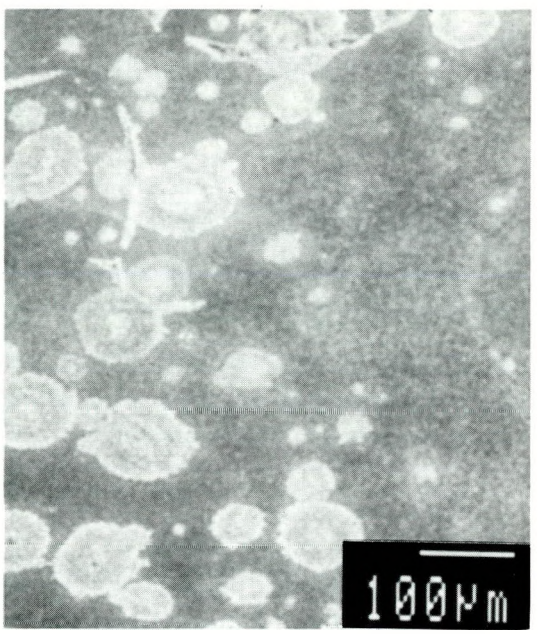

(d) 2h

Fig. 13. Oxide scale on Fe-25Cr exposed to 700°C in 1 atm O_2.

Table 9. Compositions of oxide scales by EDAX.
(Only metals percent totalling 100%)

Alloy	Exposure Condition	Location Ref: Fig.	Fe	Cr	Ni	Hf	Pt	Remarks
Fe-25Cr	700°C/120h/O_2	Fig. 13a	1.9	98.1	-	-	-	-
		Fig. 13b	6.3	93.70	-	-	-	-
	700°C/2h/O_2	Fig. 13d:A	53.1	46.9	-	-	-	Spots
		Fig. 13d:B	71.4	28.6	-	-	-	1
	800°C/72h/O_2		2.20	97.8	-	-	-	-
	900°C/72h/O_2		1.60	98.40	-	-	-	-
Fe-25Cr-1Hf	700°C/120h/O_2	Fig. 20a	50.5	48.7	-	0.8	-	-
		Fig. 20b	7.9	26.2	-	65.9	-	[illegible]
Fe-25Cr-1Pt	700°C/120h/O_2	Fig. 21	17.7	82.3	-	-	-	-
Fe-25Cr-1Y	700°C/120h/O_2		34.1	65.9	-	-	-	-
Fe-25Cr-1.5Al_2O_3	700°C/72h/O_2	Fig. 22a	59.7	40.3	-	-	-	1
	800°C/72h/O_2	Fig. 22b	2.8	97.2	-	-	-	-
	900°C/72h/O_2	Fig. 22c	1.6	98.4	-	-	-	-
Fe-25Cr-20Ni	700°C/120h/O_2	Fig. 24a-A	84.8	10.8	4.4	-	-	G
		Fig. 24a-B	49.6	38.7	11.7	-	-	GB
		Fig. 24b	55.4	23.7	20.9	-	-	X, 1
	Cyclic/120h 700°C ↔ RT (50°C)	Fig. 25-A	25.1	69.6	5.3	-	-	-
		Fig. 25-B	69.5	27.7	2.8	-	-	-
		Fig. 25-C	77.2	20.7	2.1	-	-	-
		Fig. 25-D	85.9	11.2	2.9	-	-	-
Fe-25Cr-20Ni-1Hf	700°C/120h/O_2	Fig. 26a-A	92.1	5.8	2.1	-	-	-
		Fig. 26a-B	50.8	38.8	10.4	-	-	-
Fe-25Cr-20Ni-1Pt	700°C/120h/O_2	Fig. 26b-A	68.9	29.6	1.5	-	-	-
		Fig. 26b-B	71.6	25.4	3.0	-	-	-
		Fig. 26b-C	42.0	43.0	15	-	-	-
		Fig. 26d-A	59.4	25.5	14.1	-	-	X
		Fig. 26d-B	58.0	22.4	19.6	-	-	X
O-Imp. Fe-25Cr-20Ni	700°C/120h/O_2	Fig. 27-A	85.5	9.8	4.7	-	-	-
		Fig. 27-B	51.5	29.8	18.7	-	-	1
Si-Imp. Fe-25Cr-20Ni	700°C/120h/O_2	Fig. 28a-A	52.5	29.7	16.9	-	0.9	1
		Fig. 28a-B	53.9	26.4	18.9	-	0.8	1
		Fig. 28b	48.2	40.7	10.4	-	0.7	X
Fe-25Cr-20Ni-1.5Al_2O_3	700°C/120h/O_2	Fig. 30a	35.1	52.2	12.7	-	-	1
	800°C/96h/O_2	Fig. 30b	2.3	97.0	0.7	-	-	-
		Fig. 31b	4.1	95.1	0.8	-	-	-
	900°C/72h/O_2	Fig. 31c	4.7	94.1	1.2	-	-	-
		Fig. 31c	1.3	98.6	0.1	-	-	-

1 = Substrate interference suspected
X = Cross section
G = Grain
GB = Boundary

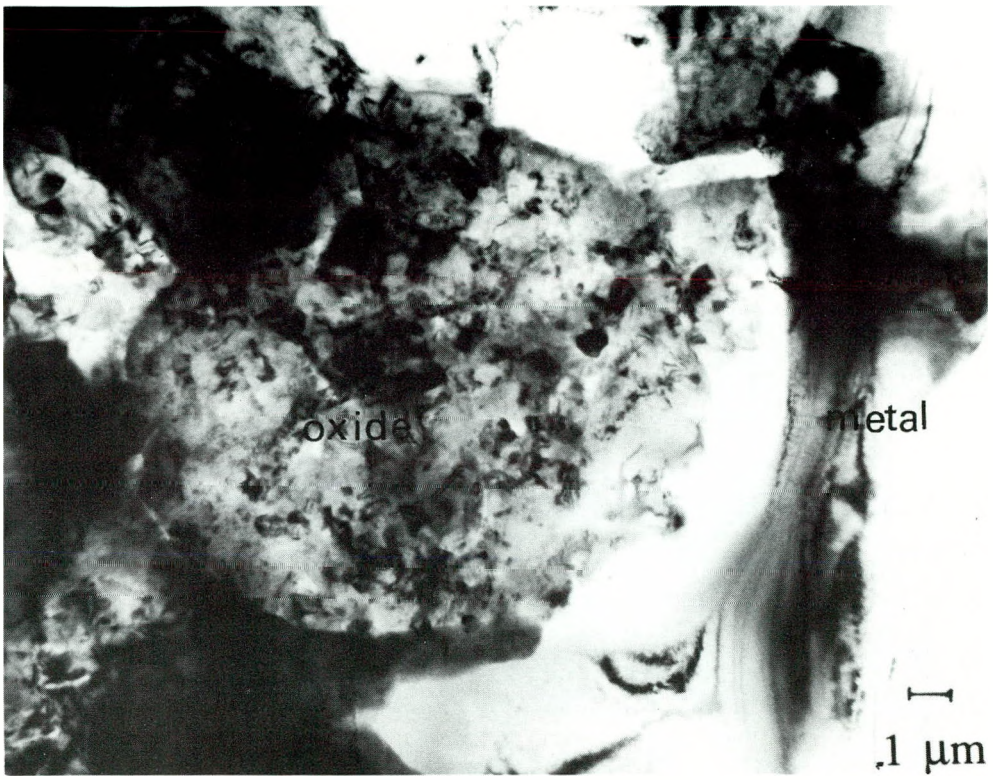

(a) Oxide/metal interface

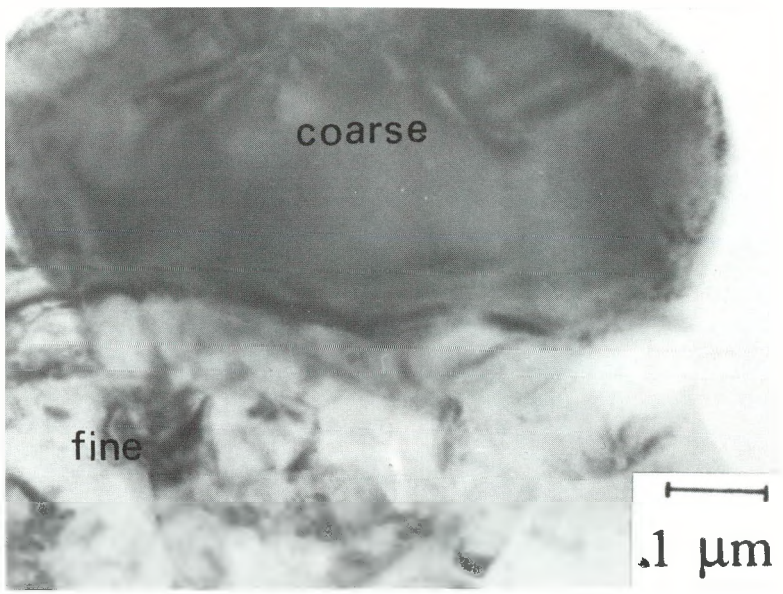

(b) Fine/coarse oxide interface

Fig. 14. Bright field images of scale on Fe-25Cr oxidized in 1 atm O_2 at 700°C for 4h.

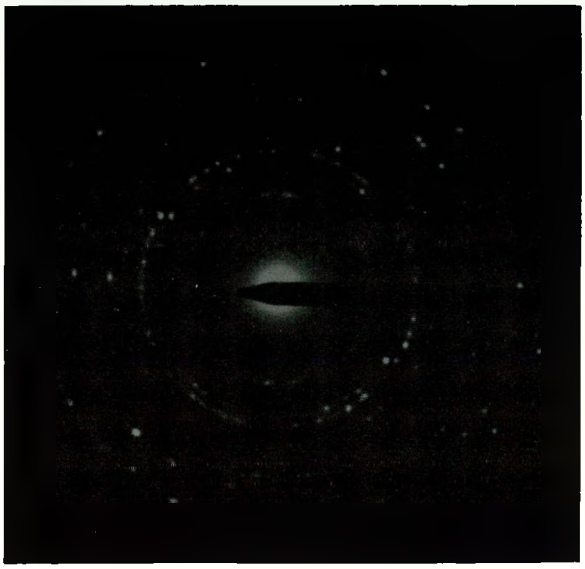

Fig. 15. SAD from fine-grain oxide on Fe-25Cr, 1 atm. O_2, 700°C, 4h; oxide is Cr_2O_3.

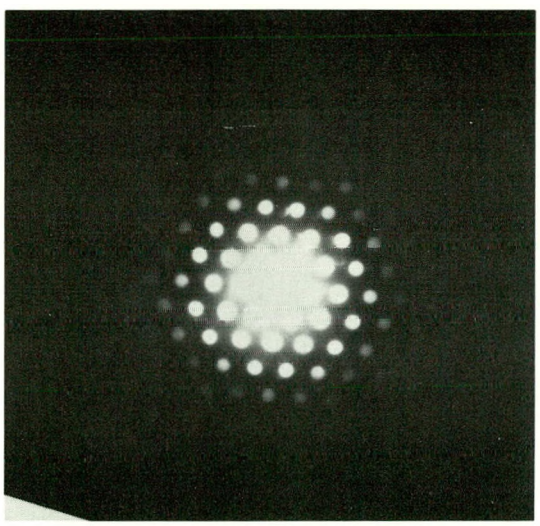

(a) [0001] Pattern of Cr_2O_3

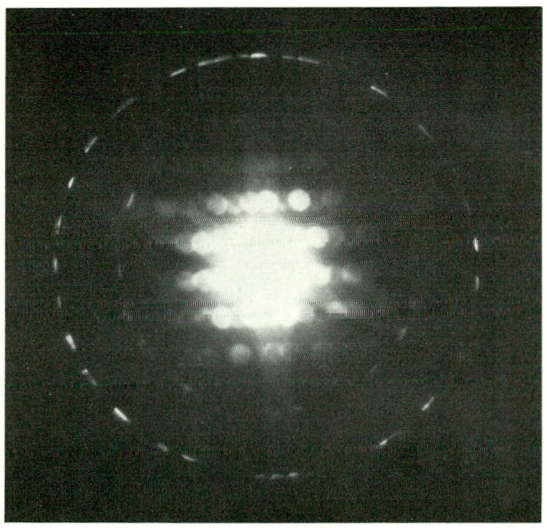

(b) Unidentified pattern

Fig. 16. Convergent beam diffraction patterns from individual coarse oxide grains.

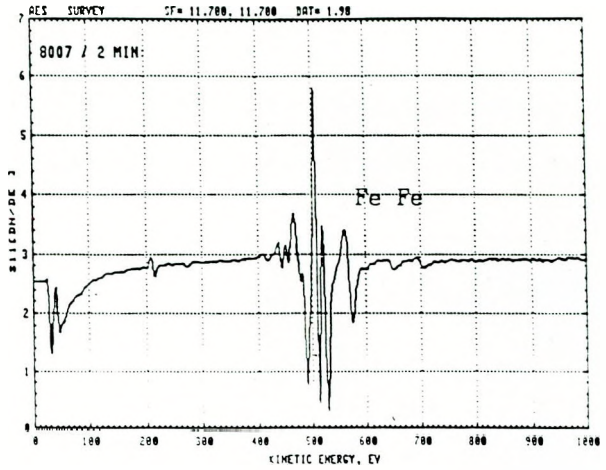

(a) Scale/gas interface

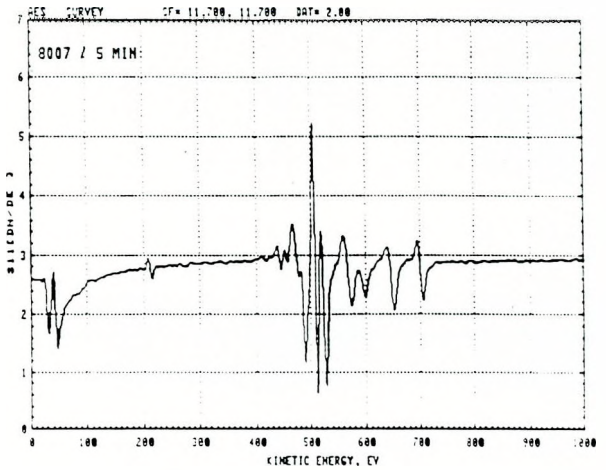

(b) 100 nm below the scale surface

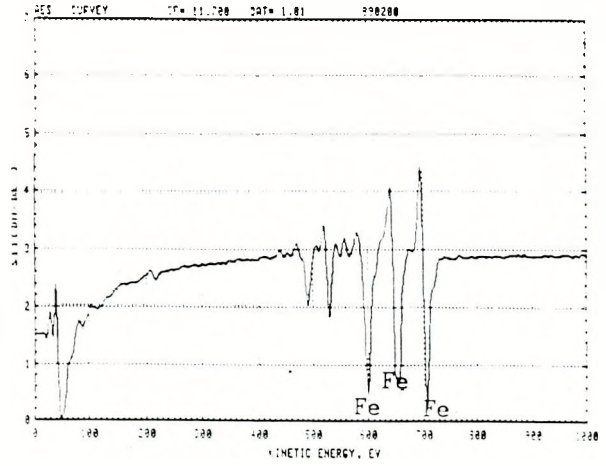

(c) 400 nm below the scale surface

Fig. 17. Auger spectra from different depths of the scale.

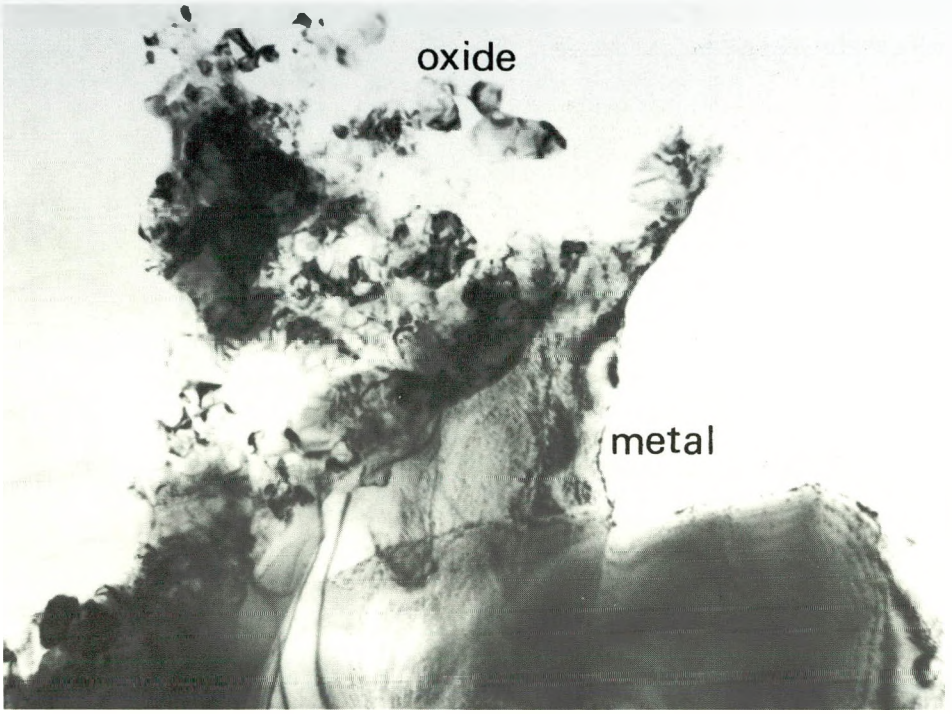

(a) Bright field

(b) Dark field

Fig. 18. Metal/oxide interface in Fe-25Cr-1Ce oxidized in 1 atm O_2 at 700°C for 4h.

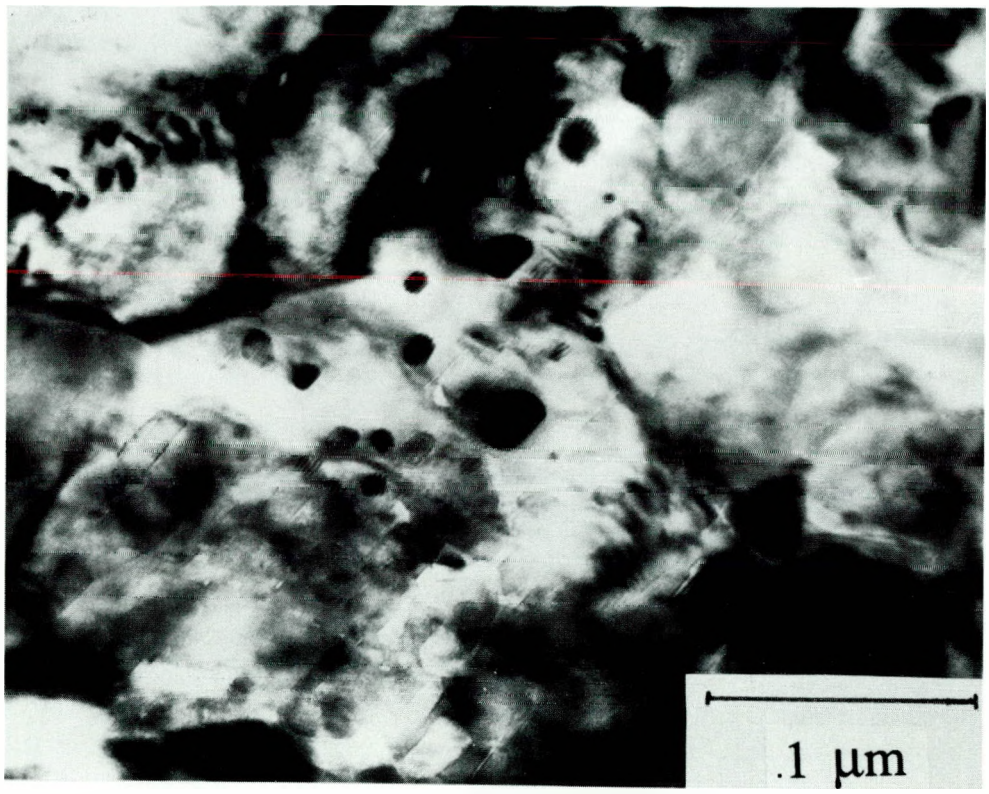

(a) Bright field image

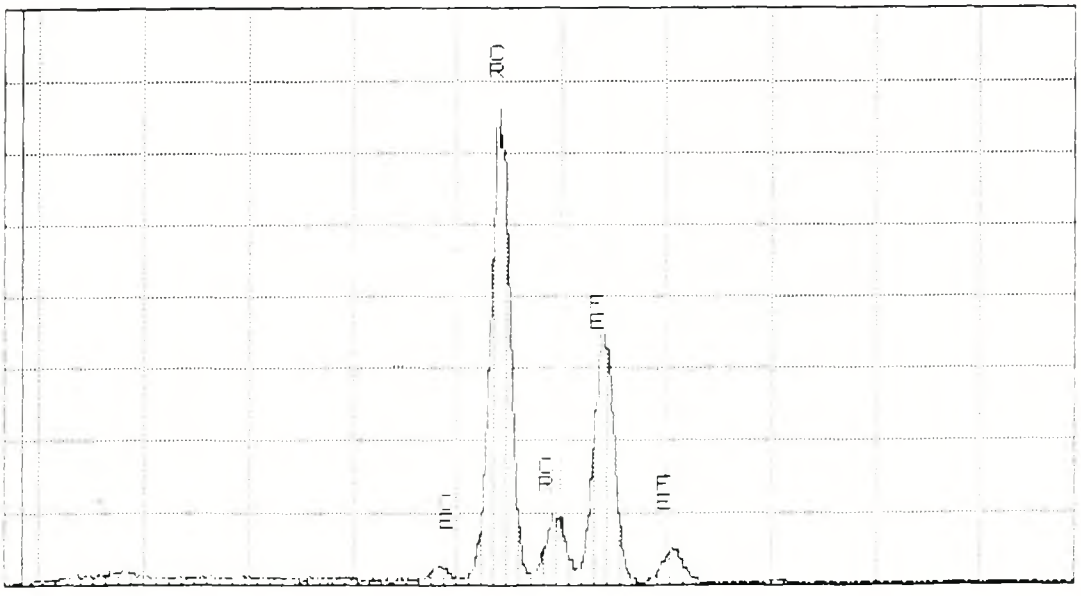

(b) EDAX spectrum from fine grain oxide with Ce-rich phase

Fig. 19. Oxide scale on Fe-25Ce-1Cr oxidized in 1 atm. O_2 at 700°C for 4h.

The oxide scales observed after isothermal oxidation of Fe-25Cr-1Hf and Fe-25Cr-1Pt in O_2 at 700°C for 120 h have granular appearance, Figures 20 and 21 as those observed on the base alloy after isothermal oxidation. Scales of similar morphology is also observed after cyclic oxidation. The Cr content of the scale on Fe-25Cr-1Hf is significantly less compared to that of the scale on the base alloy without Hf addition, Table 9. Hf is also detected by the EDAX. However, the oxide scale formed on Fe-25Cr-1Pt has a significant amount of Cr, Table 9. Cross-sectional SEMs of the oxide scale formed on Fe-25Cr-1Hf during isothermal oxidation at 700°C are shown in Figures 20b. In backscattered electron image (BEI), Figure 20b, Hf rich particles/phases are seen in the scale as well as in the substrate. The scale is adherent and uniform, Figure 20b, and no voids are seen at the scale/metal interface.

4.3.2 (P/M) Fe-25Cr-1.5Al_2O_3 Alloy

Chromia rich granular oxide scales(Cr_2O_3) formed on Fe-25Cr-1.5Al_2O_3 (Fe-25Cr-2 Vol. Al_2O_3) alloys exposed to 1 atm O_2 at 700°, 800°, and 900°C for 72 h, Figures 22a-c. As the temperature is increased, the nodule formation becomes significant. Cross sections of the scales are shown in Figures 23a-c. The scale formed at 700°C is very thin. Al_2O_3 particles are seen as dark phases in the matrix. The EDAX analysis of the sample oxidized at 700°C in 1 atm O_2 for 72 h is not representative of the scale composition because of significant contribution of the matrix due to very thin oxide scale <1 μ. The compositions of scales formed at 800° and 900°C are essentially chromium and oxygen as determined by EDAX, Table 9.

Increasing weight gain at a given time with increasing temperature is consistent with the increased scale thickness, shown in Figures 23a-c. These SEMs are taken in BEI (compositional) mode. The thinness of oxide scale on sample exposed to 700°C is obvious in Figure 23a.

4.3.3 (I/M) Fe-25Cr-20Ni and Fe-25Cr-20Ni-X Alloys

Figure 24a-b show the surface and cross sections of the oxide scale observed on the base alloy Fe-25Cr-20Ni oxidized in O_2 at 700°C for 120 h. The scales on the substrate grains and along the substrate grain boundaries have distinct compositional and morphological differences; the scales on the substrate grain boundaries are thinner with more Cr and Ni as indicated by the EDAX analysis, Table 9. The scales on the substrate grains, on the other hand, are thick and rich in Fe with relatively small amounts of Cr and Ni. A cross sectional SEM of the oxide scale by backscattered electrons (BEI compositional) is shown in Figure 24b. Except for a few voids along the scale/metal interface, the scale composition is similar to that of scale on the substrate grains, rich in Fe, Table 9.

The oxide scale shown in Figure 24a-b is a mixture of Fe_2O_3, $FeCr_2O_4$ and Cr_2O_3, and this was deduced by comparing the observed XRD lines with the XRD data files available.

Thermal cycling between 700°C and RT (~50°C) lead to oxide scales that are similar to the isothermally formed ones. Scales on the cyclically oxidized Fe-25Cr-20Ni differ in their compositions and morphologies depending on whether they are on the substrate grain

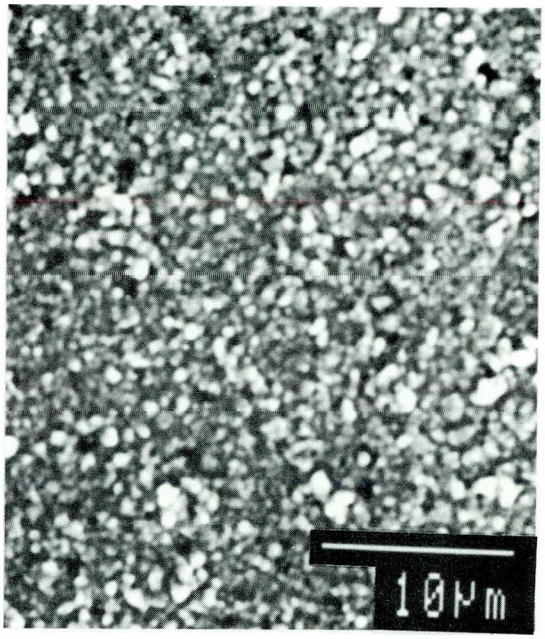

(a) Surface

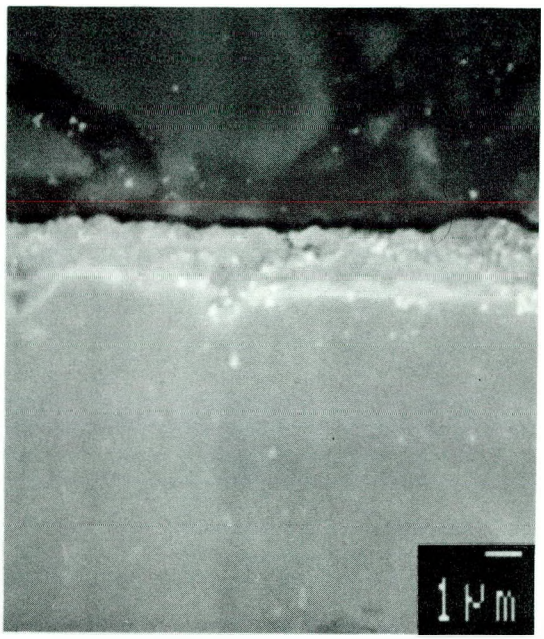

(b) X-section (BEI)

Fig. 20. Oxide scale on Fe-25Cr-1Hf oxidized in 1 atm O_2 at 700°C for 120h.

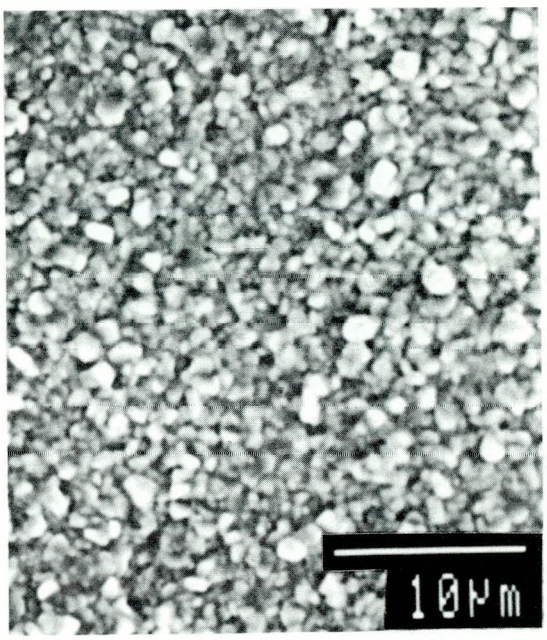

Fig. 21. Oxide surface on Fe-25Cr-1Pt oxidized in 1 atm O_2 at 700°C for 120h.

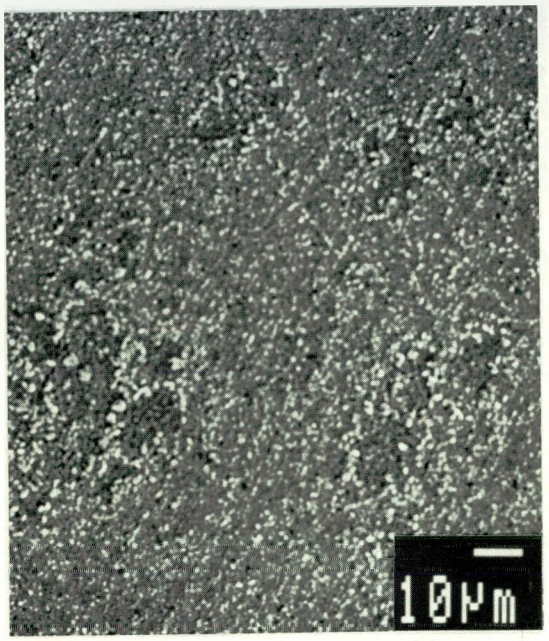

(a) 700°C

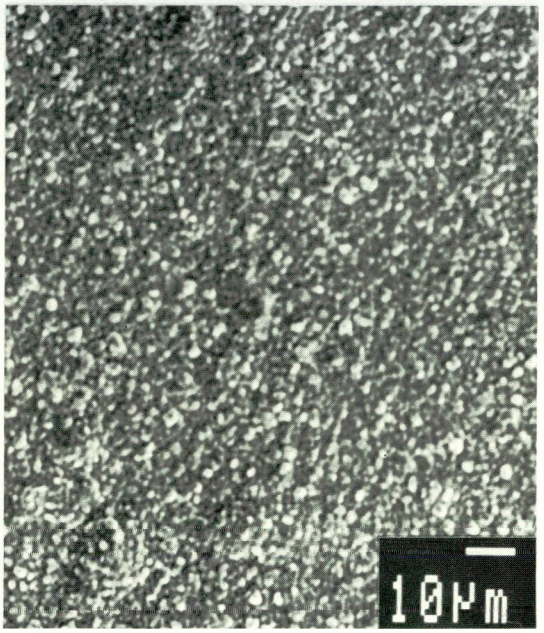

(b) 800°C

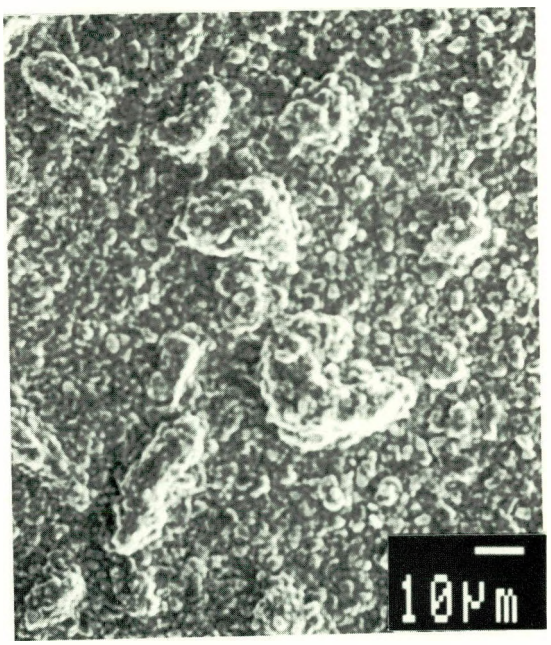

(c) 900°C

Fig. 22. Surface of oxide on Fe-25Cr-1.5Al_2O_3 oxidized in 1 atm O_2 for 72h.

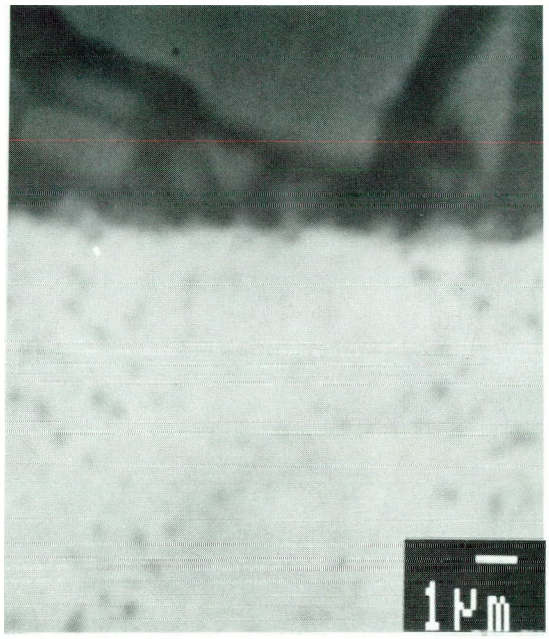

(a) 700°C

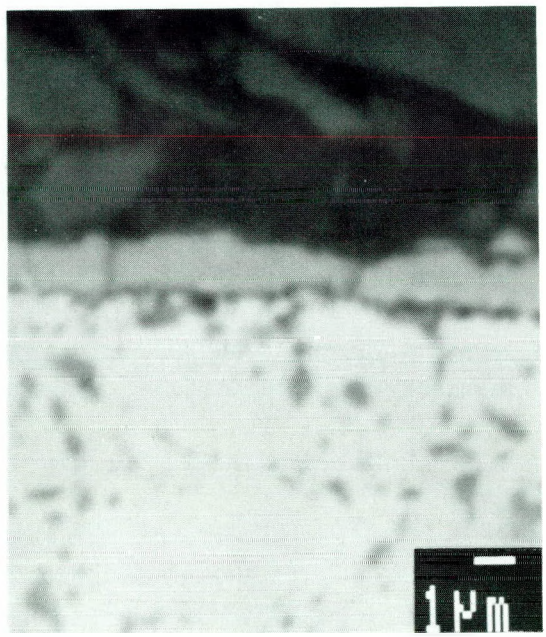

(b) 800°C

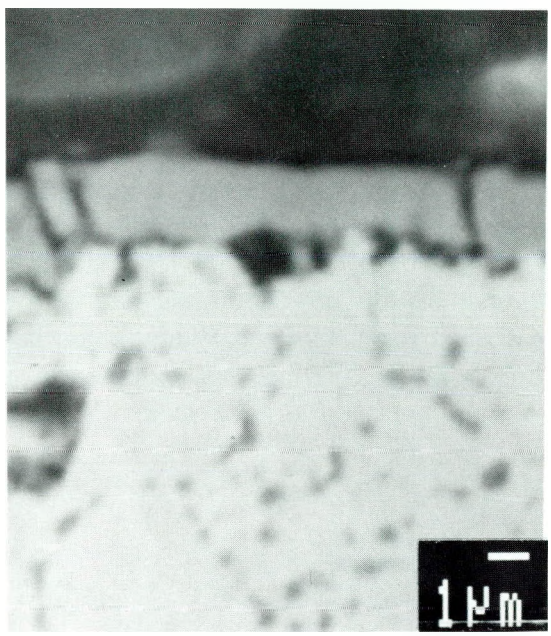

(c) 900°C

Fig. 23. X-sections of oxide scales on Fe-25Cr-1.5Al_2O_3 oxidized in 1 atm O_2 for 72h, (BEI).

boundaries or not, Figure 25. The scale features include thick, blocky regions on some substrate grains and at random locations along the substrate grain boundaries, granular oxides on other substrate grains and relatively thin featureless scale near the substrate grain boundaries. The EDAX analyses of the above regions give different scale compositions, Table 9 suggesting inhomogeneous nature of the scale.

The effect of bulk addition of Hf or Pt on the oxide scale morphology is shown in Figures 26a-d. Figure 26a-c describe the scale surfaces on isothermally oxidized Fe-25Cr-20Ni-1Hf and Fe-25Cr-20Ni-1Pt. Figure 26d describes cross section in the case of oxidized Fe-25Cr-20Ni-1Pt. The chemical compositions at different locations of the scales in the case of each one of the above samples are given in Table 9. The bulk addition of Hf or Pt at 1% level has not changed the scale character significantly. However, the addition of Pt seems to promote scale spallation, Figure 26c, although the scale adherence is good without interfacial voids, Figure 26d.

4.3.4 Ion Implanted Fe-25Cr-20Ni

Oxide scale characteristics were examined in the cases of O- and Si-implanted alloys. Again, the oxide scales formed isothermally on the substrate grains and grain boundaries of O- and Si-implanted/oxidized Fe-25Cr-20Ni differ in their morphology, Figures 27 and 28a. The EDAX analysis shows that the scales on the substrate grains of O implanted alloy are richer in Fe than those on the substrate grain boundaries, and this observation is similar to that made on the base alloy, Table 9. However, no variation in the Cr content of the scales on the substrate grains and grain boundaries is obvious in the case of Si implanted alloy, Table 9, although the overall Cr content in the scale is high, Figure 28b. Backscattered electron image (BEI) of the scale cross section on Si implanted Fe-25Cr-20Ni shows no compositional variation and voids across the scale, Figure 28b. The scale is adherent, and the metal/scale interface is smooth without voids.

Concentration depth profiles of elements across the oxide scales of O-, and Si-implanted Fe-25Cr-20Ni by sputter AES are shown in Figures 29a-b respectively. The sputter rate determined using Si_3N_4 was about 8 nm/min. Thick iron oxide, $\sim$2.4 μ has formed on chromium rich oxide, Cr_2O_3 in the case of O implanted alloy, and sputtering was discontinued short of scale/metal interface. The outer part of the scale has more Cr. The scale is significantly thinner $\sim$0.4 μ on oxidized Si implanted Fe-25Cr-20Ni and is Fe-Cr rich oxide, $FeCr_2O_4$. The above differences in the oxide scale thickness may not be translated into different total weight gains because the thick scales on O implanted alloy may be nonuniformly covering the exposed surface and the scale compactness may differ.

4.3.5 (P/M) Fe-25Cr-20Ni-1.5Al_2o_3 Alloy

The surfaces and the cross sections of oxide scales formed on Fe-25Cr-20Ni-1.5Al_2O_3 (2 Vol Al_2O_3) during oxidation in 1 atm O_2 at 700°, 800° and 900°C for up to 120 h are shown in Figures 30 and 31. The scales formed isothermally at 700° and 800°C are uniform with granular structure. However, the scale formed at 900°C has several nodules and is no longer granular. Sintering of scale seems to have occurred at 900°C, and local spallation of nodules is also apparent. The weight gain curve is smooth (Figure 9b) suggesting that

(a) Oxide surface

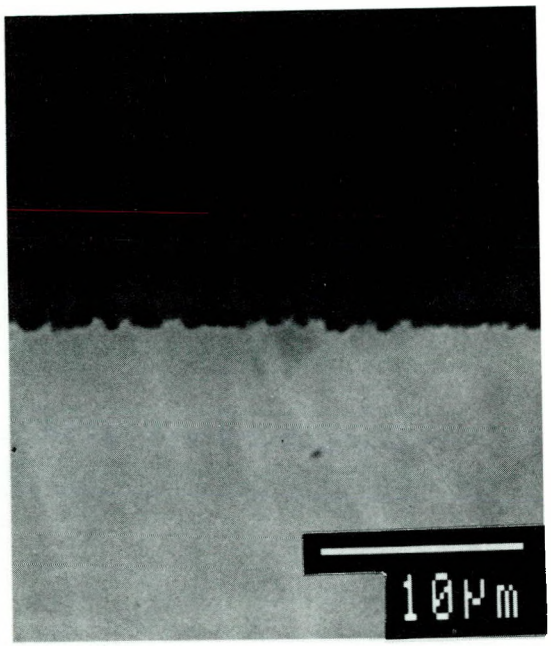

(b) Oxide X-section

Fig. 24. Fe-25Cr-20Ni oxidized in 1 atm O_2 at 700°C for 120h.

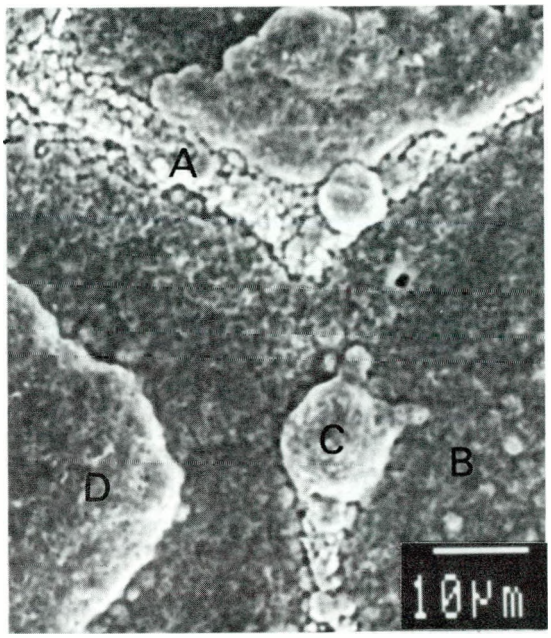

Fig. 25. Oxide scale on cyclically (700°↔50°C) oxidized Fe-25Cr-20Ni in 1 atm O_2 for 120h (120 cy).

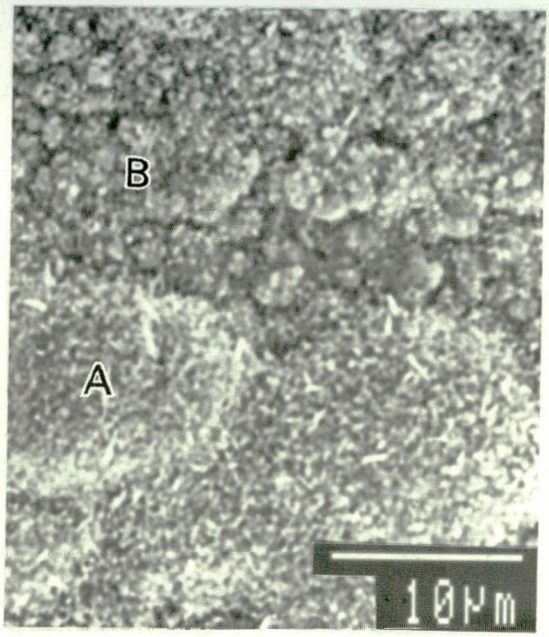

(a) Fe-25Cr-20Ni-1Hf

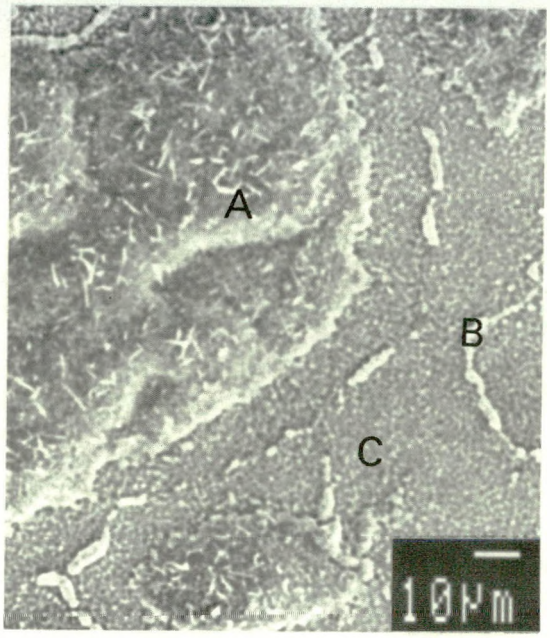

(b) Fe-25Cr-20Ni-Pt

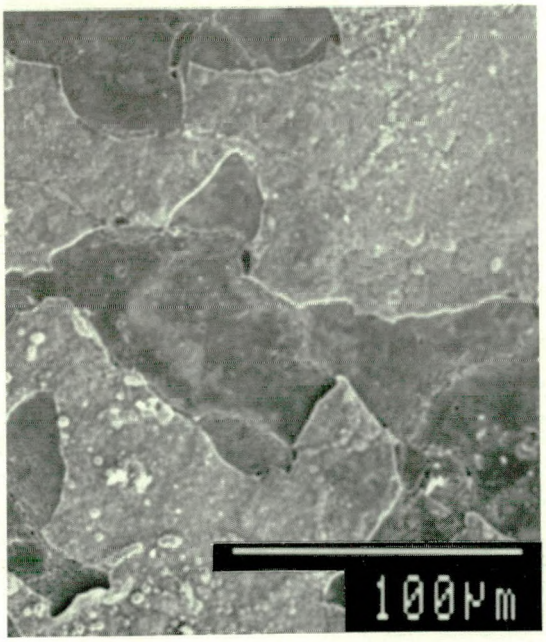

(c) Fe-25Cr-20Ni-1Pt

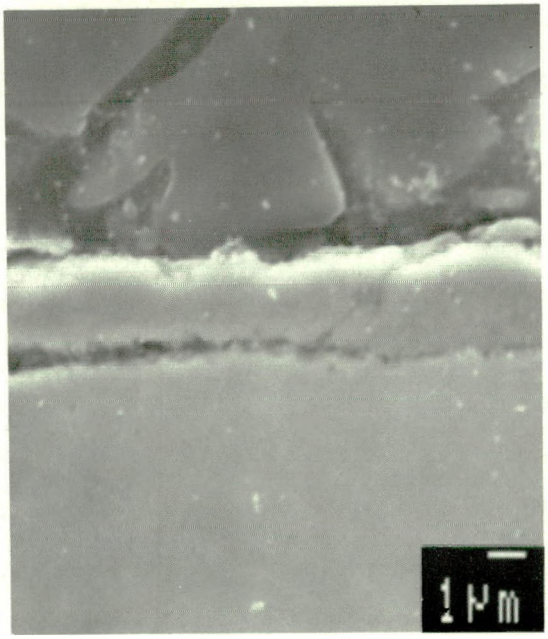

(d) X-section: Fe-25Cr-20Ni-1Pt

Fig. 26. Oxide scale on Fe-25Cr-20Ni-X alloys formed in 1 atm O_2 at 700°C, 120h.

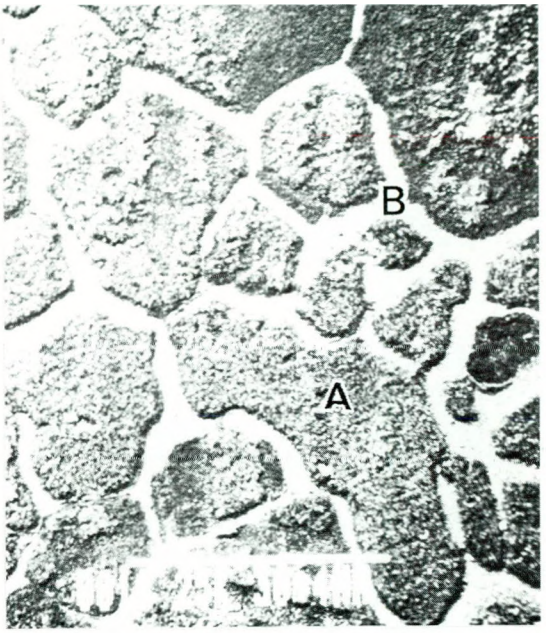

Fig. 27. Oxide scale on O-implanted Fe-25Cr-20Ni oxidized in 1 atm O_2 at 700°C for 120h.

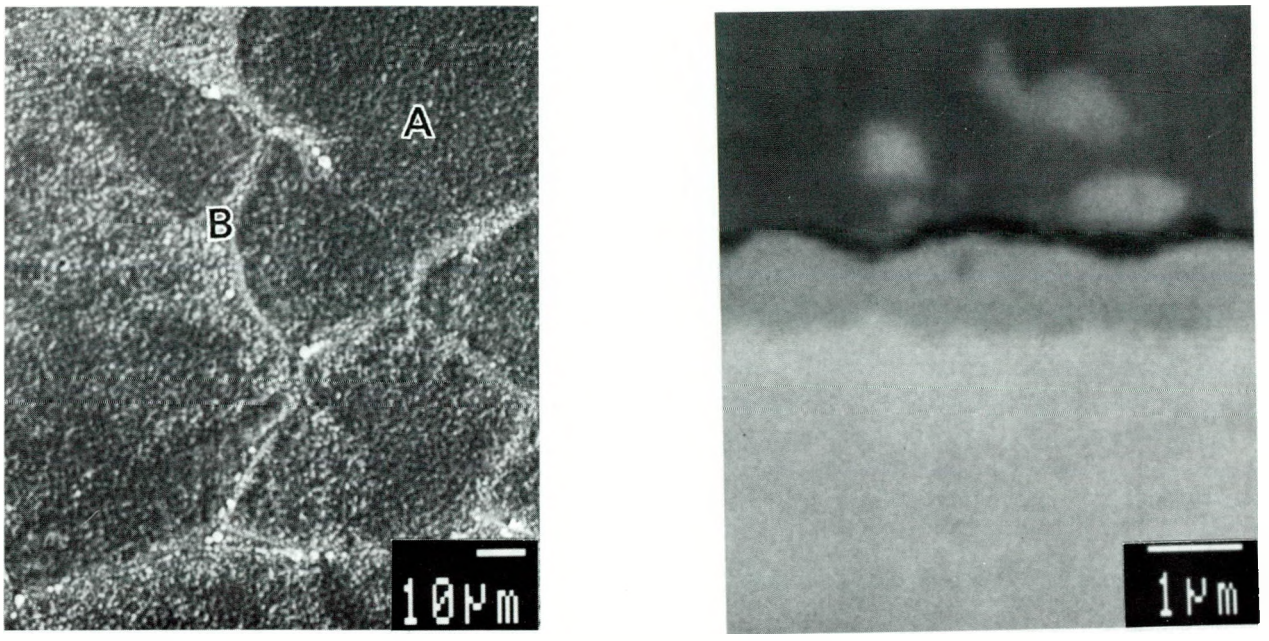

(a) Oxide surface

(b) Oxide X-section

Fig. 28. Si-implanted Fe-25Cr-20Ni oxidized in 1 atm O_2 at 700°C for 120h.

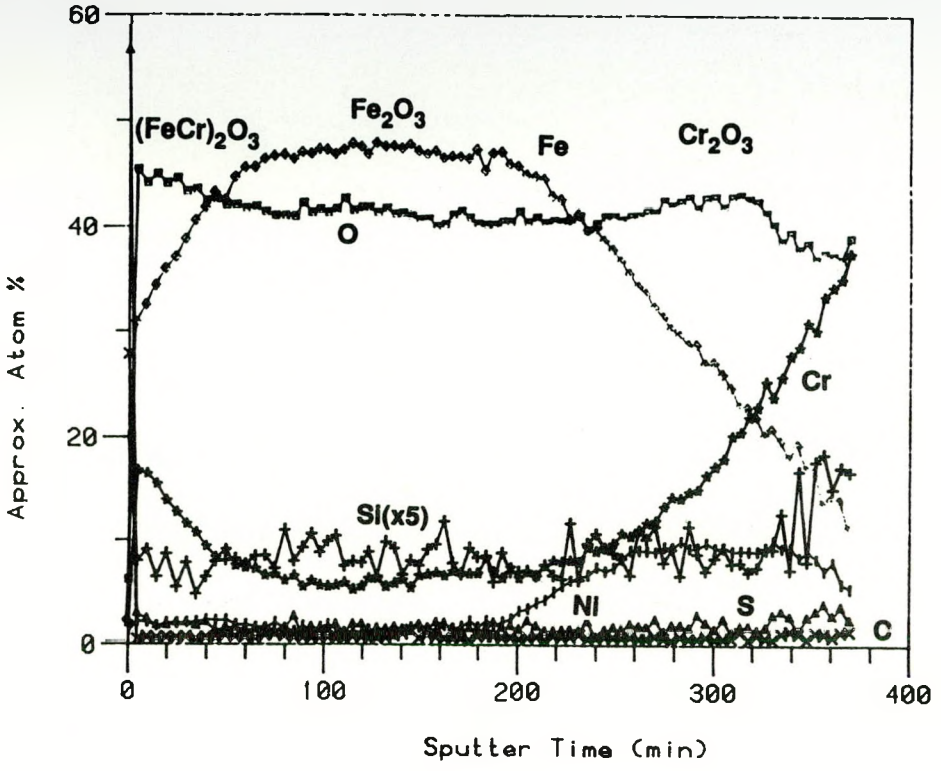

(a)

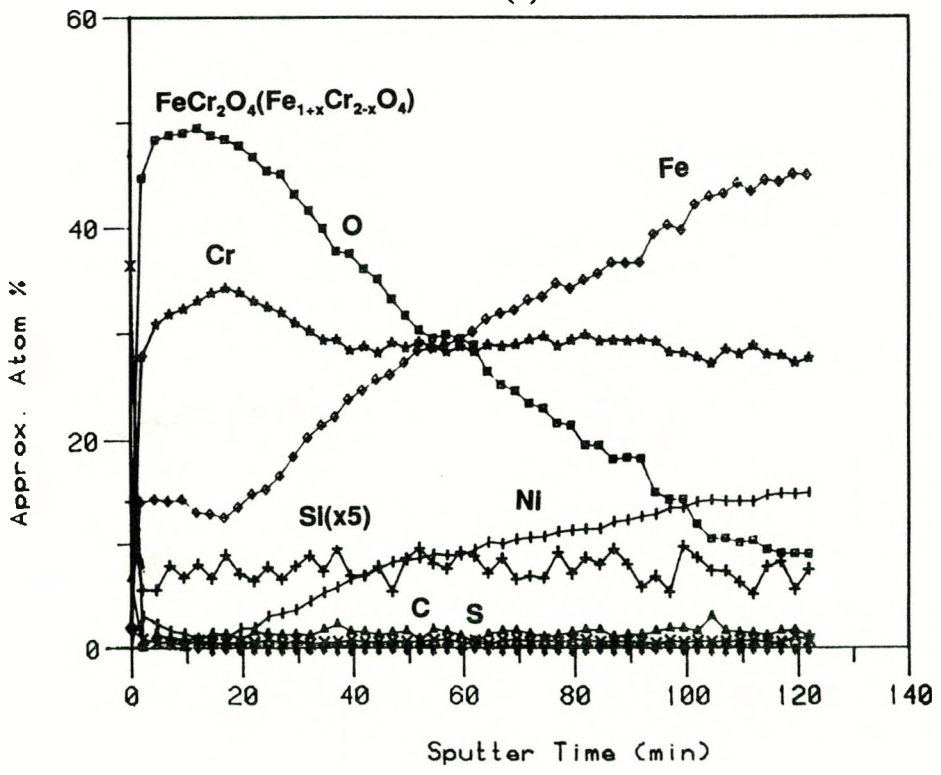

(b)

Fig. 29. AES depth profiles of oxides formed in 1 atm O_2 at 700°C for 120h.

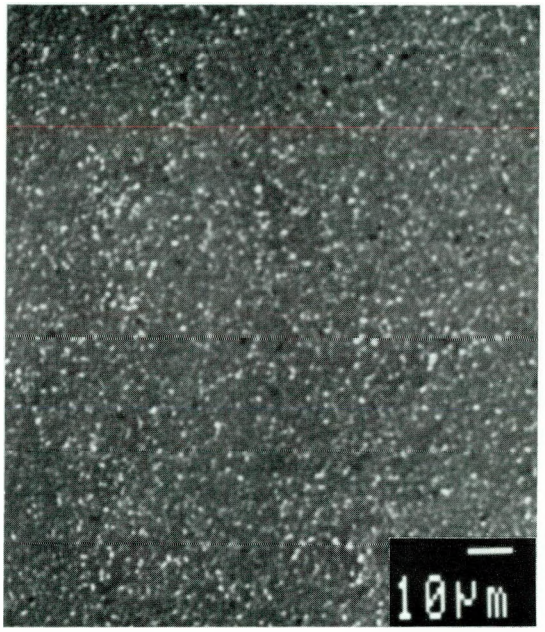

(a) 700°C: 120h

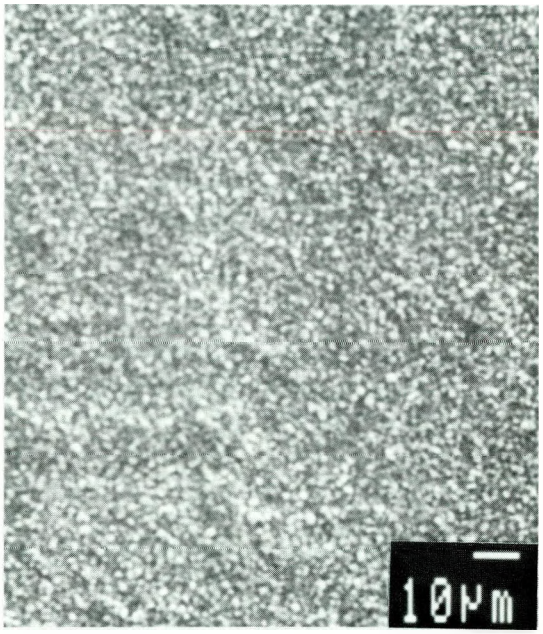

(b) 800°C: 96h

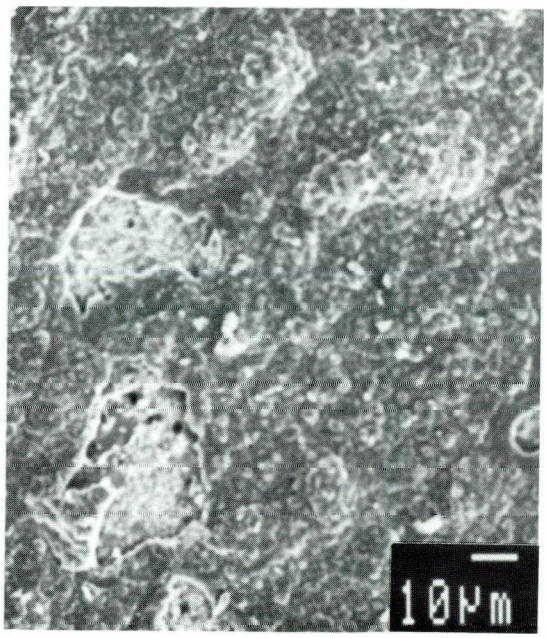

(c) 900°C: 72h

Fig. 30. Surfaces of oxide scales formed on Fe-25Cr-20Ni-1.5Al_2O_3 in 1 atm O_2.

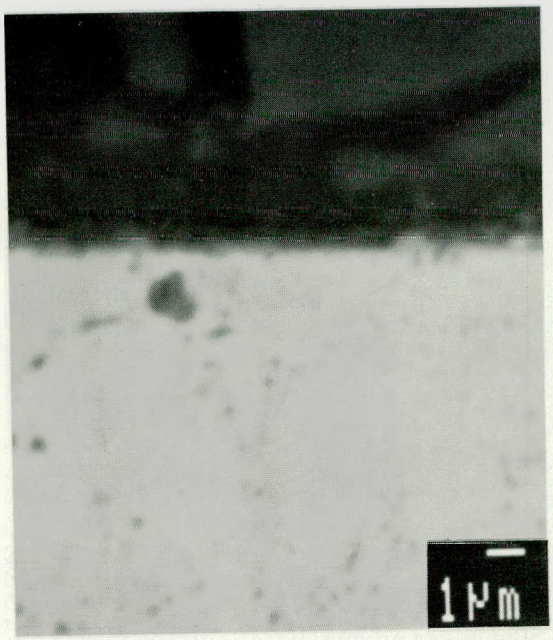

(a) 700°C: 120h

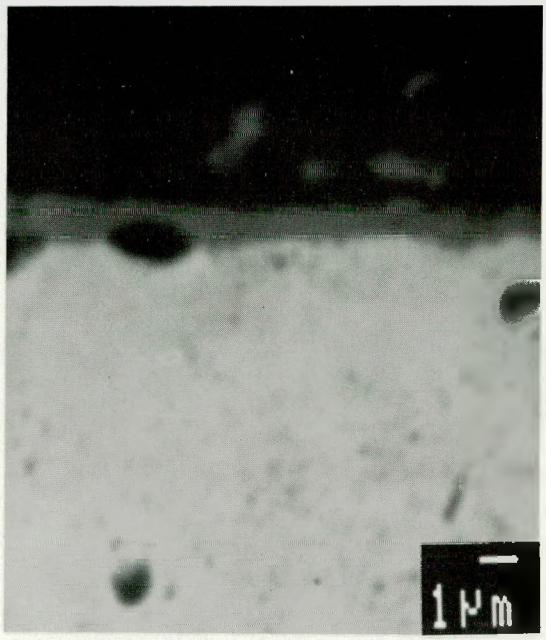

(b) 800°C: 96h

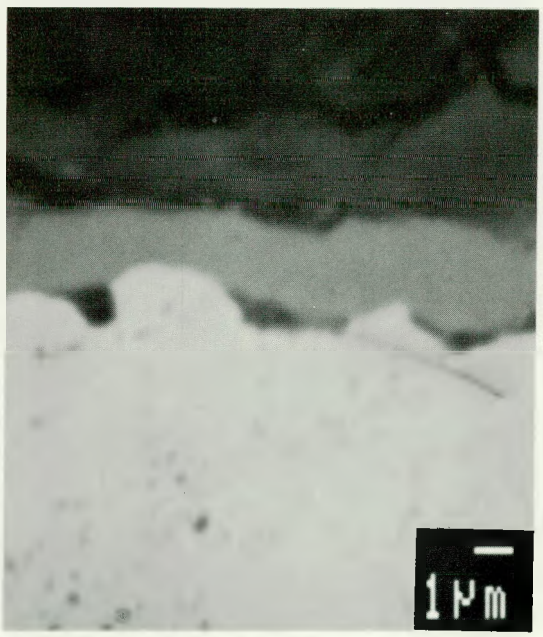

(c) 900°C: 72h

Fig. 31. X-sections of oxide scales formed on Fe-25Cr-20Ni-1.5Al_2O_3 in 1 atm O_2; BEI.

spallation most likely occurred during the cooling of the sample from the test temperature. The scale on the sample exposed to 700°C is very thin, submicron in thickness, Figure 31a. This should be compared with that of base alloy, Figure 24b. The alumina dispersoids appear dark in the matrices, Figures 31a-c.

The scales are essentially Cr rich oxides, Table 9. The composition of the scale on the sample exposed to 700°C does not reflect that of scale alone because the scale is too thin (Figure 31a) and significant interference from the substrate below vitiates the analysis.

4.3.6 (I/M) Fe-25Cr-6Al

The oxide surface is not shown here, but the scale is thin and translucent.

4.4 ISOTHERMAL KINETICS IN $H_2/H_2O/H_2S$/Ar GAS MIXTURE

4.4.1 Kinetics of Base Alloys

The variations of specific weight (mg/cm^2) with time are given in Figure 32a for the base alloys, Fe-25Cr, Fe-25Cr-20Ni and Fe-25Cr-6Al exposed to $H_2/H_2O/H_2S$/Ar gas mixture B at 700°C. Figure 32b describes the initial kinetics for Fe-25Cr-20Ni. The partial pressures of oxygen and sulfur were $1.17x10^{-20}$ and $1.22x10^{-8}$ atm respectively. The kinetics of Fe-25Cr-6Al is the slowest with a k_p value of less than about 10^{-7} mg^2/cm^4 min. The highest specific weight gain is experienced by Fe-25Cr-20Ni. The initial shape of the weight gain curve, Figure 32b, suggests a well defined nucleation-growth process of scale on Fe-25Cr-20Ni in gas mixture B. A similar stage is operative in Fe-25Cr alloy under similar exposure conditions. Both Fe-25Cr and Fe-25Cr-20Ni exhibit a two stage scaling behavior in oxygen-sulfur atmosphere, Figures 33a-b. The isothermal kinetics of scaling is not parabolic in either stage. The initial rates are fast with time exponents 1.78 and 2.86 respectively for Fe-25Cr and Fe-25Cr-20Ni. These values are very high compared to 0.5 (parabolic kinetics) observed for these two alloys under purely oxidizing condition. This time exponent decreases to 0.3 for both the alloys in stage II, Figures 33a-b. The rate constants, k, for Fe-25Cr and Fe-25Cr-20Ni in stages I and II are respectively: Fe-25Cr: $k_I=1.54x10^{-5}$, $k_{II}=2.6x10^{-2}$ mg/cm^2 min; Fe-25Cr-20Ni: $k_I=2.28x10^{-8}$ and 0.34 mg/cm^2 min.

4.4.2 Kinetics of (I/M) Alloys with Microconstituents

A remarkable reduction in the scaling kinetics of Fe-25Cr-20Ni is observed, Figure 34, when Si or Al_2O_3 is added. This was observed in the gas mixture B at 700°C.

4.5 SCALE MICROSTRUCTURE: ISOTHERMAL AND CYCLIC EXPOSURE TO GAS MIXTURE, $H_2/H_2O/H_2S$/Ar

4.5.1 (I/M) Fe-25Cr and Fe-25Cr-X Alloys

Alloys were exposed to the above gas mixture at 700°C for times up to 192 h. The oxygen and sulfur activities were $1.17x10^{-20}$ and $1.22x10^{-8}$ atm, gas mixture B. The general observations on Fe-25Cr and Fe-25Cr-X (where X=Ce, Hf, La, Pt, and Y) alloys are that the

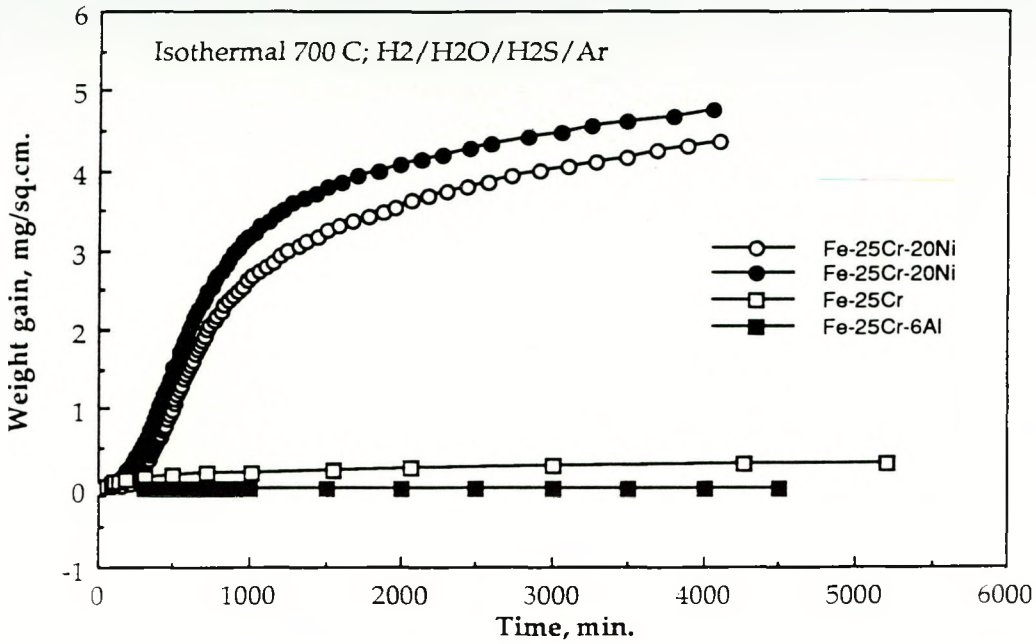

(a) Base alloys

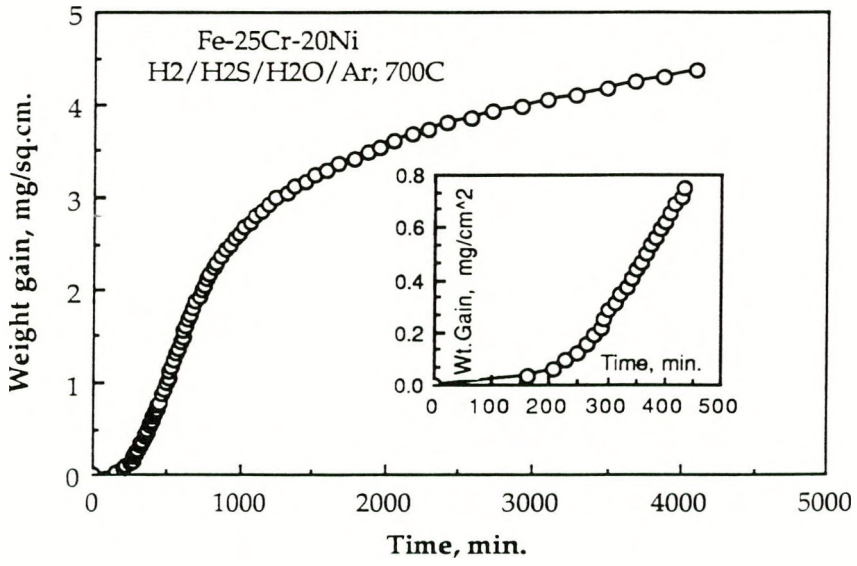

(b) Initial kinetics in Fe-25Cr-20Ni

Fig. 32. Specific weight gains vs time for base alloys in gas mixture B at 700°C for up to 96h.

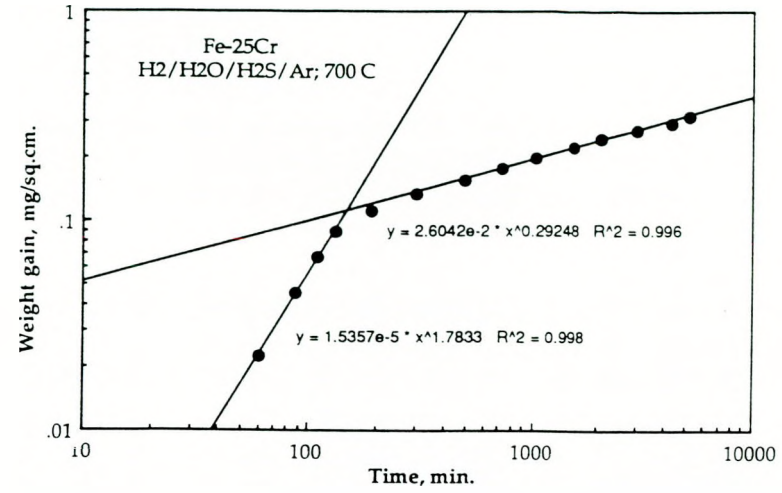

(a)

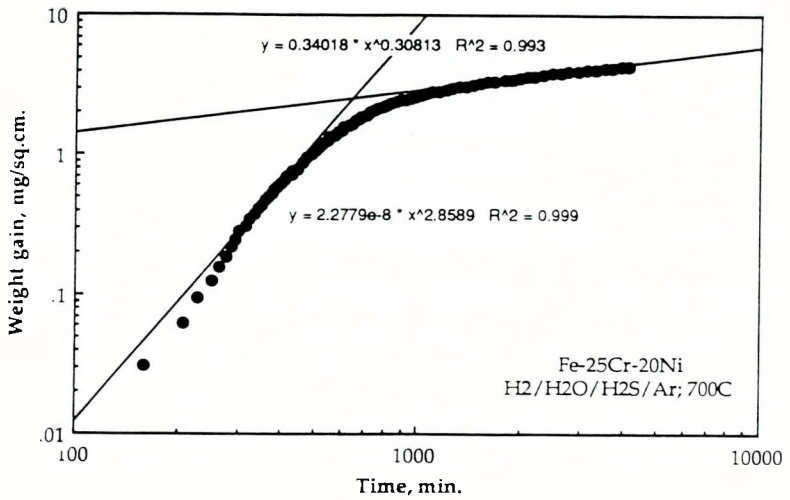

(b)

Fig. 33. Two stage scaling in gas mixture B.

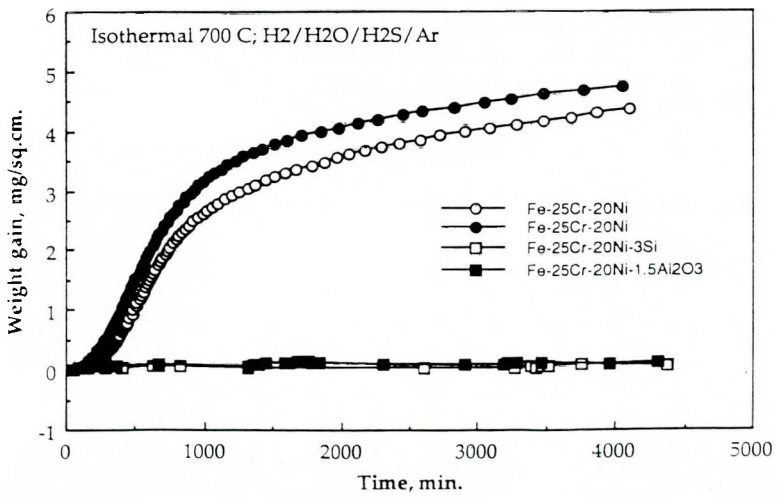

Fig. 34. Time dependence of specific weight gain in gas mixture B.

Cr rich oxide scale breaks down locally by forming S rich islands/nodules. The shape and the extent of the nodules differ. This attack occurs early along the specimen edges. Scale formed on the base alloy on exposure to mixed gas at 700°C for 24 h is shown in Figure 35a. Sulfidation attack is seen locally at the edge. The scale away from this region is Cr rich oxide as determined by AES depth profile (not shown) and EDAX (83Cr-17Fe) and a small amount of S is also detected at the scale/metal interface. The scale thickness is about 740 nm (0.74 μ). Local scale breakdown (47Fe-40Cr-13S) is still seen even after 144 h exposure, Figures 35b-c. The addition of Ce has not changed the behavior significantly, Figure 36a-b. The mode of scale breakdown is shown in Figures 36c-d for Fe-25Cr-1Hf. More Hf is found in the oxide scale formed along the substrate grain boundary (not shown). After 96 h exposure to gas mixture B, local breakdown of otherwise uniform Cr_2O_3 scale is obvious in these pictures. The scale is particularly thick, Figure 36c in the sulfidized regions as a result of exposure to gas mixture B at 700°C for 96 h. External scale, Figure 36d, has a nominal composition of 74Fe-2Cr-24S-0.6Hf, while the scale near the scale/metal interface has 33Fe-63Cr-3S-1.3Hf. Local sulfidation of Cr rich oxide scale continues to occur more extensively at longer times, Figures 37a-b.

La containing alloys also develop uniformly Cr rich scales which break down locally on continued exposure, Figure 38a. The islands are sulfide nodules; spot: 69.7La-22.0Fe-5.8Cr-2.5S; thin scale: 93.6Cr-6.2Fe-0.2S. A cross section through the sulfide nodule is shown in Figures 38b-c. The scales shown in Figures 38a-c result from exposure to gas mixture, B at 700°C/144 h. There is a compositional variation across the scale, Figure 38c. Layer 1 is essentially iron sulfide 74Fe-2.7Cr-23S, while Layer 2 is essentially Cr-Fe oxide (45.0Fe-53.5Cr-1.1S-0.4La). Below this layer lies Cr rich Fe sulfide (35.6Fe-52.8Cr-10.7S) (Layer 3). White spots in the Layer 3 are La rich particle with significant Fe (22Fe-5.8Cr-69.6La-2.6S), and the detected Cr and S may have come from the background. Scales formed on the substrate grain boundaries appear thicker in Fe-25Cr-1Y alloy, when they are not broken down, Figure 39a, and local scale breakdown is obvious, Figure 39b-c. This alloy was exposed to the gas mixture B at 700°C for 144 h.

Scales formed on Fe-25Cr-3Si are thin and have dark and light regions, Figures 40a-c. They are Cr rich oxides with 96-98Cr-3-1Fe-0.4-0.5Si. There is not much change in the composition with time. Less than 0.5% S is detected, which is present as surface impurity.

4.5.2 Cerium Ion Implanted Fe-25Cr

As-implanted microstructure was characterized by STEM. Matrix away from the implanted region has large ferrite grains, and this is confirmed by the [001] single crystal diffraction pattern. Bright field image of the Ce implanted region shows, Figures 41a-b, fine grain structure which produces a ring pattern of electron diffraction. Ce rich regions A in Figure 41a are obvious. Rings, in addition to that of ferrite, are present, and are attributed to the presence of Fe_7Ce phase. The implanted region does not contain any contaminant such as oxygen and carbon.

The energy and fluence of Ce were 160 KeV and $4x10^{16}$ ion/sq. cm.

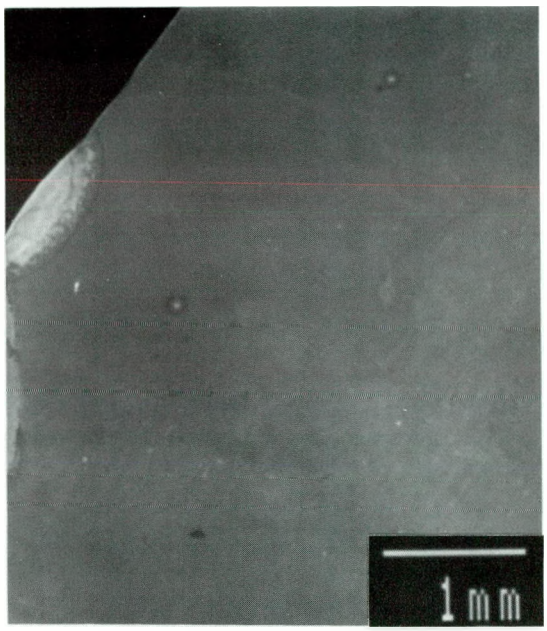

(a) 24h. Breakdown at edges

(b) 144h. General appearance

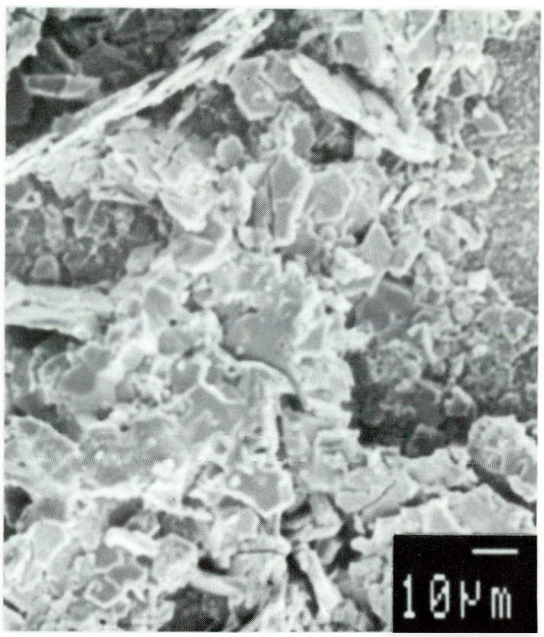

(c) 144h. Local breakdown (47Fe-40Cr-13S)

Fig. 35. Scale formed on Fe-25Cr in gas mixture B, at 700°C.

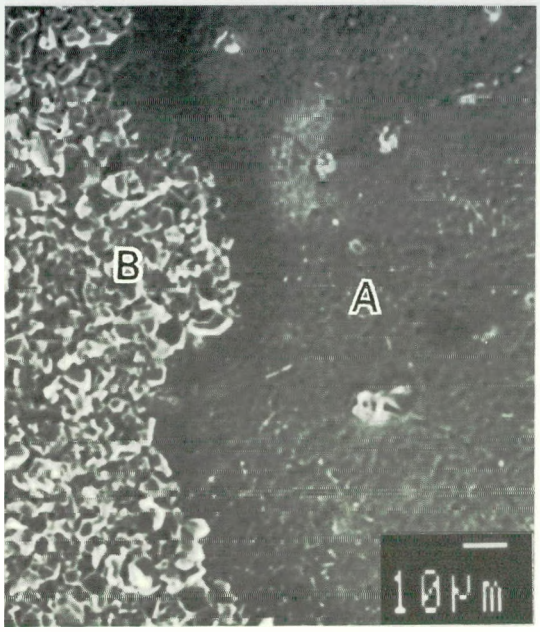

(a) Fe-25Cr-1Ce
A: 95.3Cr-4.5Fe-0.2Ce
B: 36.5Cr-42.8Fe-0.6Ce-20.1S

(b) Fe-25Cr-1Ce; X-Section (BEI)

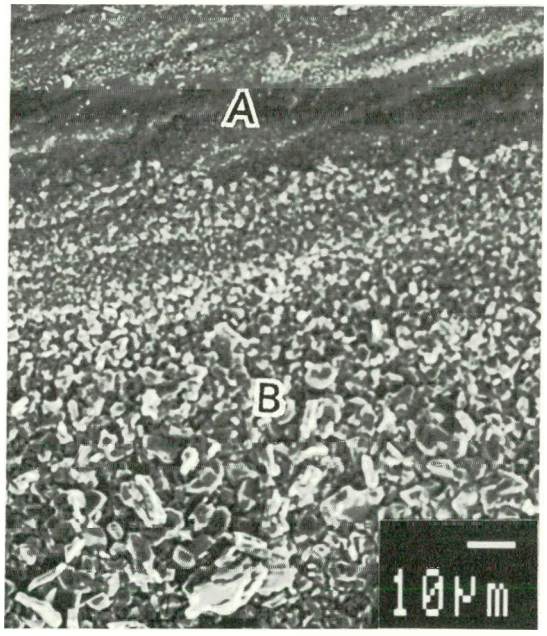

(c) Fe-25Cr-1Hf
A: 97.0Cr-2.6Fe-0.4Hf-.04S
B: 14.1Cr-56.8Fe-29.1S

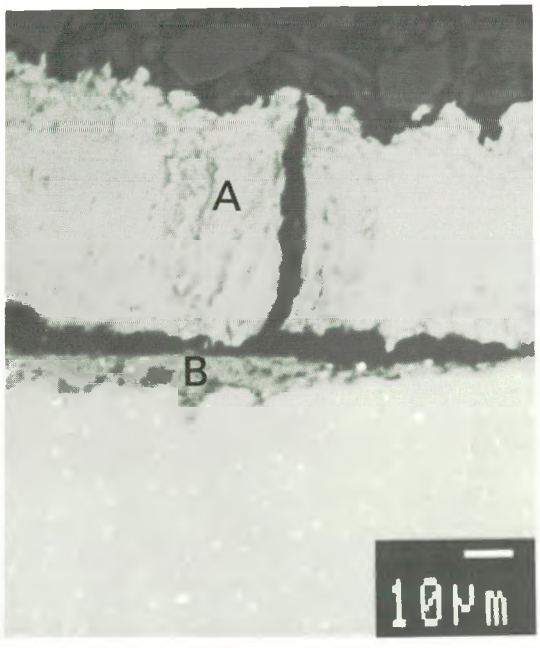

(d) Fe-25Cr-1Hf; X-section (BEI)
A: 2Cr-74Fe-0.6Hf-24S
B: 63Cr-33Fe-1.3Hf-3S

Fig. 36. Scale on Fe-25Cr-X formed in gas mixture B, 700°C, 96h.

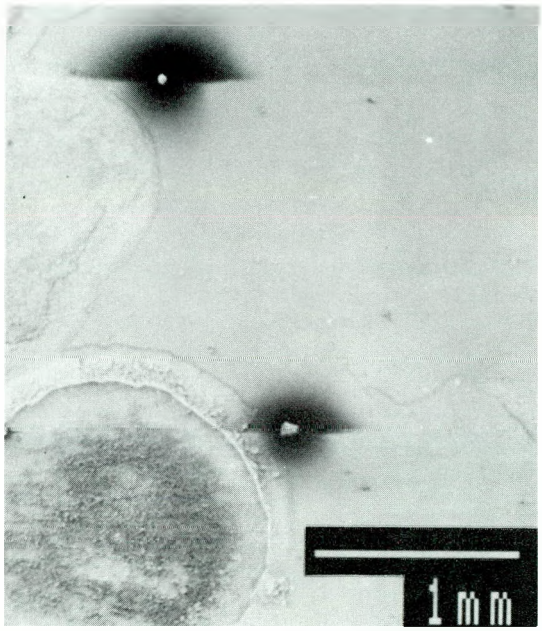

(a) Low magnification.

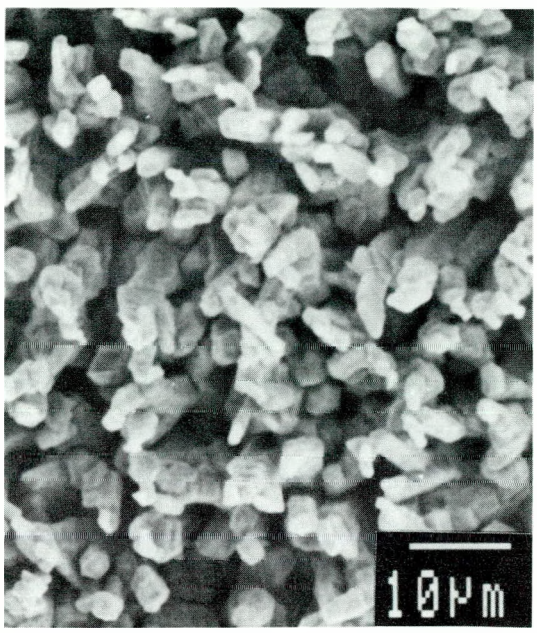

(b) Sulfidized area at high magnification: 31.9Cr-55.8Fe-12.4S

Fig. 37. Local breakdown of Cr_2O_3 scale on Fe-25Cr-1Hf exposed gas mixture B at 700°C for 144h.

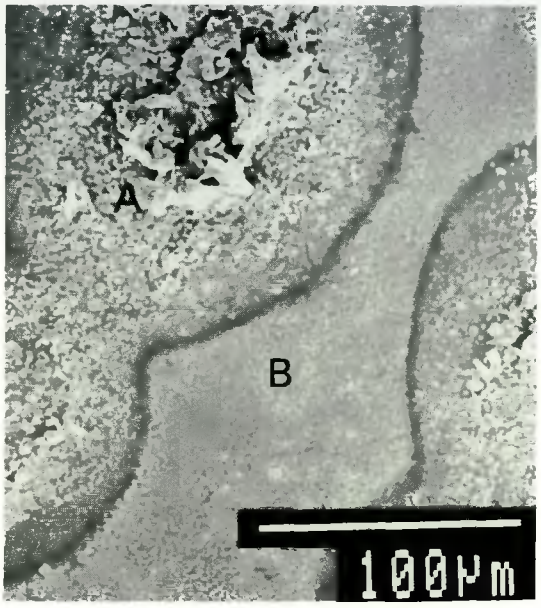

(a) Sulfide nodules
A: 69.7La-22.0Fe-5.8Cr-2.5S
B: 93.6Cr-6.2Fe-0.2S

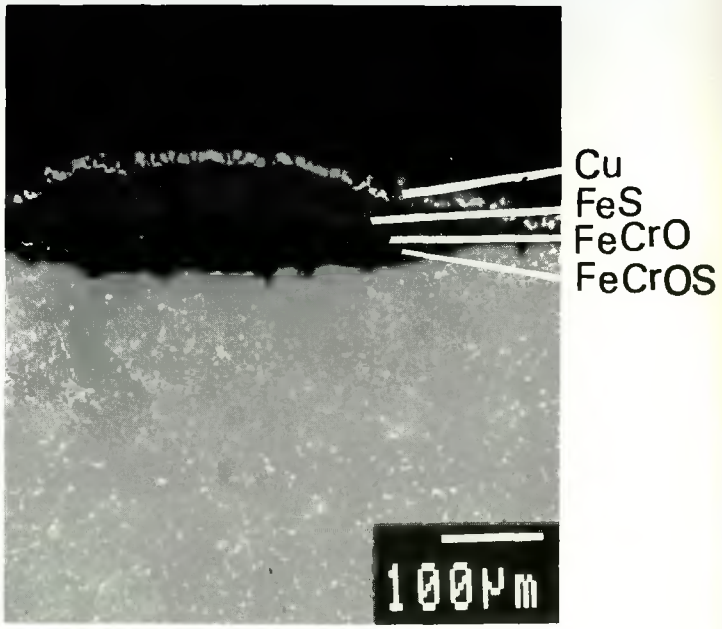

(b) X-section (BEI)

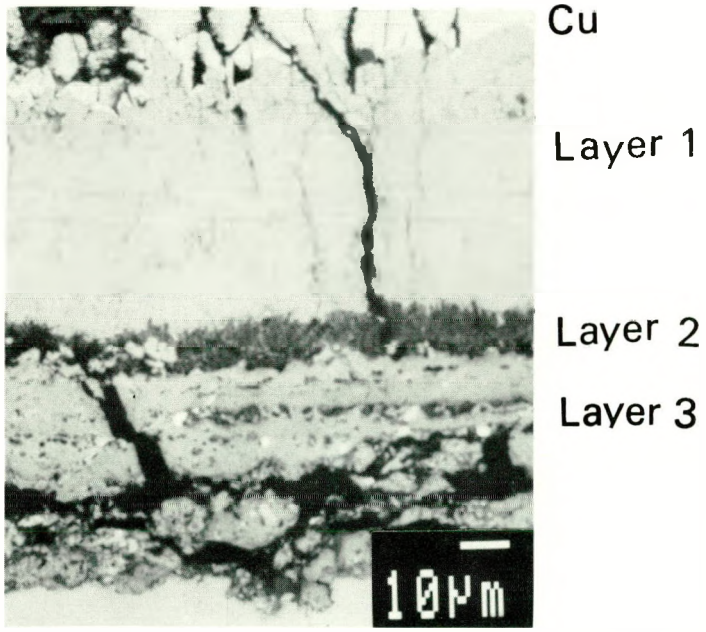

(c) X-section (BEI)

Fig. 38. Local breakdown of chromia scale on Fe-25Cr-1La in gas mixture B, 700°C, 144h.

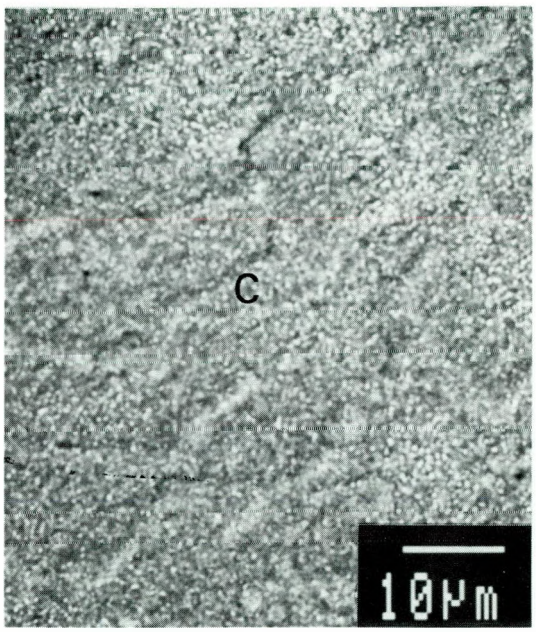

(a) Scale away from nodule
C: 95.5Cr-4.5Fe

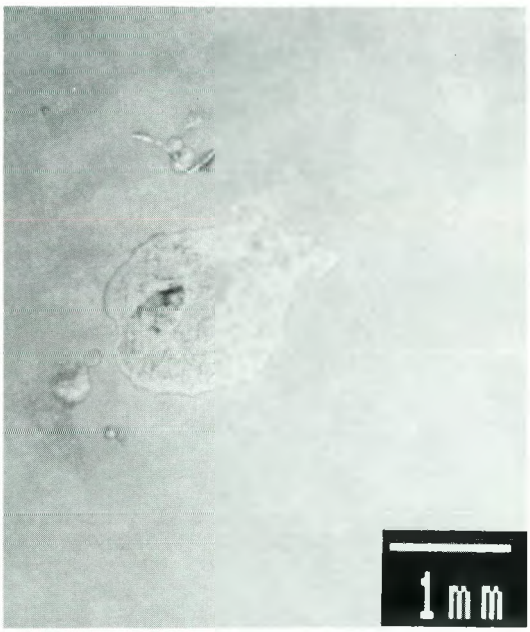

(b) Local breakdown

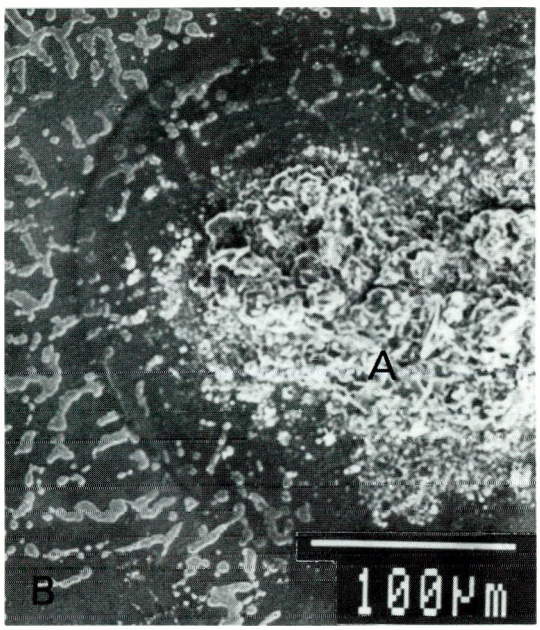

(c) Local breakdown, A: 35.4Cr-44Fe-0.02Y-20.6S; B: 80.2Cr-19.8Fe,
C: 95.5Cr-4.5Fe

Fig. 39. Local breakdown of chromia scale on Fe-25Cr-1Y exposed to gas mixture B, 700°C, 144h.

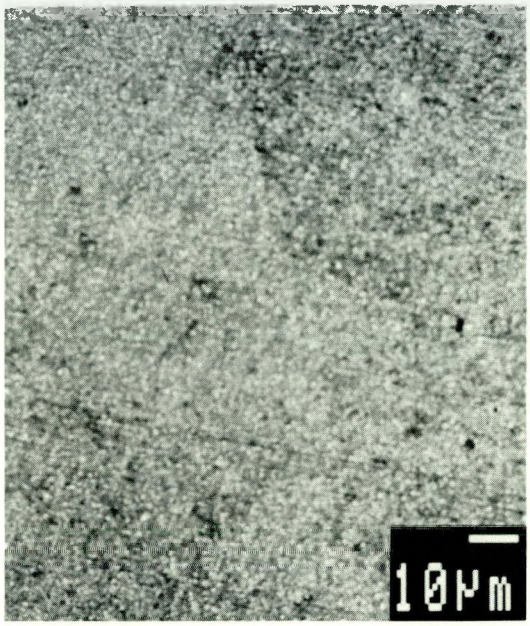

(a) 48h

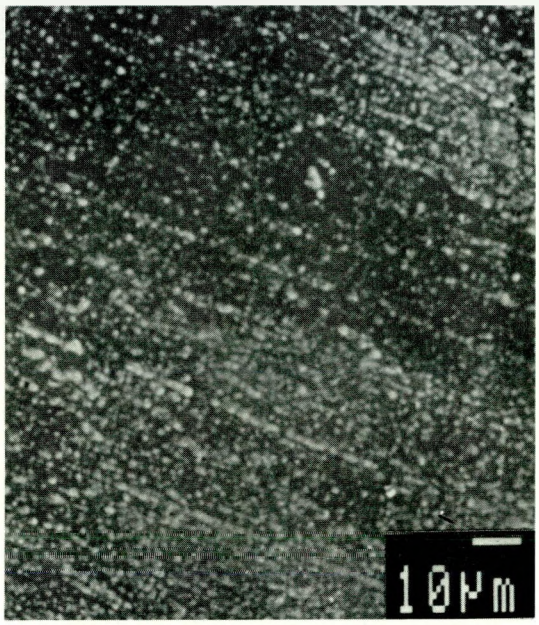

(b) 96h

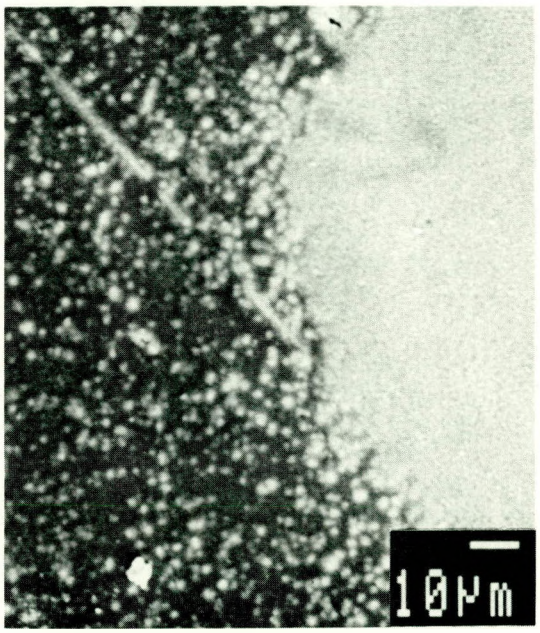

(c) 192h

Fig. 40. Oxide scale on Fe-25Cr-3Si formed in gas mixture B, 700°C.

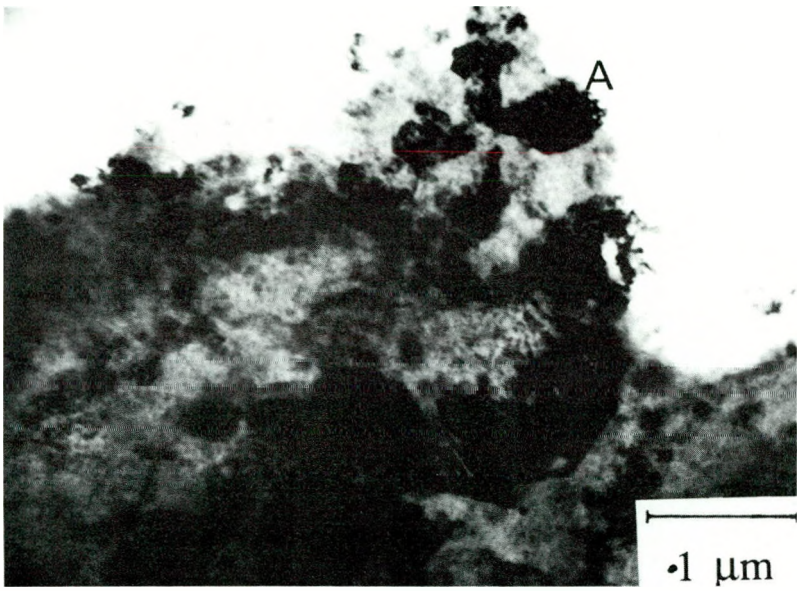

(a) Bright field image, A is Fe_7Ce

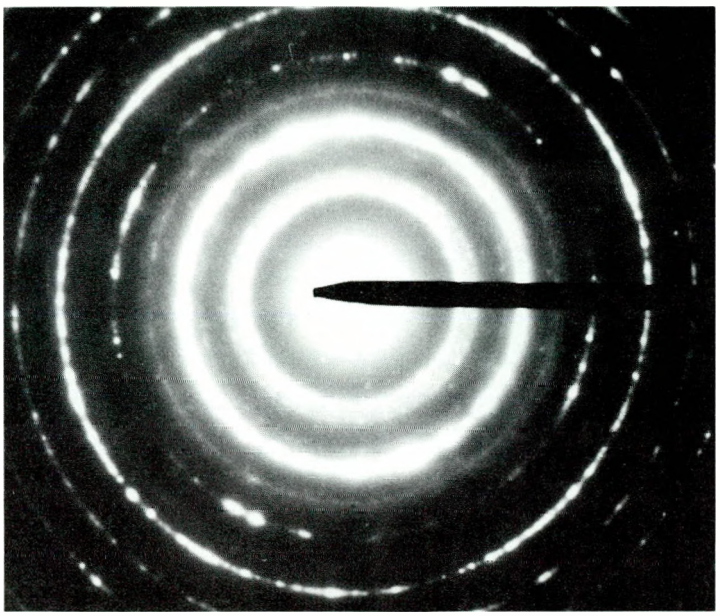

(b) Diffraction pattern due to fine grains

Fig. 41. TEM and ED of Ce-implanted region in Fe-25Cr which develops fine grain and Fe_7Ce phases (A).

Ce implanted Fe-25Cr on exposure to the gas mixture B for 24 h develop Cr rich scales with nodules, Figure 42a-b. S was detected in all the nodules A, B, and C, Figure 42a-b: (A) 86.4Cr-11.2Fe-1.70Ce-0.7S, (B) 86.2Cr-10.9Fe-2.2Ce-0.7S, (C) 78.7Cr-17.1Fe-3.2Ce-0.9S.

Scanning Auger maps of the scale are shown in Figures 43a-c. The secondary electron image, Figure 43a shows two nodules marked 1 and 2. The iron map, Figure 43b shows the presence of Fe in nodules 1 and 2. Only the nodule 2 has sulfur as indicated by the sulfur map, Figure 43c. Auger spectrum of nodule 2 confirmed the presence of more Fe than that detected at nodule 1 and its existence with S. Oxide scale far away from these nodules is Cr rich oxide, (Auger spectrum not shown). AES depth profile of the scale off the nodules, Figure 44a suggests essentially Cr rich oxide scale with significant S and Ce at the metal/scale interface. The resolution of this AES instrument is of the order of 5 μm. The scale thickness is about 0.54 μ as estimated using the sputtering rate of 16 nm/min. Cr rich sulfide with Fe is detected through the scale thickness (~1.8 μ) on the nodule, (2, Figure 43a) Figure 44b. S concentration decreases inward. The metal/scale interface below the nodule 2 (Figure 43a) is not sharp, Figure 44b, suggesting rough interface.

4.5.3 (P/M) Fe-25Cr-1.5Al_2O_3 Alloys

The P/M Fe-25Cr-1.5Al_2O_3 alloys develop a thin uniform Cr rich oxide scale of about 1 μ in thickness when they are exposed to mixed gas ixture B at 700°C for 96 h, Figure 45a-b. The EDAX analysis of the scale gives 98.2Cr-1.8Fe, and no sulfur is detected. No interfacial voids at the scale/metal interface are seen.

However, under thermal cycles, local scale breakdown occurs, Figures 45c-d. Although the scale is essentially thin Cr_2O_3, 12Fe-88Cr (Figure 45c), local nodules of sulfides (56Fe-26.8Cr-17.2S) form and lead to break away corrosion. However, unattacked Cr_2O_3 scale is adherent without interfacial voids.

4.5.4 (I/M) Fe-25Cr-20Ni and Fe-25Cr-20Ni-X Alloys

The presence of Ni makes oxidation and mixed corrosion behavior of this base alloy different from that of Fe-25Cr. The base alloy sulfidizes (64.8Fe-10.5Cr-4.3Ni-20.4S) locally within a few minutes of exposure to gas mixture B at 700°C. The surface scale formed after 1 h exposure is shown in Figures 46a-b. Scale develops with time three different morphologies and compositions as shown in Figures 47a-d: porous (spongy), faceted and smooth regions have compositions 46.7Fe-37.1Ni-0.5Cr-15.7S, 62.3Fe-10.1Ni-8.2Cr-19.4S and 57.8Fe-6.4Ni-21.1Cr-14.8S respectively. The nominal compositions of these phases suggest that the porous phase is Fe-Ni sulfide, the faceted, (FeCr)S and the smooth scale, either oxide/sulfide spinel or any sulfides containing Fe, Cr, Ni and S. The cross section of the scale is shown in Figure 47d, and compositions vary across the scale.

The addition of reactive element or Pt does not totally change the corrosion response of the resulting alloy. Fe-25Cr-20Ni-1Ce undergoes sulfidation locally (62.9Fe-4.3Ni-13.7Cr-19.1S) in one hour as the base alloy, Figures 48a-b. After a few hours (<24 h) the same three scale morphologies, porous (spongy), faceted and relative smooth

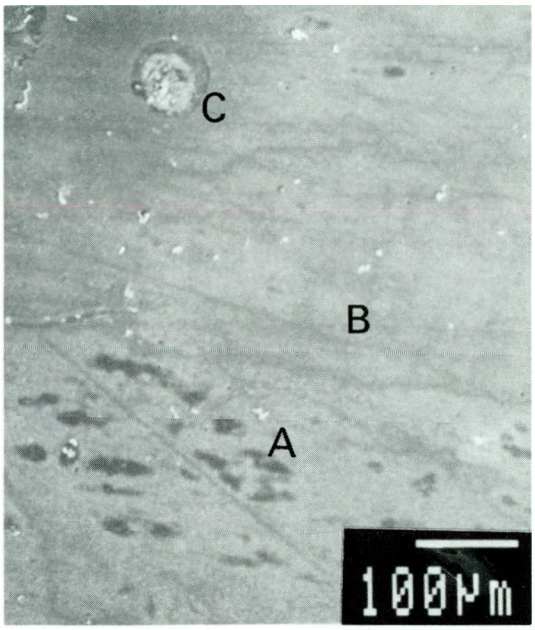

(a) General Scale, A: 86.4Cr-11.2Fe-1.7Ce-0.7S; B: 86.2Cr-10.9Fe-2.2Ce-0.7S; C: 78.7Cr-17.1Fe-3.2Ce-0.9S

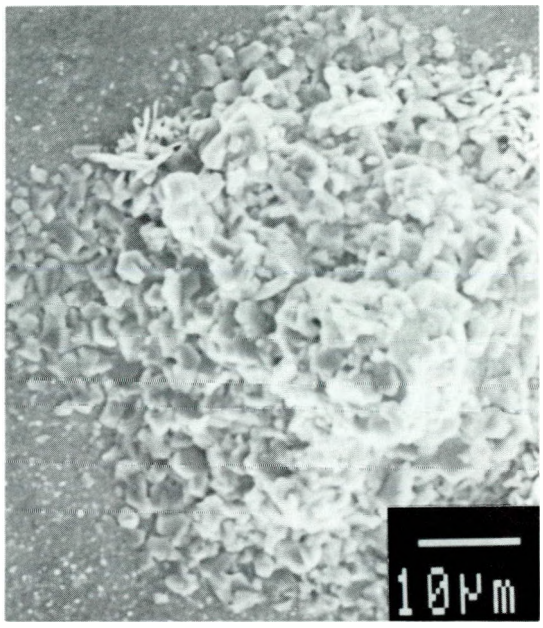

(b) Nodule C at high magnification

Fig. 42. Scale on Ce-implanted Fe-25Cr formed in gas mixture B, 700°C, 24h.

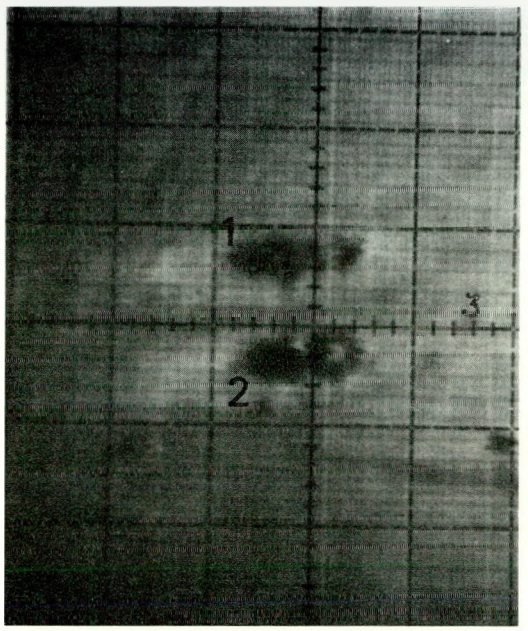

(a) SEM

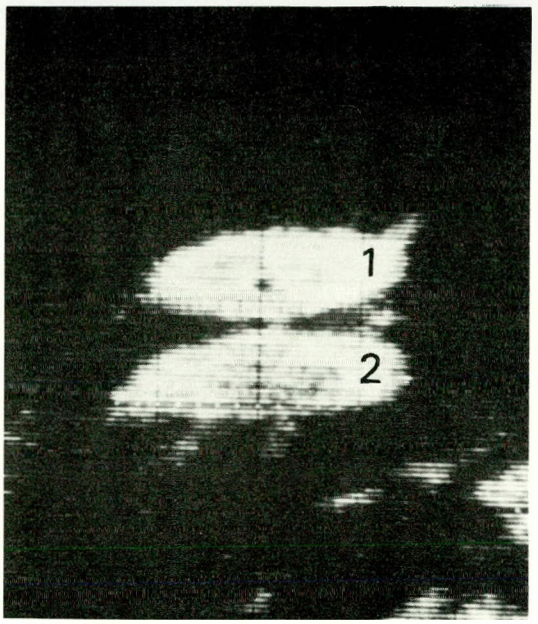

(b) Fe-map

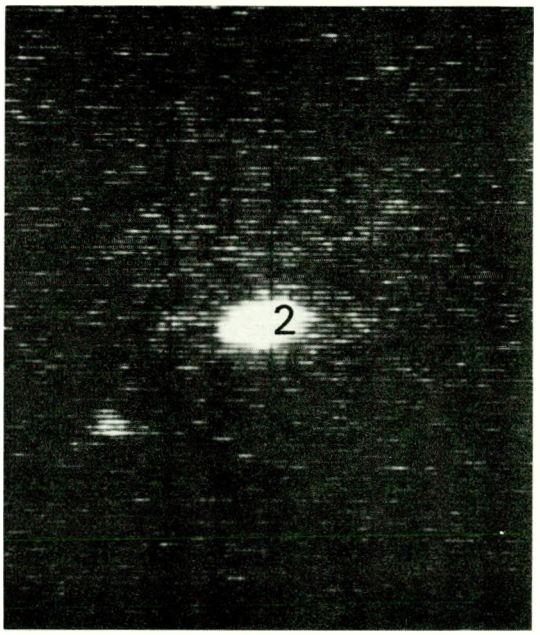

(c) S-map

Fig. 43. SEM and Scanning Auger elemental maps of scale on Fe-25Cr-imp. Ce formed in gas mixture B, 700°C, 24h. ×250

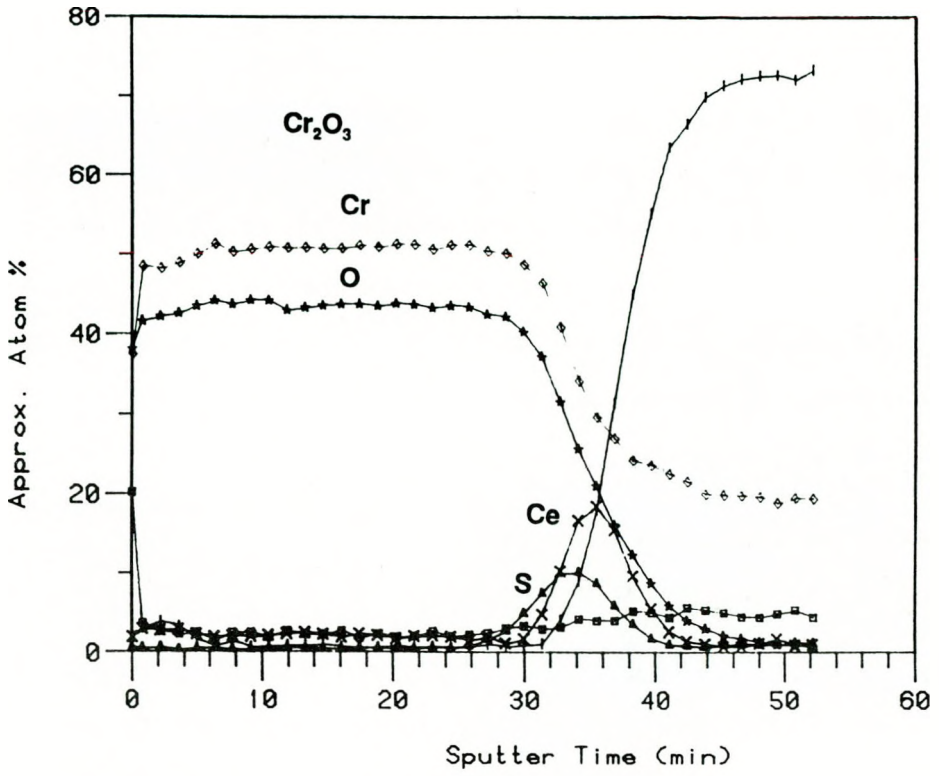

(a) Area 3 in Fig. 43(a).

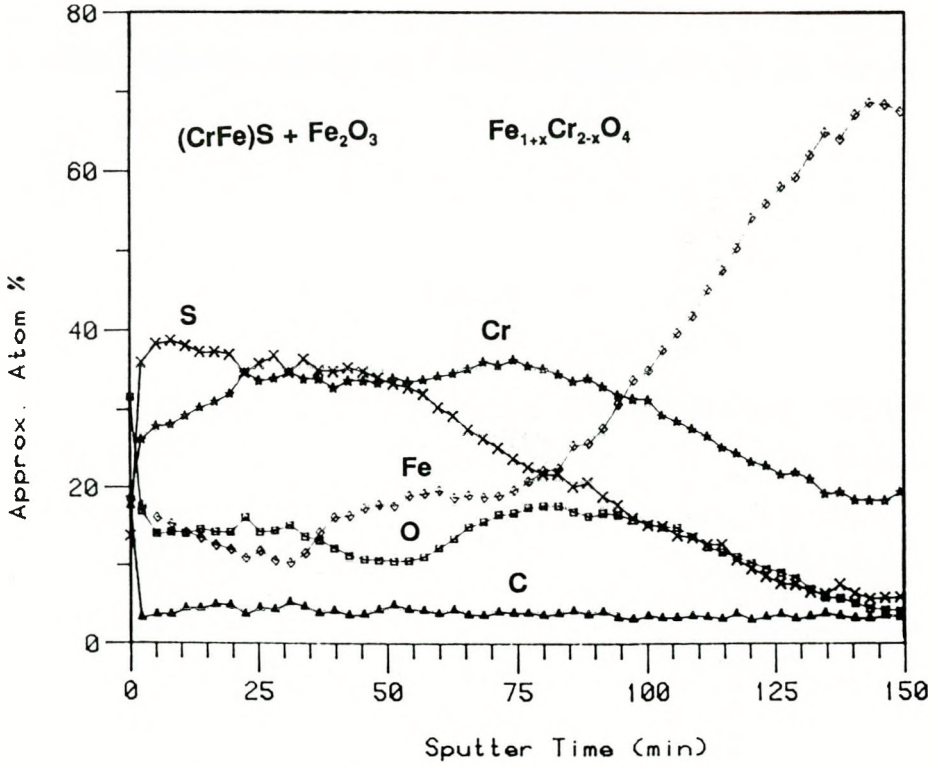

(b) Area 2 (Spot) in Fig. 43(c).

Fig. 44. AES depth profiles of scale on Ce-implanted Fe-25Cr exposed to gas mixture B, 700°C, 24h.

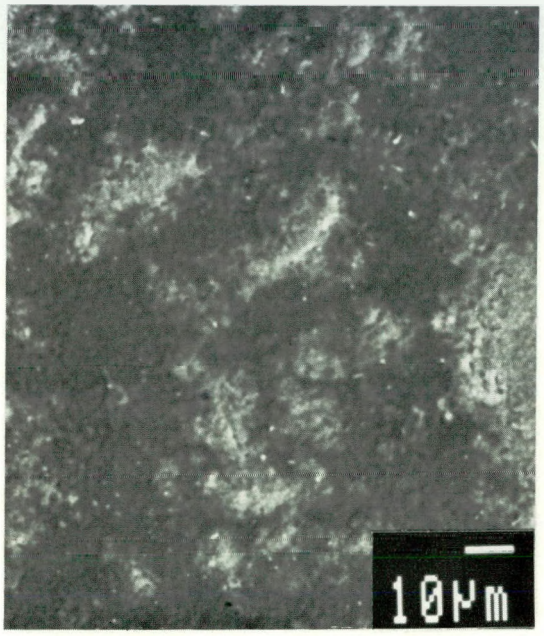

(a) Isothermal

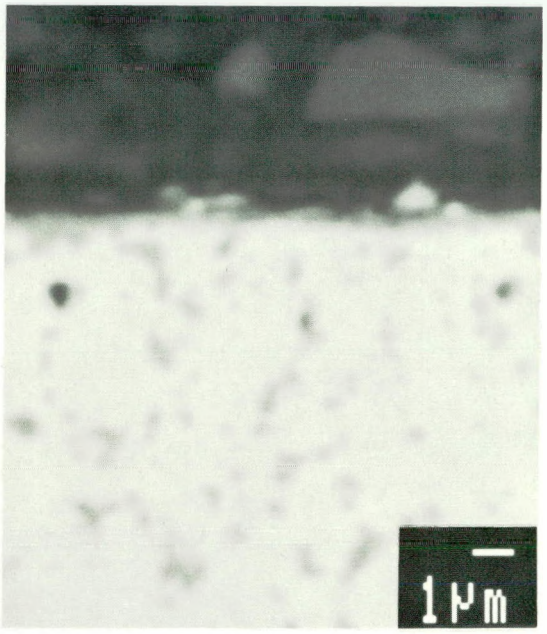

(b) X-section; Isothermal (BEI)

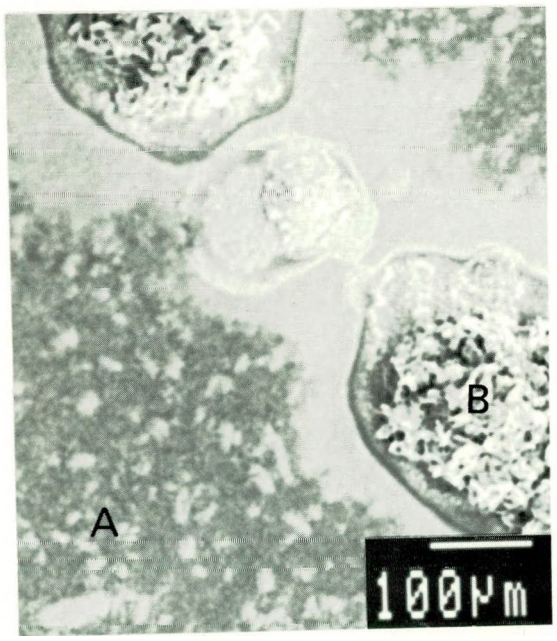

(c) Cyclic: 700°↔50°C: Local breakdown
A: 12Fe-88Cr
B: 56.0Fe-26.8Cr-17.2S

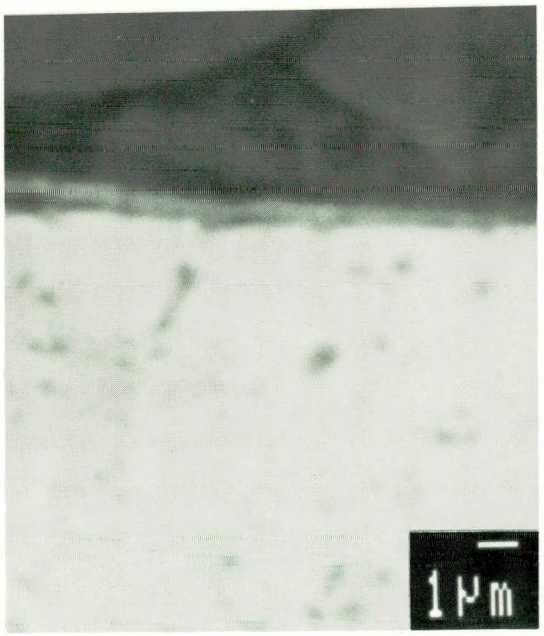

(d) X-section, Cyclic (BEI)

Fig. 45. Scale on Fe-25Cr-1.5Al_2O_3 exposed to gas mixture B, 700°C, 72h.

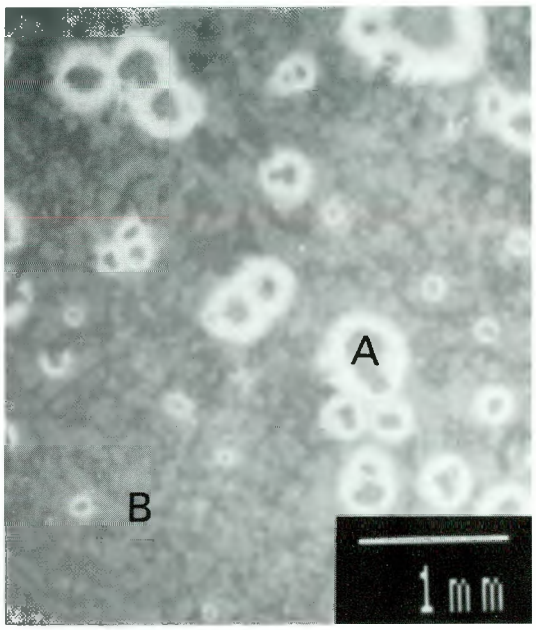

(a) Low magnification
A: 64.8Fe-10.5Cr-4.3Ni-20.4S
B: 52.5Fe-30.9Cr-16.3Ni-0.3S

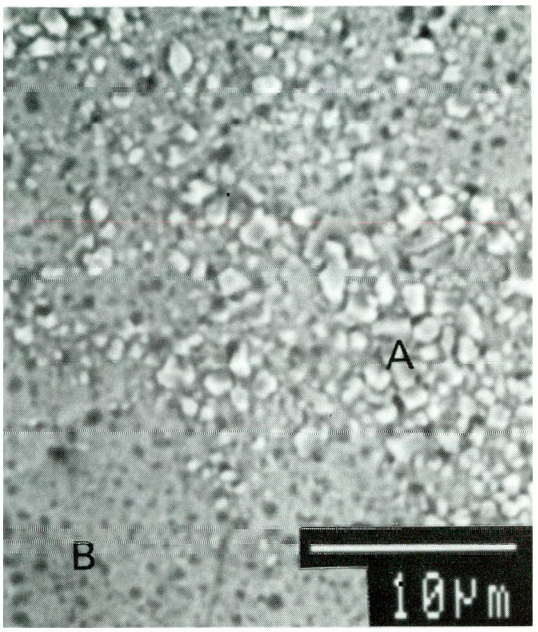

(b) High magnification

Fig. 46. Local scale breakdown on Fe-25Cr-20Ni exposed to gas mixture B, 700°C, 1h.

(a) General appearance

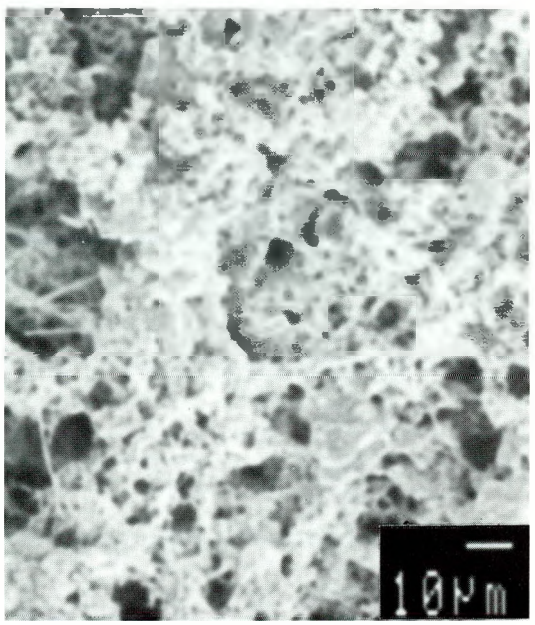

(b) Porous, 46.7Fe-37.1Ni-0.5Cr-15.7S

Fig. 47. Scale on Fe-25Cr-20Ni exposed to gas mixture B, 700°C, 96h.

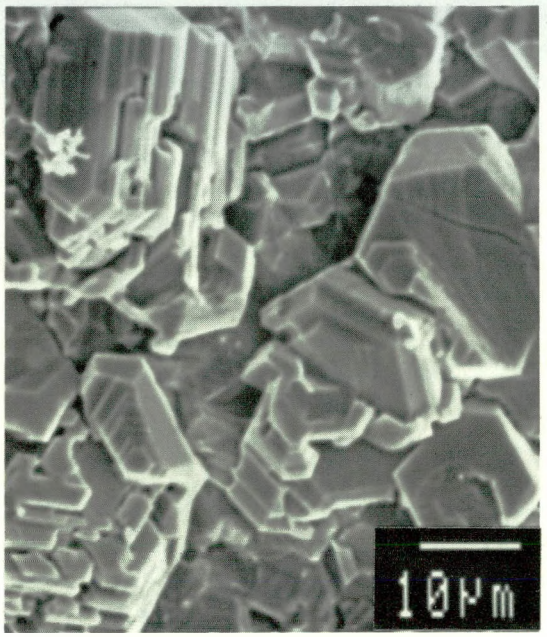

(c) Faceted; 62.3Fe-10.1Ni-8.2Cr-19.4S

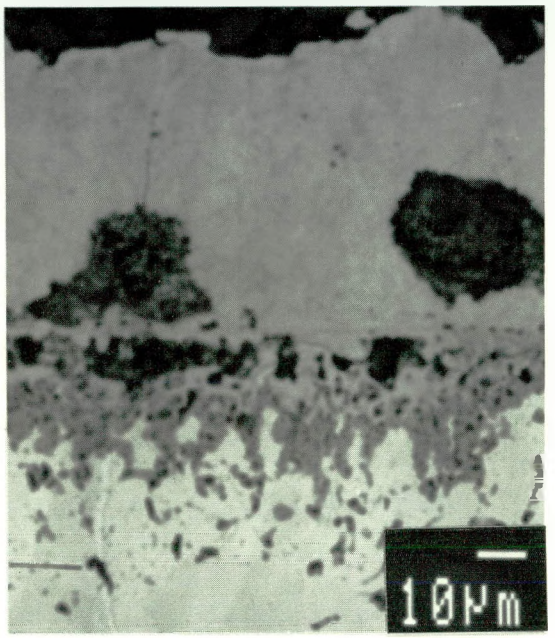

(d) X-section (BEI)

Fig. 47 (cont'd.). Scale on Fe-25Cr-20Ni exposed to gas mixture B, 700°C, 96h.

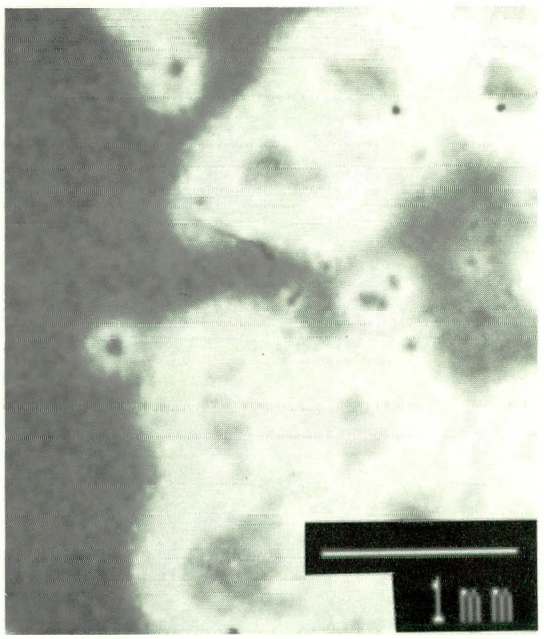

(a) Low magnification

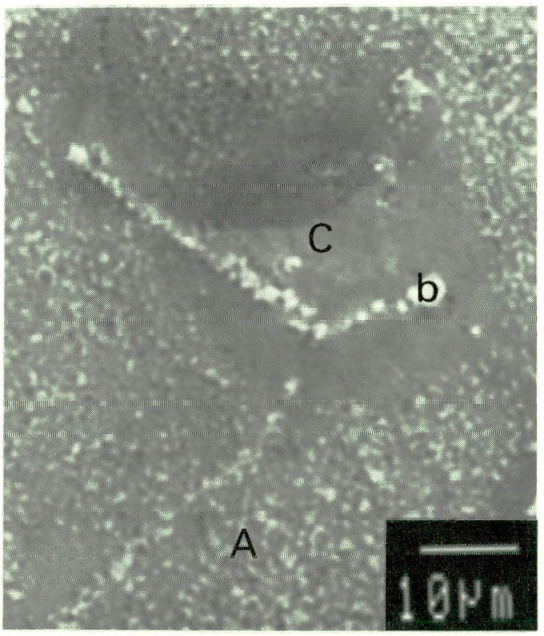

(b) High magnification

A: 62.9Fe-13.7Cr-4.3Ni-19.1S
B: 31.5Fe-23.8Cr-23.0Ni-20.4Ce-1.3S
C: 47.3Fe-28.6Cr-19.8Ni-4.1Ce-0.2S

Fig. 48. Local breakdown of scale on Fe-25Cr-20Ni-1Ce formed in gas mixture B, 700°C, 1h.

scales are established. Figures 49a-e show the scale formed on this alloy in 192 h. Figure 49e is a cross section of the scale shown in Figure 49a. Scales with similar features are observed in alloys with Hf, La, Y and Pt. The XRD lines of the scales are compared with data file, and this comparison suggests the presence of FeS and $FeCr_2S_4$ besides Cr_2O_3 and $FeCr_2O_4$ ($Fe_{1+x}Cr_{2-x}O_4$). In all these alloys the porous (spongy) phase seen in SEM appear as dark powdery phase to the unaided eyes. They were liquid or semisolid just on removing the sample from the test temperature 700°C to the cooler section of the reaction tube. They were poorly adherent.

An interestingly different scale morphology and corrosion response is observed in Fe-25Cr-20Ni-3Si. The scales formed on this alloy are shown in Figures 50a-d. After 48 h the scale thickening occurs locally and mostly along the substrate grain boundaries, Figure 50a. Even within the substrate grains individual globules are seen. The globules and the scale on the substrate grain boundaries are rich in Cr and lean in Si. The scale on the substrate grain boundaries become continuous, Figure 50b after 192 h, and the scale exhibits local spallation, Figure 50c. Sulfidation is not seen.

A cross-sectional BEI of the scale formed on Fe-25Cr-20Ni-3Si exposed to gas mixture B at 700°C for 192 h is shown in Figure 50d. The scale thickness is about 1 μ which is significantly less than the thickness of scales observed on alloys with rare earths or Pt addition, Figure 47d or 49e. The scale is Cr rich oxide with some Fe and Si, (2.8Fe-0.5Ni-94.2Cr-2.4Si-0.1S). No significant sulfur is detected in the scale. XRD study supports the above observation and suggests the presence of Fe_3O_4 in addition to Cr_2O_3.

Scanning Auger Microprobe (SAM) and secondary ions mass spectroscopy were used to characterize the scale because of the desirable behavior of the alloy and the thinness of the scale. Auger spectra were taken at different depths at two different locations to track down any sulfur presence. The sample examined with SAM is the one exposed to the gas mixture B at 700°C for 96 h. The scale morphology at the gas/scale interface is similar to Figure 50b and remains the same with depth, (at 50, 100 and 200 nm). Rough and smooth areas were included in depth profiling. Sputtering was done with Ar at an estimated rate of 16 nm/min. Fe, S and Si are detected as impurities on the scale surface, and are not present just after a brief sputtering. The scale is essentially Cr_2O_3. Si is detected in one location at 200 nm depth. Typical AES spectra from a depth, 0 and 200 nm are is shown in Figure 51a-b.

Elemental analyses of the scale were made by positive and negative SIMS. Unequivocal separation of $^{32}S^-$ and $^{32}O_2^-$ was not possible. The mass resolution required to identify the above two species is 17.8×10^{-3} amu, but the quadrapole mass resolution available at HTML/ORNL is only 1 amu. An alternate procedure would be to use "the target bias offset method," and the target bias range available is again inadequate for this purpose. The absence of S in AES analyses is taken as proof for the absence of contribution to SIMS spectra by $^{32}S^-$.

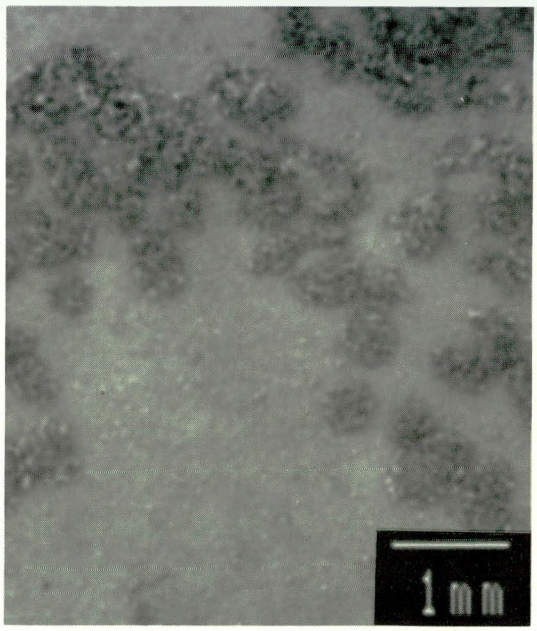

(a) General area

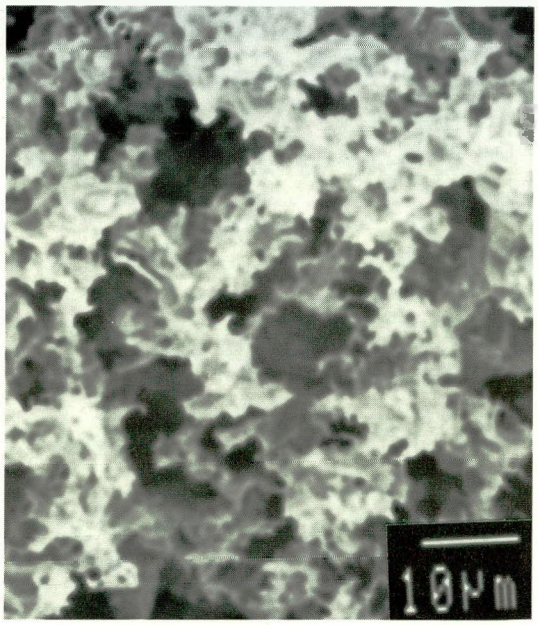

(b) Porous: 7.12Fe-0.5Cr-12.2Ni-0.2Ce-15.9S

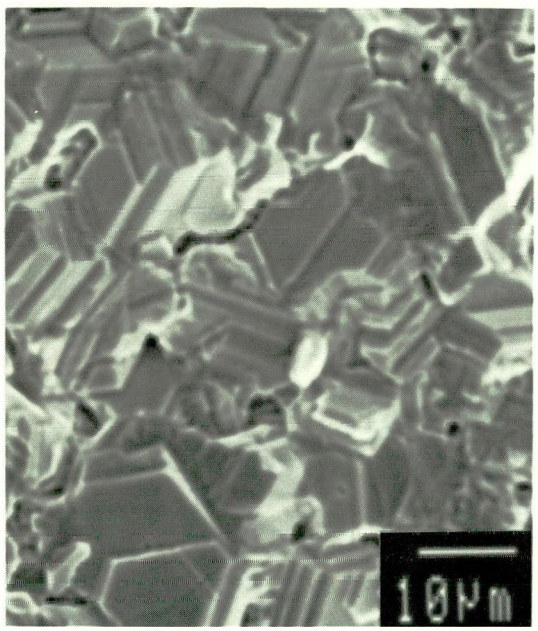

(c) Faceted: 47.0Fe-35.9Cr-4.4Ni-0.1Ce-12.6S

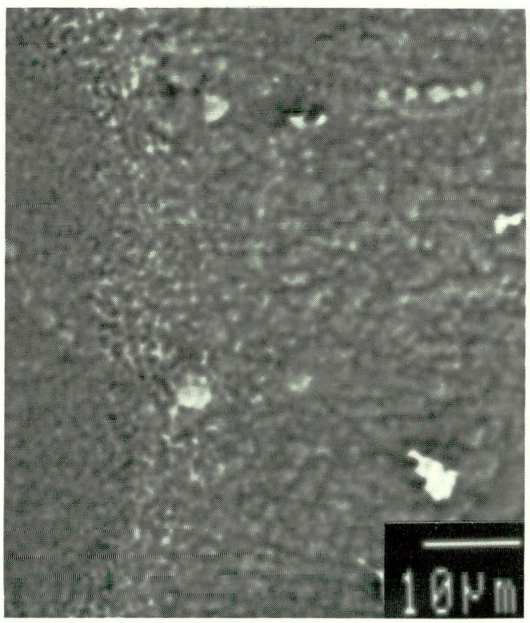

(d) Smooth: 18.7Fe-76.4Cr-4.4Ni-0.5Ce-0.1S

Fig. 49. Scale on Fe-25Cr-20Ni-1Ce exposed to gas mixture B, 700°C, 192h.

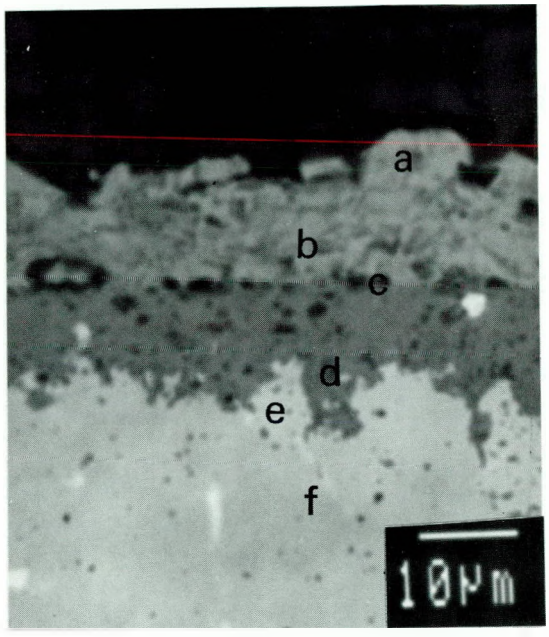

(e) X-section (BEI)

Fig. 49 (cont'd.). Scale on Fe-25Cr-20Ni-1Ce exposed to gas mixture B, 700°C, 192h.

a: 68Fe-2Cr-6Ni-0.1Ce-24S
b: 50Fe-28Cr-5Ni-0Ce-17S
c: 43Fe-51Cr-1Ni-0.04Ce-5S
d: 21Fe-77Cr-.06Ni-0Ce-2S
e: 21Fe-50Cr-4Ni-0Ce-25S
f: 56Fe-24Cr-20Ni

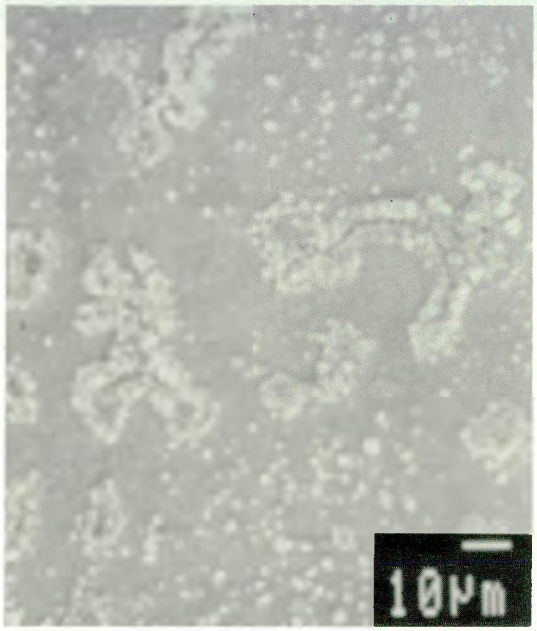

(a) 48h

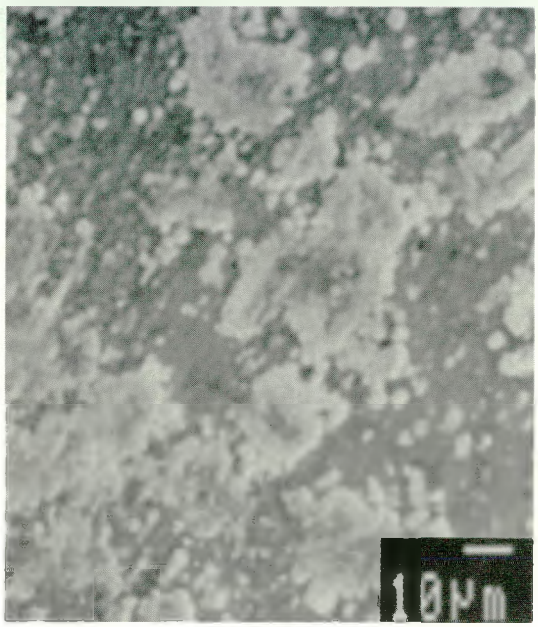

(b) 96h

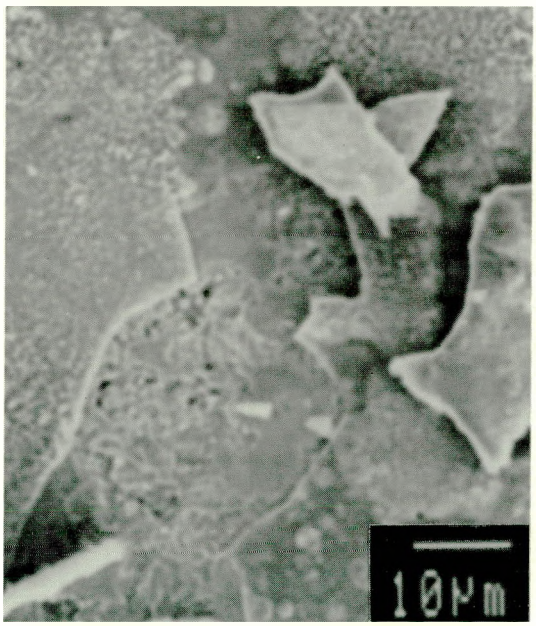

(c) 192h

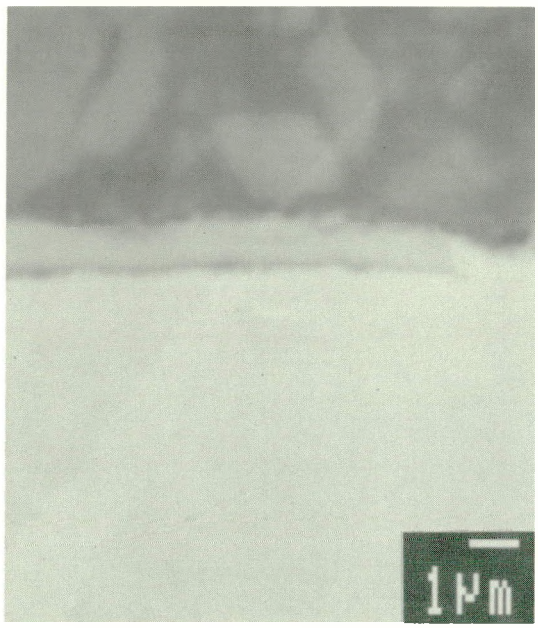

(d) X-section, 192h (BEI)

Fig. 50. Scale on Fe-25Cr-20Ni-3Si exposed to gas mixture B, 700°C.

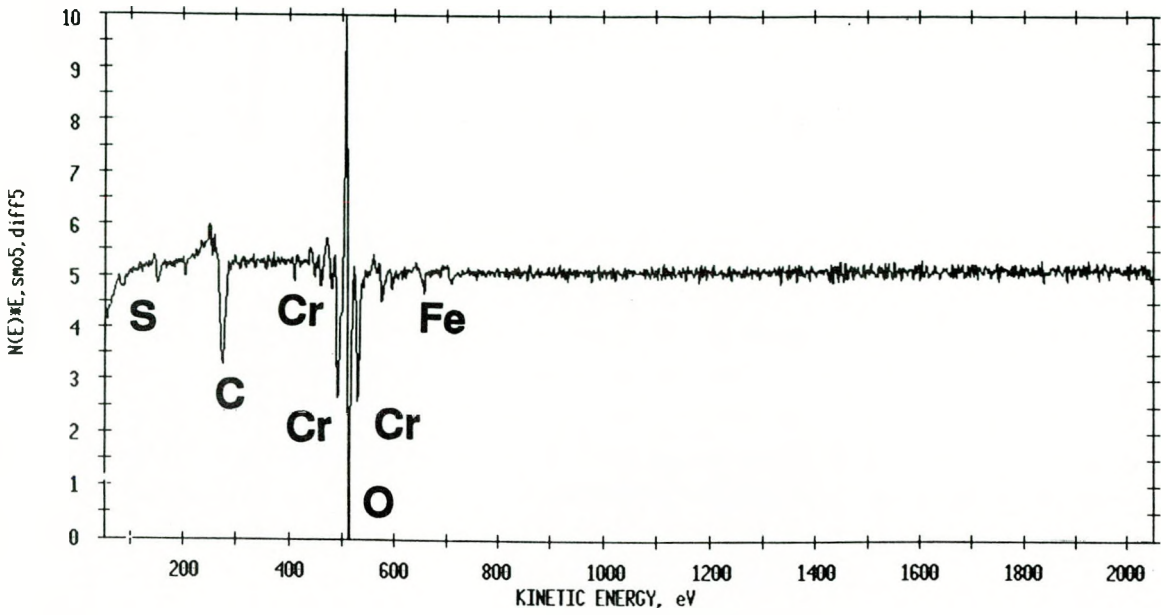

(a) Scale surface

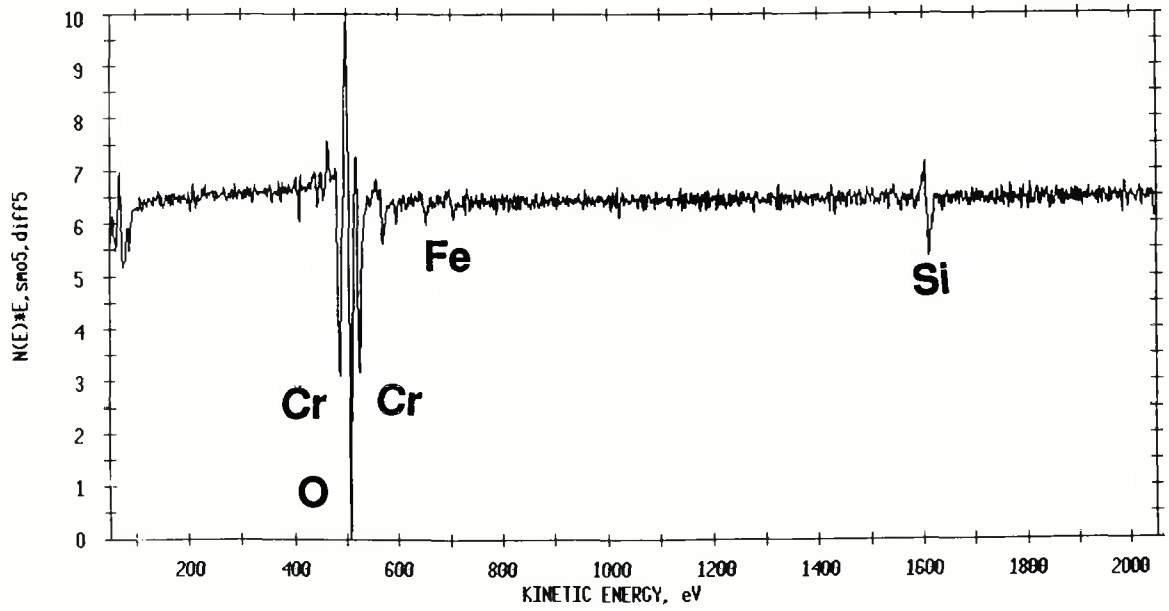

(b) From 200 nm depth

Fig. 51. SAM-Auger spectra of scale on Fe-25Cr-20Ni-3Si exposed to gas mixture B, 700°C, 96h.

The scale formed on Fe-25Cr-20Ni-3Si under thermal cycling (93 cycles) is shown in Figure 52. The scale is Cr rich oxide and similar in composition to that formed under isothermal exposure. No scale spallation and cracking was observed.

4.5.5 Ion Implanted Fe-25Cr-20Ni Alloys

Y, Si and O were the implants chosen to modify the surfaces of this alloy to investigate the method of incorporation of oxygen active or other beneficial elements. The Y implanted samples were exposed to the gas mixture B at 700°C for various times. The scale has porous, faceted and smooth regions, Figures 53a-c similar to those observed on I/M alloys with and without bulk additions of microconstituents. The RBS analysis shows the presence of S. The O- and Si-implanted alloys were exposed to a slightly lower oxygen activity gas mixture, $pO_2=2.24x10^{-21}$ and $pS_2=1.0x10^{-8}$ atm for 1 h. The scale morphology characteristic of short time exposure is shown in Figures 54a-c and 55a-d. The major components of the scales identified by XRD are $FeCr_2S_4$, $FeCr_2O_4(Fe_{1+x}Cr_{2-x}O_4)$ and FeS.

4.5.6 (P/M) Fe-25Cr-20Ni-1.5Al_2O_3

A remarkably uniform scale without any porous/spongy or faceted sulfides is observed on (P/M) Fe-25Cr-20Ni-1.5Al_2O_3 alloy on exposure to gas mixture B at 700°C for 96 h. The base alloy without the alumina dispersoids sulfidizes under the above exposure conditions within 10 min. The planar and cross sectional views of the scale are shown in Figure 56a-b. The scale is essentially Cr_2O_3, and this should be compared with the scale on the base alloy, Figures 47a-d or 49e.

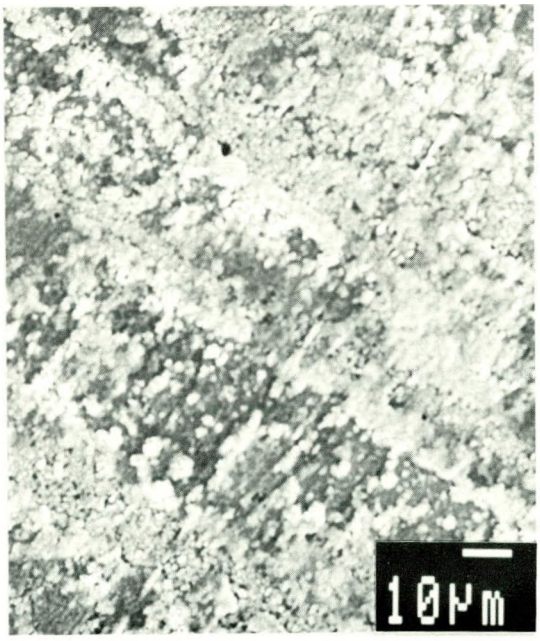

Fig. 52. Scale on Fe-25Cr-20Ni-3Si cyclically exposed to gas mixture B, 700°C, 93h.

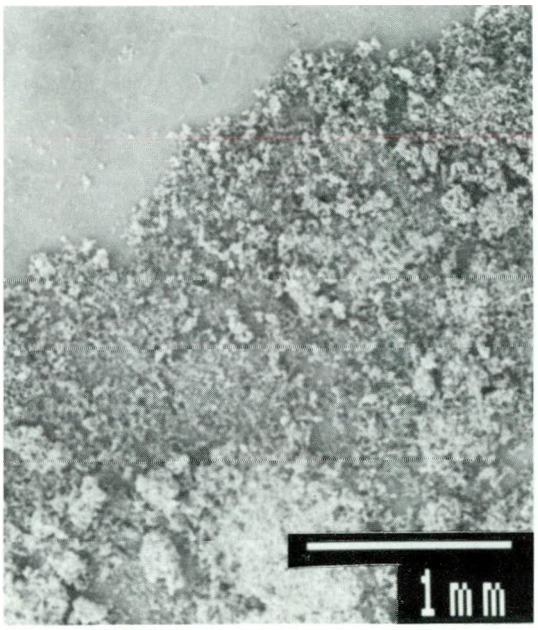

(a) General appearance

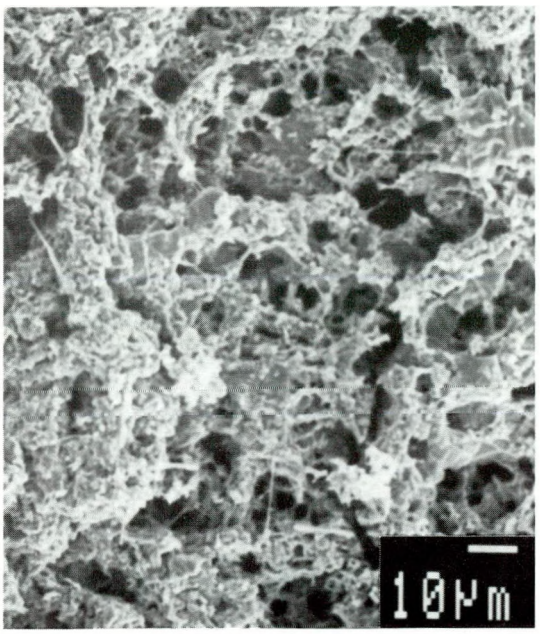

(b) Porous

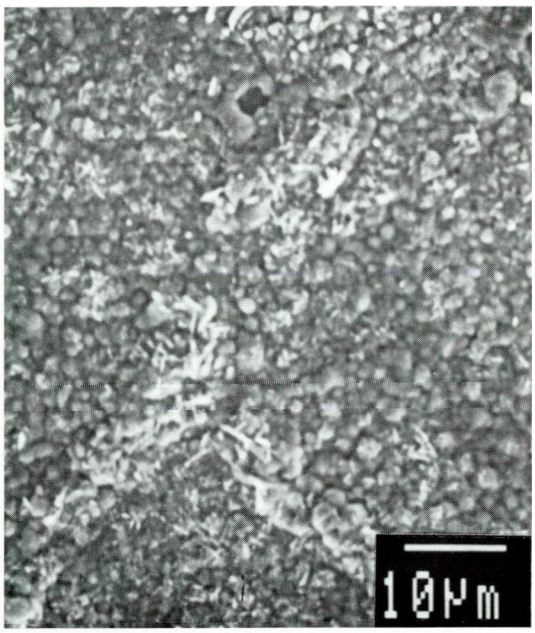

(c) Smooth

Fig. 53. Scale on Y-implanted Fe-25Cr-20Ni exposed to gas mixture B, 700°C, 90.7h.

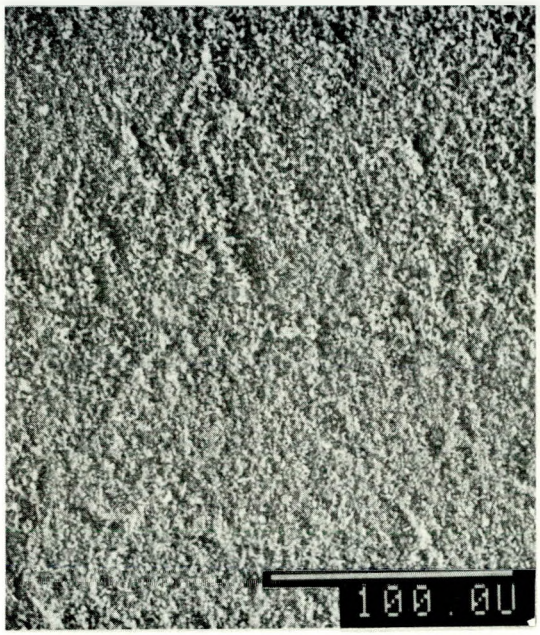

(a) Scale surface

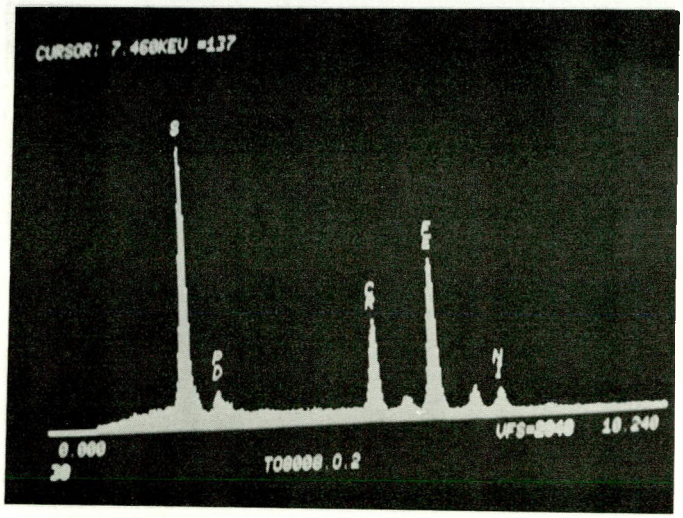

(b) EDAX of scale in (a)

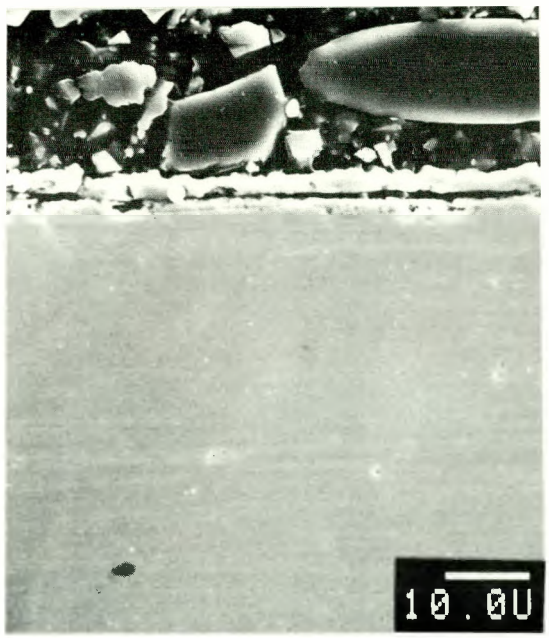

(c) X-section

Fig. 54. Scale on O-implanted Fe-25Cr20Ni; pO_2=2.2x10^{-21}, pS_2=1.0x10^{-8} atm, 700°C, 1h.

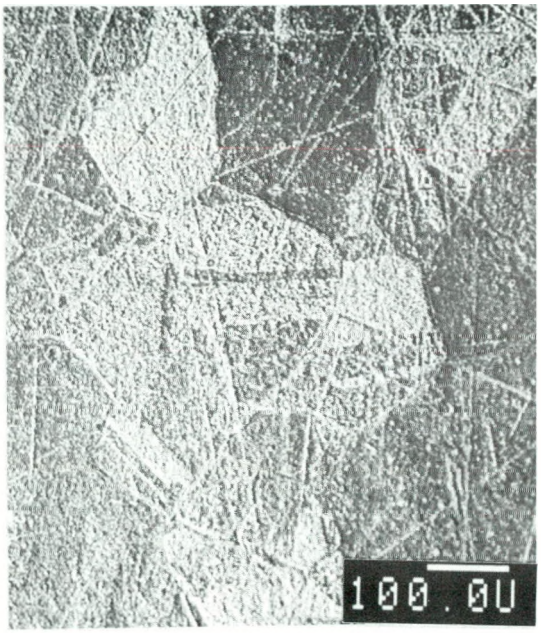

(a) Scale surface

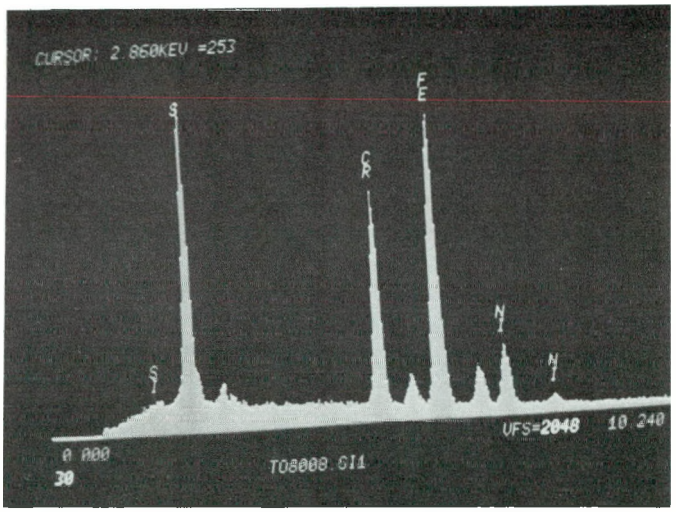

(b) EDAX of the scale in (a)

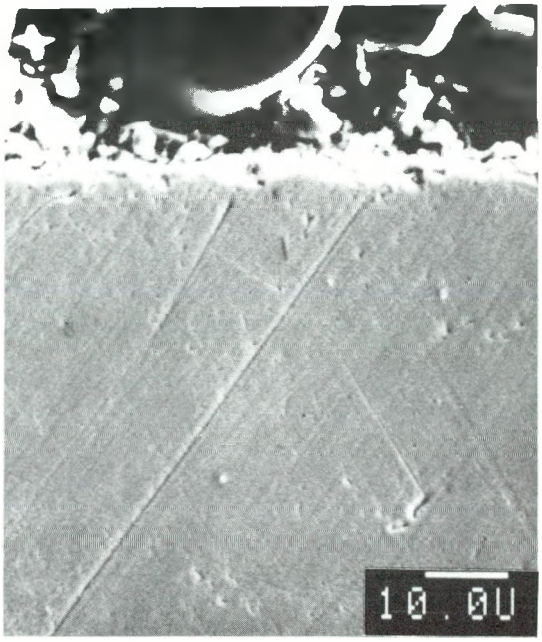

(c) X-section

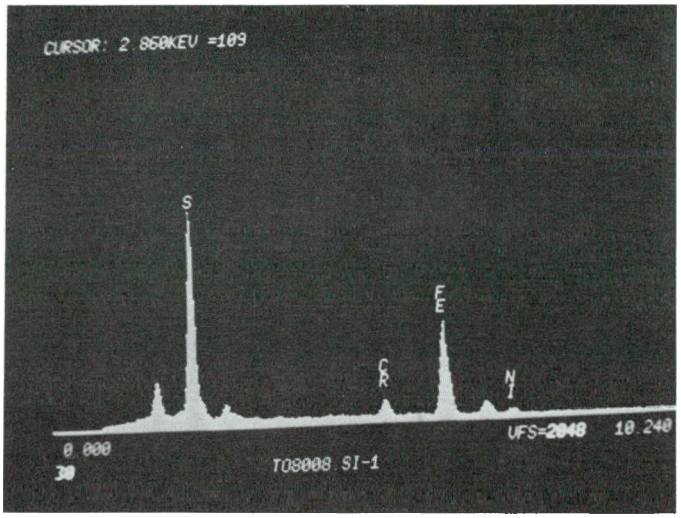

(d) EDAX of scale in (c)

Fig. 55. Scale of Si-implanted Fe-25Cr-20Ni; pO_2=2.2x10^{-21}, pS_2=1.0x10^{-8} atm, 700°C, 1h.

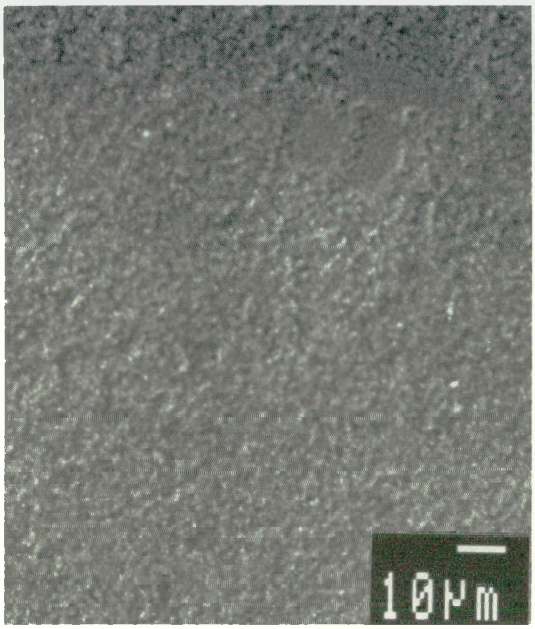

(a) Scale surface

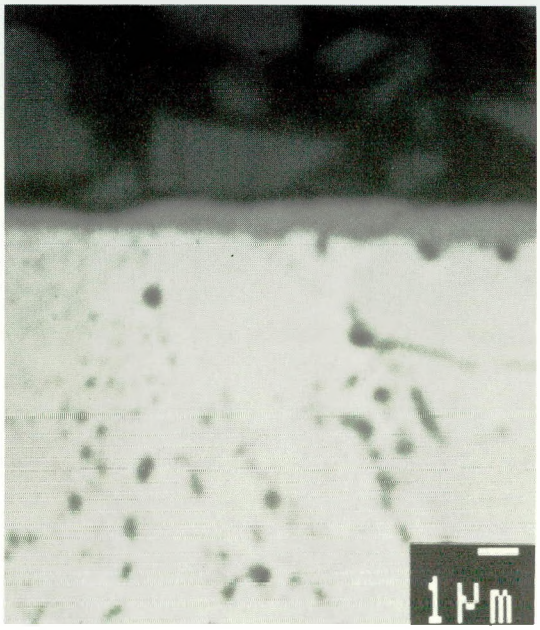

(b) X-section (BEI)

Isothermal, 700°C

(c) Scale surface

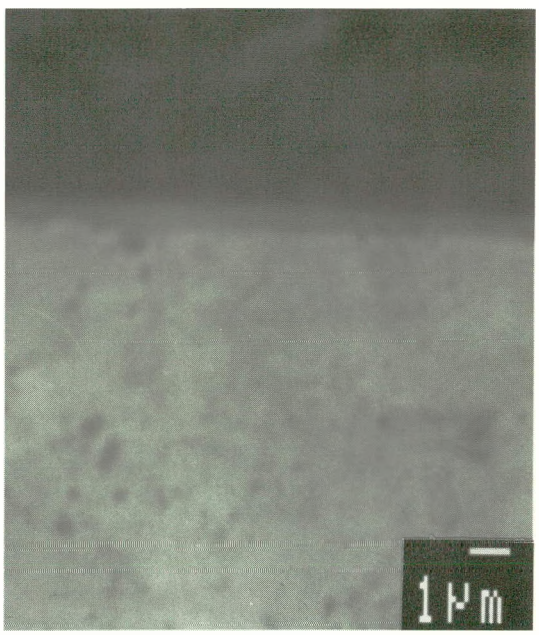

(d) X-section (BEI)

Cyclic 700°↔50°C

Fig. 56. Scale on Fe-25Cr-20Ni-1.5Al_2O_3 formed in gas mixture B, 96h.

Thermal cycles did not cause scale spallation, cracking and local sulfidation, Figure 56c-d. The scale formed under cyclic condition, Figure 56d is thin and Cr_2O_3. Spallation, interfacial voids and sulfidation are absent.

4.5.7 (I/M) Fe-25Cr-6Al and Fe-25Cr-6Al-X Alloys

The base alloy and the alloys with Ce, Hf, La, Si, Pt and Y were investigated, and were exposed to gas mixture B at 700°C.

The scales form epitaxially on the base alloys, and this epitaxial relation is apparently maintained for a long time. The scales observed after 24 and 144 h exposure are shown in Figures 57a-b. The scale is thin and nonuniform in thickness. The EDAX analysis of scales formed in shorter times is not valid because of contributions from the substrate elements. The concentration-depth profiles of scales at two (bright and dark) locations were obtained by sputter AES in the case of base alloy exposed for 24 h, Figure 58a-b. The profile of the dark region has two layer: (a) Fe-Cr-Al oxide which could be a mixture of $(CrAl)_2O_3$ and Fe, and, (b) Al_2O_3 with Cr. Only Al_2O_3 with Cr constitutes the scale in the light region. Sulfur is not detected at all in any significant amount.

The behavior of Fe-25Cr-6Al with Ce, Hf or La is similar, and, therefore, illustrated by the observation on Fe-25Cr-6Al-1Ce. The scale formed on the substrate grain of this alloy is thinner than that of the base alloy formed on the substrate grain boundaries and is shown in Figures 59a-b. The sulfidation attack is localized along the substrate grain boundaries in the form of iron sulfide with very little Cr and no Ce, in Figure 59b. The early formation of sulfides along the substrate grain boundaries is shown in Figure 59a.

Y addition also leads to significant grain boundary segregation of Y containing intermetallics. The composition of the scales on the substrate grain boundaries is rich in Y and Al, and lean in Fe and Cr, Figures 60a-b. Sulfidation occurs locally along the substrate grain boundaries, and the sulfide particles are FeS with significant amount of Al, Cr and Y. Sulfidation seems to start locally along the grain boundaries even within one hour of exposure, Figure 60a. A scanning Auger microprobe study of scale formation and breakdown was made on Fe-25Cr-6Al-1Y exposed to gas mixture B at 700°C for 1 and 24 h. A sputter crater was created providing a taper section of the scale, Figure 61 formed in 1 h. Marked in this figure are the locations of Auger study. Auger spectra of grain boundary particles 1 and 2 (referred to as halo region) at a depth of 20-50 nm and that of 3 at the bottom of sputter crater, 100 nm in depth were obtained. These spots contain Fe, Cr, O and S. Fe and S decrease, and Cr and O increase with increasing depth from the gas/scale interface. Al and O are only detected in the scale on the substrate grain at the bottom of the sputter (location 4, 100 nm depth), while in the scale above the substrate grain in the halo region at a depth of about 20-50 nm, Cr and a trace of Fe are present besides Al and O. The chemistry of the grain boundary was studied using depth profiling Auger spectroscopy. Two depth profiles were acquired at two different locations, Figure 62a-b. In location one the scale is essentially Al rich oxide with small amounts of Cr and Fe below a Cr-rich scale. No sulfur is detected. On the other hand, the depth profile of the scale in the second location clearly suggests significant sulfidation and the presence of FeS over Cr-rich oxide. The Auger spectra of the

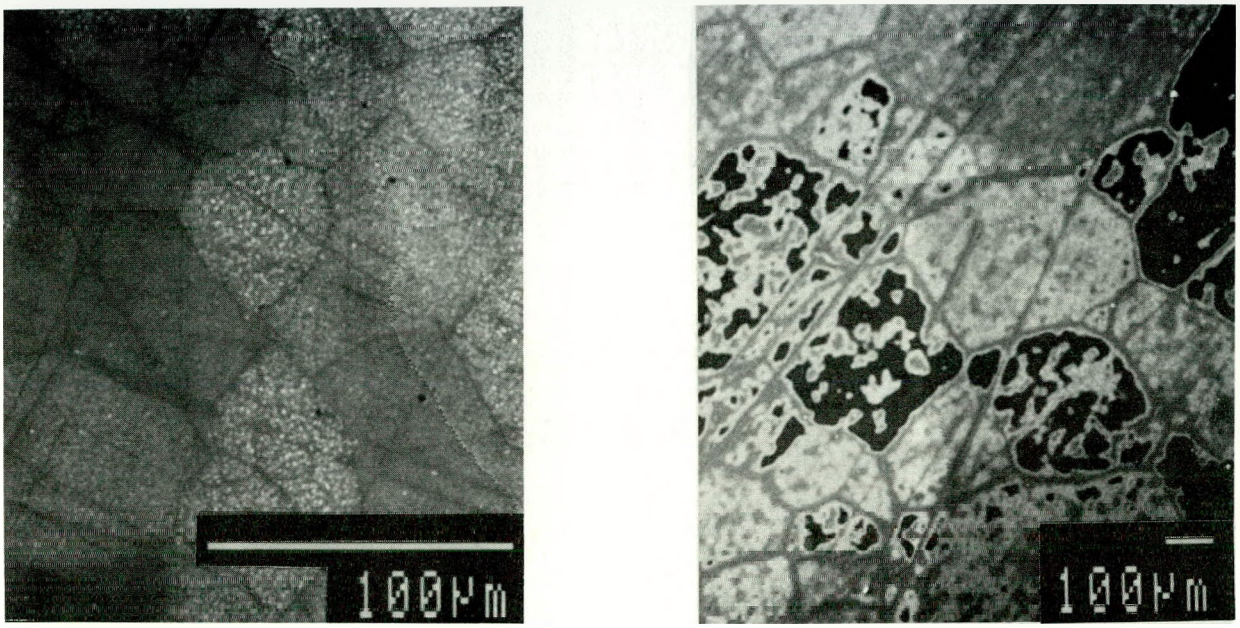

(a) 24h (b) 144h

Fig. 57. Scale on Fe-25Cr-6Al exposed to gas mixture B at 700°C.

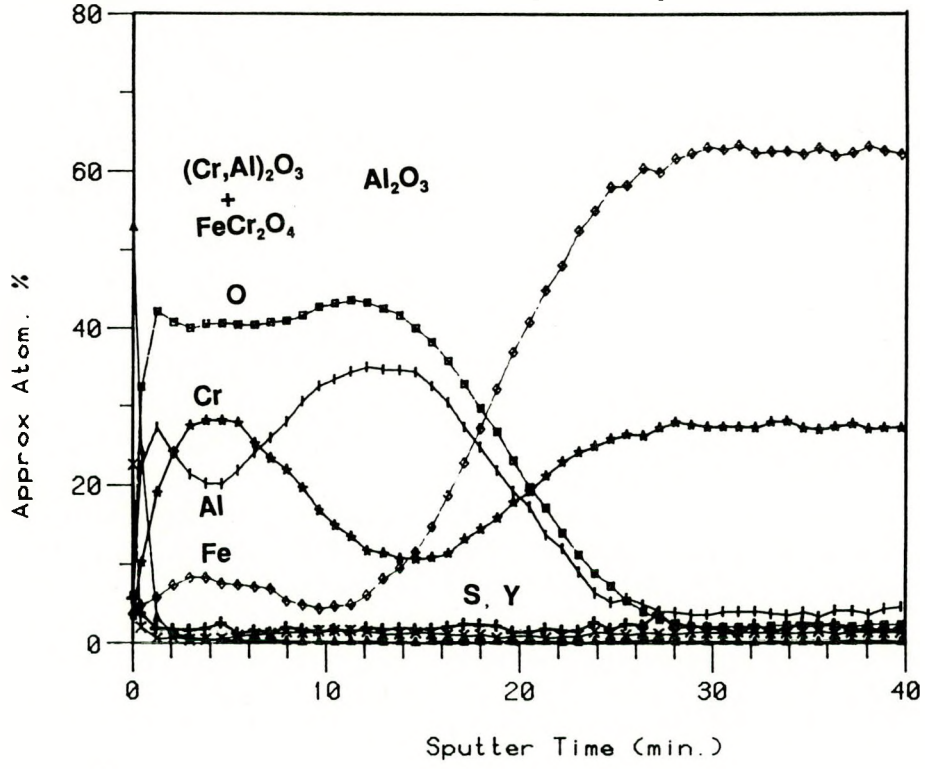

(a)

Fig. 58. AES depth profile of (a) dark and (b) light regions in Fig. 57a.

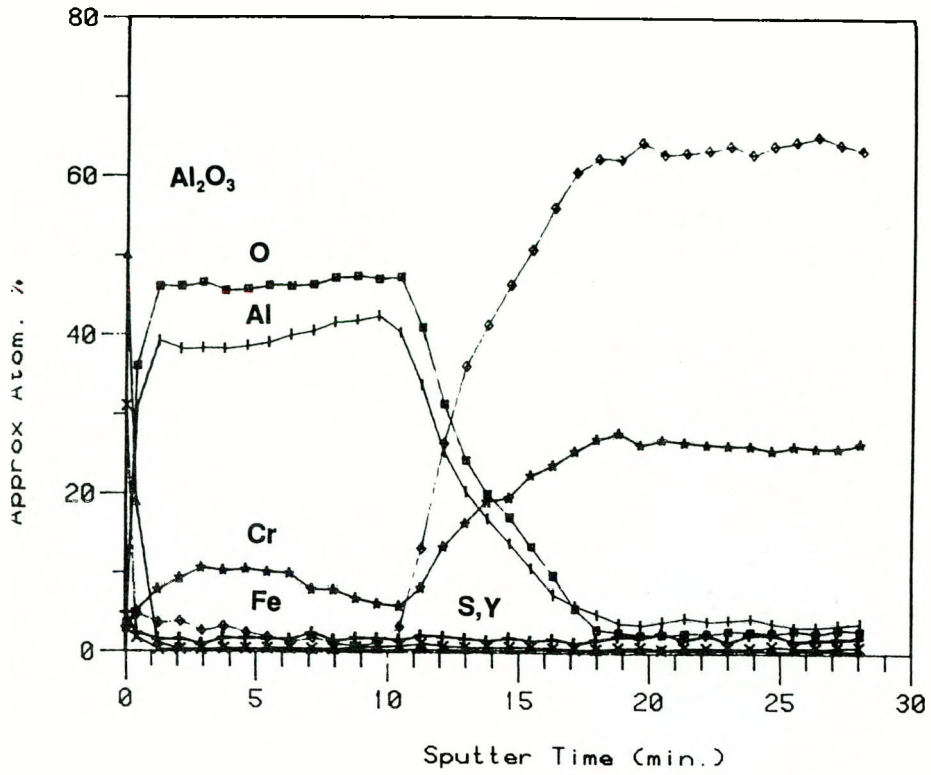

(b)

Fig. 58 (cont'd.). AES depth profile of (a) dark and (b) light regions in Fig. 57a.

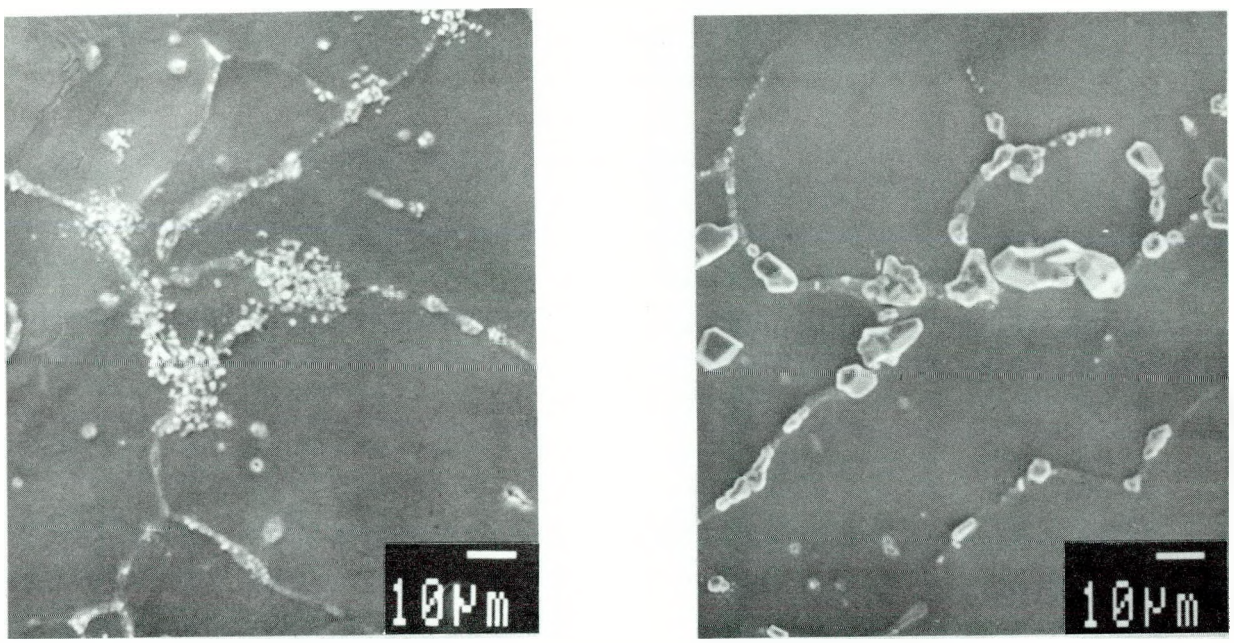

(a) 1h

(b) 144h

Fig. 59. Scale on Fe-25Cr-6Al-1Ce exposed to gas mixture B, 700°C.

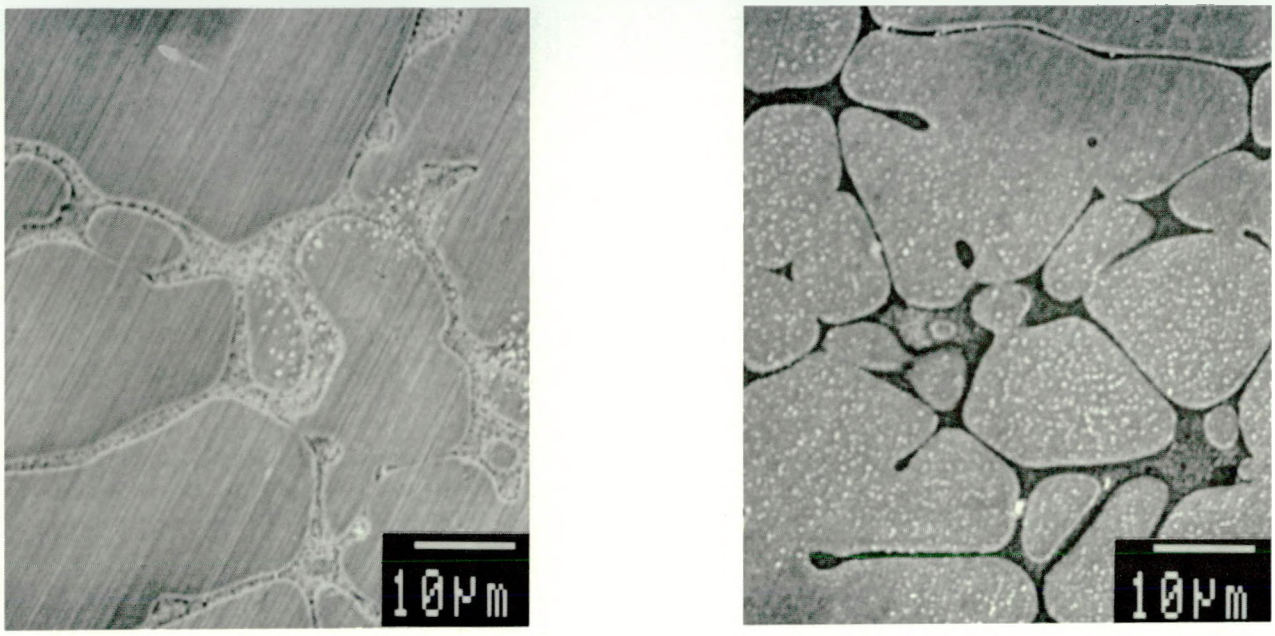

(a) 1h (b) 192h

Fig. 60. Scale on Fe-25Cr-6Al-1Y exposed to gas mixture B, 700°C.

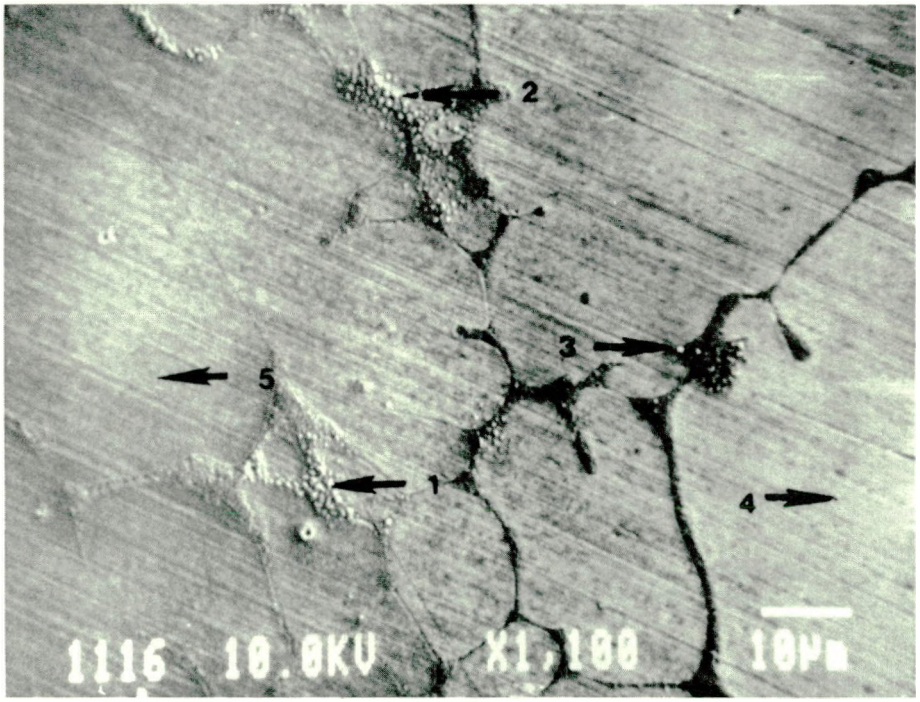

Fig. 61. A sputter crater in the scale on Fe-25Cr-6Al-1Y exposed to gas mixture B, 700°C for 1h. Numerals indicate locations from where Auger spectra obtained.

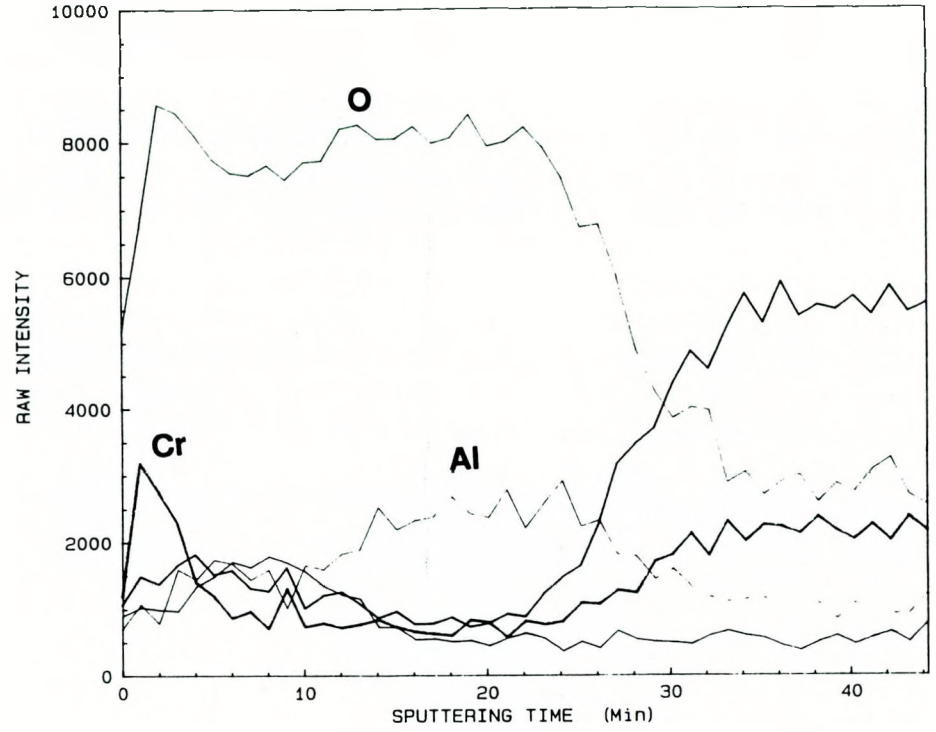

(a)

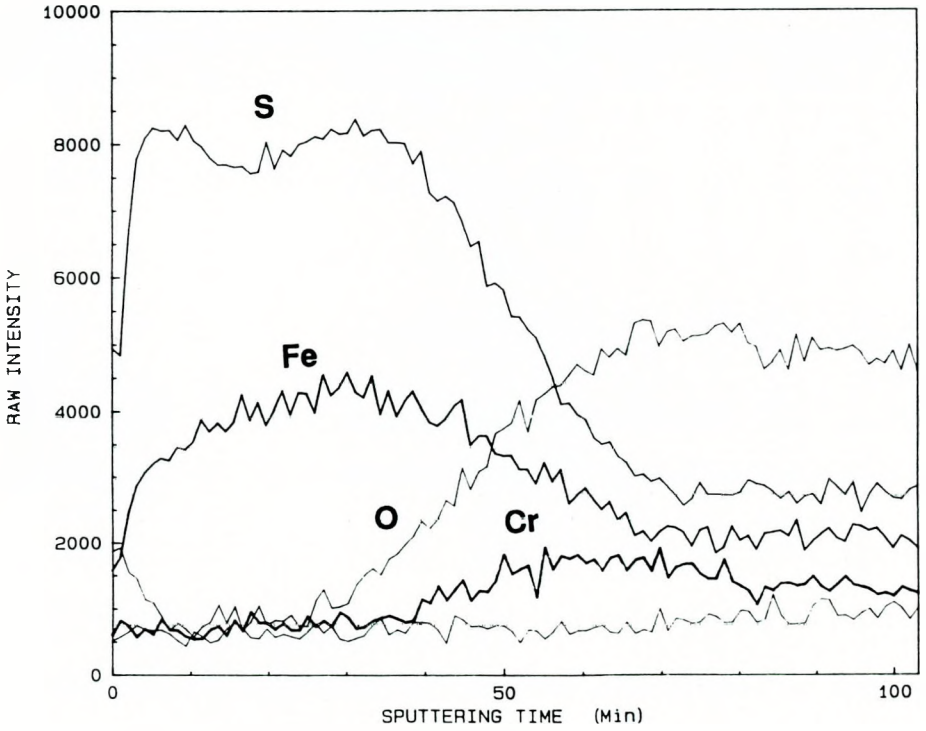

(b)

Fig. 62. AES depth profiles of scale at two locations on the substrate g.b. of Fe-25Cr-6Al-1Y exposed to gas mixture B, 700°C for 1h.

above two locations along the substrate grain boundary after significant sputtering showed the presence of Fe, Cr, Al, Y and O at location one and Fe, Cr, Al, Y, O and S at the second location. No significant change has occurred in scale formation/breakdown process in 24 h. The scale observed on Fe-25Cr-6Al-1Y after 24 h exposure is shown in Figure 63. The scale is thin, and the Y rich regions (the substrate grain boundaries and dark circular inclusions) are still distinctly seen through the scale. The white nodules are FeS with Cr, Al, Y and O as indicated by the Auger spectra of these nodules. The uniform scales on the substrate grains and grain boundaries differ in their thickness (about 90 and 500 nm, respectively) and compositions. Auger depth profiles of the scales on the above two regions are shown in Figures 64a-b. The scales in general have layers. The major components of the scale on the substrate grain seem to consist of $(CrAl)_2O_3$ over Al_2O_3. Y is not detected. The presence of Y as intermetallics along the preexposed substrate grain boundaries appears to influence the constituents of the scale that is formed along these boundaries. The Fe-Cr oxide, likely to be $Fe_{1+x}Cr_{2-x}O_4$ form over Y containing Al_2O_3, which may be Al_2O_3 with $Y_3Al_5O_{12}$. Y seems to have segregated to the interface of the spinel and the inner oxide layer of Al_2O_3.

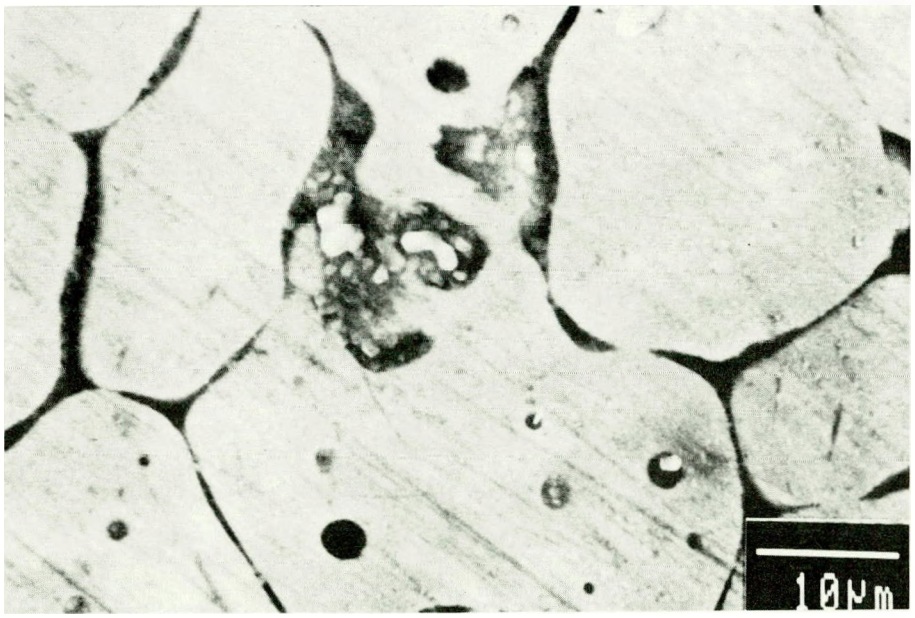

Fig. 63. Scale surface on Fe-25Cr-6Al-1Y exposed to gas mixture B, 700°C for 24h. White inclusions at the upper left and large nodule at the center analyzed with AES.

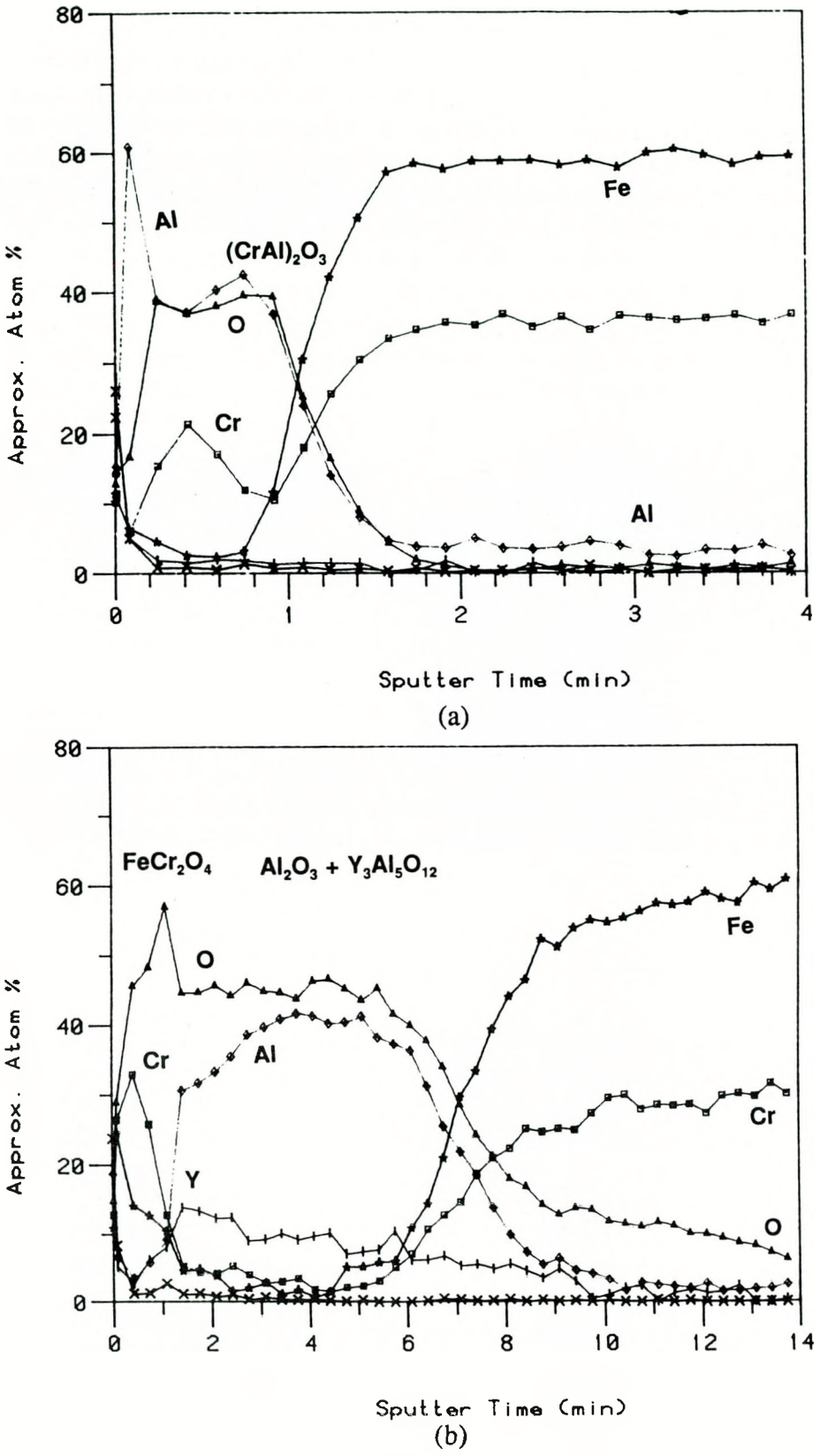

Fig. 64. AES depth profiles scales on a substrate (a) grain, and (b) g.b. of Fe-25Cr-6Al-1Y exposed to gas mixture B, 700°C for 24h.

The behavior of Fe-25Cr-6Al alloys with 1% Pt or 3% Si differs significantly from that of alloys with oxygen active elements and shows similarity to that of base alloy, Figures 65a-b. The scale is thin and the polishing scratches are still visible. The substrate grain boundaries do not appear distinct through the scale in contrast to the observations in alloys with oxygen active elements. The EDAX analyses of the scales gave compositions almost same as that of the substrate alloys, reflecting the thinness of the scale. The white specks in Figure 65a are too fine to be analyzed meaningfully using EDAX. The specks and dashes seen in Figure 65b are not so fine for the EDAX analysis. These specks are rich in Cr and Fe, and are likely to be $Fe_{1+x}Cr_{2-x}O_4$ with a small amount of Si. The dashes have more Si and Cr and less Fe relatively. They are possibly Cr_2O_3 with Si and Fe. None of the alloys showed any local grain boundary sulfidation.

Thermal cycles did not cause scale rupture, spallation or cracking, Figure 66. The scale is thin, and has composition similar to that of scale formed under isothermal condition.

4.6 THE EFFECT OF SURFACE PRETREATMENT ON CORROSION BEHAVIOR

Hot rolled (HR) and cold rolled (CR) base alloys, Fe-25Cr, Fe-25Cr-6Al and alloys with microconstituents, Fe-25Cr-0.3Hf, Fe-25Cr-0.3Y, Fe-25Cr-6Al-0.3Hf and Fe-25Cr-6Al-0.3Y were exposed to gas mixture B at 700°C for 96 h. The planar and cross sectional views of the scales observed are shown in Figures 67a-v. In Fe-25Cr-6Al alloys with and without the addition of 0.3 Hf or Y cold rolling does not have any influence, and the scales are always thin with Cr rich oxide over alumina. Cold rolling has not changed the scale composition or the propensity of Fe-25Cr and its modification with Hf or Y to local sulfidation. The uniform scale is always Cr_2O_3 with a small amount of Fe and alloying element. Oxide pegs or protrusions are seen in cross section of scales (Figure 67ℓ) on cold worked Fe-25Cr-0.3Y alloy.

4.7 THE EFFECT OF OXIDIZING CONDITIONS

Alloys that showed good resistance to sulfidation at 700°C in the gas mixture B were exposed to lower pO_2 values at the same pS_2, gas mixtures C and D (Table 5). The alloys were Fe-25Cr-3Si, Fe-25Cr-1.5Al_2O_3, Fe-25Cr-20Ni-3Si, Fe-25Cr-20Ni-1.5Al_2O_3 and Fe-25Cr-6Al. The morphology and composition of scales formed on these alloys are shown in Figures 68a-o. Except for Fe-25Cr-20Ni-1.5Al_2O_3 the alloys were relatively resistant to sulfidation even at the lowest $pO_2=1.18\times10^{-22}$ atm, and no localized sulfidation is observed. Cr rich oxide scale forms on all Fe-25Cr-X and Fe-25Cr-2Ni-Si alloys except Fe-25Cr-20Ni-1.5Al_2O_3 which is completely sulfidized at $pO_2=1.18\times10^{-22}$ atm. The alumina rich scale forms on Fe-25Cr-6Al under the conditions investigated, but thicker than that formed in gas mixture B at the same temperature.

4.8 THE EFFECT OF TEST TEMPERATURE

Only three base alloys and Hf or Y containing alloys were exposed to 500° and 600°C for times up to 96 h. The partial pressures of oxygen and sulfur at 600° and 500°C are given in Table 5, and the gas mixtures at these temperatures are designated as E and F.

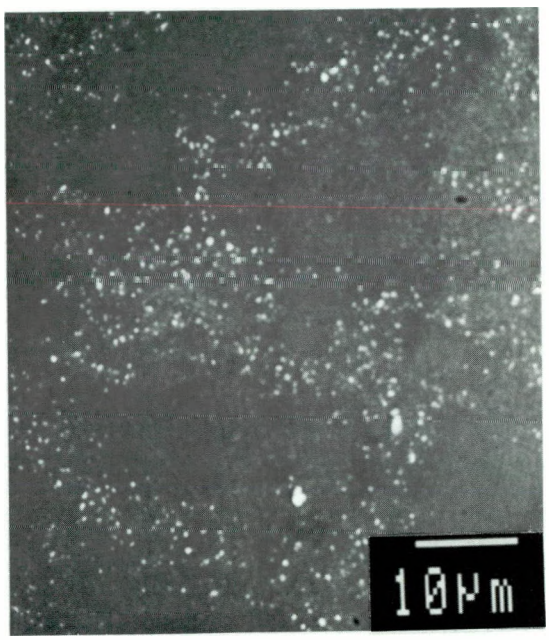

(a) Fe-25Cr-6Al-1Pt

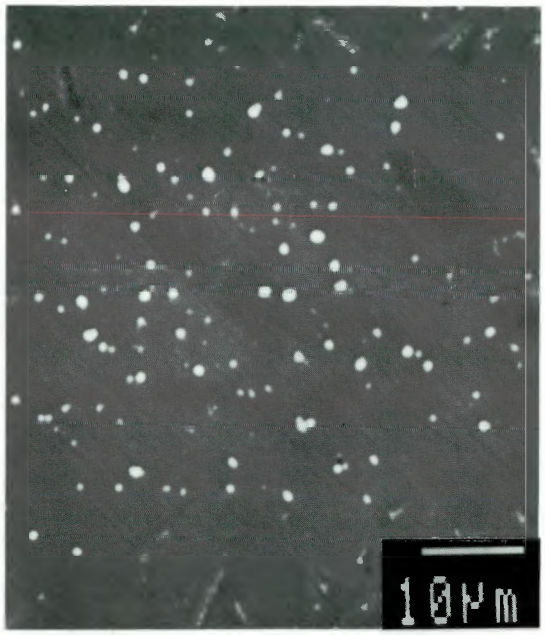

(b) Fe-25Cr-6Al-3Si

Fig. 65. Scale formed in gas mixture B, 700°C, 192h.

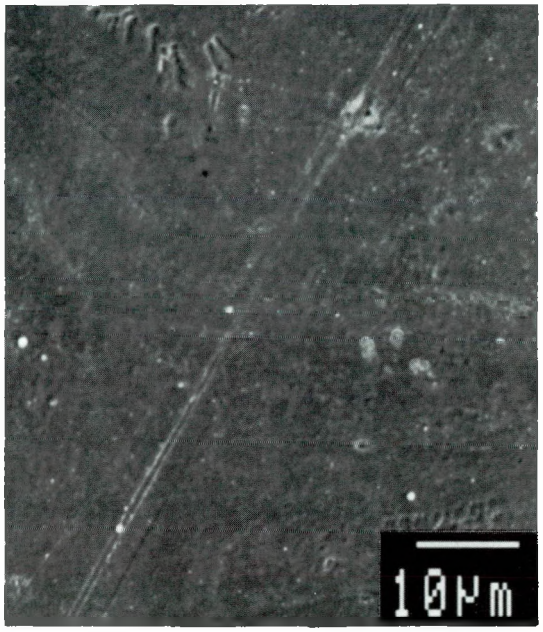

Fig. 66. Scale on Fe-25Cr-6Al cyclically (700°↔50C) exposed to gas mixture B for 96h.

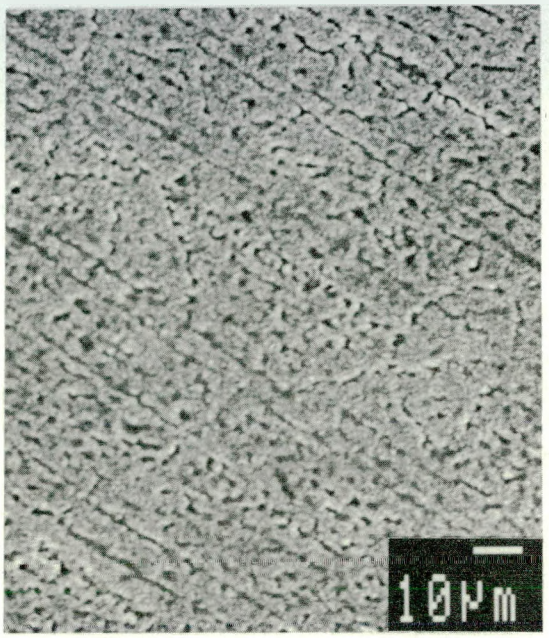

(a) Fe-25Cr, HR

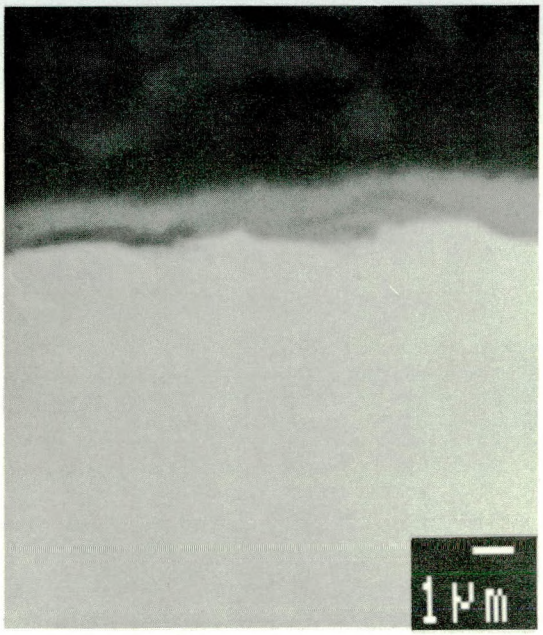

(b) X-section, Fe-25Cr, HR (BEI)

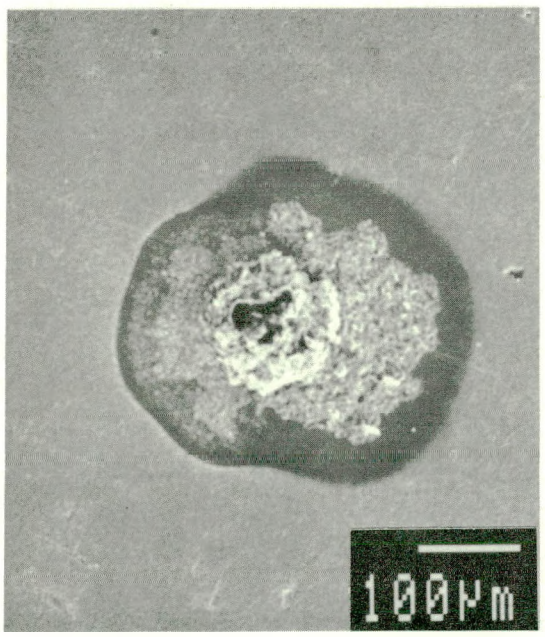

(c) Fe-25Cr, CR

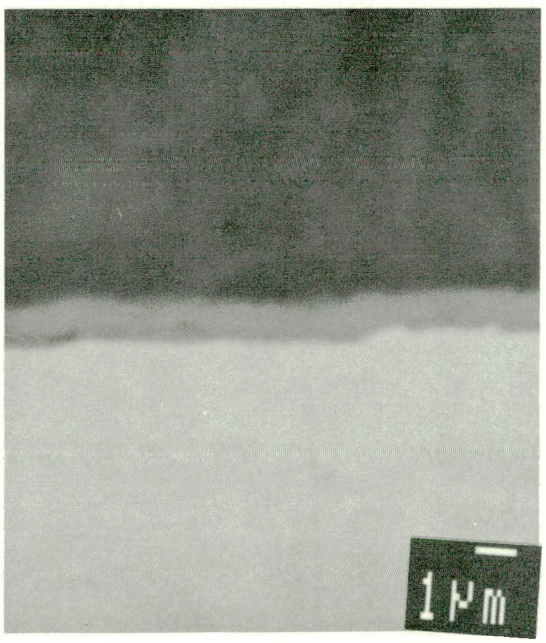

(d) X-section, Fe-25Cr, CR (BEI)

Fig. 67. Scale formed on hot rolled (HR) and cold rolled (CR) alloys in gas mixture B at 700°C, 96h.

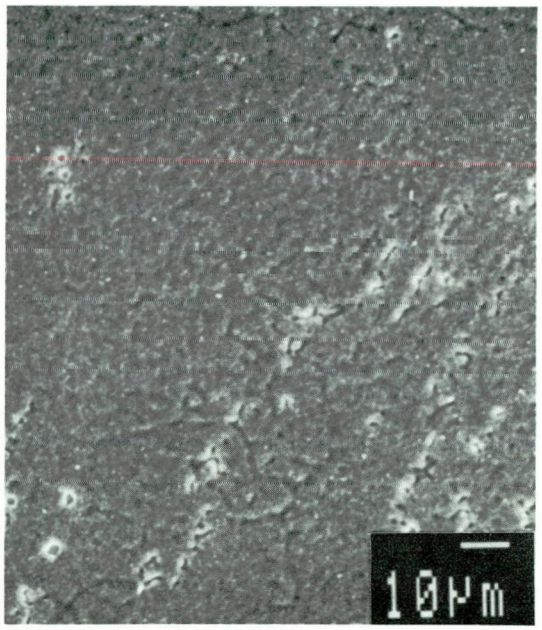

(e) Fe-25Cr-0.3Hf, HR

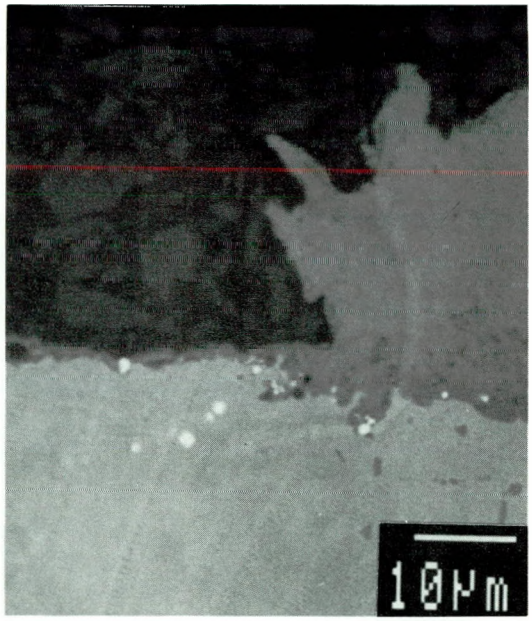

(f) X-section, Fe-25Cr-0.3Hf, CR (BEI)

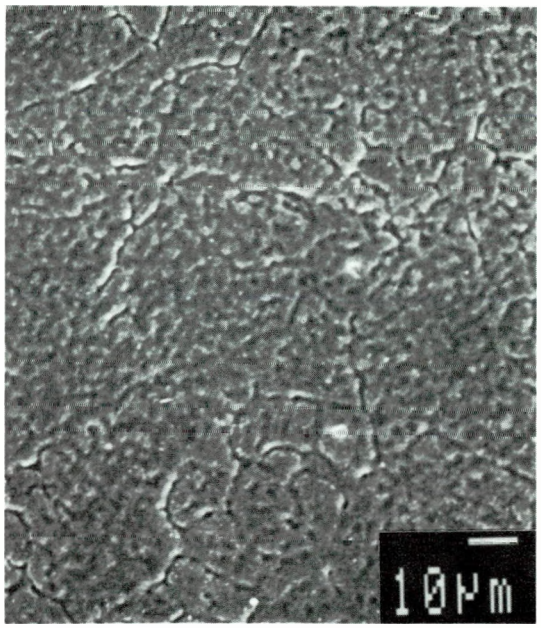

(g) Fe-25Cr-0.3Hf, CR

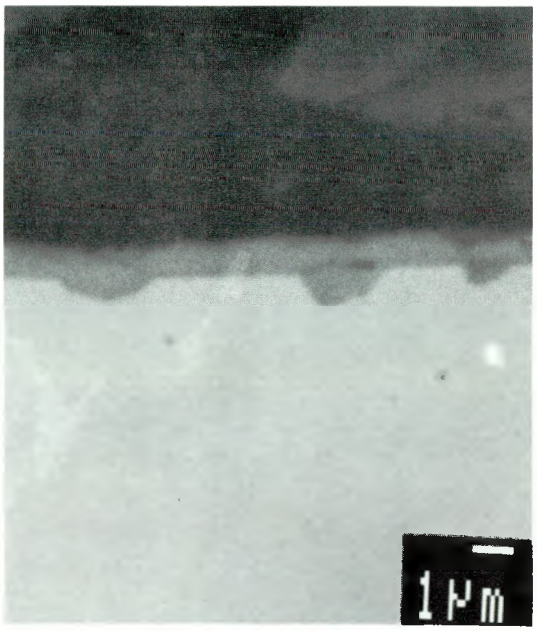

(h) X-section, Fe-25Cr-0.3Hf, CR (BEI)

Fig. 67 (cont'd.). Scale formed on hot rolled (HR) and cold rolled (CR) alloys in gas mixture B at 700°C, 96h.

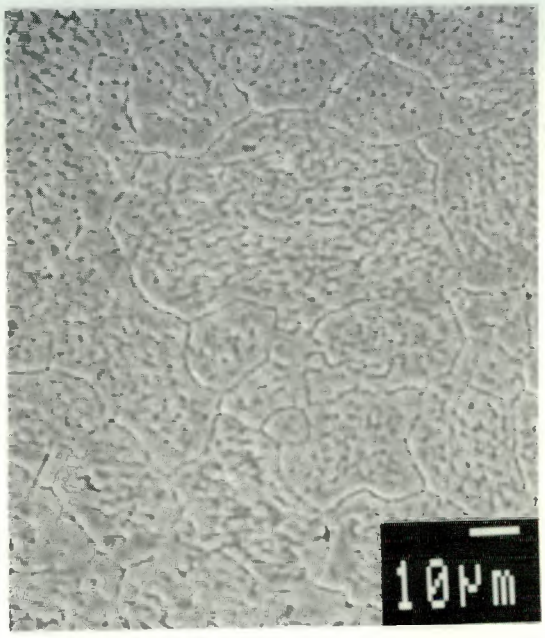

(i) Fe-25Cr-0.3Y, HR

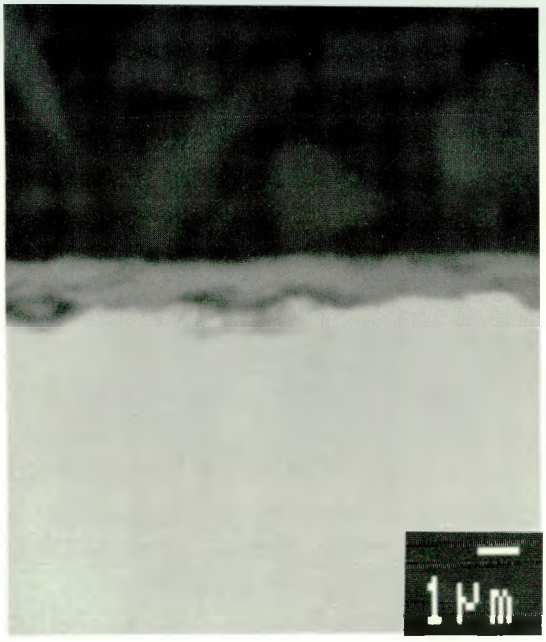

(j) X-section, Fe-25Cr-0.3Y, HR (BEI)

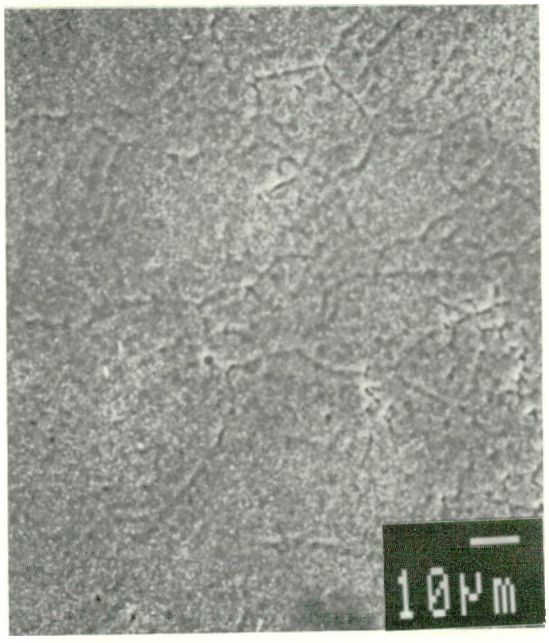

(k) Fe-25Cr-0.3Y, CR

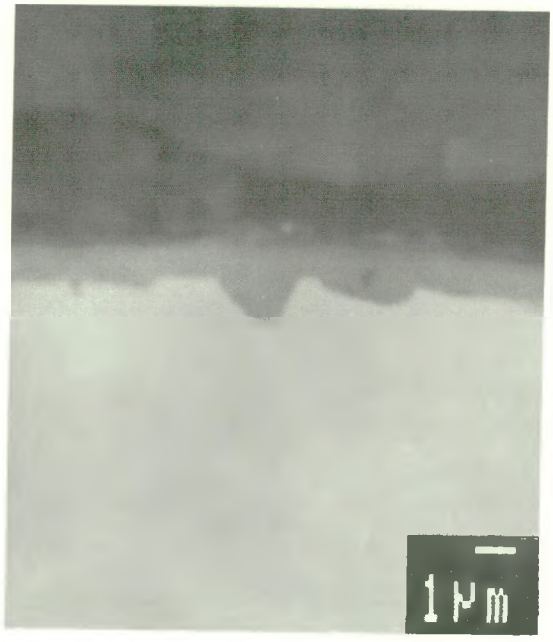

(ℓ) X-section, Fe-25Cr-0.3Y, CR (BEI)

Fig. 67 (cont'd.). Scale formed on hot rolled (HR) and cold rolled (CR) alloys in gas mixture B at 700°C, 96h.

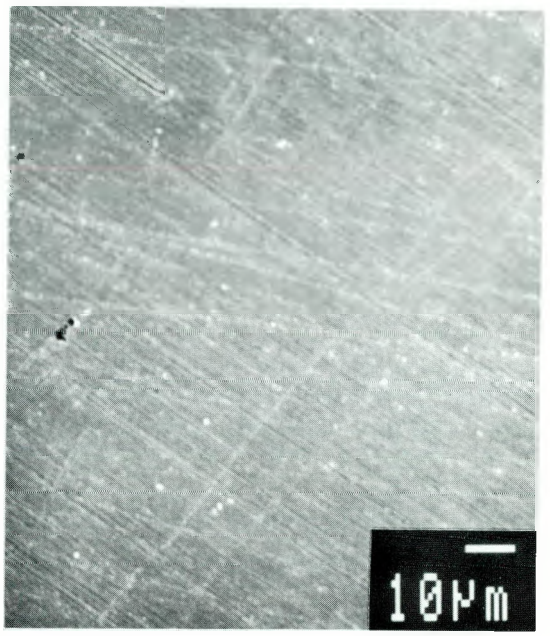

(m) Fe-25Cr-6Al, HR

(n) X-section, Fe-25Cr-6Al, HR (BEI)

(o) Fe-25Cr-6Al, CR

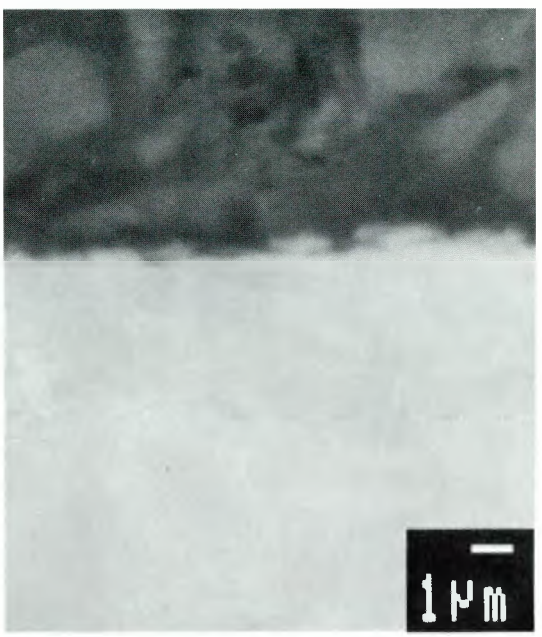

(p) X-section, Fe-25Cr-6Al, CR (BEI)

Fig. 67 (cont'd.). Scale formed on hot rolled (HR) and cold rolled (CR) alloys in gas mixture B at 700°C, 96h.

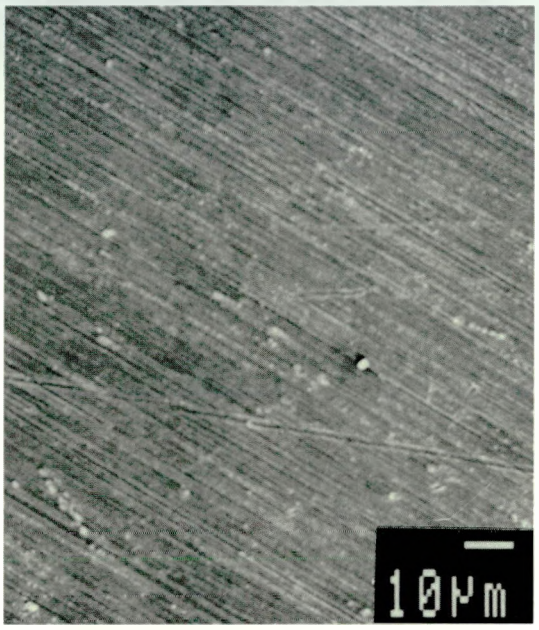

(q) Fe-25Cr-6Al-0.3Hf, HR

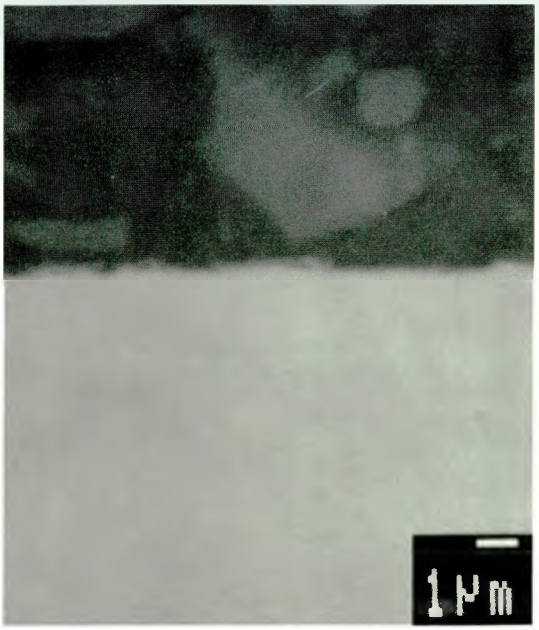

(r) X-section, Fe-25Cr-6Al-0.3Hf, HR (BEI)

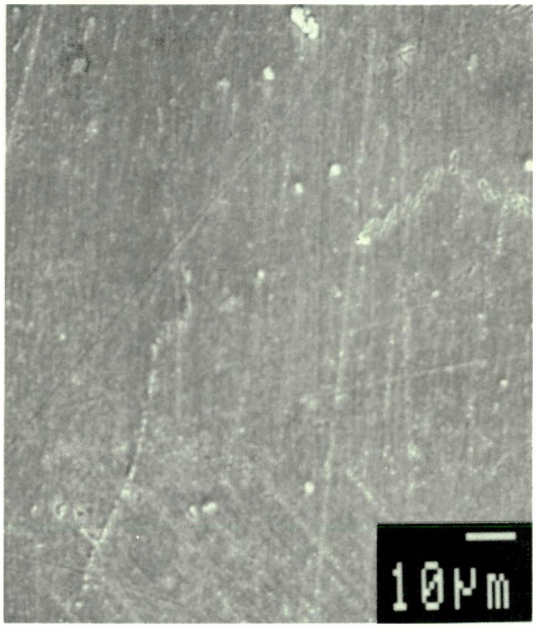

(s) Fe-25Cr-6Al-0.3Hf, CR

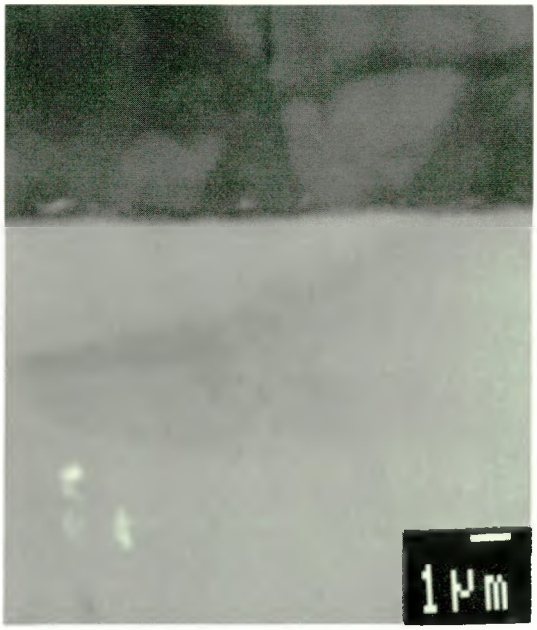

(t) X-section, Fe-25Cr-6Al-0.3Hf, CR (BEI)

Fig. 67 (cont'd.). Scale formed on hot rolled (HR) and cold rolled (CR) alloys in gas mixture B at 700°C, 96h.

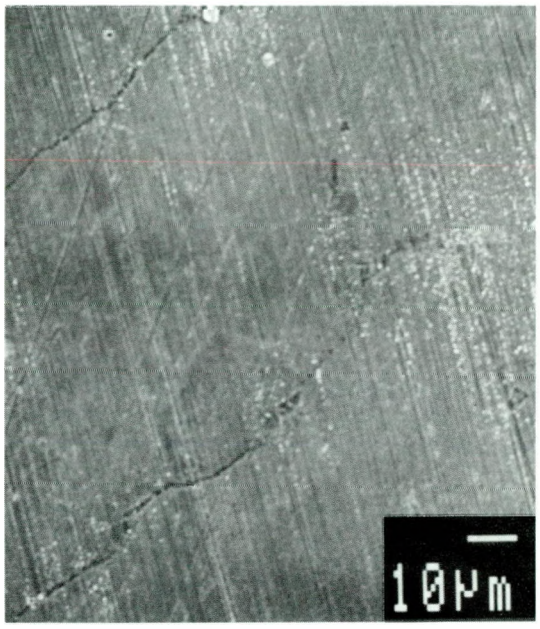

(u) Fe-25Cr-6Al-0.3Y, HR

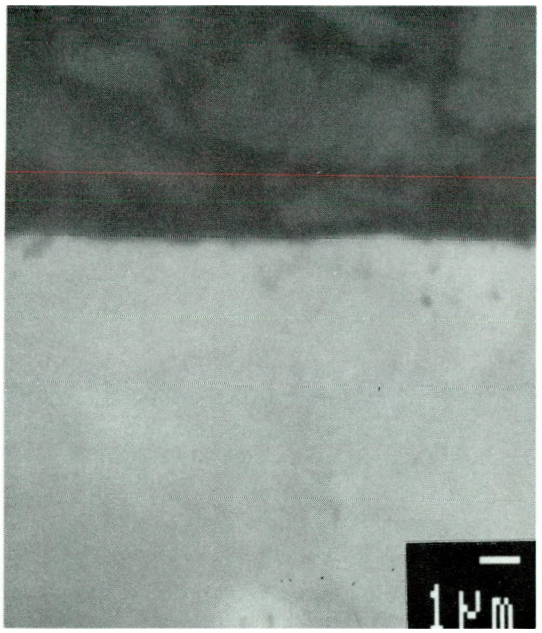

(v) X-section, Fe-25Cr-6Al-0.3Y, HR (BEI)

Fig. 67 (cont'd.). Scale formed on hot-rolled (HR) and cold-rolled (CR) alloys in gas mixture B at 700°C, 96h.

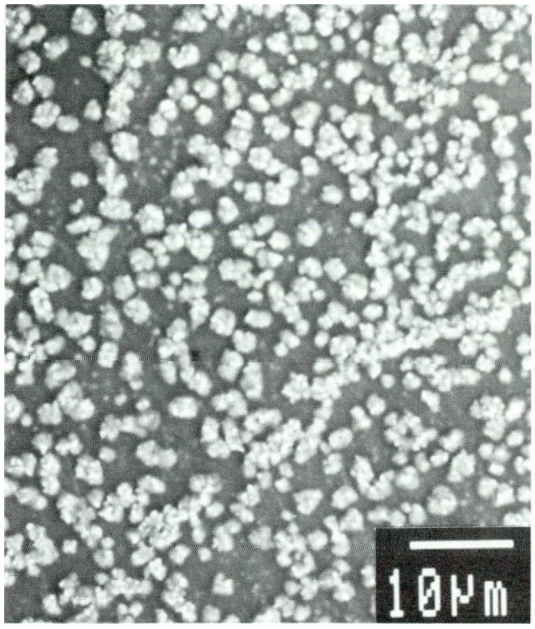

(a) Fe-25Cr-3Si

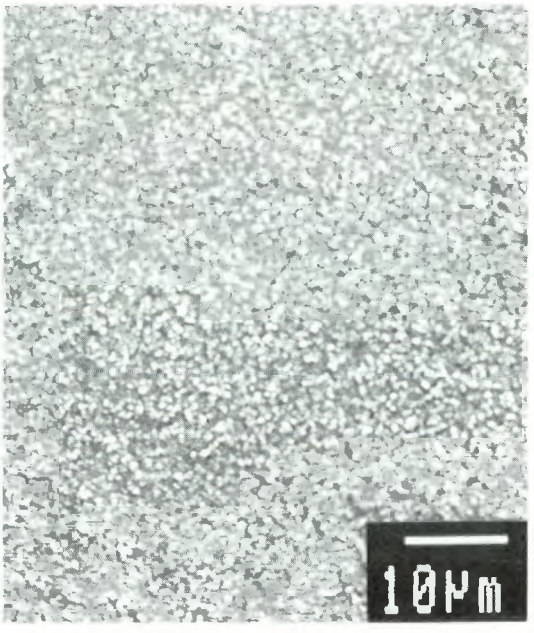

(b) Fe-25Cr-1.5Al_2O_3

Fig. 68. Scales formed at 700°C, 96h in gas mixture C.

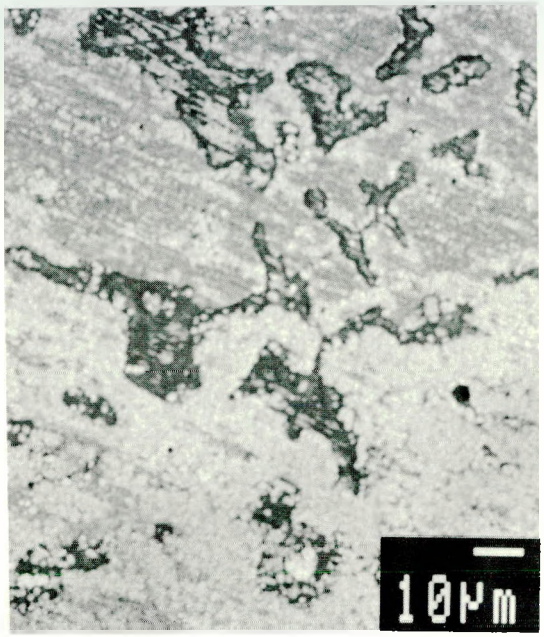

(c) Fe-25Cr-20Ni-3Si

(d) Fe-25Cr-20Ni-1.5Al_2O_3

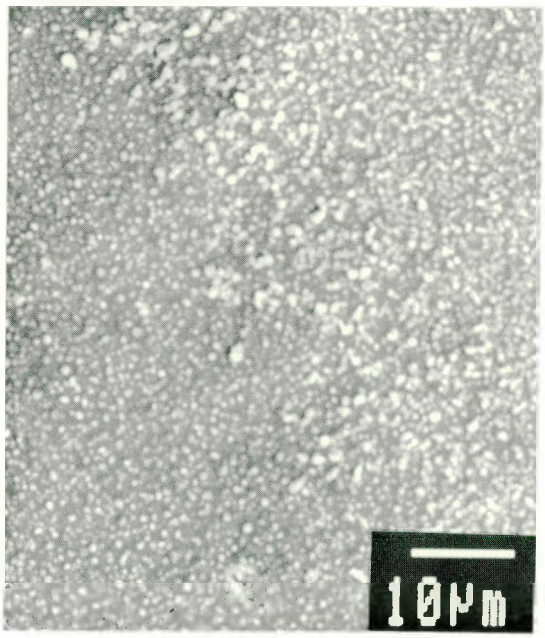

(e) Fe-25Cr-6Al, C

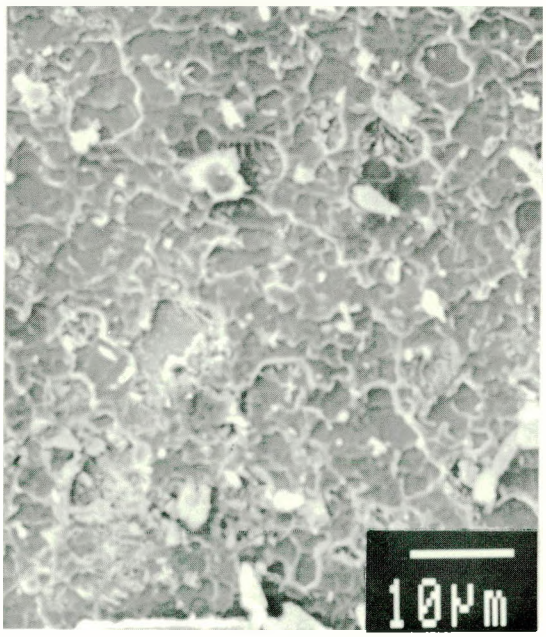

(f) Fe-25Cr-3Si, D

Fig. 68 (cont'd.). Scales formed at 700°C, 96h in gas mixture C.

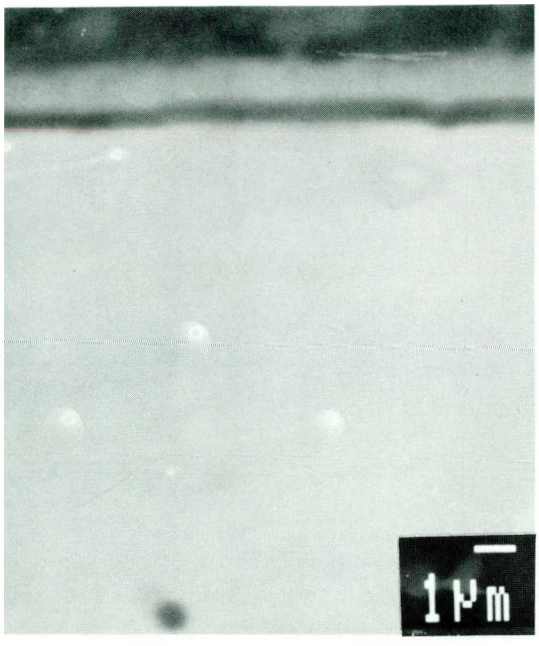

(g) X-section, Fe-25Cr-3Si, D (BEI)

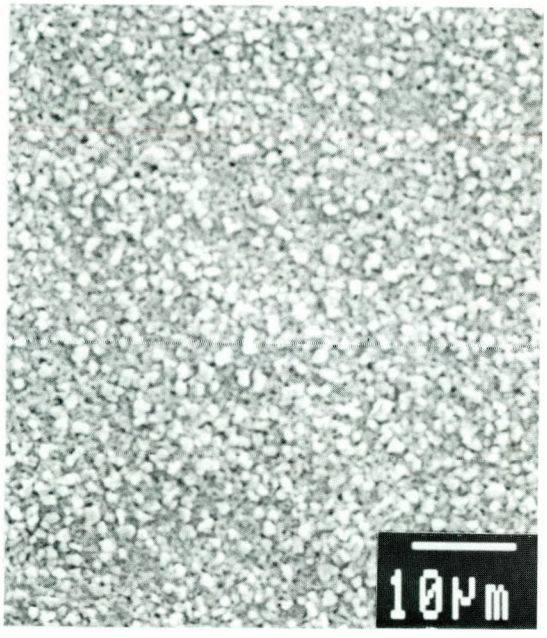

(h) Fe-25Cr-1.5Al_2O_3, D

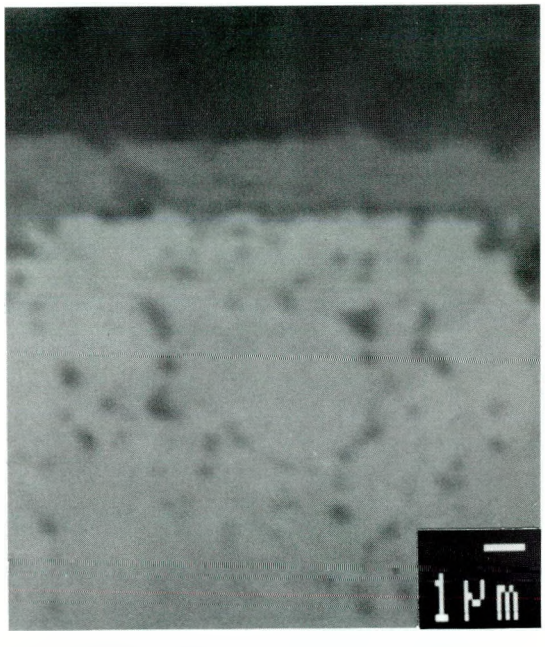

(i) X-section, Fe-25Cr-1.5Al_2O_3 (BEI)

(j) Fe-25Cr-20Ni-3Si

Fig. 68 (cont'd.). Scales formed at 700°C, 96h in gas mixture C or D.

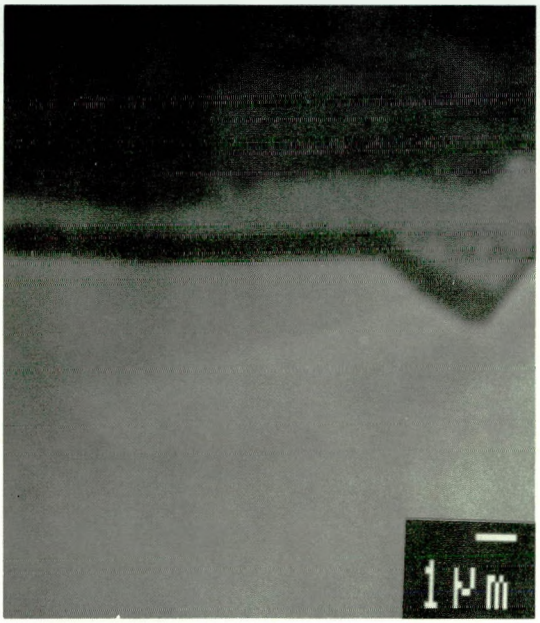

(k) X-section,
Fe-25Cr-20Ni-3Si (BEI)

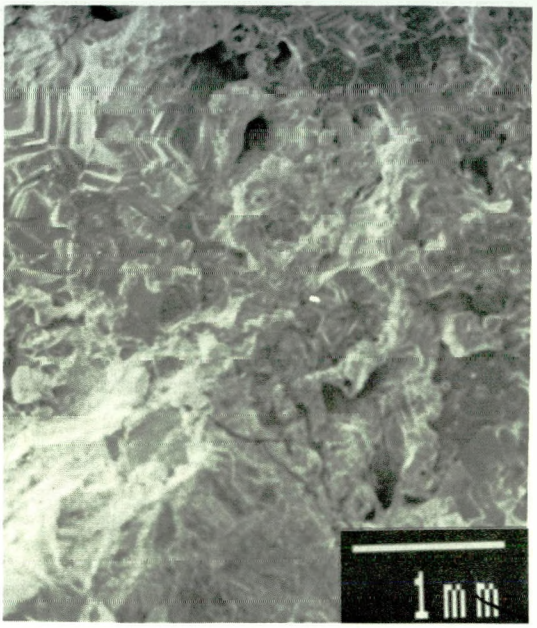

(ℓ) Fe-25Cr-20Ni-1.5Al_2O_3

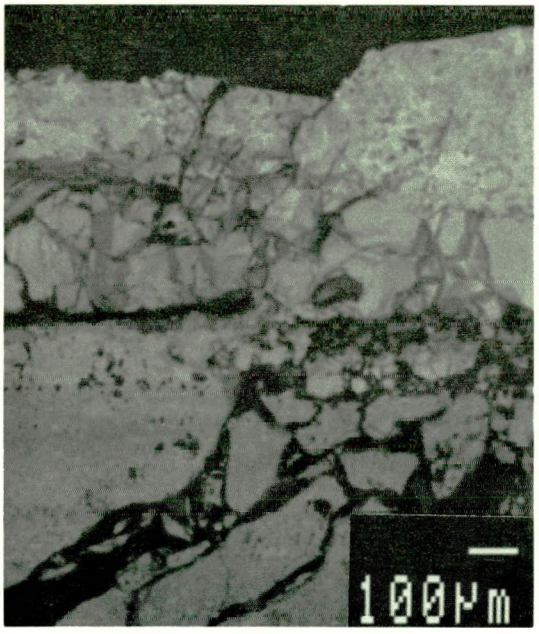

(m) X-section,
Fe-25Cr-20Ni-1.5Al_2O_3 (BEI)

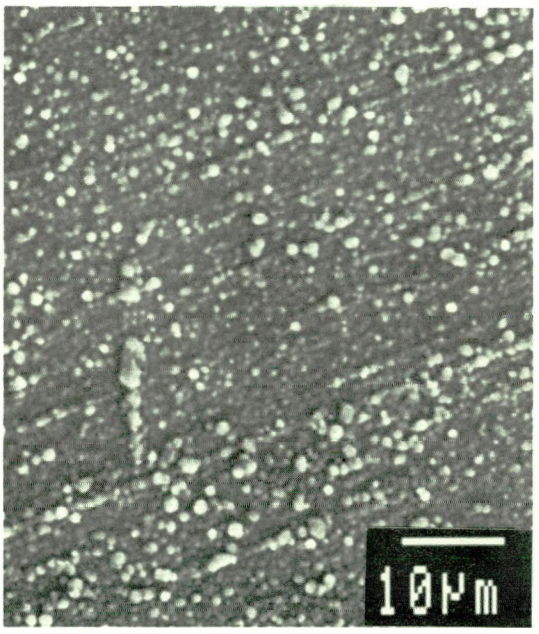

(n) Fe-25Cr-6Al

Fig. 68 (cont'd.). Scales formed at 700°C, 96h in gas mixture D.

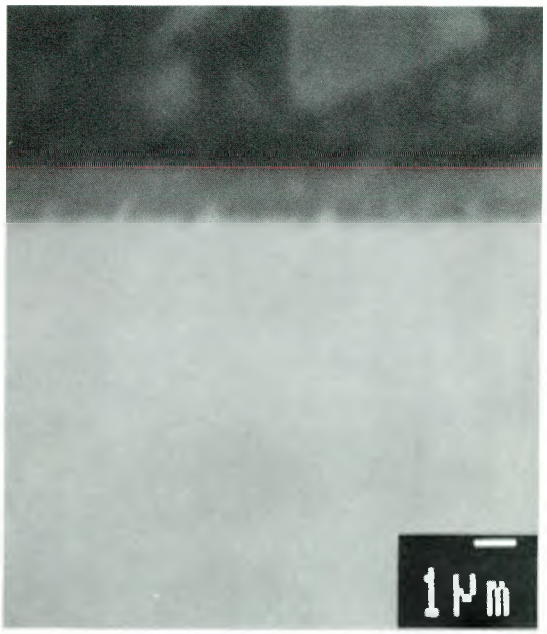

(o) X-section, Fe-25Cr-6Al (BEI)

Fig. 68 (cont'd.). Scales formed at 700°C, 96h in gas mixture D.

Fe-25Cr is sulfidized locally even within an hour of exposure at 500° and 600°C. The scales observed on samples exposed to 500° and 600°C for 96 h are shown in Figures 69a-b. S is detected only at nodules, Figure 69a, but in Figure 69b, S is detected on all grains. Sulfidation is global at 500°C while it is local at 600°C. Sulfidized regions are rich in Fe with some Cr. Addition of Hf or Y has not changed the alloy resistance to sulfidation, nor the mode of attack. Figures 70a-d show the sulfidation attack observed in Hf and Y containing Fe-25Cr alloys exposed for 96 h. At 500°C sulfidation is global in both alloys, Figures 70c-d and local at 600°C, Figures 70a-b.

Fe-25Cr-20Ni developes Ni sulfides with Fe and Fe-Cr sulfides at 500° and 600°C. Ni rich sulfide is solid at these exposure temperatures. Scales observed on this base alloy after 96 h exposure to the gas mixtures E and F are shown in Figures 71a-b. The scale shown in Figure 71a exhibits porous (spongy), faceted and smooth regions similar to those observed at 700°C, Figures 47a-d. The presence of Hf or Y has not changed significantly either the scale morphology or composition, Figures 72a-c. At low magnification the scales on Hf and Y containing alloy, Figures 72a and c appear similar to that shown in Figure 71a. The scale on Y containing alloy at 500°C has exactly similar appearance as that of Fe-25Cr-20Ni-1Hf shown in Figure 72b, and hence not shown separately.

Thin Al rich oxide scales formed on Fe-25Cr-6Al at both temperatures, Figures 73a-b. In both cases, scales on the substrate grain boundaries seem to have small amount of excess Cr than the bulk composition. Hf and Y containing alloys have the segregated Hf or Y rich

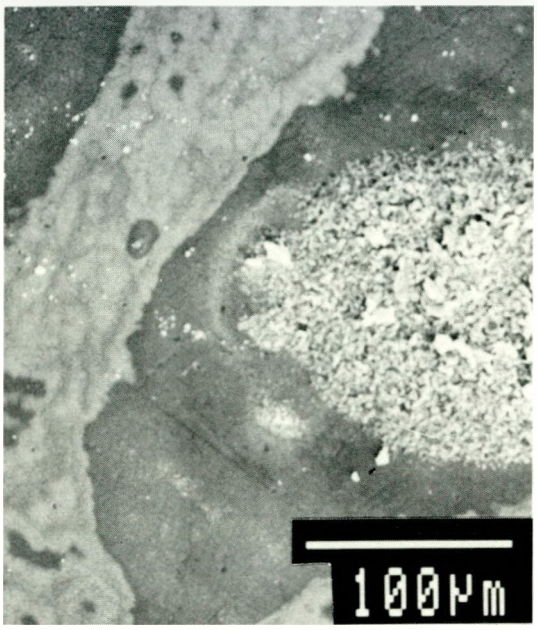

(a) E at 600°C

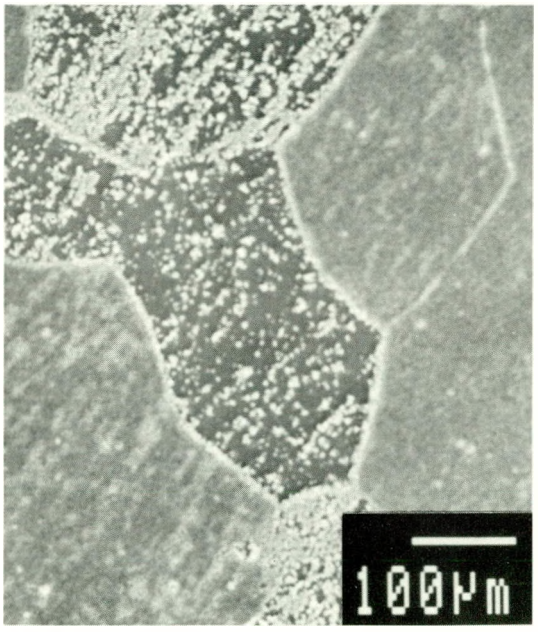

(b) F at 500°C

Fig. 69. Scales on Fe-25Cr exposed to gas mixture E or F for 96h.

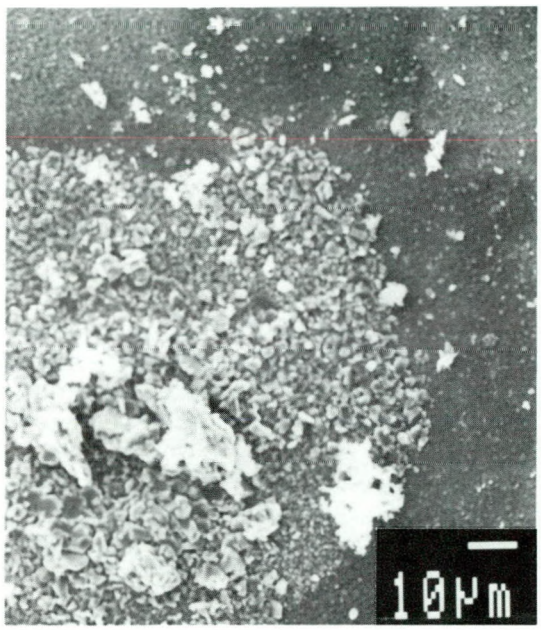

(a) Fe-25Cr-1Hf, E, 600°C

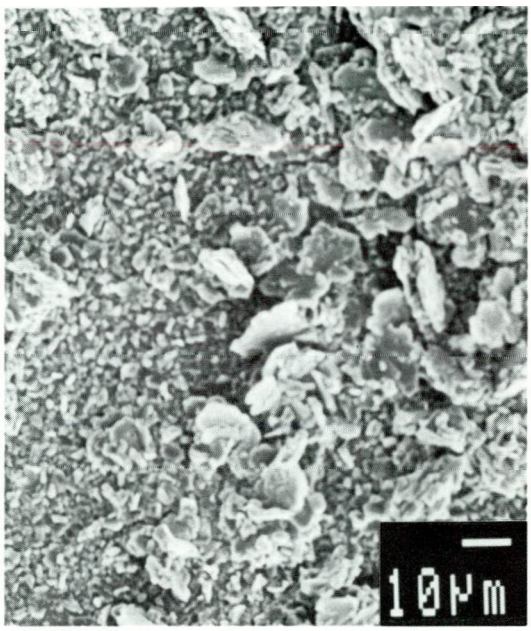

(b) Fe-25Cr-1Y, E, 600°C

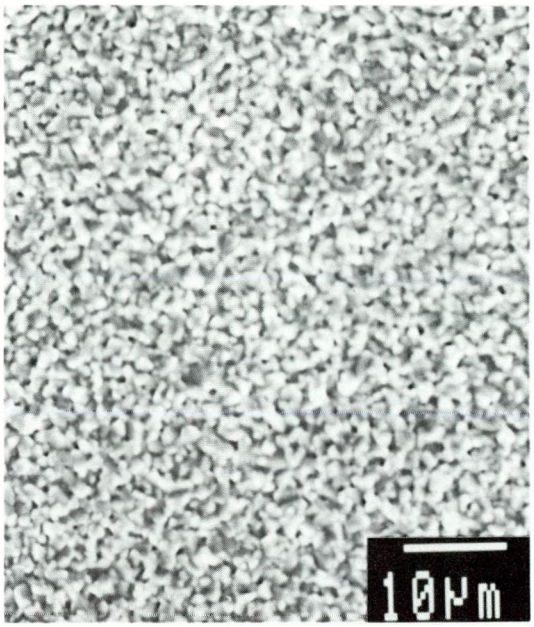

(c) Fe-25Cr-1Hf, F, 500°C

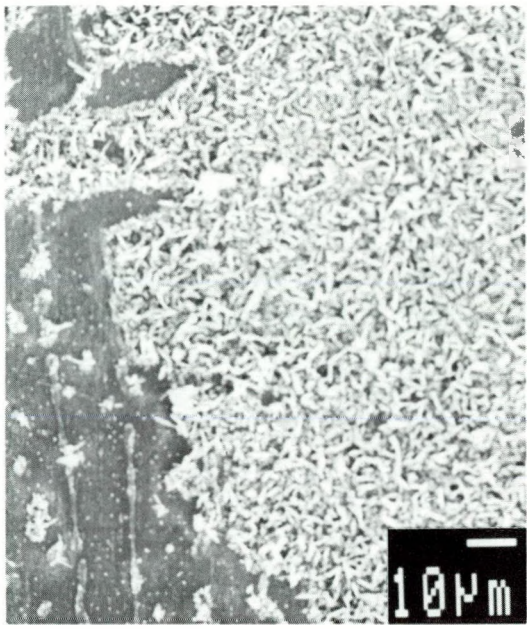

(d) Fe-25Cr-1Y, F, 500°C

Fig. 70. Scale breakdown in 96h in gas mixture E or F.

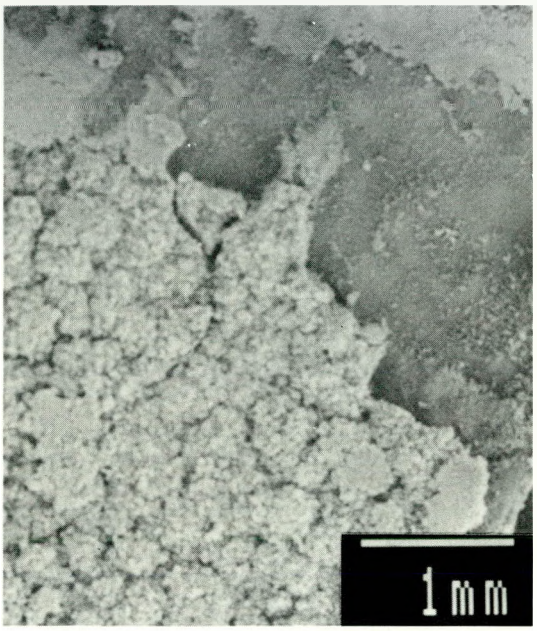

(a) E at 600°C

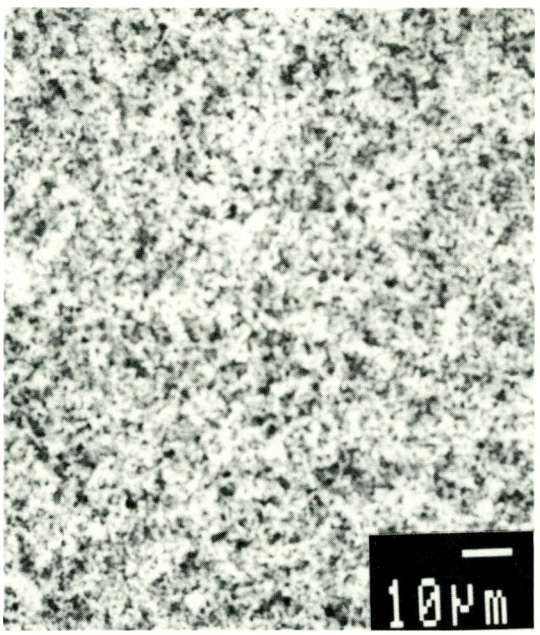

(b) F at 500°C

Fig. 71. Scale of Fe-25Cr-20Ni exposed to gas mixture E or F for 96h.

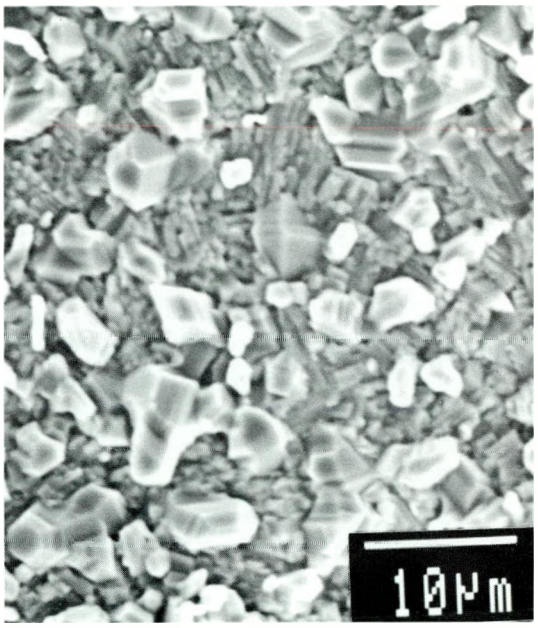

(a) Fe-25Cr-20Ni-1Hf, E, 600°C

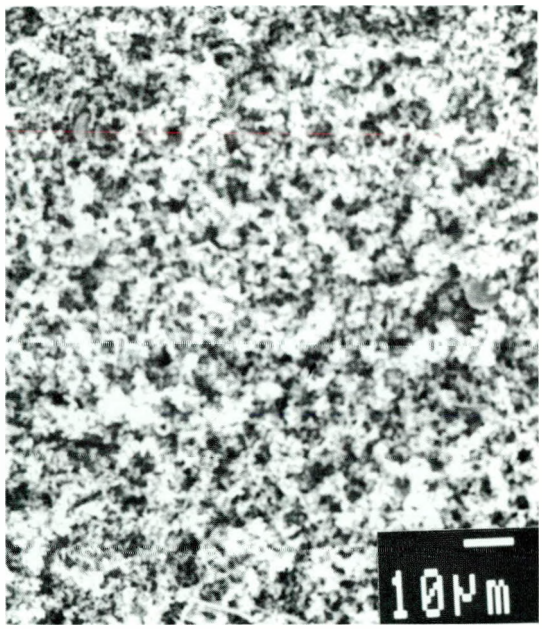

(b) Fe-25Cr-20Ni-1Hf, F, 500°C

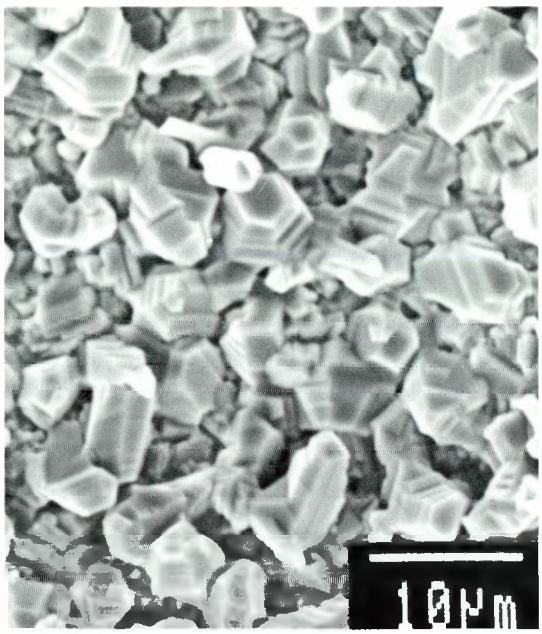

(c) Fe-25Cr-20Ni-1Y, E, 600°C

Fig. 72. Scale formed in gas mixture E or F at 96h.

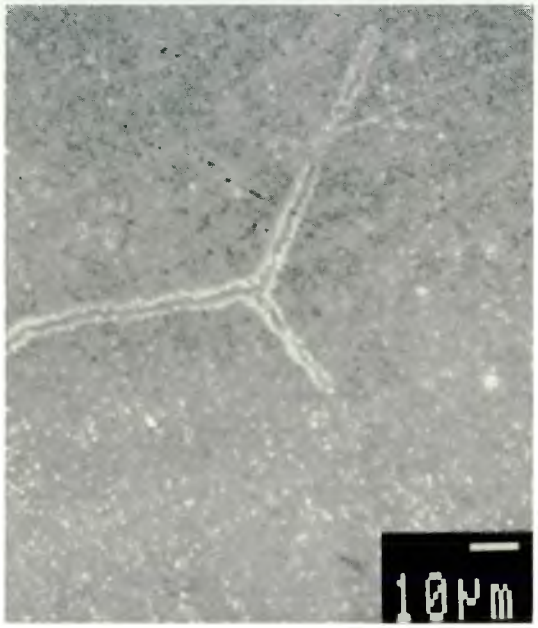

(a) Fe-25Cr-6Al, E, 600°C

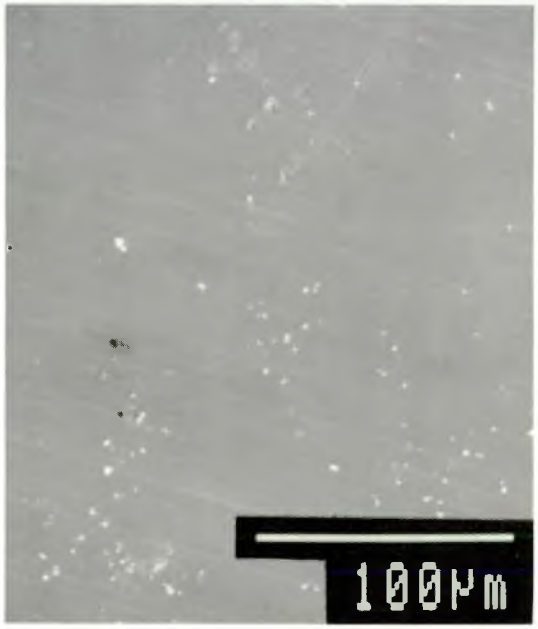

(b) Fe-25Cr-6Al, F, 500°C

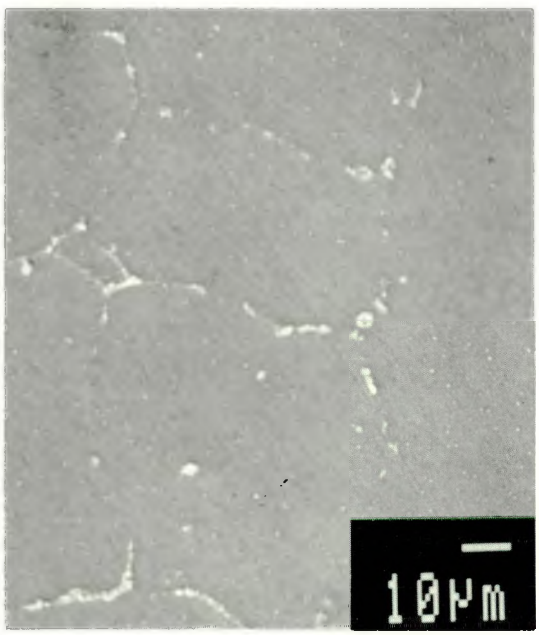

(c) Fe-25Cr-6Al-1Hf, E, 600°C

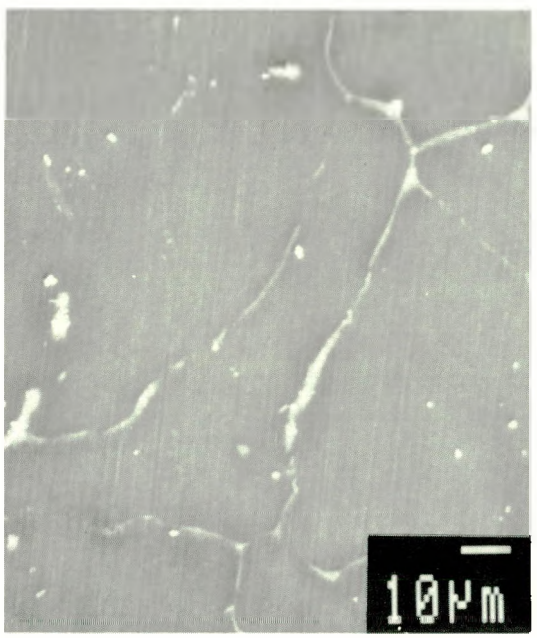

(d) Fe-25Cr-6Al-1Hf, F, 500°C

Fig. 73. Scale formed in gas mixture E or F for 96h.

phases along the substrate grain boundaries and the scales formed on these boundaries have a distinct appearance and contain more of the respective minor addition and a small amount of sulfur, Figures 73c-d and 74a-b. The scales on the substrate grains again were thin Al rich oxide. Their behavior is similar to that at 700°C.

4.9 BREAKDOWN OF PREFORMED OXIDE SCALES IN $H_2/H_2O/H_2S$/Ar GAS MIXTURES

4.9.1 (I/M) Fe-25Cr and Fe-25Cr-X Alloys

Scale formation-breakdown mechanisms were studied by exposing the preformed oxide scales to substoichiometric gas mixture of $H_2/H_2O/H_2S$/Ar. Preoxidation was performed in H_2/H_2O/Ar mixture at $pO_2=1.13\times10^{-20}$ atm at 700°C for time up to 96 h (gas mixture A). Subsequent exposure to sulfur containing gases was either at 700° or 500°C for time up to 96 h. The alloys investigated were Fe-25Cr, Fe-25Cr-1Ce, Fe-25Cr-1La, Fe-25Cr-3Si, Fe-25Cr-0.3 and 1.0Hf, and Fe-25Cr-0.3 and 1.0Y.

Oxide scale formed on the base alloy during preoxidation is essentially Cr_2O_3. The chromia scale starts forming epitaxially, Figure 75. A Cr_2O_3 scale of 140 nm in thickness (by AES depth profile) forms in 24 h. The scale formed in 96 h is about 1 μ thick Cr_2O_3 with nodules, Figures 76a-b. Addition of Ce and La results in grain boundary segregation of Ce and La rich particles. Scales formed on Fe-25Cr-1Ce and Fe-25Cr-1La in 24 h at $pO_2=1.13\times10^{-20}$ atm are shown in Figures 76c-d. The scales on the substrate grains are thin Cr_2O_3 with Fe. Ce and La are detected in the scales on the substrate grain boundaries (36.3Cr-53Fe-10.7Ce; 63.3Cr-27Fe-9.7La) which might include X-ray signal contributions

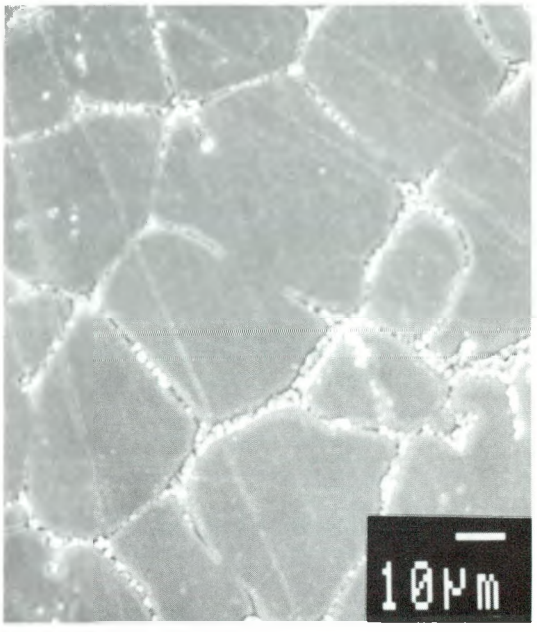

(a) E at 600°C, 96h

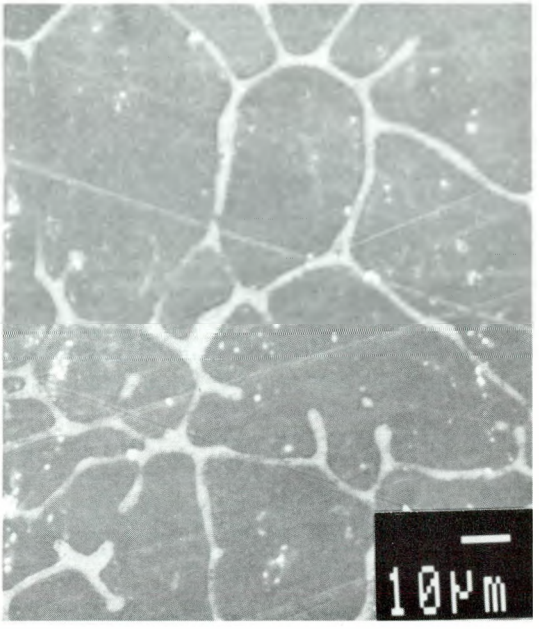

(b) F at 500°C, 96h

Fig. 74. Scale formed on Fe-25Cr-6Al-1Y in gas mixture E or F.

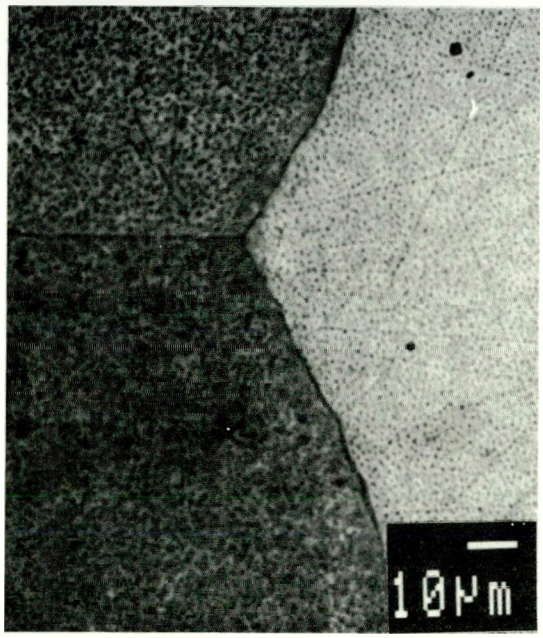

Fig. 75. Preformed oxide scale on Fe-25Cr in gas mixture A at 700°C, 2h (BEI).

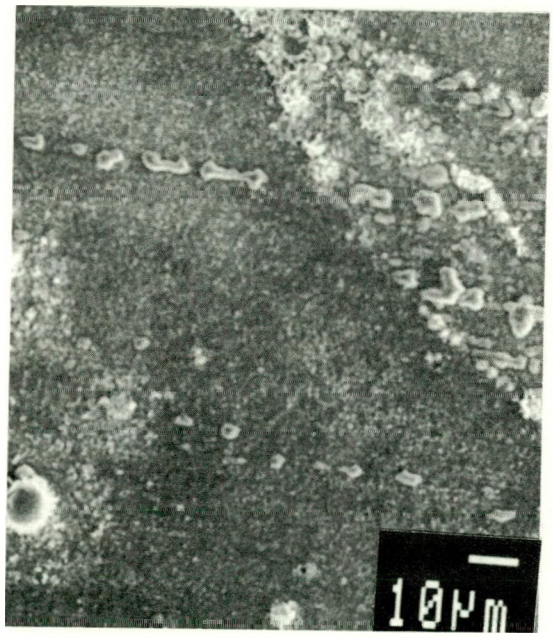

(a) Fe-25Cr

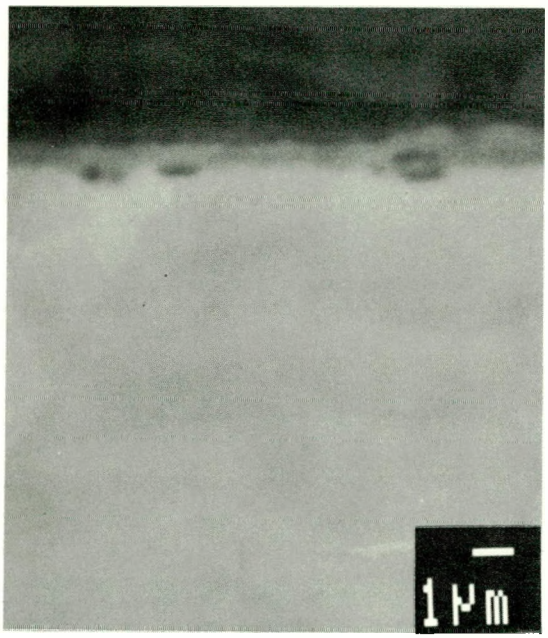

(b) Fe-25Cr, X-section (BEI)

Fig. 76. Preformed oxide scale in gas mixture A at 700°C.

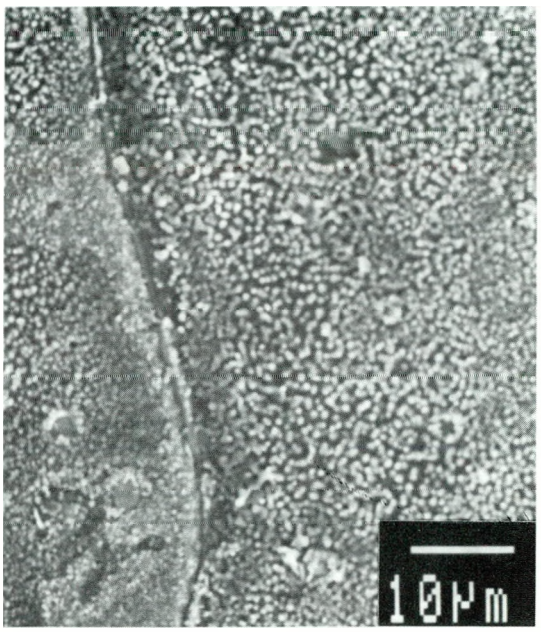

(c) Fe-25Cr-1Ce

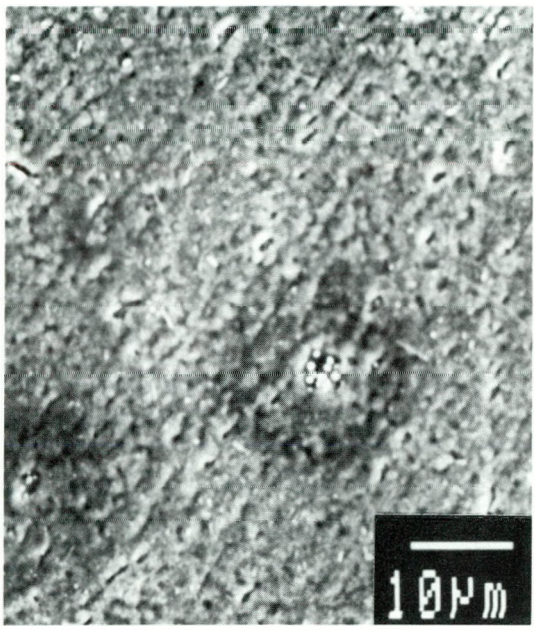

(d) Fe-25Cr-1La

Fig. 76 (cont'd.). Preformed oxide scale in gas mixture A at 700°C.

from the nonoxidized grain boundary particles below the thin scale because of larger than scale thickness electron activation volume. Si- and Cr-rich thin scale with several random white streaks forms on Fe-25Cr-3Si, Figure 77.

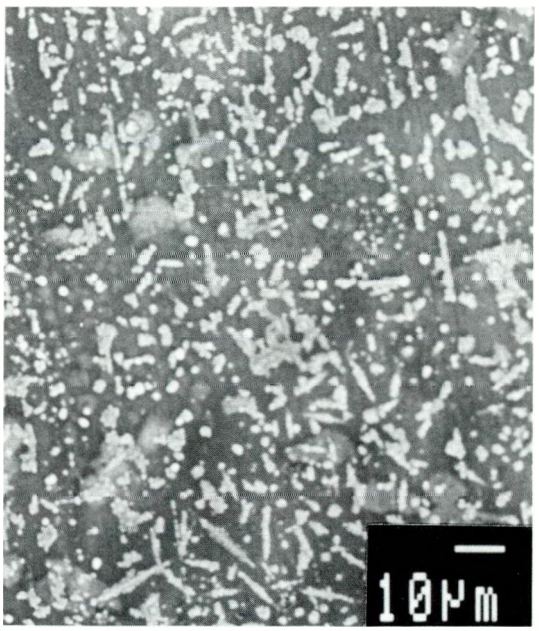

Fig. 77. Preformed oxide scale on Fe-25Cr-3Si gas mixture A, 700°C, 96h.

Oxide scales formed in 24 h at 700°C and pO_2=1.13x10^{-20} atm remain in tact after 1 h exposure to gas mixture B at 700°C, pO_2=1.17x10^{-20} and pS_2=1.22x10^{-8} atm. Even 24 h exposure to mixed gas does not lead to the breakdown of preformed oxide scale on Fe-25Cr at 700°C. The depth profiles (not shown) at two locations show that the scale is essentially Cr_2O_3 with a thickness of about 1300 nm (1.3 μ), and that there are a few spots which have 300 nm thick carbon layer over a 700 nm thick chromium oxide layer. However, continued exposure results in local sulfidation of otherwise uniform Cr_2O_3 scale. Figures 78a-c show the features of scale breakdown process. The sputter AES profiles obtained from a spot and away from the spots are reproduced in Figures 79a-b. On the spot there is an Fe-Cr sulfide layer, about 900 nm (0.9 μ) thick over a chromium oxide, $Fe_{1+x}Cr_{2-x}O_4$. layer, 900 nm (0.9 μ) thick. The general scale is Cr_2O_3 with a thickness of 1400 nm (1.4 μ). Cr_2O_3 scale formed at 700°C/96 h and pO_2=1.13x10^{-20} atm remains adherent and unattacked when exposed for 48 h to mixed gas at 700°C, pO_2=1.17x10^{-20} and pS_2=1.22x10^{-8} atm (SEMs not shown). The scale thickness is about 2 μ.

Cr_2O_3 scales formed on Fe-25Cr-1Ce and Fe-25Cr-1La in gas mixture A at 700°C and 24 h develop localized sulfides on exposure to gas mixture B at 700°C for 24 h. Shown in Figures 80a-b are the scale and local sulfides observed in Fe-25Cr-1Ce at low and high magnifications. The sulfides are rich in Fe with Cr and a small amount of Ce. Ce concentration at the substrate grain boundaries is high. Further sulfidation proceeds mostly along the substrate grain boundaries. Figure 81a shows Fe rich sulfides with Cr along the substrate grain boundaries after 72 h. This alloy was preoxidized in gas mixture A, at 700°C/24 h and subsequently exposed to gas mixture B at 700°C/72 h. La containing Fe-25Cr does not show such significant sulfidation but shows local spallation and sulfidation, Figure 81b under similar sequential exposures. La containing segregants along the substrate grain boundaries are observed.

To study the effectiveness of preformed oxide scales, oxidation was continued up to 96 h at 700°C and pO_2=1.13x10^{-20} atm before exposure to gas mixture B. Sulfide nodules are seen on the preformed scales at the gas/scale interface, and the addition of Hf or Y does not change the sulfidation resistance nor the mode of breakdown. Typical scale appearance in planar and X-section is shown in Figures 82a-b for Fe-25Cr-0.3Hf. The nodules are Cr rich sulfides with Fe and the uniform scale away from the nodules are Cr rich oxide. The sulfide nodules grow on the performed oxide scale and appear to consume the oxide scale as shown in Figure 82b. The Cr_2O_3 scale is still below the nodules, and voids are seen at the scale/metal interface, Figure 82b. Similar features are seen in Fe-25Cr and Fe-25Cr-0.3Y after similar preoxidation and mixed gas exposure. However, Si containing alloy (Fe-25Cr-3Si) does not undergo any sulfidation, and the preformed oxide scale (700°C/96 h, pO_2=1.13x10^{-20} atm) remains unaffected during exposure to mixed gas at 700°C/48 h, pO_2=1.17x10^{-20} and pS_2=1.22x10^{-8} atm, Figure 83.

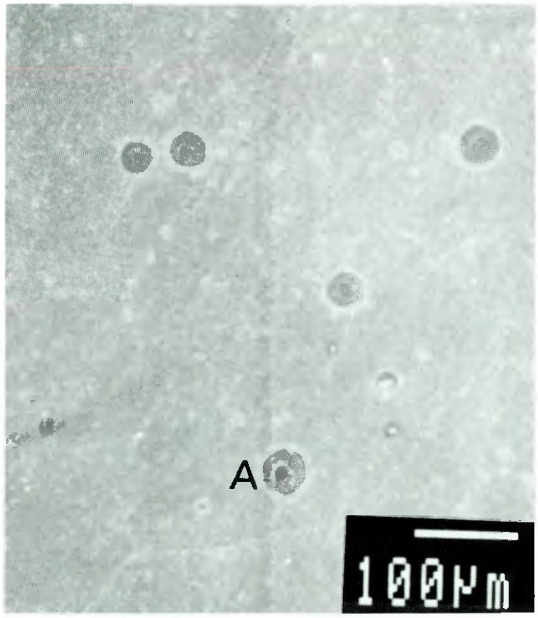

(a) Low magnification Nodule A

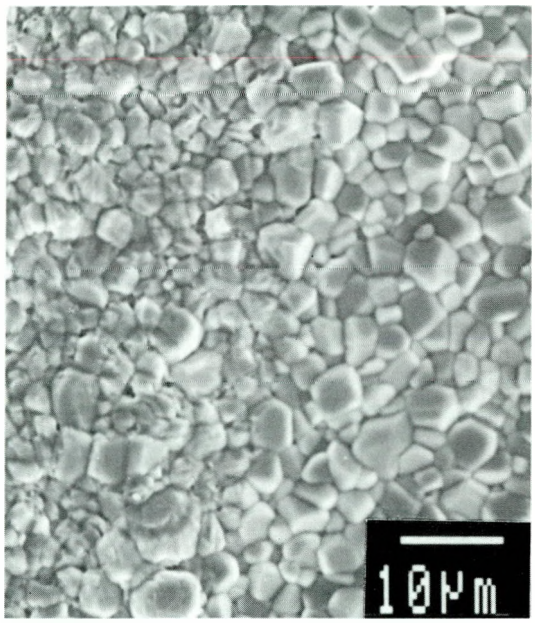

(b) High magnification, Nodule A

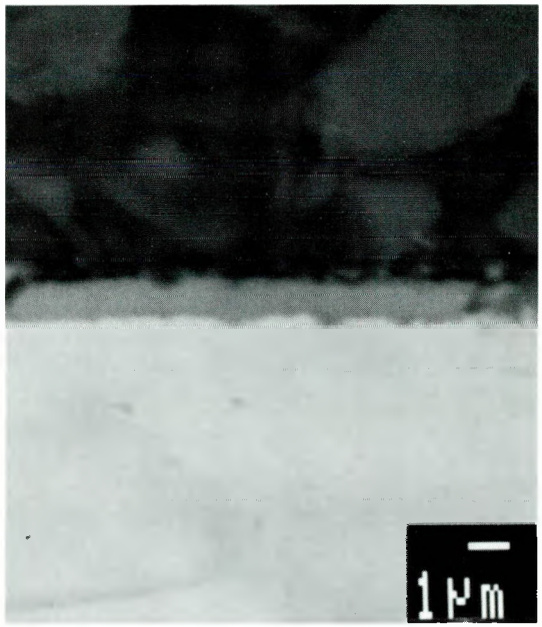

(c) X-section (BEI)

Fig. 78. Breakdown of preformed oxide scale (gas mixture A, 700°C, 24h) in gas mixture B, 700°C, 72h. Fe-25Cr.

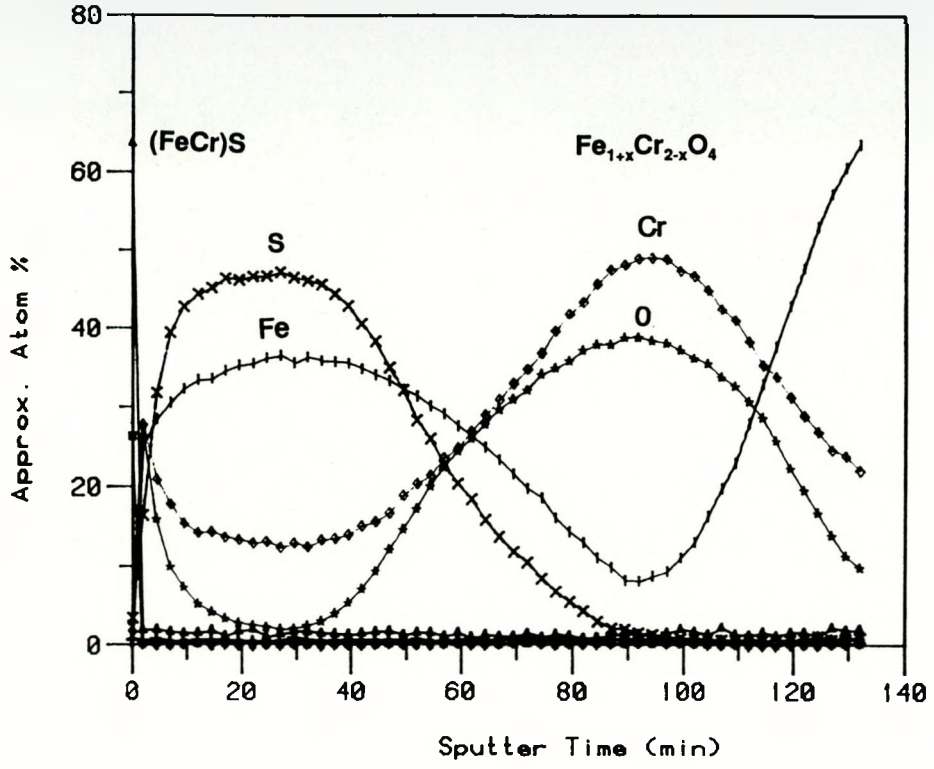

(a)

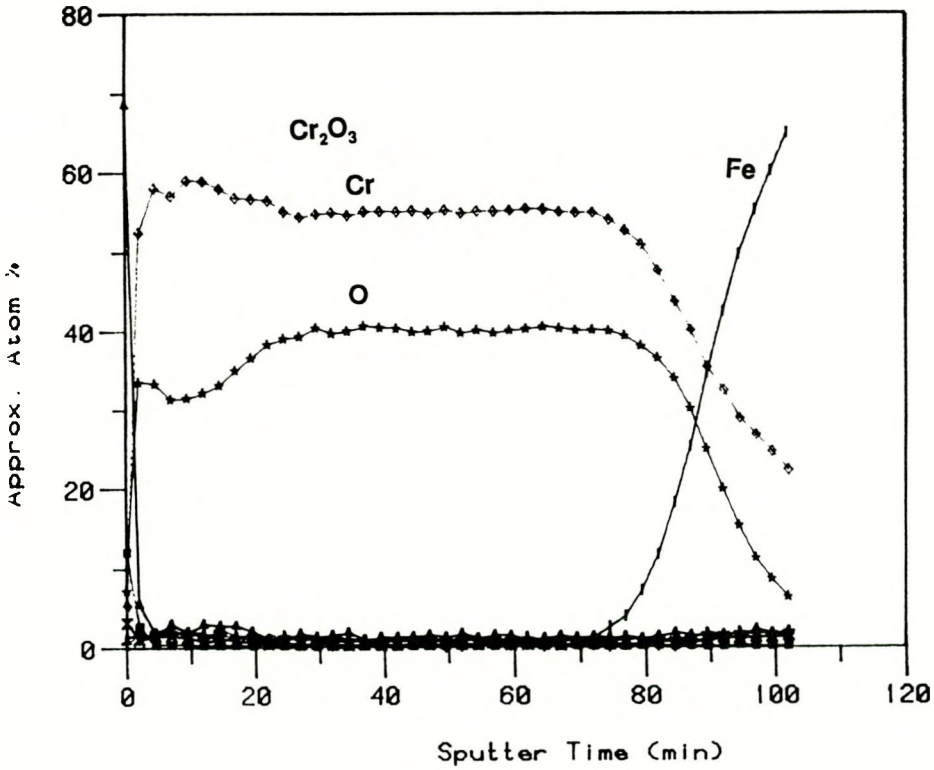

(b)

Fig. 79. AES depth profiles of (a) a sulfide nodule, and (b) unbroken scale.

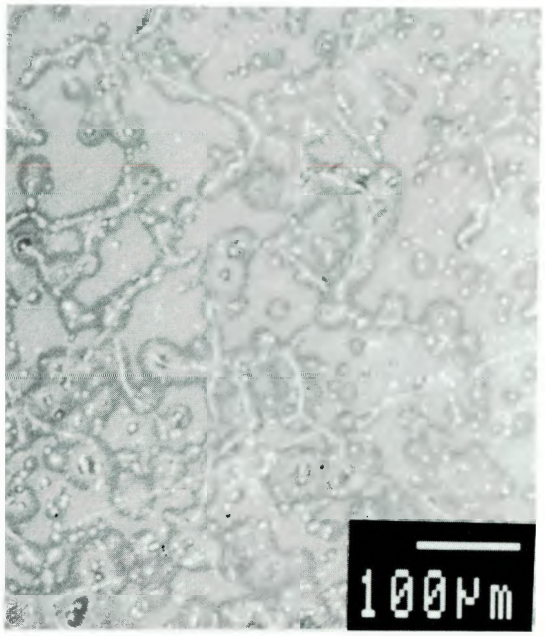

(a) Low magnification

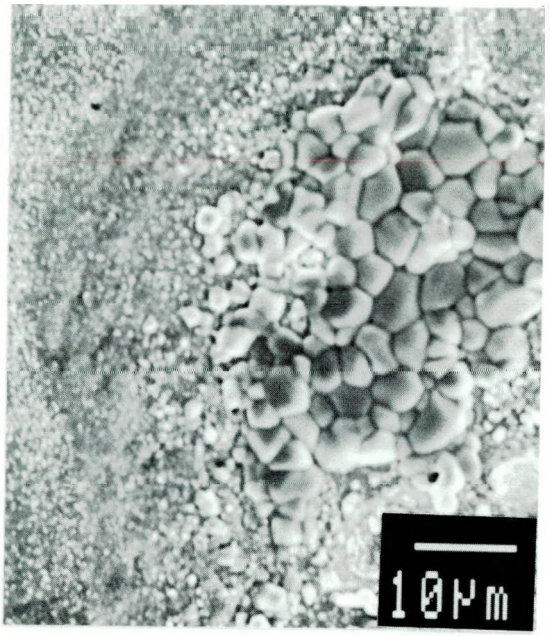

(b) Local sulfide at high magnification

Fig. 80. Breakdown of preformed scale (gas mixture A, 700°C, 24h) on Fe-25Cr-1Ce in gas mixture B, 700°C, 24h.

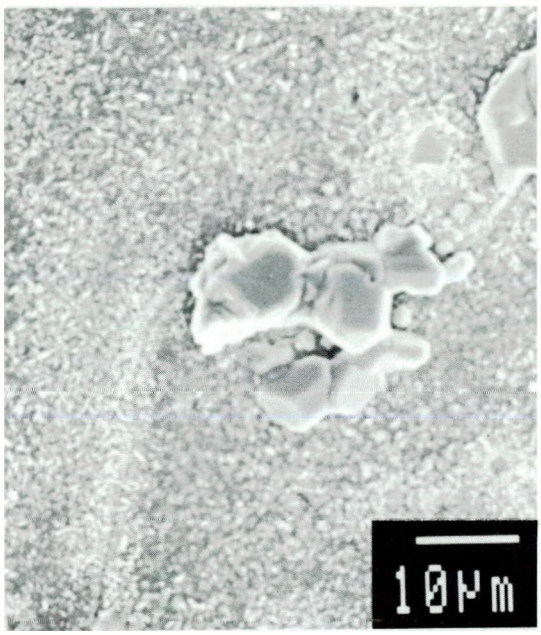

(a) Fe-25Cr-1Ce along g.b.

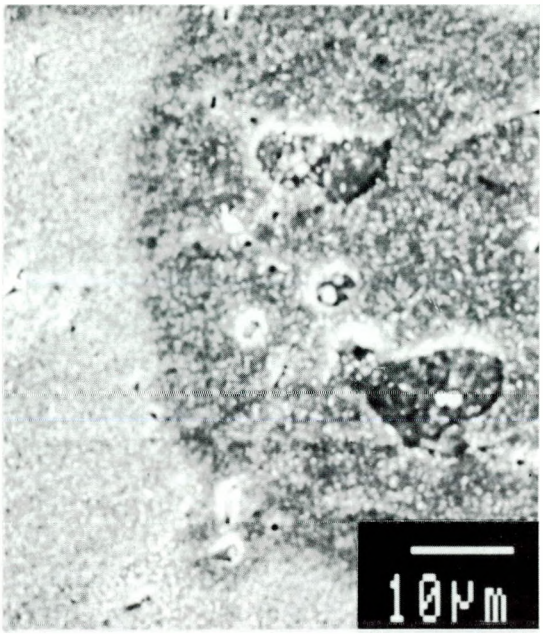

(b) Fe-25Cr-1La

Fig. 81. Breakdown of preformed oxide scale (gas mixture A, 700°C, 24h) in gas mixture B, 700°C, 72h.

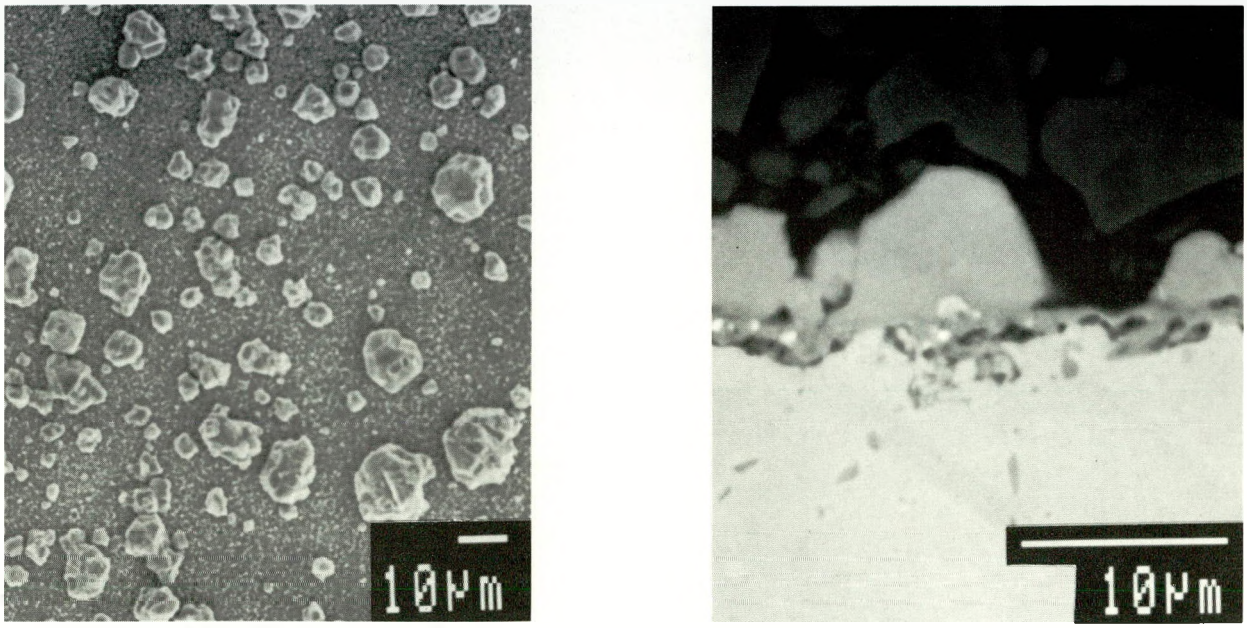

(a) Surface: Fe-25Cr-0.3Hf (b) X-section (BEI)

Fig. 82. Breakdown in gas mixture B, 700°C, 96h of preformed oxide scale in gas mixture A, 700°C, 96h.

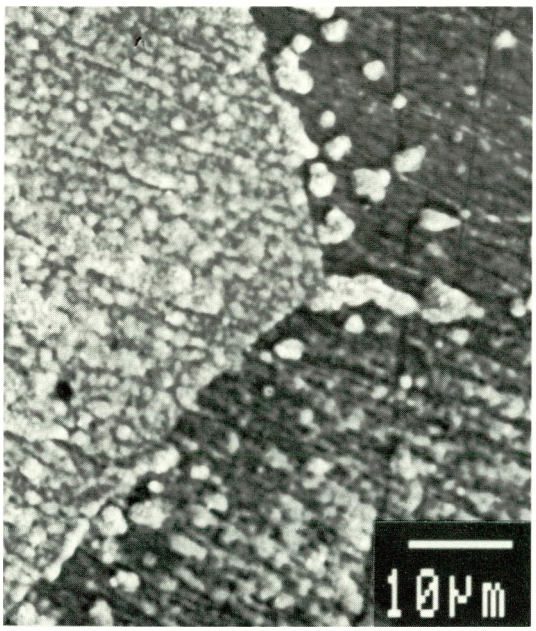

Fig. 83. Scale on Fe-25Cr-3Si after preoxidation in gas mixture A at 700°C, 96h and exposure to gas mixture B at 700°C, 48h.

The preformed Cr_2O_3 oxide scale in gas mixture A at 700°C/96 h continues to grow on exposure to mixed gas at 500°C/96 h and $pO_2=1.72x10^{-27}$ and $3.78x10^{-11}$ atm (gas mixture F) in the case of Fe-25Cr. Sulfidation is absent. The scale is adherent. These observations are common for Fe-25Cr, Fe-25Cr-0.3Hf and Fe-25Cr-0.3Y alloys. Y rich phases are detected in scale discontinuities, however, in the latter case, without any significant sulfur presence. Typical scale appearances in planar and X-sectional view are shown in Figure 84a-b for Fe-25Cr-0.3Hf alloy.

Cold rolling does not have any significant influence on preoxidation (700°C/96 h, $pO_2=1.13x10^{-20}$ atm) and breakdown of preformed scale by sulfur. (700°C/96 h, $pO_2=1.17x10^{-20}$ and $pS_2=1.22x10^{-8}$ atm). Sulfide nodules seen on cold rolled Fe-25Cr and Fe-25Cr-0.3Hf are similar to that shown in Figures 82a-b. Nodules in both cases are Cr rich sulfides with Fe. In Fe-25Cr-0.3Hf, Hf is found in some locations. However, nodules are not many in the case of Fe-25Cr-0.3Y, Figures 84c-d on the Cr_2O_3 scale. Few Cr rich sulfides without any Y are observed. Exposure of preformed scales (700°C/96 h, $pO_2=1.13x10^{-20}$ atm) to mixed gas at 500°C for 96 h, ($pO_2=1.72x10^{-27}$ and $3.78x10^{-11}$ atm) does not cause sulfidation, and the Cr rich oxide scale continues to form in all three alloys studied. The scale morphology is typically as shown in Figures 85a-b.

4.9.2 Ce Implanted Fe-25Cr

The performed oxide scale at 700°C/24 h and $pO_2=1.13x10^{-20}$ is thin. Depth profiling by sputter AES revealed a thin top layer of iron oxide (~70 nm) over a chromium oxide layer of about 200 nm thickness. At the interface between the iron oxide and chromium oxide layers a Ce peak (~18 at.%) is detected. Ce concentration decreases rapidly in the iron oxide layer, while it is present at significant level in the chromium oxide.

The bright and dark field TEM images of the preformed oxide are shown in Figures 86a-b. Second phase particles are present in the otherwise fine grained oxide. The electron diffraction pattern from the fine grain oxides, Figure 86c contain rings that belong to Cr_2O_3 and rings that cannot be attributed to Cr_2O_3. These latter rings are identified as that of $CeCr_2O_3$ which appear as second phase particles in Figure 86a.

When such a preformed oxide scale was exposed to a gas mixture, $pO_2=1.17x10^{-20}$ and $pS_2=1.22x10^{-8}$ atm for 24 h, local sulfidation occurs as shown in Figure 87. The sputter AES depth profile of the sulfide region is shown in Figure 88. Bright field images of the scale are shown in Figures 89a-b. Some channels are seen and they are rich in Ce, Fe and Cl. The presence of Cl is a surprise and is believed to be contaminant from the electrolytic solution used for thin foil preparation.

4.9.3 (P/M) Fe-25Cr-1.5Al_2O_3

Preformed oxide scales on P/M alloy is shown in planar and X-sectional views in Figures 90a-b. The scale was formed at 700°C/96 h, $pO_2=1.13x10^{-20}$ atm. The scale is relatively smooth, and thin, ~1 μ and seems to be slightly nonuniform in thickness. Cr_2O_3 oxide scale continues to form during subsequent exposure to sulfidizing gas mixture at 700°C for 48 h with $pO_2=1.17x10^{-20}$ and $pS_2=1.22x10^{-8}$ atm, Figures 91a-b. Scale sulfidation has

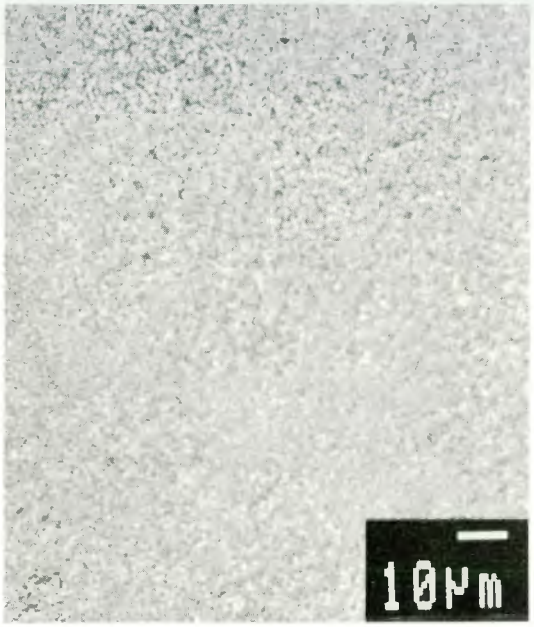

(a) Fe-25Cr-0.3Hf

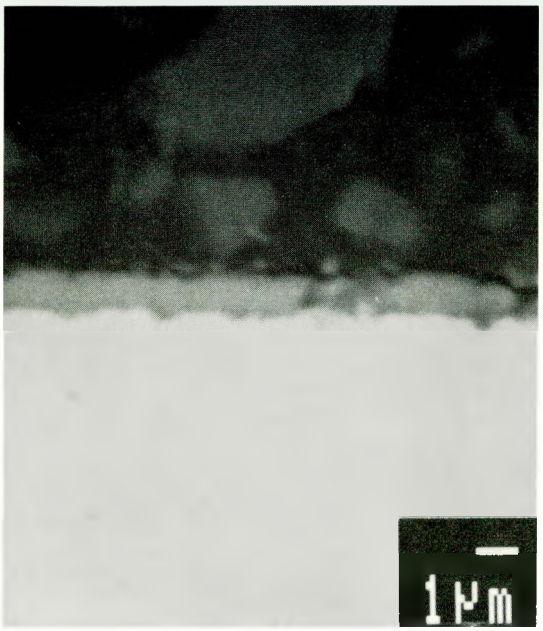

(b) X-section, Fe-25Cr-0.3Hf (BEI)

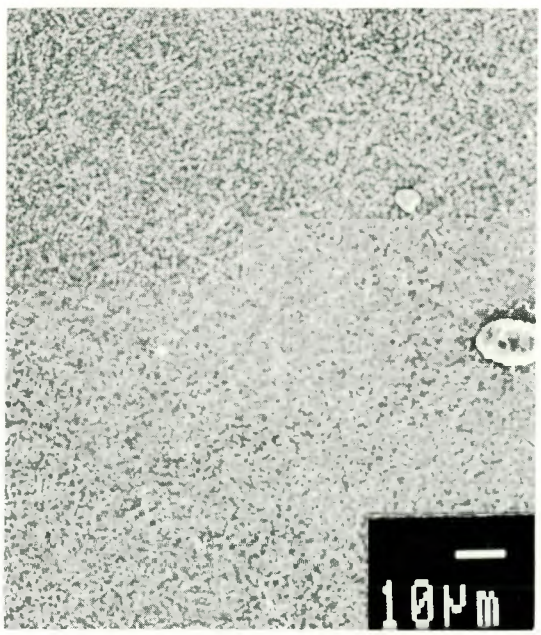

(c) Fe-25Cr-0.3Y, Cold-rolled

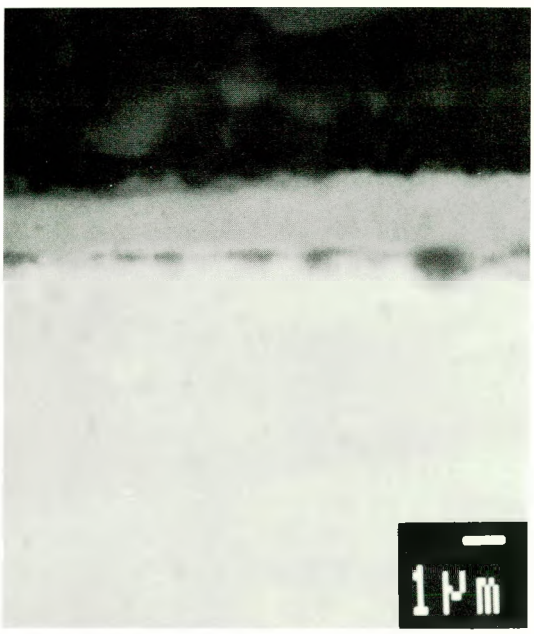

(d) X-section, Fe-25Cr-0.3Y (BEI)
Cold rolled

Fig. 84. Scales formed on preoxidation in gas mixture A, 96h and exposure to gas mixture B, 700°C, 96h.

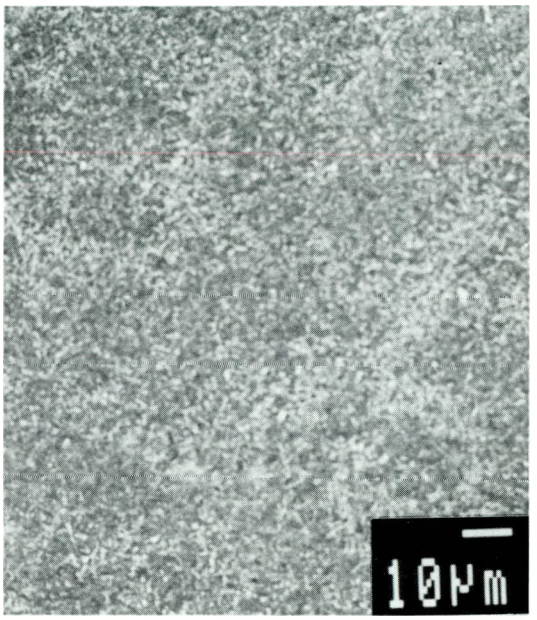

(a) Surface

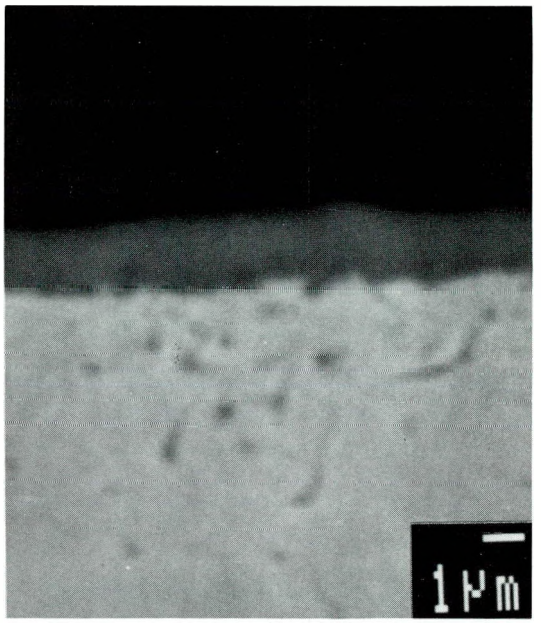

(b) X-section (BEI)

Fig. 85. Scales on cold-rolled Fe-25Cr-0.3Hf preoxidized in gas mixture A, 700°C, 96h and exposed to gas mixture B, 500°C, 96h.

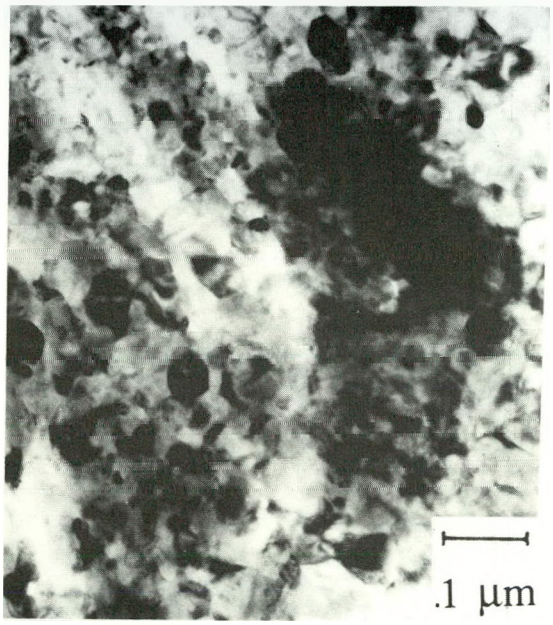

(a) Bright field
A: Second Phase

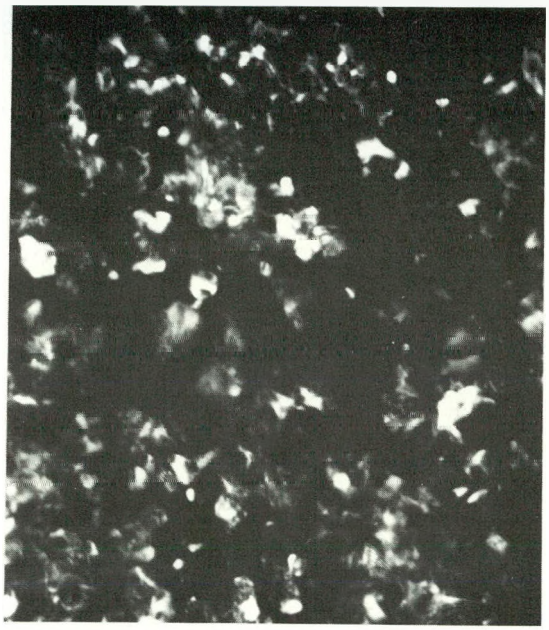

(b) Dark field

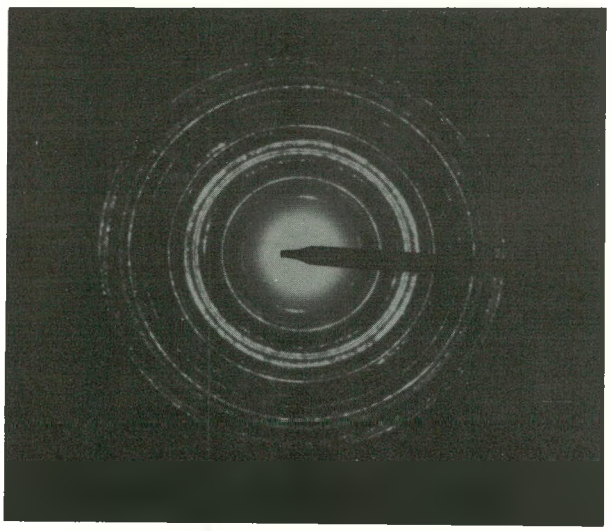

(c) Selected area diffraction

Fig. 86. TEM and SAD of preformed oxide on Ce-implanted Fe-25Cr in gas mixture A, 700°C, 24h.

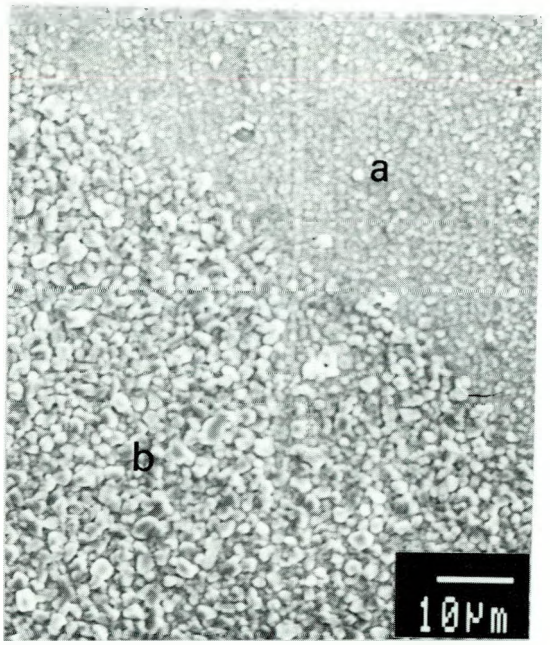

Fig. 87. Scale breakdown in Ce-implanted Fe-25Cr preoxidized in gas mixture A, 700°C, 24h and exposed to gas mixture B, 700°C, 24h.

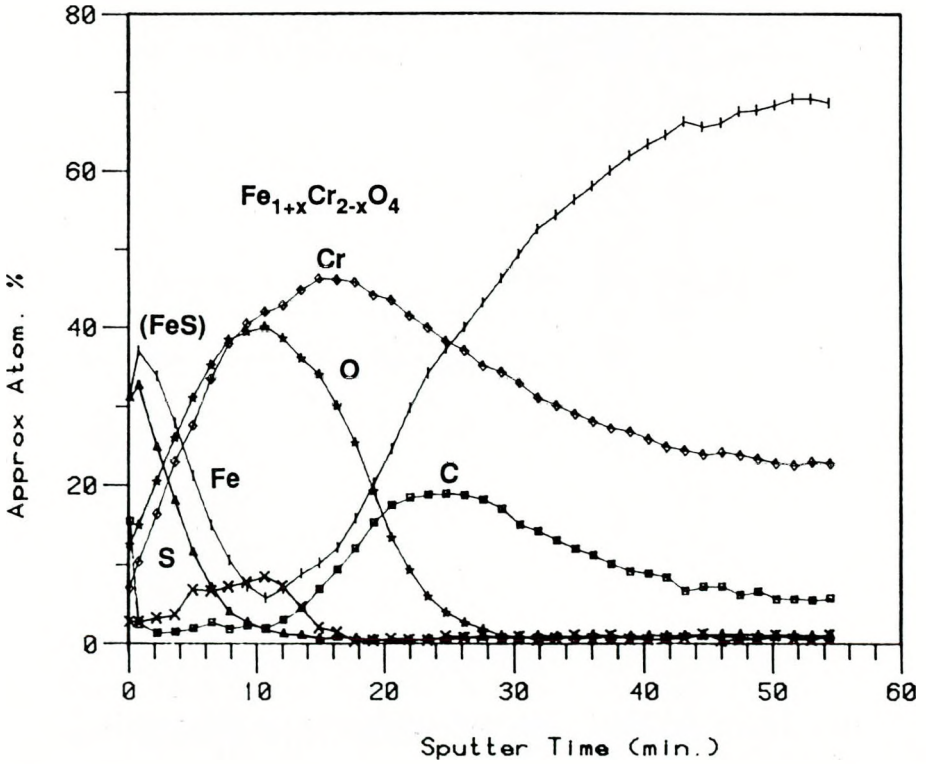

Fig. 88. AES depth profile of scale in the region of local breakdown in Fig. 87.

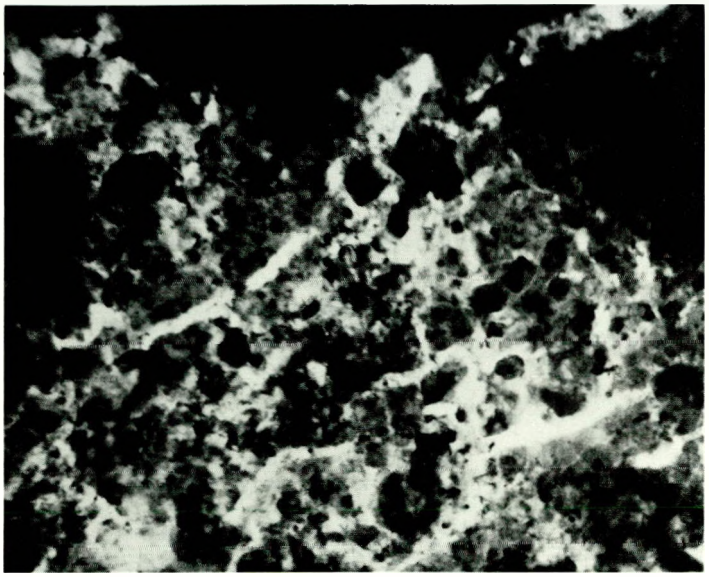

(a)

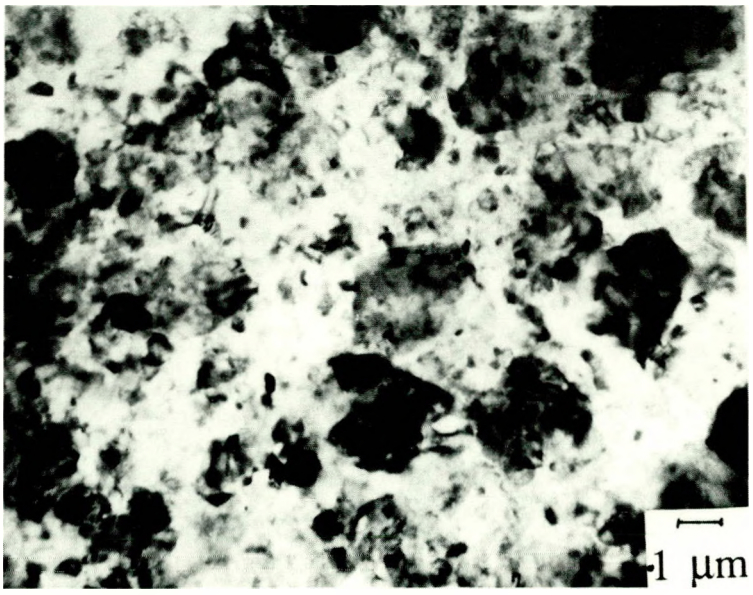

(b)

Fig. 89. Bright field images of scale of Ce-implanted Fe-25Cr preoxidized in gas mixture A, 700°C, 24h and exposed to gas mixture B, 700°C, 24h.

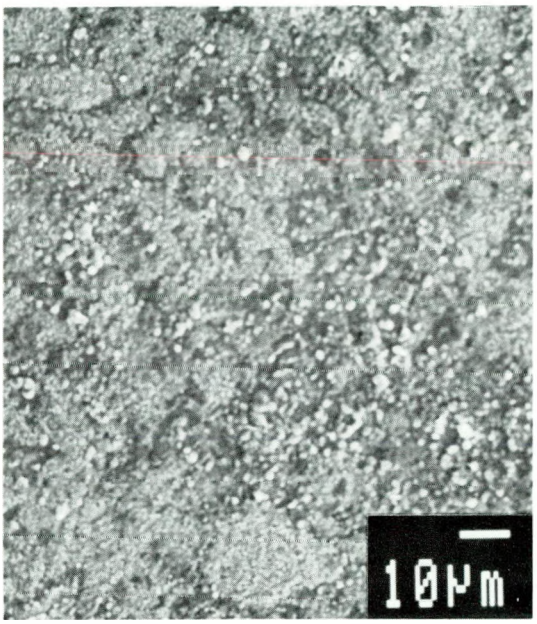

(a) Surface

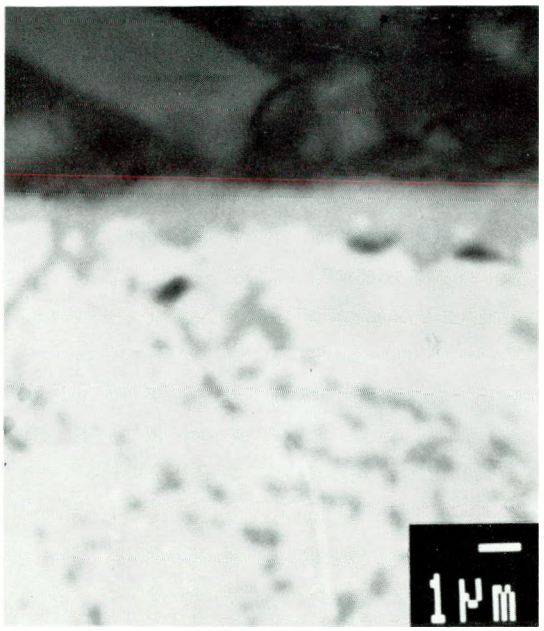

(b) X-section (BEI)

Fig. 90. Preformed oxide scale on Fe-25Cr-1.5Al_2O_3 in gas mixture A, 700°C, 96h.

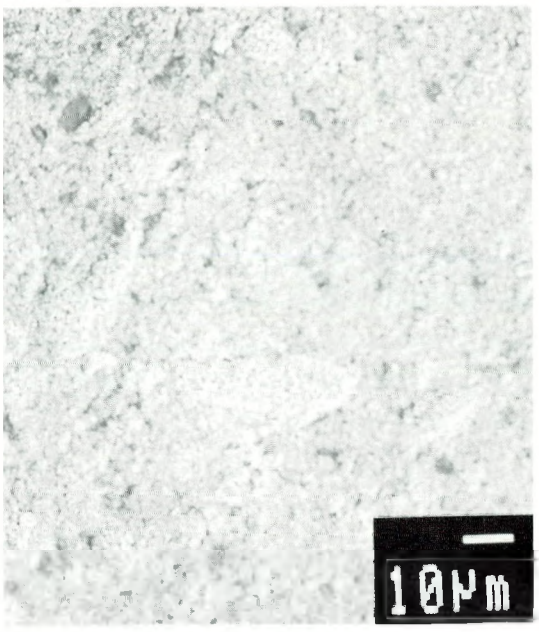

(a) Surface

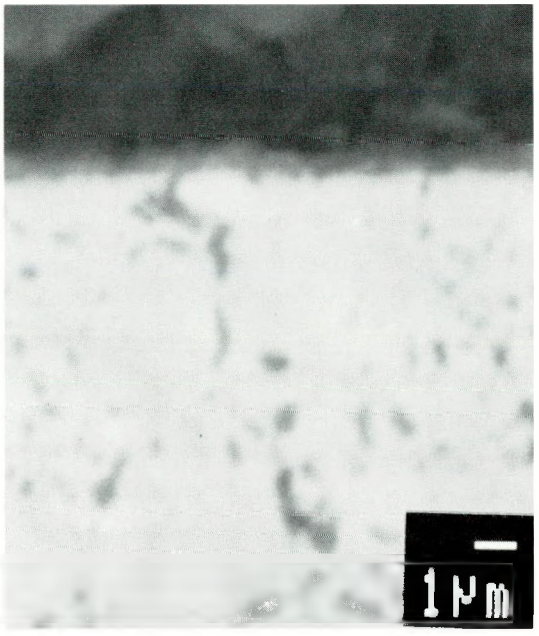

(b) X-section (BEI)

Fig. 91. Preformed oxide scale on Fe-25Cr-1.5Al_2O_3 in gas mixture A, 700°C, 96h exposed to gas mixture B, 700°C, 48h.

not started. The scale in the latter appears to be thinner than the preformed scale which is again suggesting the nonuniform nature of scale thickness.

4.9.4 (I/M) Fe-25Cr-20Ni and Fe-25Cr-20Ni-X Alloys

In general, these alloys show rapid sulfidation when exposed to mixed gases, Section 4.5.4. Therefore, several preoxidation and subsequent exposure times were used. Preoxidation at 700°C and pO_2=1.13x10^{-20} atm for 4 and 96 h has led to the formation of scales as shown in Figures 92a-c. At both exposure times, the scale has smooth and highly granulated regions. The smooth regions are rich in Cr and Fe with Ni, and granulated regions contain significantly high Fe concentration with small amounts of Cr and Ni. The EDAX analysis of scale cross section, Figure 92c gives composition similar to that of granulated regions.

The oxide scale formed in 96 h was analyzed using XPS (ESCA) at the Materials Analysis User Center of HTML, ORNL, Oak Ridge, TN. Carbon 1s peak is used as reference. The following elemental peaks, C1s, O1s, Aℓ2p, Si2p, $Cr2p_{1/2}$, $Cr2p_{3/2}$, $Fe2p_{1/2}$, $Fe2p_{3/2}$, $Ni2p_{1/2}$ and $Ni2p_{3/2}$ are monitored. Using appropriate sensitivity factors determined are the elemental concentrations (at.%): 15.71 Fe-2.36Cr-46.74O-2.71Si-32.48C. Surface contamination has contributed to the presence of C and Si. Si is present as SiO_2. From the positions and separations of Fe and Cr peaks it is determined that the oxide scale consists of about 86% of Fe_3O_4 and 13% of Cr_2O_3. Oxygen concentration nicely partitions to these oxides. Fe_2O_3 is not stable at the experimental pO_2. After 60 min of sputter the scale remains almost Fe_3O_4 rich, but seems to be oxygen deficient. In addition to a small amount of Cr_2O_3, Fe^{+3}, (Fe_3O_4), Fe^{+2} (FeO) and Fe^0 (metal) are detected in the scale after an additional 50 min of sputtering (total 110 min).

The preformed oxide scale at 700°C/4 h is broken down by patch sulfides, Figure 93a. The scale is thin with significant Cr and Fe, but the sulfidized regions have more Fe and Ni. Initial stages of the breakdown process of the preformed oxide are shown in Figure 93b. The scale breakdown of the preformed oxide scale at 700°C is already in progress after exposure to mixed gas (gas mixture B) for 10 min. Thicker the preformed oxide, longer is the time required to destroy the protective oxide scale, and this is shown in Figure 94a-c by 96 h preoxidation-48 h mixed gas-exposure study. The preoxidation and subsequent exposure were in gas mixtures A and B respectively at 700°C. The faceted and fuzzy (porous islands on the facets) are Fe-Ni sulfides and the only difference is that the fuzzy products have more Ni. The unbroken scale, Figure 94b is Cr_2O_3 and the nodules on the adherent Cr_2O_3 scale, Figure 94c are Ni-Fe sulfides (76.5Ni-10.7Fe-1Cr-1.8S). Sulfur could be more than 1.8.

Addition of Ce, or La does not influence the scale formation and breakdown process described above and, hence, no micrographs are included here. The only difference observed in Ce or La containing alloy is that the preformed scale is Fe rich oxide and no Cr rich smooth regions are observed.

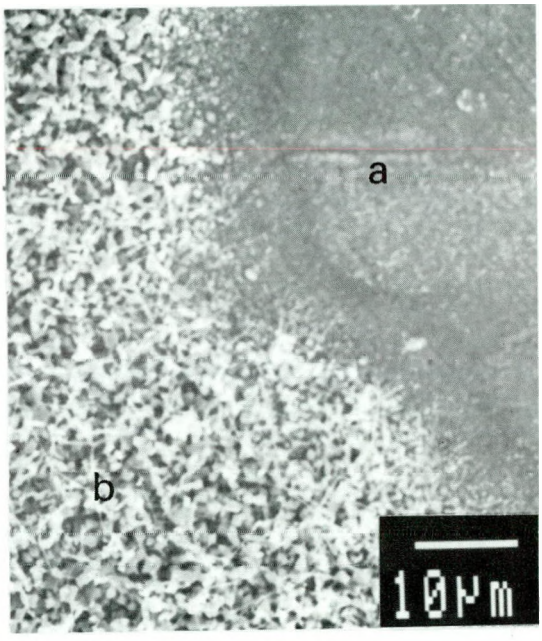

(a) 4h

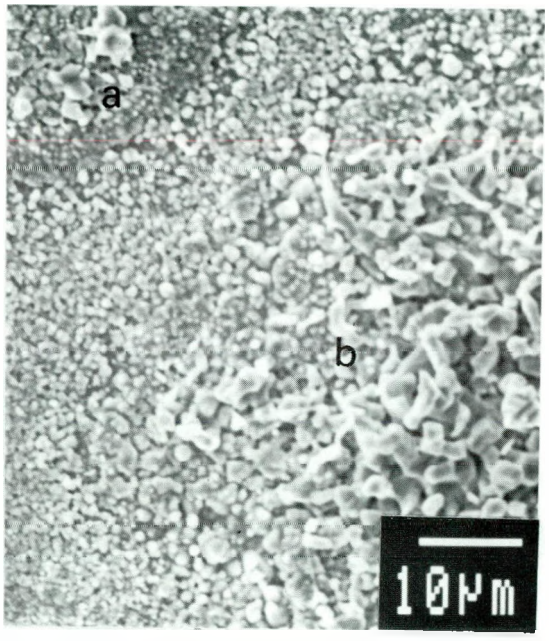

(b) 96h

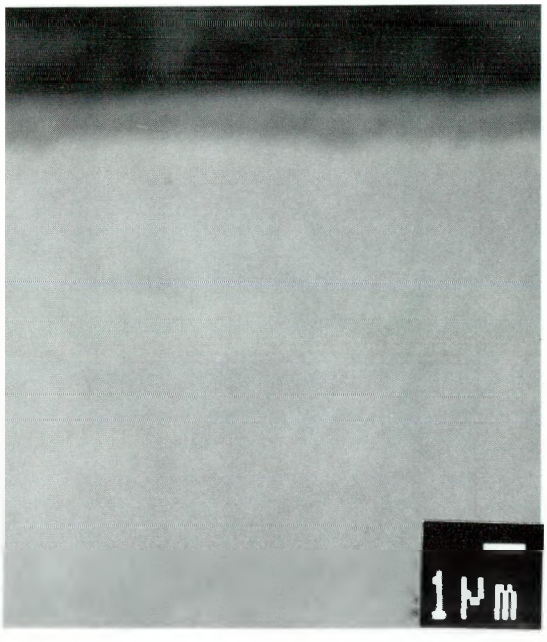

(c) X-section (BEI)

Fig. 92. Preformed oxide scale on Fe-25Cr-20Ni in gas mixture A, 700°C.

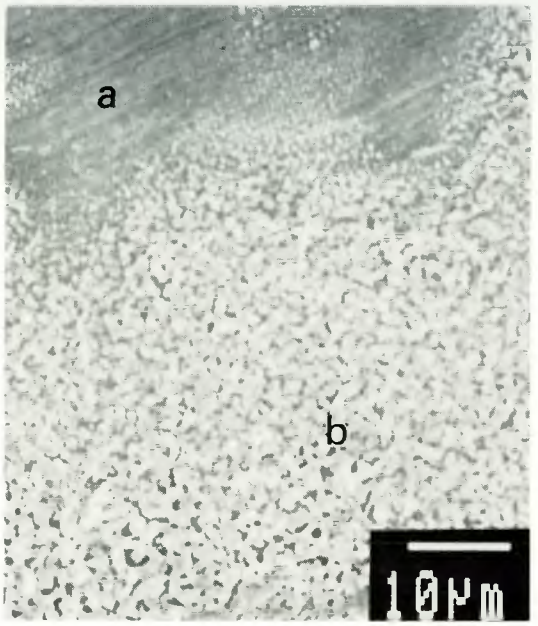

(a) 1h

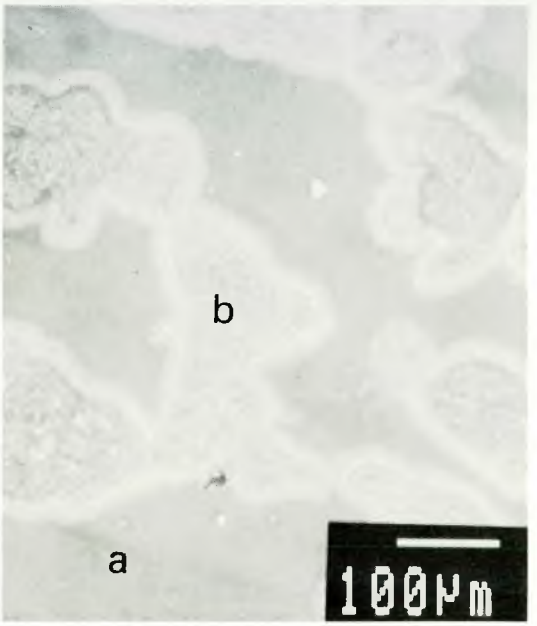

(b) 10 min, low magnification

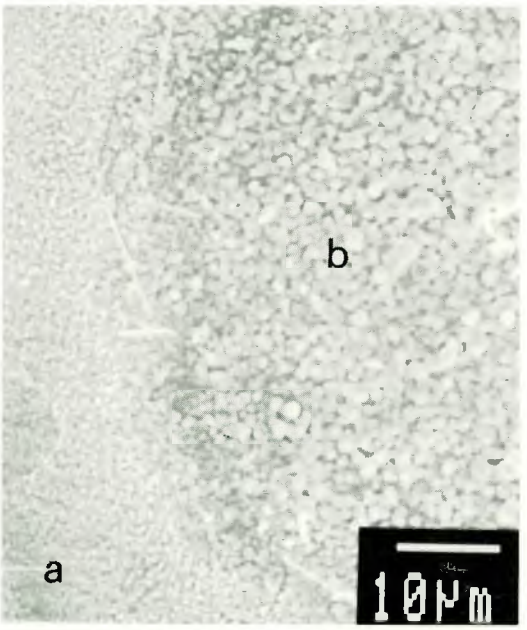

(c) 10 min, high magnification: sulfides

Fig. 93. Breakdown of preformed oxide scales in gas mixture A, 700°C, 4h exposed to gas mixture B, 700°C. Fe-25Cr-20Ni.

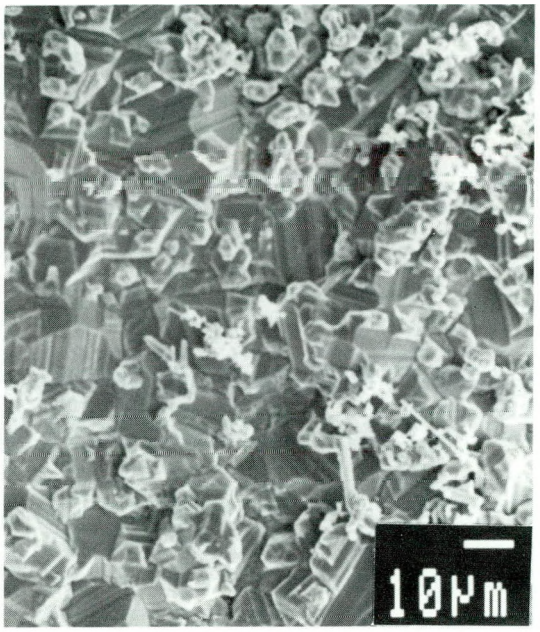

(a) Surface

(b) X-section (BEI)

(c) X-section (BEI)

Fig. 94. Breakdown of preformed oxide scale in gas mixture A, 700°C, 96h exposed to gas mixture B, 700°C, 48h. Fe-25Cr-20Ni.

Si addition has imparted considerable protectiveness to the preformed oxide scale. This is in line with the observation of protective behavior of Si containing alloys in mixed gas described earlier. Preformed oxide scales and the final scales after preoxidation and mixed gas exposure are thin. Therefore, the scales were characterized using scanning Auger microprobe (SAM) and secondary ions mass spectroscopy (SIMS), in addition to analysis by SEM/EDAX. The preformed scale on Fe-25Cr-20Ni-3Si in $pO_2=1.13x10^{-20}$ atm at 700°C/96 h is shown in Figure 95a and has light and dark areas. These regions differ in Si content but not significantly. Auger spectra were taken from the above two areas at three different depths: 0 (gas/scale interface), 50, 100 and 200 nm. Strong Fe signals are seen at 200 nm in both areas suggesting the scale/metal interface. Cr and O signals are present at all depths but the Si signal is not always present, and not at both regions at the same depth. Thus, there is a certain variability in the thickness of the scale, and not on the presence of Si at the metal/scale interface as SiO_2.

When the preformed Cr_2O_3 scale with Si was exposed to mixed gas at 700°C/48 h, $pO_2=1.17x10^{-20}$ and $pS_2=1.22x10^{-8}$ atm, no significant change or sulfidation was observed, Figure 95b. AES spectra form the light and not-so-light regions were taken from depths 0, (unsputtered gas/scale interface), 50, 100 and 200 nm. The metal/scale interface was reached at the depth of 200 nm as indicated by the strong Fe signals. Again the scale is Cr_2O_3 with some Si, and no sulfur is detected in the scale. In some cases sulfur is detected only on the unsputtered surfaces, and is believed to be contaminant due to cooling the sample while the mixed gas flow was on. The SIMS analysis was done. $^{32}S^-$ and $^{32}O_2^-$ have similar masses. The mass resolution required to distinguish between $^{32}S^-$ and $^{32}O_2^-$ is $17.8x10^{-3}$ amu, but the quadrapole mass resolution available with the unit at HTML/ORNL is 1 amu. An alternate procedure is to use the "target bias off-set method." The target bias range currently available is not adequate to accomplish this. However, the results of AES analysis have shown clearly the absence of S in the scale, and, therefore, SIMs results are taken to imply only the presence of $^{32}O_2^-$.

4.9.5 (P/M) Fe-25Cr-20Ni-1.5Al_2O_3

A uniform thin Cr_2O_3 scale formed on P/M Fe-25Cr-20Ni-1.5Al_2O_3 on preoxidation at 700°C/96 h in $pO_2=1.13x10^{-20}$ atm, Figures 96a-b. The addition of 1.5Al_2O_3 has influenced the oxide scale formation significantly. (Compare Figures 96a-b with 92b-c). EDAX analysis of scales in the light areas suggests that the scale is Cr_2O_3 with some Fe. Scale compositions were determined qualitatively by combining SAM and sputtering and XPS.

Auger spectra were obtained from the unsputtered surface (gas/scale interface), 50, 100 and 200 nm in depth at two locations (light particles and the general scale). Small amounts of Si and C were detected on the unsputtered surface as contaminants. They disappeared after a very brief sputtering. The scale is essentially Cr_2O_3 as indicated by Cr and O peaks at both places and four depths. Fe peaks are observed at the depth of 200 nm indicating the presence of metal/scale interface.

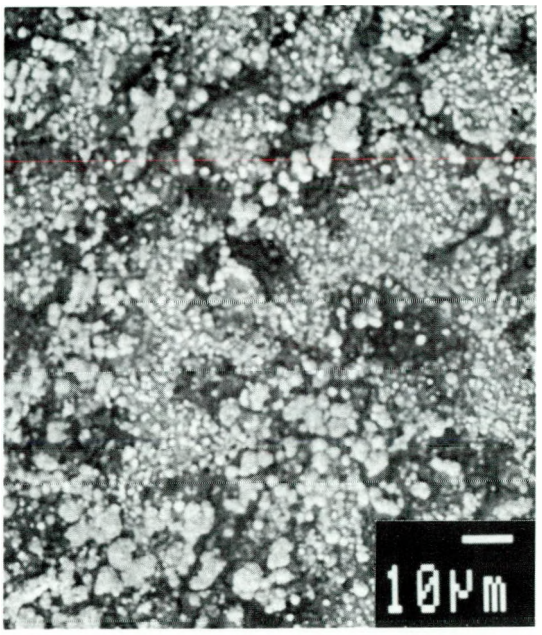

(a)

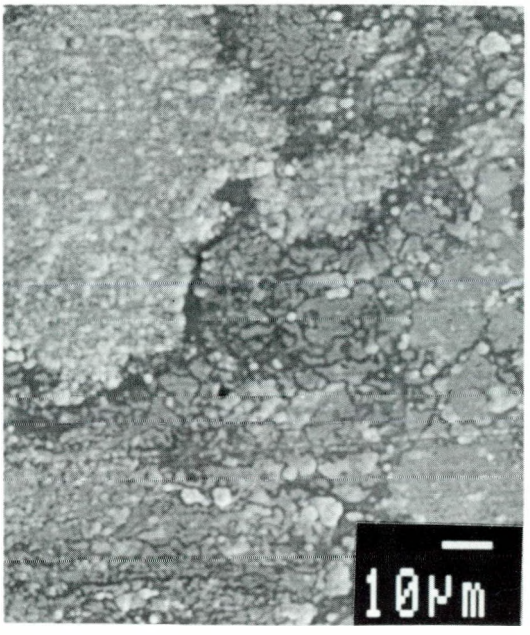

(b)

Fig. 95. Scale on Fe-25Cr-20Ni-3Si, (a) after preoxidation in gas mixture A, 700°C, 96h and (b) after preoxidation as above and exposure to gas mixture B, 700°C, 48h.

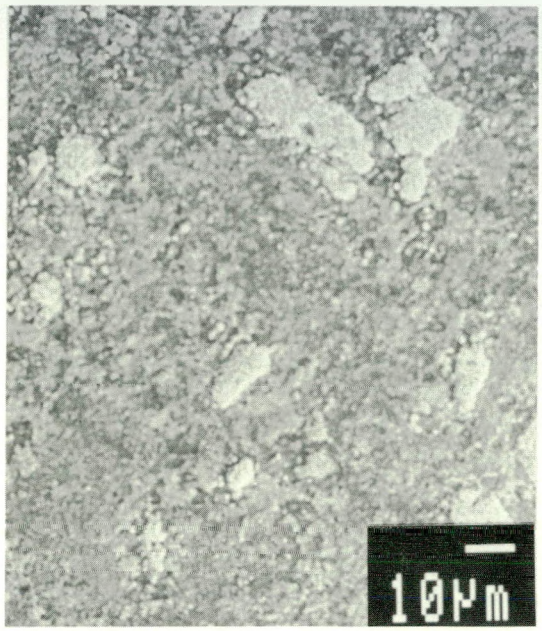

(a) Preoxidation

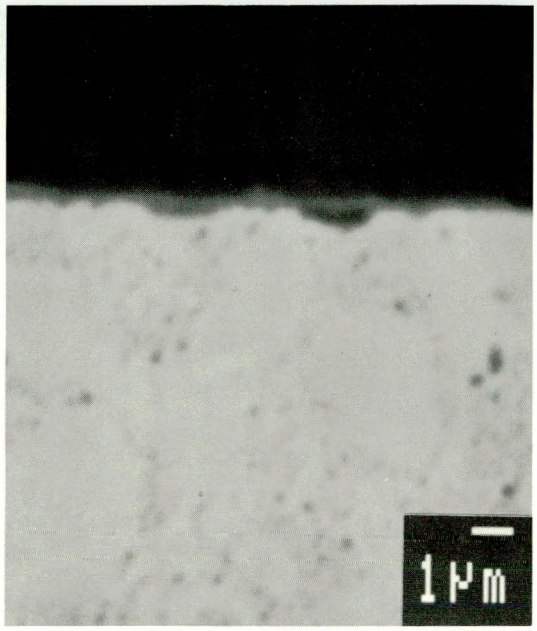

(b) X-section of (a) (BEI)

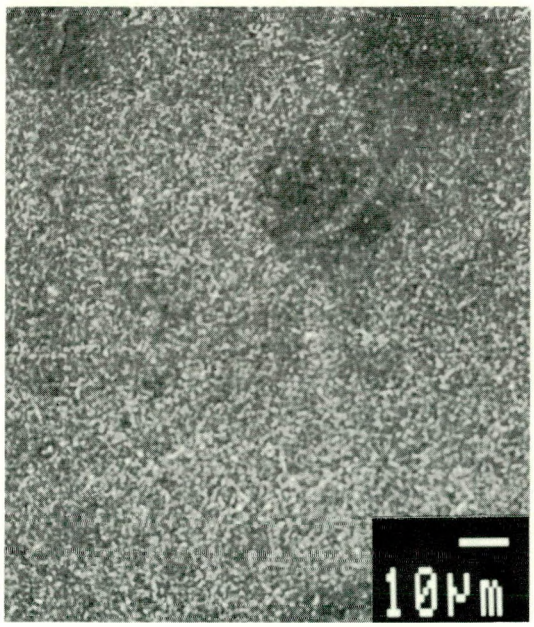

(c) Preoxidation and sulfidation

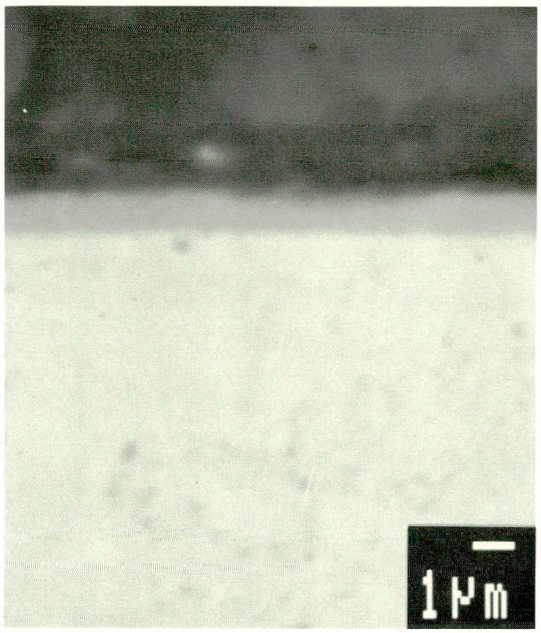

(d) X-section of (c) (BEI)

Fig. 96. Scale formed on Fe-25Cr-20Ni-1.5Al_2O_3 by preoxidation in gas mixture A, 700°C, 96h and later exposure to gas mixture B, 700°C, 48h.

The XPS (ESCA) results obtained by multiplexing/surveying combined with sputter profiling are illuminating. Carbon 1s peak was used as reference. The unsputtered surfaces had C and Si contamination; Si in the form of SiO_2. The elemental concentrations obtained at gas/scale interface using the appropriate sensitivity factors are (at.%): 5.08Fe-19.49Cr-1.13Ni-41.04O-1.69Si-0.15Al-31.41C. The peak positions and separations for Fe and Cr and the partitioning of O suggest that the scale is essentially Cr_2O_3 (79%), Fe_3O_4 (21%) and free Ni. The observed amounts of Cr_2O_3 and Fe_3O_4 in this case are just the reverse of the quantities observed in similarly exposed base alloy. After 60 min of sputtering the scale composition in at.% is: 12.72Fe-30.99Cr-1.96Ni-42.36O-11.97C. Besides Ni^0, the presence of Fe^0 and Cr^0 is deduced in otherwise predominantly Cr_2O_3 scale. At the end of an additional 45 min of sputtering (total 105 min) the scale composition shows increases in the levels of Fe, Cr and Ni and presence of unreacted Fe, Cr and Ni in addition to Cr_2O_3 (at.%) 14.91Fe-34.28Cr-2.24Ni-45.48O-2.89C.

The AES and XPS analyses confirm that the preformed oxide scale is essentially protective Cr_2O_3 throughout its depth in the case of Fe-25Cr-20Ni-1.5Al_2O_3. This is in contrast to the observation of predominantly Fe_3O_4 scale formed during preoxidation of the base alloy Fe-25Cr-20Ni.

The preformed Cr_2O_3 scale during preoxidation (700°C/96 h, $pO_2=1.13x10^{-20}$ atm) remains protective during the subsequent exposure to mixed gas at 700°C/48 h, $pO_2=1.17x10^{-20}$ and $pS_2=1.22x10^{-8}$, Figures 96c-d. The EDAX analysis shows the scale to be Cr_2O_3 and no sulfur was detected. Under similar conditions of exposures the base alloy undergoes significant breakdown of preformed oxide, Figures 94a-c. Further confirmation of the protective behavior of the preformed Cr_2O_3 scale in sulfur bearing atmosphere was obtained from the sputter SAM study of the scale. Auger spectra are obtained at locations from different depths: the unsputtered scale surface, 50, 100, 200 and 300 nm. Sulfur, carbon and silicon are detected only on the unsputtered surface, as surface contaminants. No sulfur is detected at any depth investigated nor at the scale/metal interface, Figure 96d.

4.9.6 (I/M) Fe-25Cr-6Al and Fe-25Cr-6Al-X Alloys

The formation of protective scale in Fe-25Cr-6Al and Fe-25Cr-6Al-X alloys at 700°C is very slow. Hence, preoxidation was performed not only at 700°C but at 1000°C for times up to 96 h. The preformed oxide scales at 700°C/96 h ($pO_2=1.13x10^{-20}$ atm) and 1000°C/48 h ($pO_2=1.97x10^{-14}$ atm) are shown in Figures 97a-d. The scale formed at lower temperature is very thin and EDAX analysis is not reliable. Auger spectra show the scale is Al rich and spots are Al-Cr rich. However, the scale formed at 1000°C/48h is essentially alumina.

The effect of minor additions is described with respect to Ce, Hf, Y and Pt. The behavior of La containing alloy is similar to that of Fe-25Cr-6Al-1Ce, and the scales formed on Fe-25Cr-6Al-3Si spall off forming flakes. Preformed oxide scales at 700° and 1000°C in 96 h on Ce, Hf, Pt and Y containing alloys are shown in Figures 98a-k. In all cases, except Fe-25Cr-6Al-1Pt, scales formed at both the temperatures have different morphology and composition along the substrate grain boundaries. Scales formed at 1000°C on the substrate grains are alumina, and at 700°C, the scales are mixed, Al_2O_3,and $(CrAl)_2O_3$. Relatively

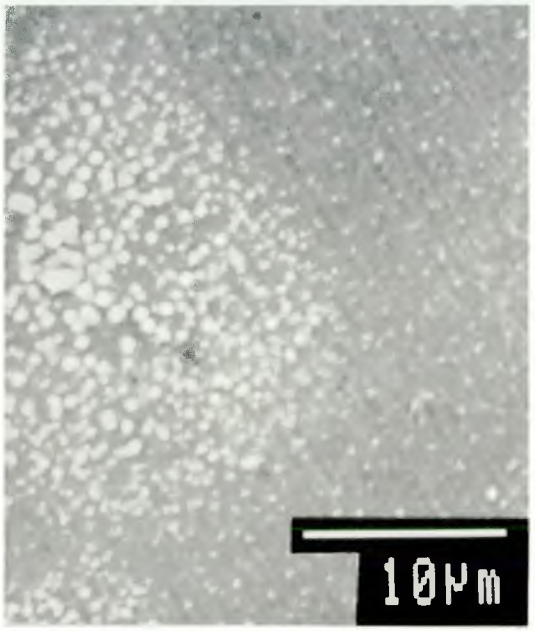

(a) A, 700°C, 96h

(b) X-section of (a) (BEI)

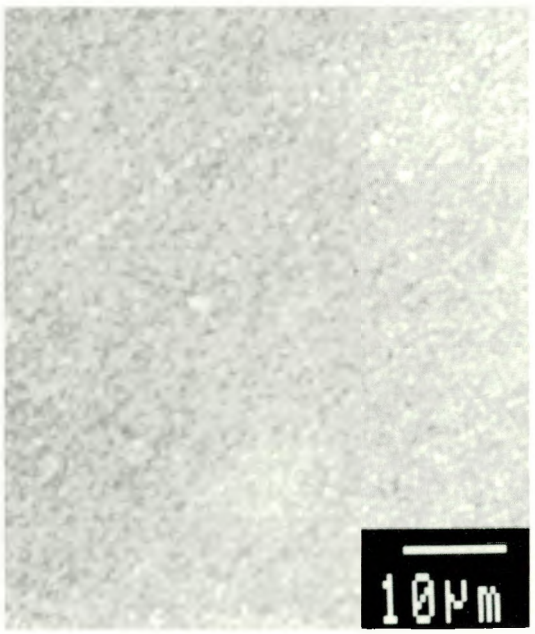

(c) G, 1000°C, 48h

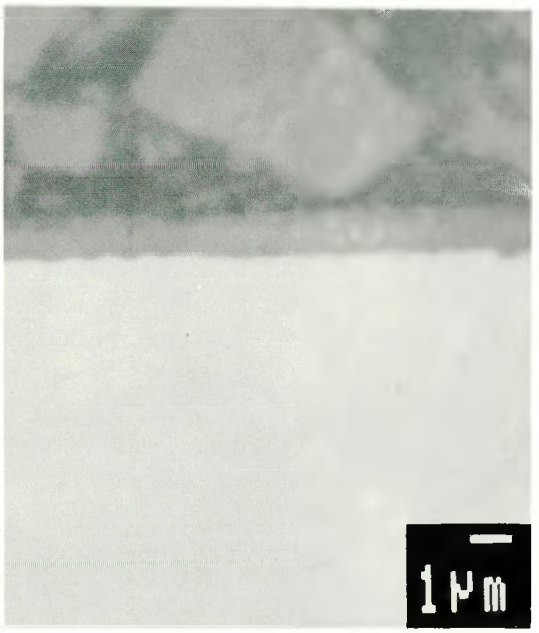

(d) X-section of (c) (BEI)

Fig. 97. Preoxidation of Fe-25Cr-6Al in gas mixture, A, 700°C or G, 1000°C.

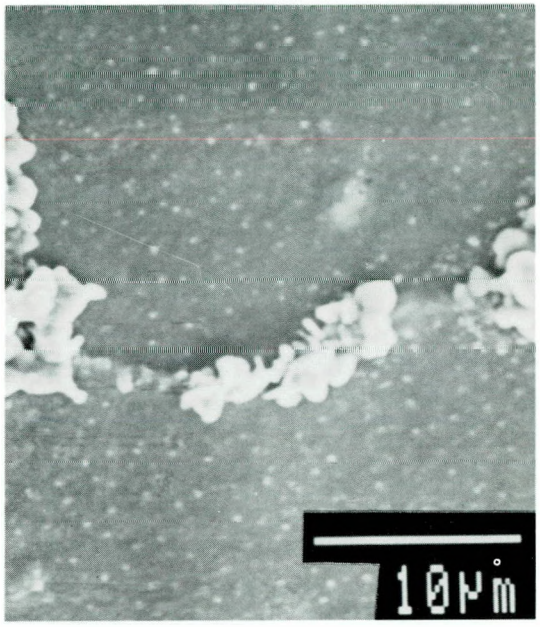

(a) Fe-25Cr6Al-1Ce, A

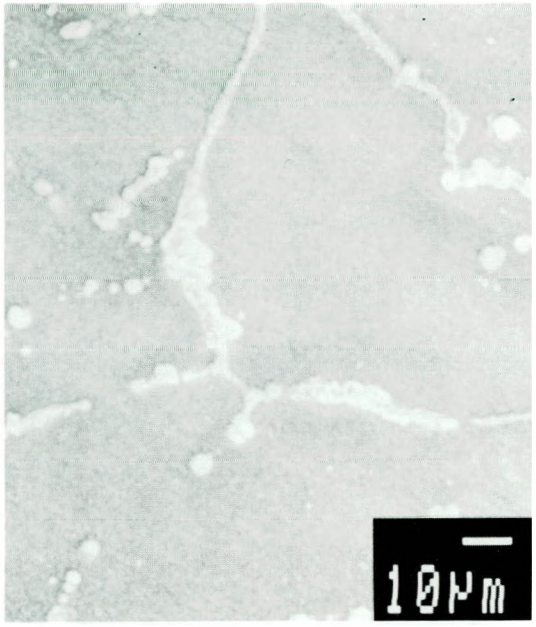

(b) Fe-25Cr-6Al-1Ce, G

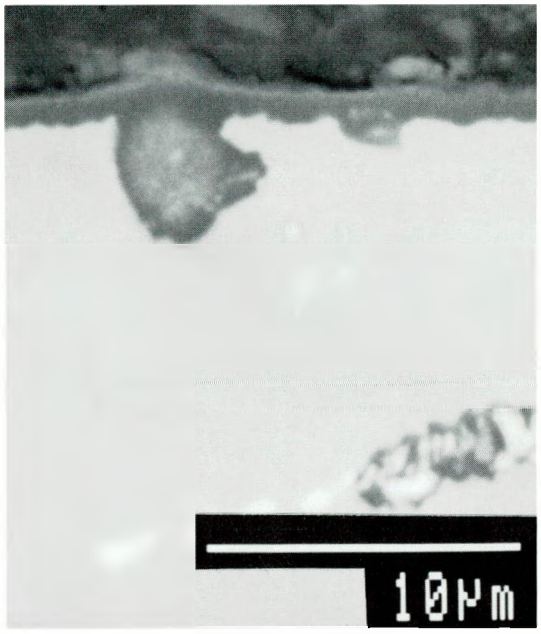

(c) X-section of (b) (BEI)

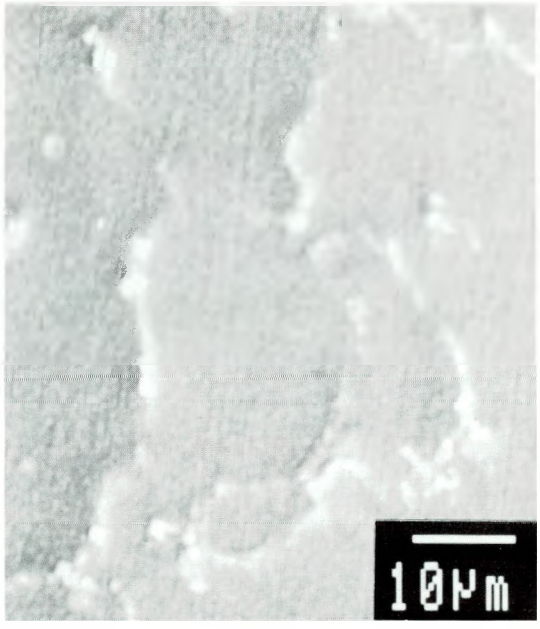

(d) Fe-25Cr-6Al-1Hf, A

Fig. 98. Preformed oxide scale in gas mixture A, 700°C, 96h or G, 1000°C, 48h.

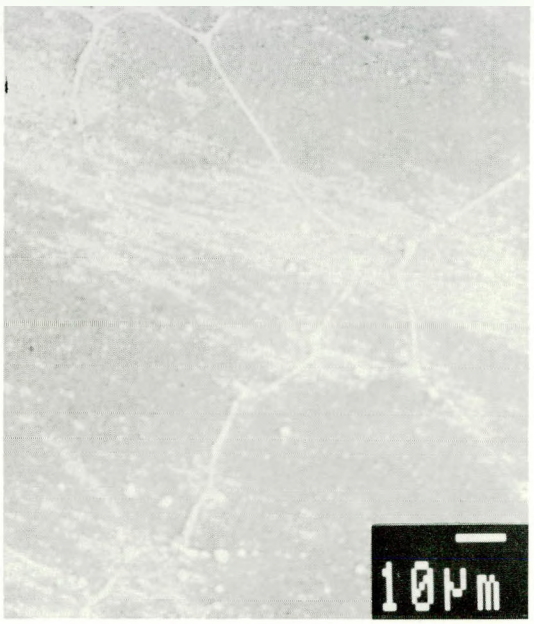

(e) Fe-25Cr-6Al-1Hf, G

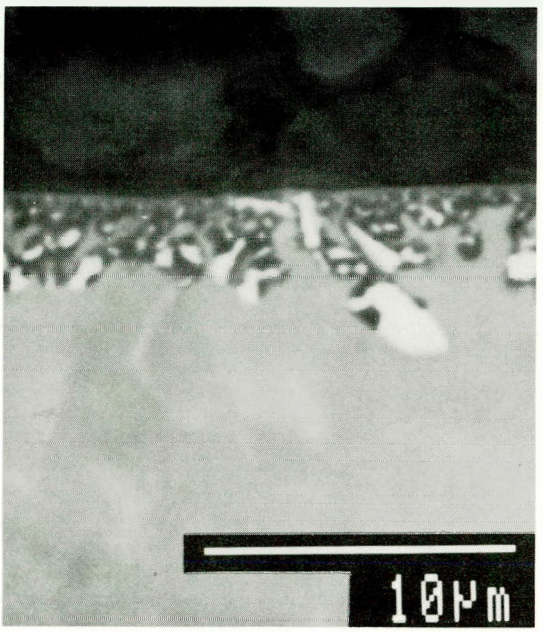

(f) X-section of (e) (BEI)

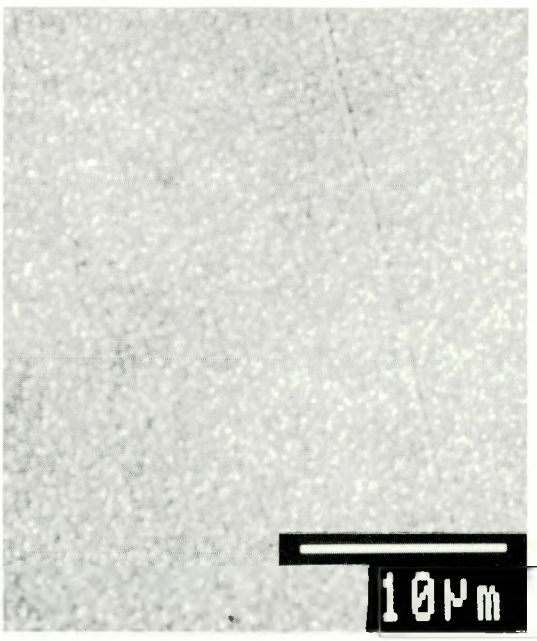

(g) Fe-25Cr-6Al-1Pt, A

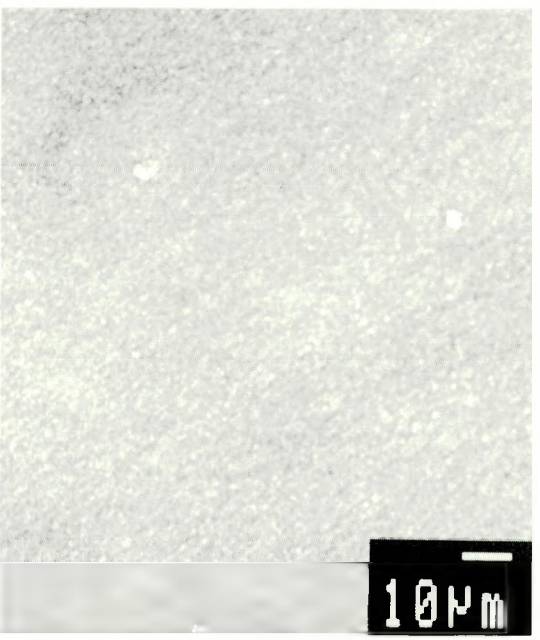

(h) Fe-25Cr-6Al-1Pt, G

Fig. 98 (cont'd.). Preformed oxide scale in gas mixture A, 700°C, 96h or G, 1000°C, 48h.

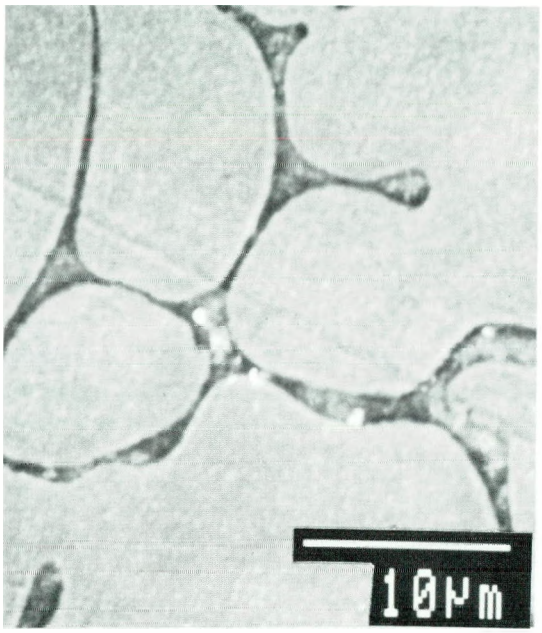

(i) Fe-25Cr-6Al-1Y, A

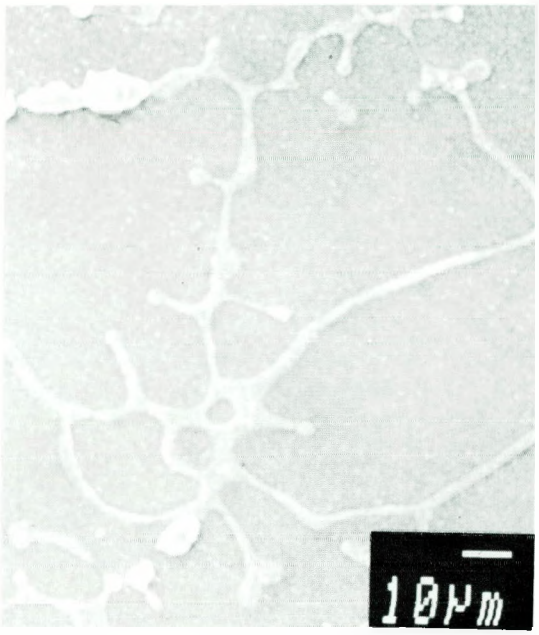

(j) Fe-25Cr-6Al-1Y, G

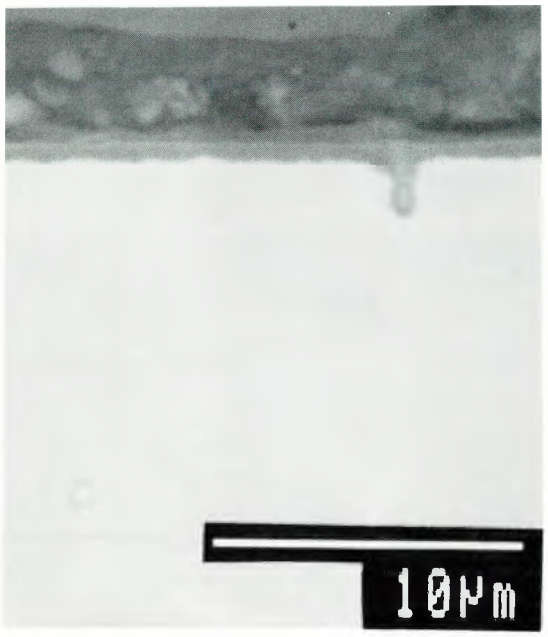

(k) X-section of (j) (BEI)

Fig. 98 (cont'd.). Preformed oxide scale in gas mixture A, 700°C, 96h or G, 1000°C, 48h.

more Ce, Hf, or Y is detected along the scale on the substrate grain boundaries. Oxide pegs are obvious in alloys with Ce, Hf, and Y.

On exposing the preformed oxide scales to mixed gas at 700° and 500°C, (gas mixtures B and F) sulfidation is observed in most of the alloys preferentially along the substrate grain boundaries. At first the results of exposure of preformed oxide scales at 1000°C or 700°C to mixed gas at 700°C for 96 h are presented. The preformed scales (alumina at 1000°C/96 h and alumina + $(CrAl)_2O_3$ at 700°C/96 h) on the base alloy remain unsulfidized, Figures 99a-b and 100a. No internal sulfidation or scale failure/separation is observed in Figure 99b. When preoxidation is done at 1000°C, (alumina scale thickness $\simeq$1 μ), subsequent exposure to mixed gas at 700°C for 96 h does not cause scale breakdown by local or global sulfidation in all alloys with microconstituents, Figures 99c-h. However, such resistance to sulfidation is not observed in the case of protective oxide scales preformed on alloys with Ce, La and Y additions at 700°C/96 h on subsequent exposure to mixed gas at 700°C/96 h, Figures 100b-d. Sulfidation under the above exposure condition proceeds locally along the substrate grain boundaries of alloys with Ce, La and Y, Figures 100b-d in the form of Fe rich sulfides. Ce or Y content of the sulfides is not much. On the other hand, alloys with Hf, Pt and Si retain the protectiveness of the preformed oxide scale during exposure to mixed gas at 700°C/96 h.

The morphology and appearance of scales that result from preoxidation at 700°C/96 h (pO_2=1.13x10^{-20} atm) and subsequent exposure to 500°C/96 h (pO_2=1.72x10^{-27} and pS_2=3.78x10^{-11} atm) do not differ much from that shown in Figure 99 and 100. But no preferential sulfidation of the scale along the substrate grain boundaries is observed even in alloys with La and Y. This observation differs from that made on the same alloys which are preoxidized similarly but exposed subsequently at 700°C/96 h.

The cold worked Fe-25Cr-6Al-0.3Hf exhibits similar behavior as that of annealed (hot rolled) alloy. No breakdown of preformed oxide scale (700°C/96 h, pO_2=1.13x10^{-20} atm) is observed on exposure to mixed gas at 700°C/96 h or 500°C/96 h. However, cold worked Fe-25Cr-6Al-0.3Y exhibits local breakdown of the preformed oxide scale (700°C/96 h, pO_2=1.13x10^{-20} atm) as shown in Figure 101a only on exposure to mixed gas at 700°C/96 h, not at 500°C/96 h, Figure 101b.

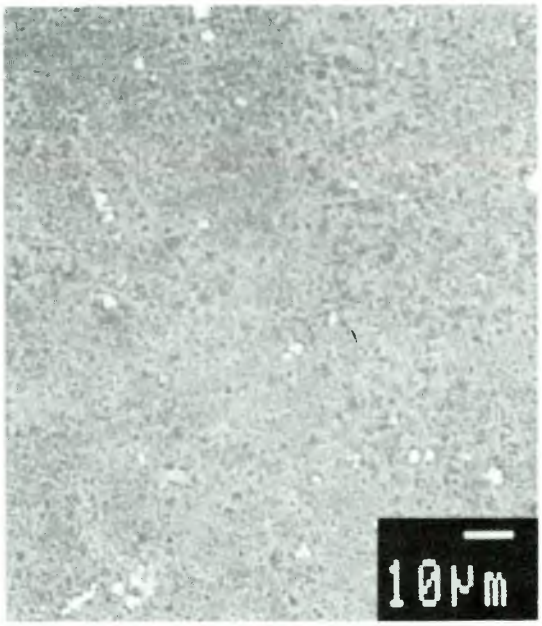

(a) Fe-25Cr-6Al

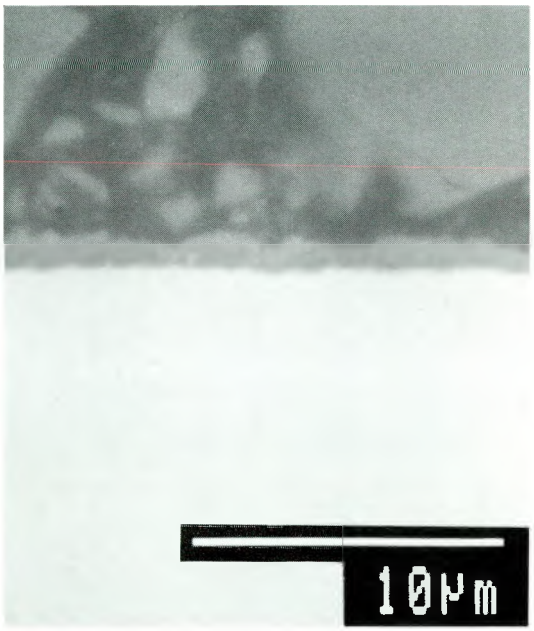

(b) X-section of (a) (BEI)

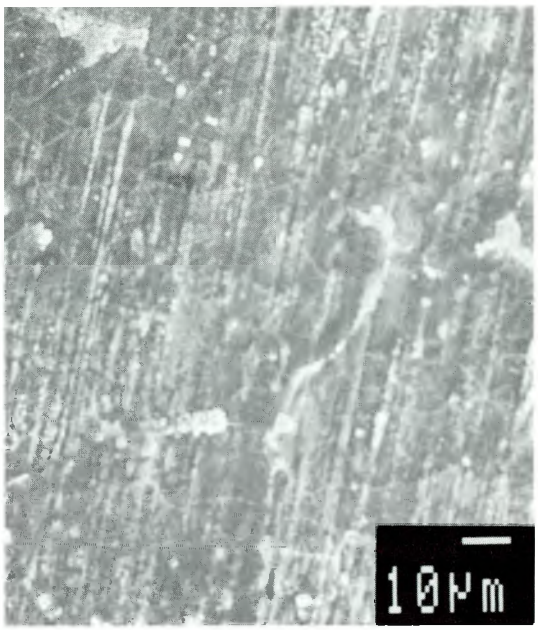

(c) Fe-25Cr-6Al-1Ce

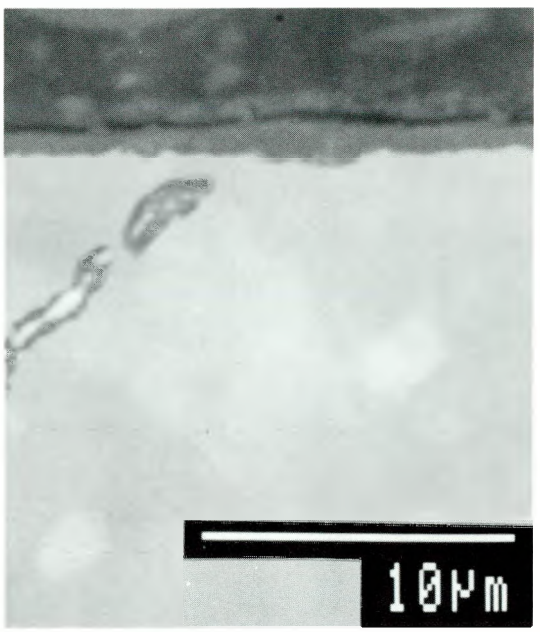

(d) X-section of (c) (BEI)

Fig. 99. Preoxidized in gas mixture G, 1000°C, 48h and exposed to gas mixture B, 700°C, 96h.

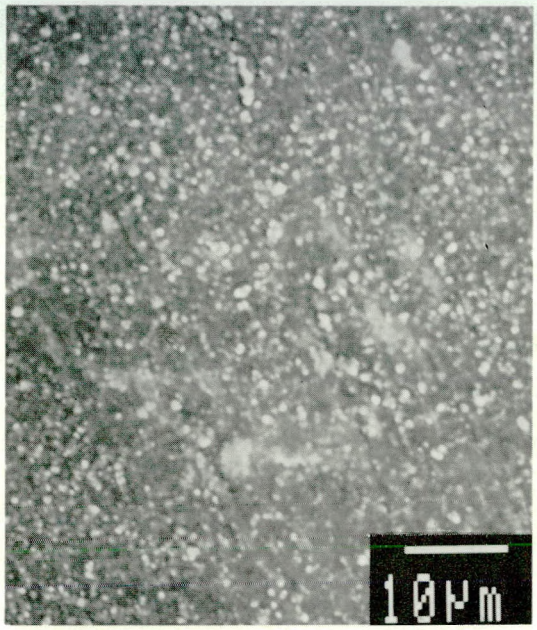

(e) Fe-25Cr-6Al-1Hf

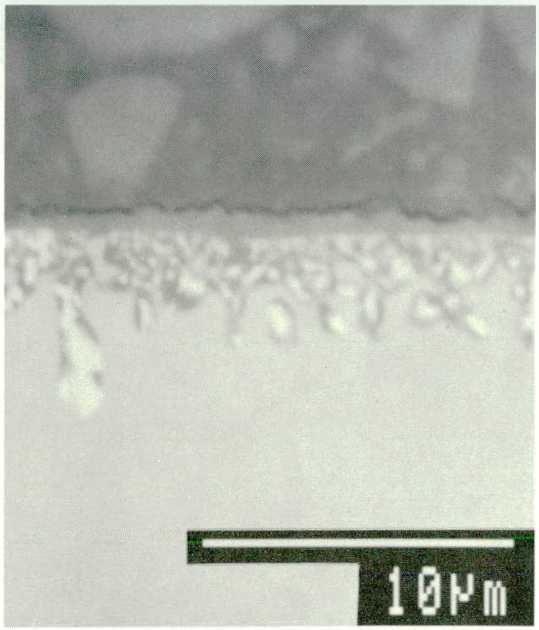

(f) X-section of (e) (BEI)

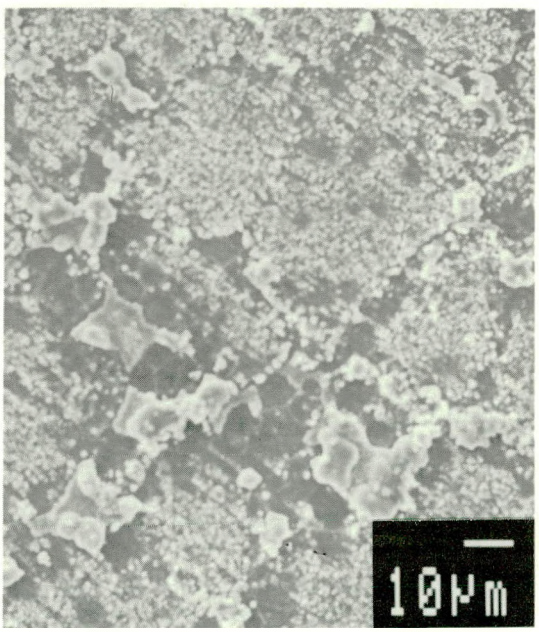

(g) Fe-25Cr-6Al-1Y

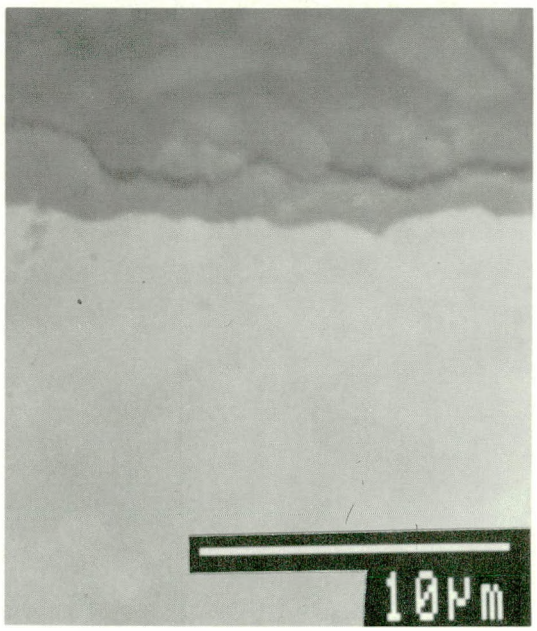

(h) X-section of (g) (BEI)

Fig. 99 (cont'd.). Preoxidized in gas mixture G, 1000°C, 48h and exposed to gas mixture B, 700°C, 96h.

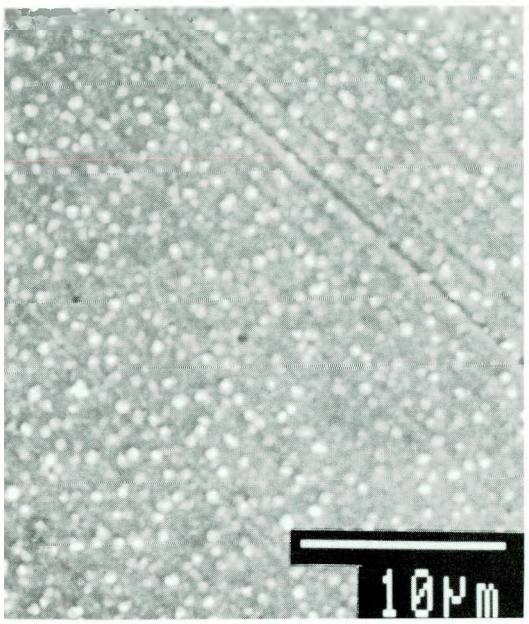

(a) Fe-25Cr-6Al

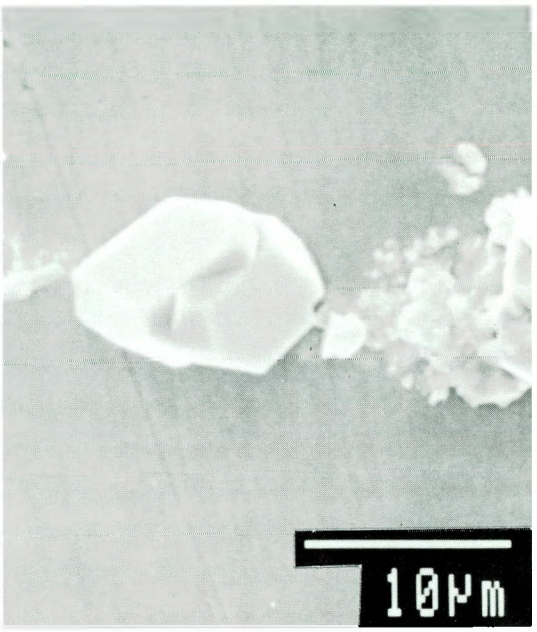

(b) Fe-25Cr-6Al-1Ce

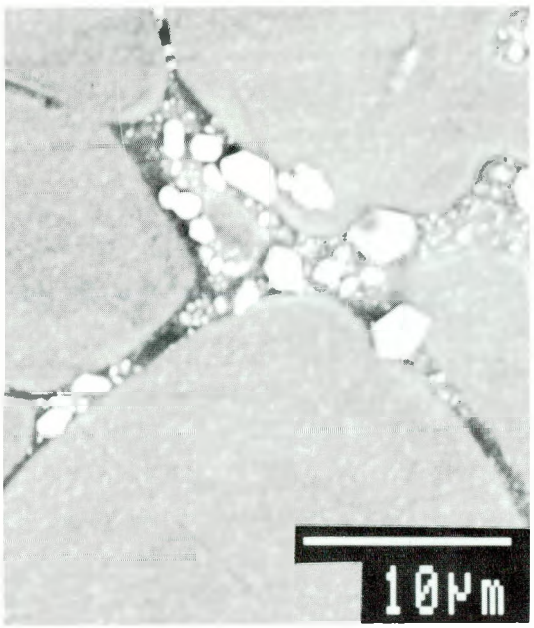

(c) Fe-25Cr-6Al-1Y

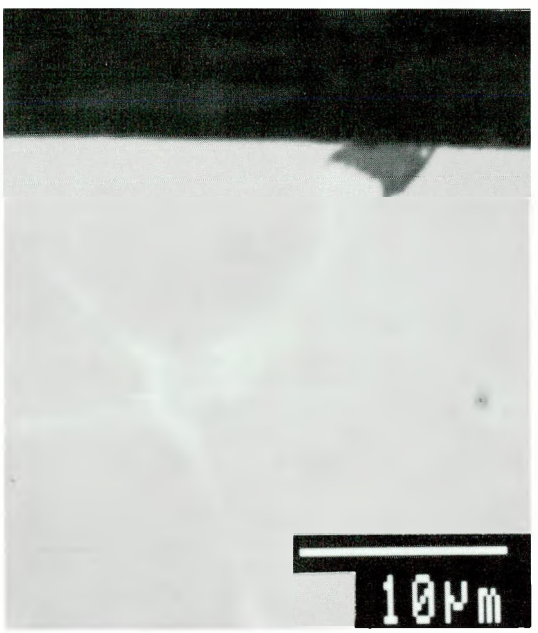

(d) X-section of (c) (BEI)

Fig. 100. Preoxidized in gas mixture A, 700°C, 96h and exposed to gas mixture B, 700°C, 96h.

(a) Gas mixture B, 700°C

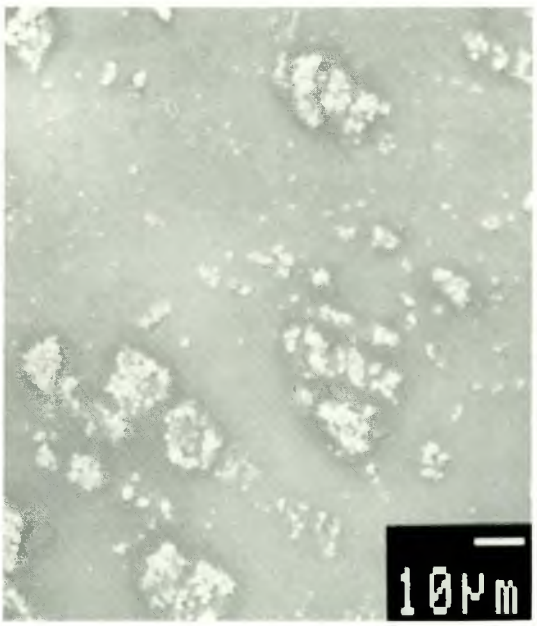

(b) Gas mixture, F, 500°C

Fig. 101. Cold rolled Fe-25Cr-6Al-0.3Y preoxidized in gas mixture A, 700°C, 96h and exposed to gas mixture B, 700°C or F, 500°C, 96h.

5.0 MECHANICAL PROPERTIES OF SCALES

Scales formed at 700°C are, in general, thin and approximately have thicknesses around or less than 1 μ. Consequently, a Nanoindentor was used to characterize the mechanical properties, particularly the Young Moduli of scales formed under different exposure conditions. The use of this mechanical property probe to characterize the mechanical properties of thin films and nanophase materials is well known [50,51]. No attempt was made to study fracture characteristics of scales because the dominant mode of scale breakdown appears to be chemical and occurs much earlier than the time the scales take to reach critical fracture stress. Hardness tests were also made on scales formed in mixed oxidant gases.

The indenter is a triangular pyramid shaped diamond with the same ratio of area-to-depth as that of Vickers pyramid. A typical test involves moving the indenter to the surface of the material at a controlled speed and measuring the forces and displacements continuously during the indentation process. A matrix of nine locations with sufficient separation was selected in most of the cases studied, and hardness/unloading characteristics were obtained at three depths, 50, 100 and 150 nm. A typical loading/unloading-displacement/depth curve is shown in Figure 102. The principle and details of calculations of hardness and Young's Modulus are given elsewhere [50,51].

Figure 103 is a typical hardness vs. depth relationship. Table 10 gives the E of scales along with exposure conditions. E is calculated from the slope of the compliance curve, dY/dP vs. 1/Y reciprocal of plastic depth, shown in Figure 104 and using a correction for machine compliance. The compliance, in turn, is obtained from the initial portion of the each unloading segment. It is assumed that during this period the indenter had maintained rigid contact with the substrate. The Young modulus values of thermally grown Cr_2O_3 and Al rich oxides at 700°C and Al_2O_3 at 1000°C are considerably less than the corresponding values obtained from respective single crystals. Robertson and Manning [52] quote 283 and 419 GPa for the Young moduli of single crystals Cr_2O_3 and Al_2O_3. Possible reasons for this difference is discussed later. In the present work scales were 1 μ or more in thickness, and the penetration depth of the nanoindentor was only up to 0.15 μ (150 nm). Thus the influence of the substrates is expected to be minimal on the values measured. Temperature and partial pressure of oxygen seem to influence the Young modulus of the thermally grown scales. The scales grown in the presence of S seem to have higher values for their Young moduli. Further work is required with more rigorous definition and analysis to make this kind of data statistically relevant and scientifically more meaningful.

Table 10. Young's moduli of scales formed under oxidizing and sulfidizing conditions.

Alloy	Sample/Exposure Condition	E (GPa)
Fe-25Cr	Polished	251
	Isothermal Oxidation, 700°C/120h, O_2	138
Fe-25Cr-1Y	Isothermal Oxidation, 700°C/120h, O_2	136
Fe-25Cr-20Ni-3Si	Preoxidation: 700°C/96h, $pO_2=1.13x10^{-20}$	77
	Preoxidation as above plus mixed gas exposure 700°C/48h, $pO_2=1.17x10^{-20}$ and $pS_2=1.22x10^{-8}$ atm.	123
	Mixed gas exposure, 700°C/96h, $pO_2=1.17x10^{-20}$ and $1.22x^{-8}$ atm.	162
Fe-25Cr-6Al	Polished	252
	Isothermal oxidation 700°C/120h/O_2	182
	Preoxidation, 1000°C/48h, $pO_2=1x10^{-14}$ atm.	104
	Preoxidation, 700°C/96h, $pO_2=1.13x10^{-20}$ atm.	147
	Preoxidation as above and mixed gas exposure at 700°C/96h, $pO_2=1.17x10^{-20}$ and $1.22x10^{-8}$ atm.	188
	Mixed gas exposure, $pO_2=1.17x10^{-20}$, $pS_2=1.22x10^{-8}$ 700°C/24h	154
	Mixed gas exposure, $pO_2=1.11x10^{-23}$, $pS_2=9.43x10^{-10}$ atm.; 600°C/48h	185*/145**
Fe-25Cr-6Al-1Y	Polished	280
	Mixed gas, $pO_2=1.17x10^{-20}$, $pO_2=1.22x10^{-8}$ atm. 700°C	145*/190**

* = Scale on substrate grains
** = Scale on substrate grain boundaries

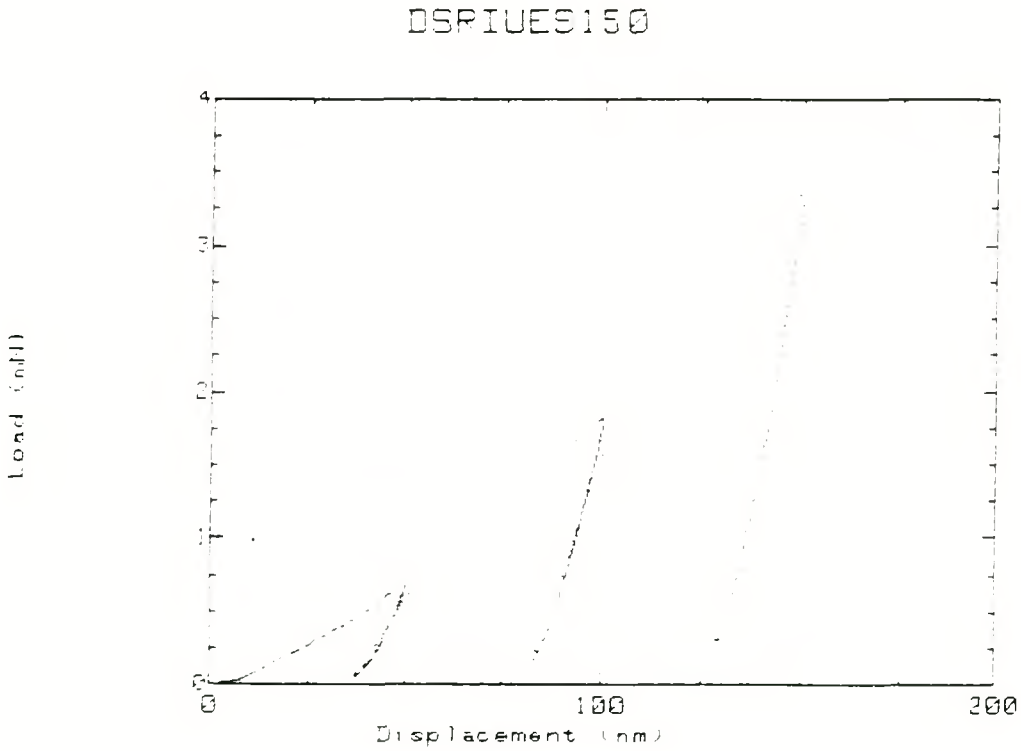

Fig. 102. Typical load-displacement plot with unloading segments in a Nanoindentor test.

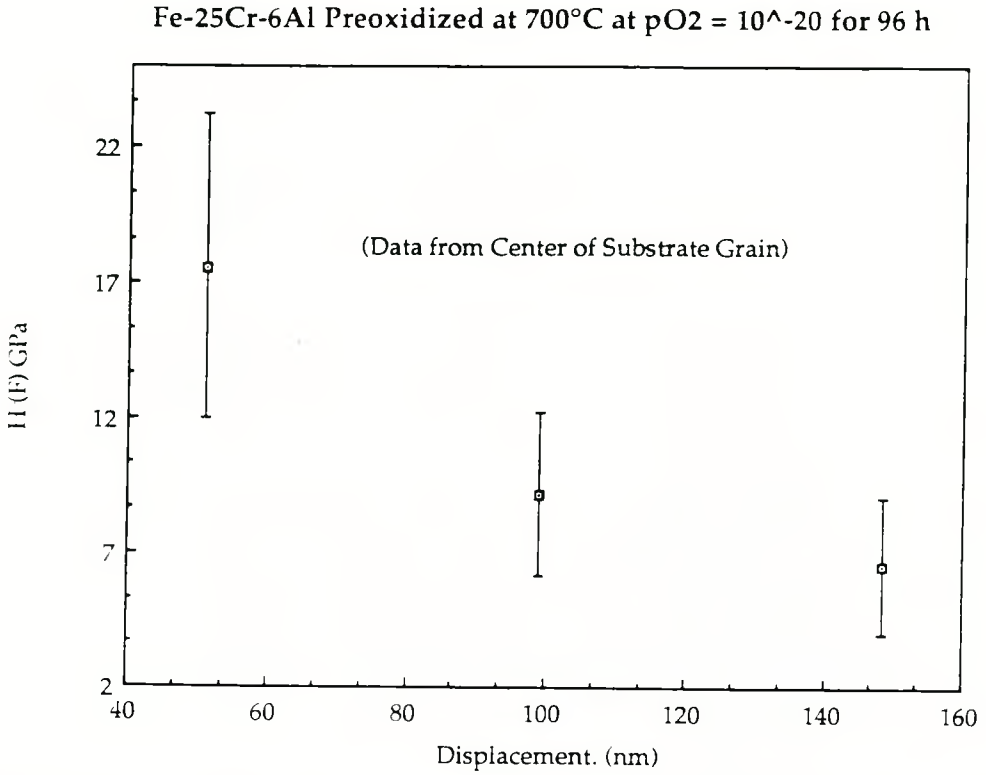

Fig. 103. Hardness vs depth for oxide formed in gas mixture A, 700°C, 96h.

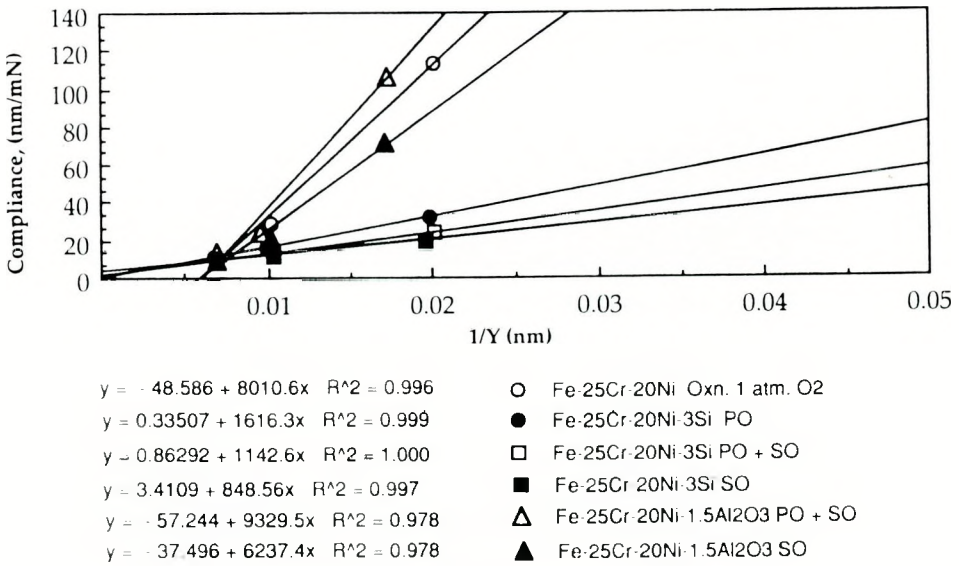

Fig. 104. Relationship between stiffness and reciprocal of displacement, PO=preoxidation in gas mixture A, 700°C, 96h; SO=exposure to gas mixture B, 700°C, 48h.

6.0 DISCUSSION

6.1 SELECTIVE OXIDATION AND FORMATION OF PROTECTIVE OXIDE SCALES

The formation and properties of protective oxides are influenced by the substrate chemistry and impurity contents. The effect of common alloying additions such as Mn is well documented [4]. Type 310SS does not form pure Cr_2O_3 because of the presence of Mn. In the present work controlled purity base Fe-25Cr, Fe-25Cr-20Ni and Fe-25Cr-6Al alloys and their derivatives with minor alloying additions are used to discern the possible effect of intentionally added minor elements. The commercial equivalents of these base alloys are AISI 446, Type 310 and the Kanthal-type Fe-25Cr-4Al. An increased Al content in FeCrAl was chosen here to increase the Al activities at the lower temperatures, 500°-700°C, investigated. Fe-25Cr and Fe-25Cr-6Al (their derivatives) are ferritic with BCC matrix, and Fe-25Cr-20Ni with and without minor additions are austenitic, FCC. Grain sizes of base alloys are large and no attempt was made to obtain same grain sizes in all the base alloys through any annealing treatment. However, grain size effects on selective oxidation become significant only at fine and ultra fine grain sizes [53]. The above three base alloys represent the two broad categories of chromia and alumina formers. Fe-25Cr and Fe-25Cr-20Ni have Cr>20 at.% to form chromia, and Fe-25Cr-6Al has sufficient Al (Eq. 1) to form alumina under appropriate oxidizing conditions.

The observations on the oxidation behavior in O_2 at 1 atm of the base alloys Fe-25Cr, Fe-25Cr-20Ni and Fe-25Cr-6Al provide a data base to understand the effects of the major alloying elements, Ni and Al, to Fe-25Cr.

Pure Cr_2O_3 scale forms on Fe-25Cr at and above 700°C. Its equilibrium dissociation pressure at 700°C is about 10^{-32} atm. Chromia scales form by outward diffusion of Cr^{3+} cations. In Cr_2O_3 the diffusion mechanism depends on the partial pressure of oxygen. At high pO_2, diffusion occurs through chromium vacancies, and at low pO_2, Cr interstitial defects are considered to be responsible for diffusion [54]. There is a chemical potential gradient of oxygen across the thermally grown Cr_2O_3. The chemical potential at the gas/scale interface is the ambient pressure of oxygen and that at the metal/scale interface corresponds to the Cr/Cr_2O_3 dissociation pressure. Consequently, the scale near the metal/scale interface will be n-type and it will exhibit p-type behavior at the outer part of the scale during oxidation at 1 atm. Thus there is a switch over from Cr-interstitial controlled diffusion of Cr^{3+} near the metal/scale interface to cation vacancy controlled diffusion of Cr^{3+} near the outer portion of the scale. Also possible is the short circuit diffusion through oxide grain boundaries. Oxidation of unalloyed Cr has been considered by several investigations and data have been summarized in Ref. 54. The estimated activation energy for oxidation is about 57 Kcal/mole. A similar activation energy, 58.2 Kcal/mole for oxidation of Ni-30Cr and Ni-30Cr-0.5Ti has been reported by Ramanarayanan et al. in the range 1000° to 1200°C [46]. A value of 46 Kcal/mole is estimated for Cr_2O_3 formation from the available literature data on Fe-Cr alloys [16]. The value of 40 Kcal/mole obtained in the present investigation is lower than the above reported values.

The data for Cr diffusion in Cr_2O_3 have been obtained under different experimental conditions using polycrystalline and single crystal of Cr_2O_3 [55-58], and the activation energy

varies from about 69 to 100 Kcal/mole. The lower value of activation energy is estimated using the data of Hagel and Seybolt [55] who made measurements on polycrystalline Cr_2O_3 with excess Cr near the decomposition pressure of Cr_2O_3. The available diffusion data thus do not lend themselves for direct comparison with the oxidation data. Further, the activation energy for oxidation is always less than that for bulk diffusion of scale-forming species through the scale. It is believed that Cr diffuses through grain boundary regions of the oxide through cation defects to form oxide predominantly at the gas/scale interface.

The formation of pure Cr_2O_3 scale on Fe-25Cr-20Ni is implicity assumed the relatively high Cr level. However, the presence of Ni and austenitic matrix make the scale no longer pure Cr_2O_3 and increases the Fe activity in the scale leading to the formation of Fe rich oxides particularly on the substrate grains. The Fe rich oxides observed on the substrate grains are Fe_2O_3, and $FeCr_2O_4$ ($Fe_{1+x}Cr_{2-x}O_4$) at 1 atm O_2. Interdiffusion of Cr in ferritic BCC Fe-25Cr is faster than in austenitic FCC Fe-25Cr-20Ni which has a close packed structure. Besides this crystallographic structure effect, Ni may have a chemical effect on the interdiffusion coefficient of Cr. However, fast diffusion of Cr still can occur along the alloy substrate grain boundaries and dislocation cores. This explains the observation of Cr rich scale on the substrate grain boundaries and Fe rich scales on the substrate grains in Fe-25Cr-20Ni. Initial cold working and ultra fine grains provide fast diffusion (short circuit) paths for Cr in the form of dislocations and increased grain boundaries respectively. Under both conditions the formation of Cr_2O_3 scale on Fe-25Cr-20Ni or Type 310SS is reported to be relatively fast [4,40,53]. The parabolic rate constant, k_p, for Fe-25Cr-20Ni is slightly higher than that of Fe-25Cr (Table 7). The activation energy for oxide scale formation is about 32 Kcal/mole, Table 8. The inhomogeneous nature of the scale precludes just one single element diffusion process, and, therefore, it is suggested that the activation energy obtained is most likely to be an effective activation energy associated with the diffusion of Fe^{2+} and Cr^{3+} in the oxide lattice.

In the gas mixture B with $pO_2=1.13x10^{-20}$ atm the scale formed is predominantly Fe_3O_4 as indicated by the present XPS study. Ni^0 (metal) is not detected in the scale. This Fe rich oxide is not protective in oxygen-sulfur atmospheres.

Addition of Al at levels 4-6% to Fe-25Cr changes totally the scaling behavior of Fe-25Cr from a chromia former to an alumina former. α-Al_2O_3 forms at temperatures above about 800°C, while at lower temperatures α-Al_2O_3 or $(CrAl)_2O_3$ forms [59]. Attempts to identify phases in the scale formed on Fe-25Cr-6Al at 700°C using glancing angle X-rays (Read camera) were not helpful. SAM analysis suggests oxide layers consisting of Cr, Al and O and Al and O. The kinetics of oxidation of this alloy is so slow at 700°C that a meaningful estimate of parabolic rate constant requires longer exposures. The reported value for the activation energy for alumina formation in Fe-Cr-Al is about 92.8 Kcal/mole [46], which is higher than the value reported for oxidation of Ni_3Al and NiAl, 70 Kcal/mole [60,61].

Lower weight gains at 700°C are observed in Fe-25Cr with volume addition of reactive elements, Ce, Hf, or Y. At 700°C scales remain essentially chromia, but the oxide surface grains seem to be smaller at the gas/scale interface, Figures 20 and 21. Bulk addition of Ce does not alter the basic scale morphology and composition. Oxide grains are equiaxed

in both Fe-25Cr and Fe-25Cr-1Ce, but there is a change in the grain size across the scale. The oxide grain size is fine near the metal/scale interface, and becomes coarser as the gas/scale interface is approached. Thus, Ce does not have any effect on the grain structure of Cr_2O_3, and Ce is present in the scale as a second phase, $CeCrO_3$, (Figure 19). However, Ce implantation promoted fine grain Cr_2O_3 with dispersed $CeCrO_3$ at 700°C and low pO_2 (gas mixture A), Figures 86a-b. These observations do not differ much from these made on MA 754 and Ce implanted Ni-30Cr at temperatures well above 700°C [24,46].
Y implantation, however, has an effect on the through thickness scale morphology in the case of Co-25Cr [30,31]: the oxide grain is fine near the outer scale and coarse adjacent to the metal. The reduction in the oxidation kinetics of Ce or Y containing Fe-25Cr at 700°C is not as marked as it is at higher temperatures [24,30,31,46,62-65]. The modest decrease in the kinetics observed here in the above alloys is attributed to decreased diffusion rate of Cr^{3+} due to doping of Cr_2O_3 grain and grain boundaries by Ce or Y [24,30,31,46]. Addition of Pt does not have any significant effect on the oxidation kinetics, Table 7.

Addition of Al_2O_3 dispersoids to Fe-25Cr has influenced the kinetics more than Ce or Y incorporation, and the oxidation kinetics is about 4 times less, Table 7. The scale is thin, and adherent, Figures 22 and 23. The scale is essentially Cr_2O_3, Table 9. The activation energy for oxidation of Al_2O_3 dispersed Fe-25Cr is 35.15 Kcal/mole which is close to that obtained for the base alloy, but significantly less than the values reported in literature [24,46]. Normally an increase in the activation energy is observed in chromia formers with reactive elements or oxide dispersoids, in contrast to alumina-formers where no change in the activation energy occurs [24,46]. The above observation of similar activation energy for both base and Al_2O_3 containing alloys suggests that the same activation process occurs in both alloys.

Several explanations in terms of the physical and mechanical effects of oxide dispersoids have been proposed to account for reduced kinetics and improved scale adherence. According to Giggins and Pettit [66] the dispersoids accumulate at the scale/metal interface and reduce the area of Cr_2O_3 available for Cr transport, but experiments show no strong dependence of oxidation rate on the volume fraction of dispersoids [67]. Stringer et al. [68] postulated increased nucleation sites contributed by the dispersoid with attendantly reduced Cr_2O_3 grain size. The smaller oxide grains eliminate dislocations that would otherwise provide short circuit paths for Cr diffusion and increase the grain boundaries for predominant anion O diffusion. However, oxide dispersions do not appear to reduce the grain size of Cr_2O_3 significantly [46]. Experimental observations seem to support the postulate that defect structure of Cr_2O_3 gets modified in the oxide dispersion strengthened alloys and in alloys with reactive elements in such a manner to reduce the kinetics [24,46,69]. Cr_2O_3 behaves like n-type oxide at low oxygen potentials, and at high oxygen partial pressure it exhibits p-type behavior [54]. Consequently, Cr_2O_3 scale at the metal/scale interface is n-type and p-type at the gas/scale interface (O_2 at 1 atm). Accordingly, the defect structure responsible for Cr^{3+} diffusion changes from $Cr_i^{\cdots}$ to $V_{Cr}^{'''}$. Doping trivalent oxides with elements like Y as a donor reduces chromium interstitials $Cr_i^{\cdots}$ at low oxygen potentials and increases $V_{Cr}^{'''}$ at high oxygen potentials. Such doping is not possible by Al^{3+} which has the same valence as Cr^{3+} and cannot be a donor. It is speculated that Al_2O_3 dissolves in Cr_2O_3 and the resultant Al^{3+} in oxide grains and grain boundaries reduces Cr^{3+} interstitials and diffusion. Once Cr^{3+} diffusion is reduced, O diffusion along the oxide grain boundaries becomes dominant,

reversing the scale growth direction. We note here that the recent observation of Park and Natesan [70] that Cr_2O_3 exhibits only p-type behavior is in variance with earlier observations [54].

In the case of Fe-25Cr-20Ni alloy the bulk addition of Hf or Pt seems to adversely affect the oxidation rate, Table 7. The effect of O implantation seems to be neutral. However, this alloy with implanted Si exhibits an order of magnitude lower oxidation rate. Incorporation of α-Al_2O_3 dispersoids in this alloy produces a similar effect on the oxidation behavior to that in Fe-25Cr. Scales are adherent and thinner, Figures 26, 28b and 31c. In all the above cases, oxidation was performed in O_2 at 1 atm at 700°C or above. Scales on Si implanted and Al_2O_3 containing Fe-25Cr-20Ni formed at 700°C under pO_2=1 atm and $1.13x10^{-20}$ atm are purely Cr_2O_3. Under thermal cycling Si implanted alloy significant scale spallation which is characteristic of Si containing alloy [71]. Scales are highly adherent in Fe-25Cr-20Ni-1.5Al_2O_3.

Reduction in the oxidation rates due to Si implantation is believed to be due to changes in the chemistry of the scale: from a scale consisting of Fe_2O_3 and $FeCr_2O_4$ on Fe-25Cr-20Ni to Cr_2O_3 rich scale on Si containing alloy and formation of thin SiO_2 layer. Further, Si is tetravalent and can dope trivalent Cr_2O_3 grains and grain boundaries as a donor. It eliminates $Cr_i^{\cdots}$ significantly, thereby reducing the Cr^{3+} diffusion near the metal/scale interface where the Cr_2O_3 exhibits n-type behavior because of very low pO_2 ($\simeq$ decomposition pressure). As a result, oxygen diffusion becomes dominant and scale growth occurs inwardly.

Fe-25Cr-20Ni is austenitic, and in this phase oxygen solubility and diffusivity are relatively high [72]. Further, the interdiffusion coefficient of Cr is low. This steel develops oxide scales with Fe_2O_3 and $FeCr_2O_4$ as the major components in pO_2=1 atm at 700°C. At the same temperature, but at low $pO_2=1.13x10^{-20}$ atm, the scale chemistry becomes predominantly Fe_3O_4. Addition of Si and Al_2O_3 brings about a total change in the scale chemistry, and promotes the formation of Cr_2O_3 under both conditions. It is speculated that Al_2O_3 addition decreases the oxygen solubility and diffusivity in the alloy and increases the interdiffusion coefficient of Cr. Once the Cr_2O_3 scale forms, the mechanism by which Al_2O_3 restrains the oxide growth is not clear. As discussed earlier, Al_2O_3 dissolves in Cr_2O_3 and reprecipitates in the oxide grain and grain boundaries blocking the outward diffusion of Cr^{3+}. Consequently, anion diffusion becomes rate controlling and inward scale growth results.

6.2 FORMATION AND BREAKDOWN OF PROTECTIVE OXIDE SCALES IN OXYGEN-SULFUR GAS MIXTURES

6.2.1 Thermochemical Stability of Corrosion Products

Scales are formed in, or preoxidized samples are exposed to, gas mixtures B to F. In these gas mixtures, Cr_2O_3, $NiS_y(l)$, $Ni_6S_5(s)$ and $FeS_{1+x}(s)$ are stable as shown in the thermochemical stability diagrams, Figures 105a-j. These ternary M-O-S diagrams are based on unit metal activity and do not consider the formation of spinels and solid solutions of compounds. These diagrams are used as guides to understand the stability regions of various reaction products. In reality, the oxide/sulfide boundaries get shifted toward higher oxygen

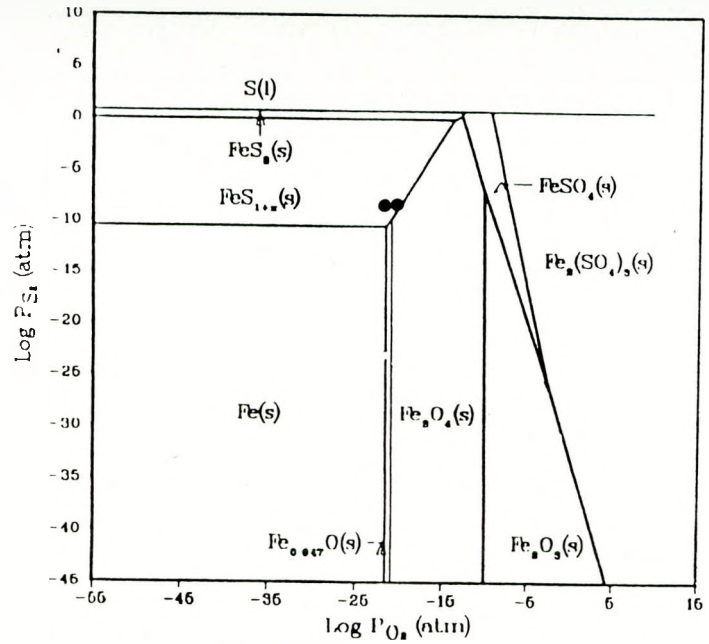

(a) Fe-O-S, 700°C

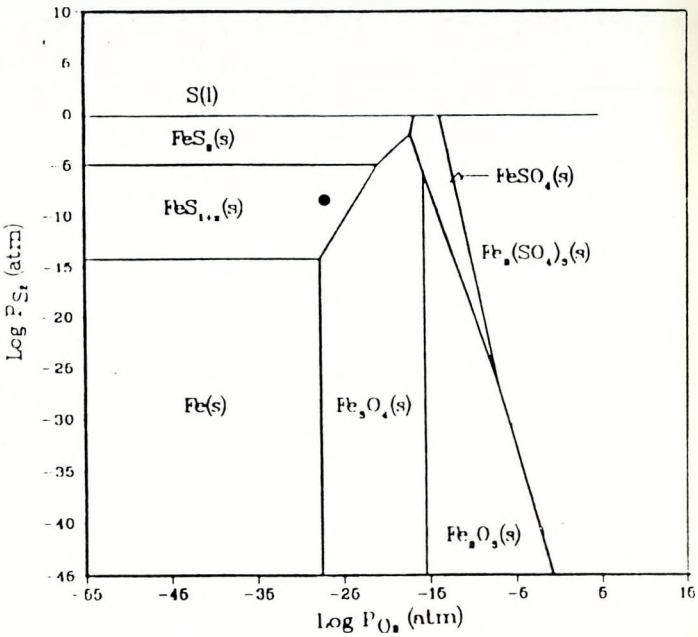

(b) Fe-O-S, 500°C

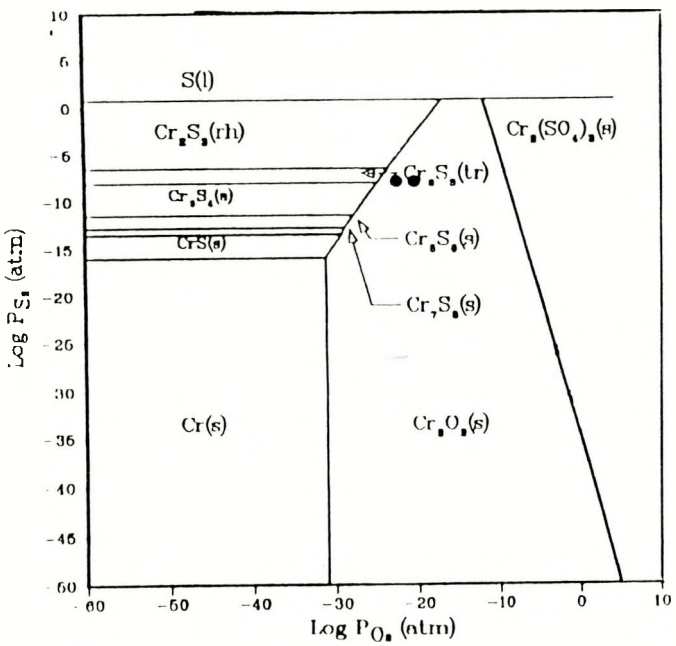

(c) Cr-O-S, 700°C

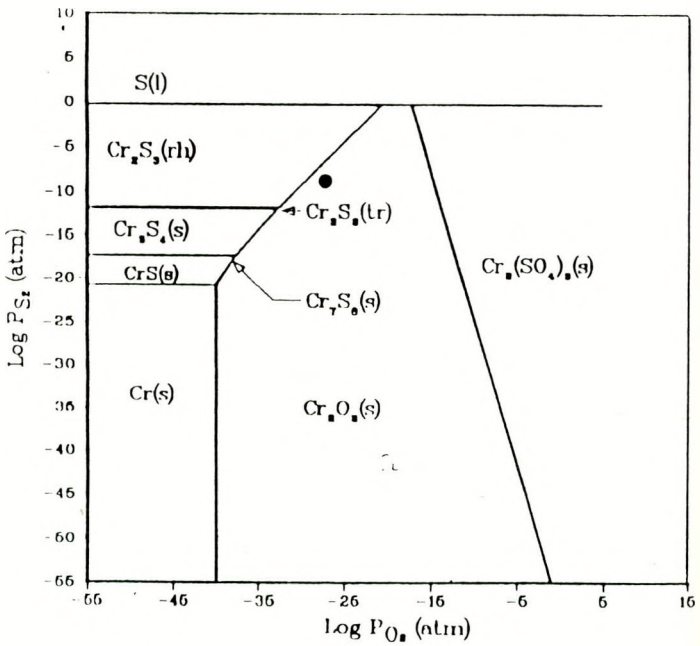

(d) Cr-O-S, 500°C

Fig. 105. Thermochemical stability diagrams.

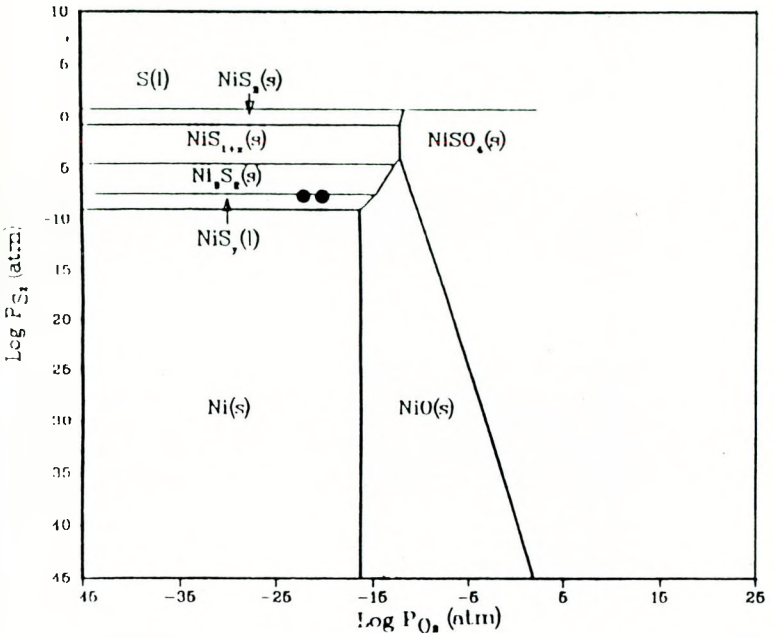

(e) Ni-O-S, 700°C

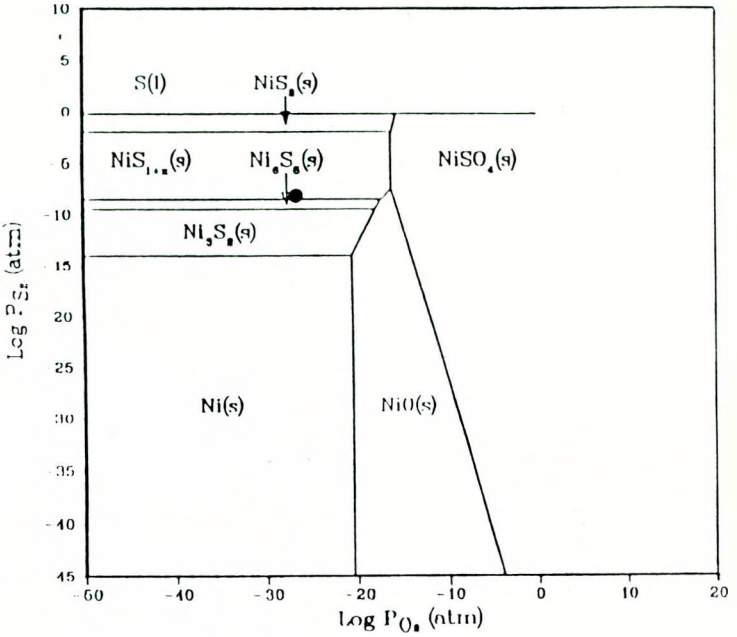

(f) Ni-O-S, 500°C

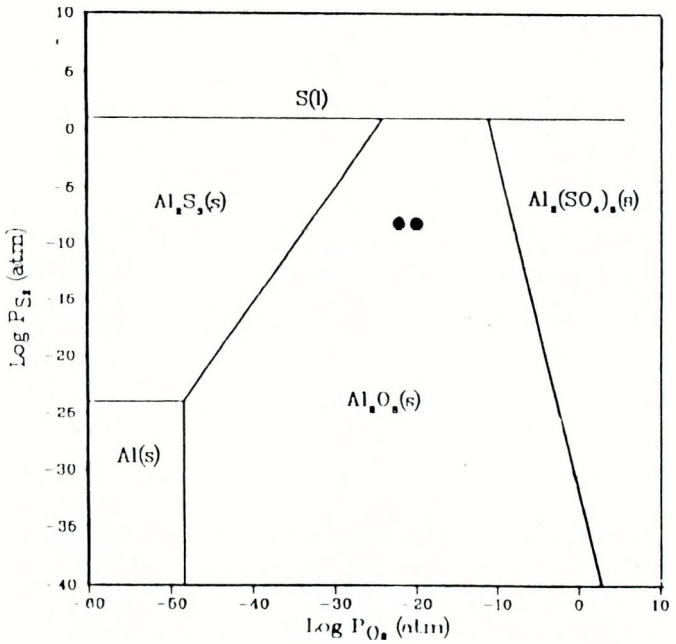

(g) Al-O-S, 700°C

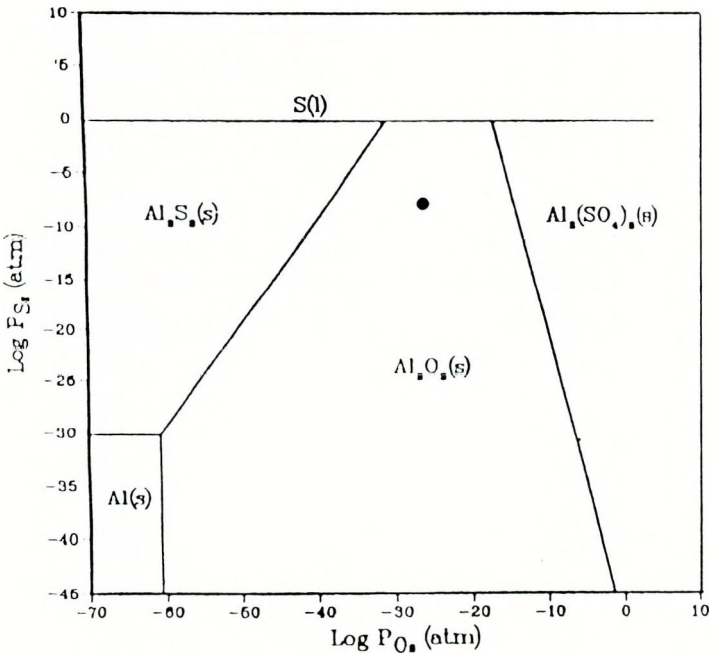

(h) Al-O-S, 500°C

Fig. 105 (cont'd.). Thermochemical stability diagrams.

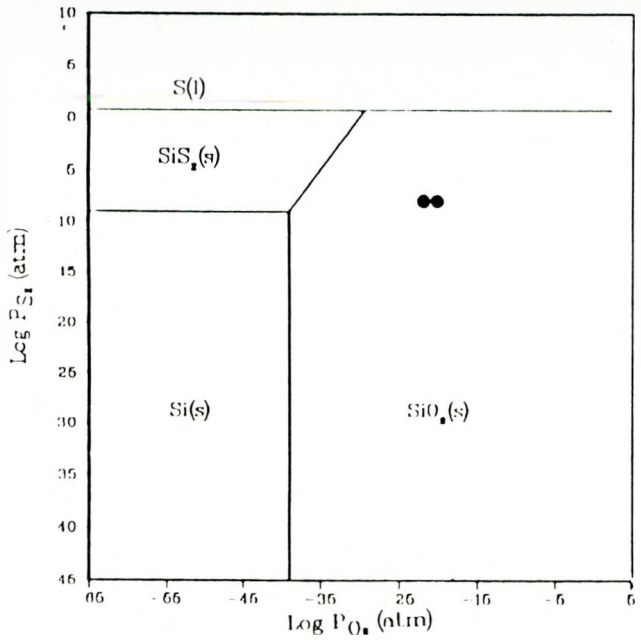

(i) Si-O-S, 700°C

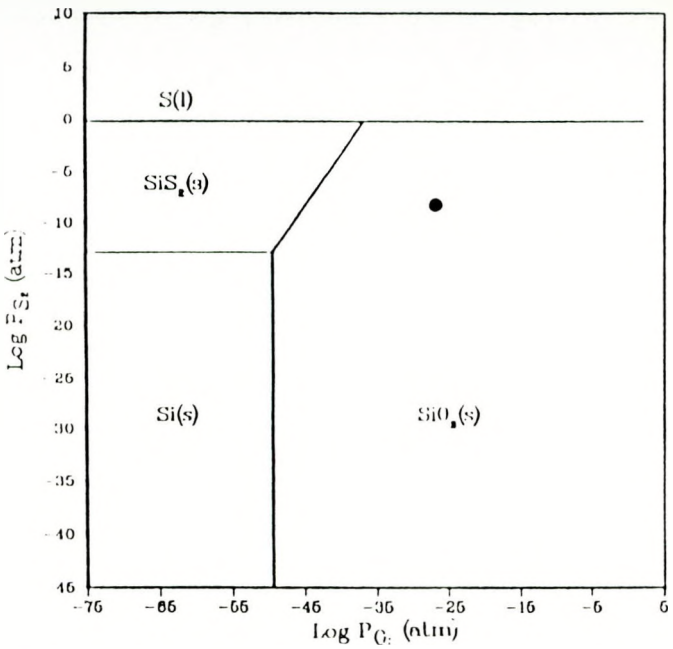

(j) Si-O-S, 500°C

Fig. 105 (cont'd.). Thermochemical stability diagrams.

potential because of kinetics, and this shift could be more than 3 orders of magnitude greater than the thermodynamic equilibrium pO_2 of "CrS"/Cr_2O_3 thermodynamic boundary. However, additions like Nb bring the kinetic boundary closer to the equilibrium oxide/sulfide thermodynamic boundary [1,2,42].

Rahmel et al. [36] considered the variation in the activities of Cr in Fe-Cr alloys and the formation of spinels and solid solutions of corrosion products in developing more realistic thermochemical stability diagrams for oxygen-sulfur atmospheres at 800°-1000°C. A section of their Fe-Cr-O-S phase diagram at 800°C reproduced in Figure 106. The Cr content of their Fe-Cr alloy (21 at.%) is slightly less than the Cr content of the base alloy Fe-25Cr (26.4 at.%) used here. Taking into account the possible shift in the thermodynamic boundaries due to a decrease in the temperature and the chemical potentials of various components, the equilibrium reaction products expected in gas mixture B are (CrFe)S and $Fe_{1+x}Cr_{2-x}O_4$ for Fe-25Cr.

Such improved condensed phase equilibria are not available for Fe-25Cr-20Ni and Fe-25Cr-6Al.

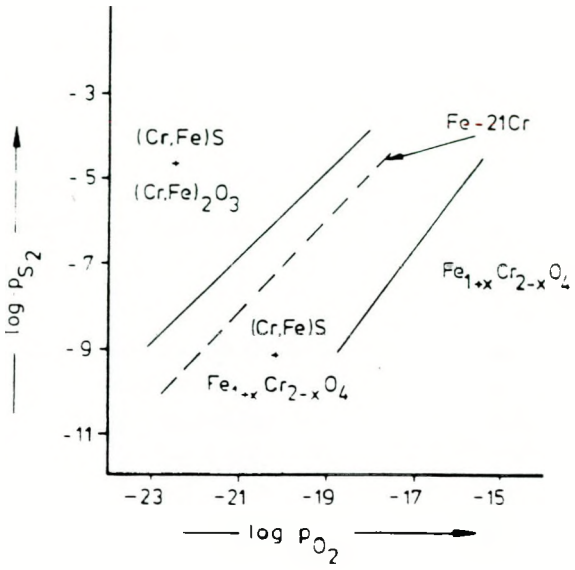

Fig. 106. Section of the Fe-Cr-O-S phase diagram at 800°C and 21 at.% Cr and the kinetic boundary for Fe-21 at.% Cr [36].

6.2.2 Effects of Microconstituent Additions and the Method of Incorporation

Initial conditions of the alloys and the manner of initiating the gas-metal reaction play an important role in determining the long term behavior. All alloys with bulk additions or implants had the same surface finish and were exposed to gas mixtures following the same procedure. However, the nature of native oxide film present on the samples may differ because of the difference in the alloy chemistry. The native oxide film is considered as part of the alloy and its effect, if any, on corrosion is considered as part of the substrate alloy effect. No attempt was made to characterize the corrosion (or oxidation) behavior of an alloy with and without this film.

All gas mixtures used in this investigation (Table 5) fall in the stability regions of Cr_2O_3 and Al_2O_3 to the right of "CrS"/Cr_2O_3 and Al_2S_3/A_2O_3 thermodynamic boundaries. FeS and Ni_3S_2 are also stable in these gas mixtures according to M-O-S (M=Fe, Cr or Al) phase equilibria diagrams. When the most realistic values for the activities of the alloying elements are taken, the experimental gas mixtures for Fe-Cr lie in the stability regions of (CrFe)S and $Fe_{1+x}Cr_{2-x}O_4$ [36].

The additives are grouped into three categories on the basis of their effects observed here on the corrosion behavior of Fe-25Cr-X and Fe-25Cr-20Ni-X alloys: elemental additives which include Ce, Hf, La, Pt and Y; oxide additive, Al_2O_3 and Si additive.

A uniform Cr_2O_3 scale forms quickly on Fe-25Cr-X alloys on exposure to gas mixture B at 700°C. Elemental additives seem to have no significant influence. The scale has small grains near the metal/scale interface and develops larger grains as it grows. Sulfides (Fe) and oxides nucleate initially, but oxide overgrows. Sulfur is detected below Cr_2O_3 in Fe-25Cr after 24 h exposure to gas mixture B. Similar observation has been made by Perkins et al. [4,40]. These sulfide nuclei do not apparently form sulfur channels leading to breakaway sulfidation. Several observations reported herein suggest that sulfidation begins at the gas/scale interface and works through inward locally. Cr and Fe enrichment in the scale occurs locally as shown in Auger elemental maps, Figures 43a-c. These are potential sites for the initiation of sulfidation. One such location where sulfidation has started is shown in Figure 43c. It is important and interesting to note that the general scale far away from such nodules or islands is purely Cr_2O_3 scale without any detectable Fe. The significance of this observation is discussed later. No sulfur is detected at the oxide/metal interface of the preoxidized samples. Therefore, the sulfur observed in Fe-25Cr and Ce implanted Fe-25Cr at the scale/metal interface is not due to surface segregation of native sulfur, but only represents possibly the remnants of sulfides formed initially which is later submerged. (FeCr)S forms on Fe containing Cr-rich oxide which is likely to be $Fe_{1+x}Cr_{2-x}O_4$, Figure 44b, as suggested by the phase stability diagram of Rahmel et al. [36]. O detected along (FeCr)S is either dissolved oxygen in (FeCr)S or due to interference/signal contribution from outside the nodule or sulfidation region. Far away from the sulfides the scale is Cr_2O_3 without any significant Fe but with Ce and S at the metal scale interface, Figure 44a. A similar local breakdown process is confirmed in preformed oxide scale on Fe-25Cr, Figures 78a-b. Locally (FeCr)S forms over $Fe_{1+x}Cr_{2-x}O_4$ scale in the oxide.

Formation of Cr rich sulfides on the surface of chromic oxide has been reported by Perkins, Coons and Vonk [4], Huang, et al. [73] and Rahmel et al. [36] in Fe-Cr-Ni, Ni-Cr and Fe-Cr alloys. Often this sulfide contains a significant amount of Fe when formed on Fe-base alloys. This requires transport of Fe and excess chromium through Cr_2O_3. The above investigators proposed Fe diffusion through Cr_2O_3 scale. Diffusion of Fe in Cr_2O_3 is faster than that of Cr. We did a few careful AES and XPS analyses of scales formed on Fe-25Cr and Fe-25Cr-1Y in gas mixtures A and B. The quantitative data are given in Tables 11 and 12 along with times of exposures. In these experiments, exposed samples were transferred to a Perkin-Elmer 560 multiprobe without exposing the reacted samples to laboratory atmosphere by means of "anoxic" transfer procedure. Both AES and XPS data indicated Cr_2O_3 formed on Fe-25Cr and Fe-25Cr-1Y during preoxidation with negligible or almost zero percent Fe. However, on exposure to oxygen-sulfur containing gas (mixture B) the Fe content in the scale is increased. The high value of Fe detected in the preformed oxide scale of Fe-25Cr-1Y is highly doubtful and no significance is attached because of limited data. S detected by AES appears to be due to surface impurities because it is removed, as observed by AES within a few nanometers of sputter removal. SIMs profiles of scale on Fe-25Cr-1Y after exposure to gas mixtures A and B, suggests Y accumulation at the metal/scale interface and Fe-enrichment at the outer part of the scale.

Table 11. AES data.

Alloy	Preoxidation Time (h) in Gas Mixture A, 700°C	Subsequent Exposure (h) Gas Mixture B, 700°C	Atomic Percentage						
			Cr	Fe	Ni	Al	O	C	S
Fe-25Cr	24	0	22.0	1.1	-	-	64.8	11.8	0.26
	29	1	17.1	4.9	-	-	55.8	16.6	5.7
	19	4	15.5	8.5	-	-	62.4	13.2	0.38
Fe-25Cr-1Y	24	0	17.0	7.5*	-	-	68.7	6.5	0.28
	29	1	21.6	1.0	-	-	62.0	12.2	3.2
	19	4	22.5	1.4	-	-	64.6	10.3	1.1
Fe-25Cr-20Ni	24	0	-	26.4	0.7	-	55.8	16.7	0.4
	29	1	-	22.3	6.9	-	41.7	17.0	12.1
	19	4	-	25.6	0.7	-	53.3	19.0	1.3
Fe-25Cr-6Al	24	0	-	1.0	-	25.7	62.5	10.5	0.3
	29	1	-	1.1	-	26.2	68.4	4.0	0.3
	19	4	-	3.5	-	27.1	63.7	5.6	0.3

*Error in measurement

Table 12. XPS data.

Alloy	Preoxidation in Gas Mixture A, 700°C, h	Subsequent Exposure to Gas Mixture B, 700°C, h	Atomic Percentage						
			Cr	Fe	Al	O	C	S	Si
Fe-25Cr	24	0	26.0	-	-	64.0	6.3	-	4.0
	24	48	24.0	1.8	-	59.0	10.0	-	3.6
Fe-25Cr-20Ni	4	0	trace	16.0	2.8	53.0	22.0	-	6.6
	4	0.25	1.0	20.0	(1-2)	53.0	16.0	2.4	6.2
Fe-25Cr-6Al	48	0	-	1.5	26.0	58.0	7.8	-	5.7
	48	48	-	0.8	30.0	58.0	9.8	-	4.9

The diffusion of S in polycrystalline Cr_2O_3 has been studied by Seybolt [74] and Chang, Nemoto and Wagner [75]. The diffusion rates vary from about $5x10^{-11}$ at 700°C to about $5.2x10^{-10}$ cm^2/sec at 1050°C. S requires, therefore, only about 200 sec to diffuse through a preformed oxide scale of 1 μ thickness to reach the metal/scale interface at 700°C. This process is most unlikely rate controlling in view of the earlier discussion. To explain "CrS" formation on preformed Cr_2O_3 in Cr, Romeo, Spacil and Pasko [76] proposed that sulfur enters the otherwise intact oxide as an electron donor and enhances the concentration of chromium vacancies and interstitials, thereby increasing Cr^{3+} diffusion in the scale. Excess Cr at the gas/scale interface reacts with S to form (CrS). However, a similar mechanism based on incorporation of an electron donor, Ce^{4+} or Y^{3+} in Cr_2O_3 has been proposed by Patibandla et al. [24] and Ramanarayanan et al. [46] to explain a decrease in Cr^{3+} diffusion and hence in oxidation kinetics in Ni-30Cr with Ce implants and MA 754. How different electron donors can bring about exactly opposite effects remains to be resolved by further work. Cr_2O_3 is a p-type semiconductor at high pO_2 and cation vacancies are responsible for Cr^{3+} diffusion. At low oxygen potentials, it exhibits n-type behavior where cation interstitials dominate and control Cr^{3+} diffusion. Similar defect mechanisms may be operative for Fe^{3+} diffusion also. The type of Cr_2O_3 behavior that is dominant in the presence of S is not clear. Based on our observations we propose that Fe^{3+} diffusion is initially enhanced in several local areas in the Cr_2O_3 scale either preformed or formed in oxygen-sulfur mixture by a "mechanism" similar to the one suggested by Romeo et al. [76]. The choice of these local areas is purely statistical and is not related to substrate grain boundaries or triple points. This diffusion process leads to the formation of $Fe_{1+x}Cr_{2-x}O_4$ phase under appropriate condition. Cr^{+3} diffusion occurs outward through this phase. When the Cr and Fe activities at the scale/gas interface reach a critical value, (CrFe)S forms which is thermodynamically stable in the gas mixture B. Subsequent sulfidation is most likely to occur at the interface between (CrFe)S and $Fe_{1+x}Cr_{2-x}O_4$ progressing downward. Once such channels are established, break-away corrosion begins. This will result in a scale microstructure as shown in Figures 38b-c.

Except for La and Y, other additives Ce, Hf and Pt are tetravalent. All of them can be electronic donors in Cr_2O_3 because of higher valency or larger ionic radius [60,76]. In spite of this, Cr^{3+} diffusion in Cr_2O_3 in the presence of S is not slow. The addition of the above elements may cause premature local sulfidation. Ce is present in Fe-25Cr-1Ce or Ce-implanted Fe-25Cr as Fe_7Ce. When this compound is consumed by oxidation, $CeCrO_3$ forms, releasing Fe. In fact, the oxide grains in the vicinity of such particles are rich in Fe, and this excess Fe soon forms local iron sulfides.

The Si containing alloy exhibits the most sulfidation resistance. This effect is believed to be due to formation of thin continuous SiO_2 layer below Cr rich oxide layer and to chemical influence of Si on interdiffusion coefficients and Fe activity in the scale. Adachi and Meier [71] suggested that SiO_2 formed during pure oxidation acts a diffusion barrier to Fe diffusion outward. However, further research is necessary to understand the Si influence.

Scale formation and breakdown processes in oxide dispersion strengthened Fe-25Cr are similar to that discussed above in the case of base Fe-25Cr. Finer grains of the alloy do not apparently have much influence on the chemistry of Cr_2O_3 scale, but are expected to result in finer oxide grains. No substantial improvement in the corrosion behavior of Fe-25Cr

has resulted by the addition of submicron Al_2O_3 dispersoids. This result is unexpected considering noticeable decrease in oxide or kinetics.

Fe-25Cr-20Ni which is a high purity form of commercial Type 310SS with and without the reactive elements exhibits the poorest sulfidation resistance. The oxide scale formed at low pO_2 (gas mixture) is not pure Cr_2O_3 but has Fe_3O_4 as the major component. This is also confirmed by "anoxic" transfer experiments described earlier, Tables 11 and 12. $Fe_{1+x}Cr_{2-x}O_4$ is likely to be present in the scale. Similar scales are expected to form initially in gas mixture B. Fe^{3+} diffusion is not necessary as it is postulated in the case of Cr_2O_3 scale breakdown. Cr^{3+} diffusion through the Fe rich oxides occurs leading to the formation of (CrFe)S which constitutes the faceted scale. Since sulfidation is fast in this alloy, local sulfidation could be seen even in samples exposed for less than 15 min. Ni diffuses out through (CrFe)S sulfides and nucleates Ni-containing sulfides (FeNi)S on the facets of (CrFe)S, Figures 47c and 49c. (FeNi)S is liquid at 700°C (melting point of NiS_y is about 635°C) and this slags the scale to cause fast and extensive scale breakdown. Although the reactive elements and Pt do not have any positive effect on the sulfidation resistance of Fe-25Cr-20Ni, they seem to influence Fe, Cr and Ni contents of the scale components: porous faceted and smooth (unbroken). The interdiffusion coefficient of Cr in this alloy is less compared to the oxidation rate and hence formation of interfacial voids at the metal/scale interface is common. [72] Additions of reactive elements have not eliminated the voids, Figure 47.

Fe-25Cr-20Ni with Si and α-Al_2O_3 dispersoids show remarkable improvements in their resistance to sulfidation by forming and maintaining protective scales in oxygen-sulfur atmospheres. The base alloy which sulfidizes rapidly in gas mixture B is able to remain unsulfidized up to the termination of the exposure, 200 h at 700°C. The mechanisms of improvement operative in Fe-25Cr-20Ni-3Si and Fe-25Cr-20Ni-1.5Al_2O_3 may differ in details.

Addition of α-Al_2O_3 to Fe-25Cr-20Ni alloy has completely changed the nature and character of the scale formed. Cr_2O_3 forms predominantly on Fe-25Cr-20Ni-1.5Al_2O_3 in contrast to Fe_3O_4 formed on the base alloy under similar condition. This type of change in the scale character requires an increased interdiffusion coefficient of Cr in the substrate comparable with the oxidation rate constant, and decreased in oxygen permeability in the substrate and Fe activity in the scale. Al_2O_3 dispersoids seem to accomplish the above. Absence of significant amount of interfacial voids at the metal/scale interface, Figure 56b lends support to the suggestion that α-Al_2O_3 dispersoids increase the interdiffusion coefficient of Cr. This oxide scale formed on Fe-25Cr-20Ni-1.5Al_2O_3 is more resistant to local scale breakdown than that on Fe-25Cr-1.5Al_2O_3 under cyclic conditions. The reason for the better behavior of scale formed on Fe-25Cr-20Ni-1.5Al_2O_3 is not clear. We did not observe the breakdown of the scale on this alloy and could not study extensively the breakdown of the Cr_2O_3 formed on Fe-25Cr-20Ni-1.5Al_2O_3. However, we propose in the following process: Eventually Fe^{3+} diffusion across the scale leads to the formation of $Fe_{1+x}Cr_{2-x}O_4$. Cr^{3+} diffusion through this spinel results in the formation of (CrFe)S at the gas/scale interface. The (CrFe)S grows inward and provides an easy diffusion path for Ni. (FeNi)S nucleate on the surface of the faceted (CrFe)S and slags the scale leading to breakaway corrosion at 700°C.

Si effect seems to be similar to that of Al_2O_3 effect on the corrosion behavior of Fe-25Cr-20Ni. Si promotes the formation and maintenance of Cr_2O_3 in oxygen-sulfur environment. We are able to detect Si below Cr_2O_3 by sputter AES and SAM. The scale is thinner, Figure 50d and the scale/metal interface is free from voids. Scale is adherent under cyclic conditions, but spallation is obvious under isothermal condition at 192 h, Figure 50c. The spallation has not led to sulfidation, and it appears that a healing layer always exists. We speculate that the breakdown process will be similar to that described for Al_2O_3 containing alloys.

For Fe-25Cr-6Al-X alloys the experimental gas mixtures fall in the stability regions of Al_2O_3 and FeS in their respective thermochemical stability diagrams of M-O-S where M=Al, Cr or Fe. We did some theoretical calculations for the formation of possible corrosion products in the Fe-Cr-Al system as a function of Al concentration at a constant Cr concentration of 25% [77]. The total concentrations include only the metallic components which might exist in any phase, such as oxide, other than the alloy solution, so long as the sum of Fe, Cr and Al remains 100%. Sulfur and oxygen are not included as part of the composition because their activities are kept constant, Table 5. For an example, the existence of an equal amount of FeS and Al_2O_3 results in 33% Fe, 67% Al and 0% Cr. It is to be noted that the composition of the scale exposed to the gas mixture can be quite different from that of the substrate; in the scale the Al and Cr concentrations should be significantly higher. A prediction of the corrosion products based only on the substrate composition, therefore, will be inadequate. The results of the thermodynamic calculation using SOLGASMIX are given in Table 13. Free energy values are taken from JANAF Thermochemical Tables. The presentation of compounds within the parenthesis, such as $(AlCr)_2O_3$ indicates mixtures with a second metal existing relatively as a minor component. The spinel phases are presented in the form $Fe_{1+x}Cr_{2-x}O_4$ to indicate possible deviation from stoichiometry. The calculations do not predict spinel sulfides at 500°, 600° and 700°C.

Fe-25Cr-6Al alloy is the most corrosion-resistant among three base alloys. The Al rich oxide scale forms and remains intact restricting the transport of reactants to form sulfides. Oxide scale formation in high oxygen activities is slow. α-Al_2O_3 forms in such alloys at temperatures above 900°C [59]. At temperatures 700°-850°C clear amorphous films and possible θ-Al_2O_3 have been reported [59]. The initial stage of scale formation is dictated by the crystallographic constraints. Scale formation is inhomogeneous initially. On some grains Al rich $(CrAl)_2O_3$ scales form, and on others two-layer scale forms with a mixture of $(CrAl)_2O_3$ and $Fe_{1+x}Cr_{2-x}O_4$ over $(CrAl)_2O_3$ when Fe-25Al-6Al exposed to gas mixture B for 24 h, Figures 58a-b. The scale is not pure Al_2O_3. No attempt was made to study the oxide grain size and distribution in detail since their insignificant role in breakdown process. It is believed that the oxide grains are equiaxed as reported in a similar alloy under purely oxidation condition [46]. The oxide scale formed in purely oxidizing gas mixture A seem to contain $(CrAl)_2O_3$ and Al rich oxide with less Fe than the scale formed in gas mixture B, and the spinel phase may not be present in the former. In our "anoxic" transfer experiments, more Fe was detected in preformed scale at longer times of exposure to oxygen-sulfur. The increase in Fe will help form the spinel $Fe_{1+x}Cr_{2-x}O_4$, and no mixed FeS is seen. The solubility of S in α-Al_2O_3, or $(CrAl)_2O_3$ is not known. However, S can enter the oxide scale

Table 13. Thermodynamic calculations by SOLGASMIX for the possible phase formations of Fe-Cr-Al in mixed gas where (Cr) = 25 wt.% at all times.

Composition	Temp. °C		
	700*	600*	500*
Fe-25Cr-0Al	FeS and $Fe_{1+x}Cr_{2-x}O_4$	FeS and $Fe_{1+x}Cr_{2-x}O_4$	FeS and $Fe_{1+x}Cr_{2-x}O_4$
Fe-25Cr-5Al	FeS $Fe_{1+x}Cr_{2-x}O_4$ Al_2O_3	FeS and $Fe_{1+x}(Cr,Al)_{2-x}O_4$	FeS and $Fe_{1+x}(Cr,Al)_{2-x}O_4$
Fe-25Cr-15Al		FeS and $Fe_{1+x}(Al,Cr)_{2-x}O_4$	FeS and $Fe_{1+x}(Al,Cr)_{2-x}O_4$
Fe-25Cr-30Al		$Fe_{1+x}(Al,Cr)_{2-x}O_4$ only	
Fe-25Cr-35Al		$Fe(Al,Cr)_2O_4$ and Al_2O_3	$Fe(Al,Cr)_2O_4$ and Al_2O_3
Fe-25Cr-50Al		$Fe(Cr,Al)_2O_4$ Al_2O_3	$Fe(Cr,Al)_2O_4$ Al_2O_3
Fe-25Cr-65Al	$FeCr_2O_4$ and $(Al,Cr)_2O_3$	$FeCr_2O_4$ and $(Al,Cr)_2O_3$	$FeCr_2O_4$ and $(Al,Cr)_2O_3$
25Cr-75Al	$(Al,Cr)_2O_3$ only	$(Al,Cr)_2O_3$ only	$(Al,Cr)_2O_3$ only

*For oxygen and sulfur activities see Table 5.

as an electron donor, but how S increases Fe diffusion is not clear. The scale $(CrAl)_2O_3$ appears to be resistant to corrosion and spallation.

Addition of reactive elements at levels of 0.3% or more leads to segregation of compounds containing them to the alloy grain boundaries. Although comparison of the X-ray diffraction pattern with available data suggest $Fe_{23}Y_6$ or $Fe_{17}Y_2$ in Fe-25Cr-6Al-1Y, the actual composition is likely to be $(FeCr)_4(AlY)$ [23,46]. Similar phases with Fe, Cr, Al and the added reactive element are possible in alloys with reactive elements. Pt is more soluble than the rare-earths, and hence segregation is virtually absent. Scale formation in gas mixture B on Fe-25Cr-6Al with reactive elements is similar on the substrate grains. The AES and SAM analysis show that the scale consists of $(CrAl)_2O_3$ at the outer part of the scale above Al-rich oxide at the metal/scale interface. The rare earth addition is not found in the scale. This is in agreement with the observation that the solubility of rare earth in alumina is very low [78]. Sulfidation preferentially occurs along the substrate grain boundaries at discrete locations. This type of scale breakdown is believed to occur in the following

sequence: the intermetallic segregant is rich in Fe and contains the reactive element. When the compound oxidizes, a significant amount of Fe is released, which reacts with S to form FeS. Similar explanation has been proposed by Kim and Meier for local sulfidation of Fe-18Cr-6Al-1Hf alloy [3].

Fe-25Cr-6Al with Si on Pt does not exhibit any sulfidation and the scale on the substrate grains and grain boundaries is uniform in composition and morphology.

Addition of reactive elements can retard sulfidation by maintaining adherent protective scale if the mechanical failure by spallation and cracking is responsible for sulfur transport to form sulfides in alloys without such additions. The reactive elements improve the scale plasticity particularly that of Al_2O_3 by promoting fine oxide grain sizes, thereby making the scale resistant to fracture. They also modify the scale defect structure to reduce Cr^{3+} diffusion in Cr_2O_3. Their effects on reducing Fe^{3+} diffusion in Cr_2O_3 scale or the formation of a barrier layer for Fe^{3+} diffusion are not well understood. In all the alloys studied here, the scale breakdown is brought about by chemical process. Sulfidation begins at the gas/scale interface when Fe and/or Cr attain critical values. Therefore, the improvement in scale adherence and plasticity are important, but not sufficient to improve sulfidation resistance of these alloys. Under these circumstances it requires that additives should form a barrier layer such as SiO_2 or Nb-oxide layer observed by Natesan and Park [42] in Nb-containing Fe-25Cr-20Ni and Fe-25Cr in oxygen-sulfur atmosphere or that they modify the defect structure to reduce diffusion of Fe^{3+} or Cr^{3+} in the scale as being postulated here. We have not seen any beneficial effects of reactive elements even at lower levels of addition, 0.3%. Positive effects of alumina dispersion and Si addition are believed to be due to formation of a barrier layer (SiO_2) near the metal/scale interface and restricted Fe^{3+} and Cr^{3+} diffusion in Cr_2O_3 by modification of scale defect structure. Both the above postulates need further careful study for their substantiation.

Implantation of various reactive elements in all three base alloys does not improve the sulfidation resistance. Recently Ce implantation in 800H has been shown to improve sulfidation resistance at 700°C [45]. The absence of such improvement in implanted base alloys is likely to be due to significant difference in alloy chemistry between the present alloys and 800H.

The absence of reactive element effect is likely to be due to lower test temperatures. Scale formation and breakdown processes are not influenced significantly. Local scale breakdown at the gas/scale interface leads to breakaway corrosion. Different sulfides form depending on the substrate composition.

6.2.3 Effect of Cold Work

Dislocations are generated in large numbers by cold work. They provide short circuit paths for Cr^{3+} or Al^{3+} diffusion to the surface. Cold worked alloys normally establish protective Cr_2O_3 or Al_2O_3 scales quickly. Cold working reduces or eliminates the formation of nonprotective transient oxides above their decomposition pressures, but does not influence the defect structure of protective scales. Since the maintenance of protective scale is not alone sufficient to avoid sulfidation, cold working per se will not be very effective.

Cold working has not changed the scale defects or chemistry of either the base alloys or alloys with Hf or Y significantly.

6.2.4 Effect of Oxidizing Conditions

It is interesting to note that even at the lowest oxygen $pO_2=1.18x10^{-22}$ atm in gas mixture D at 700°C scales remain intact without any internal sulfidation or interstitial voids in the case of Fe-25Cr-3Si, Fe-25Cr-1.5Al_2O_3, Fe-25Cr-20Ni-3Si and Fe-25Cr-6Al. Significant scale spallation in Fe-25Cr-20Ni-3Si (Figure 68j) does not lead to sulfidation whereas the same alloy without Si sulfidizes quickly even in a gas mixture with higher pO_2. Alloys with reactive element additions would not have resisted sulfidation as effectively as Si and alumina containing chromia formers, and base Fe-25Cr-6Al. It is believed that beneficial modification of scale defect structure by Al_2O_3 and Si with or without a barrier layer is responsible for the protective behavior of scales formed on Fe-25Cr and Fe-25Cr-20Ni with Al_2O_3 and Si. S in the atmosphere seems to have an effect on the Al_2O_3 scale growth. The scale grown on Fe-25Cr-6Al at 700°C, in gas mixture B ($pO_2=1.17x10^{-20}$ and $pS_2=1.22x10^{-8}$ atm) is considerably thinner than the scale grown at the same temperature in gas mixture D, $pO_2=1.18x10^{-22}$ and $pS_2=1.19x10^{-8}$ atm. It has been reported that the diffusivity of Cr^{3+} in Cr_2O_3 scale increases with the presence and the activity of S in the atmosphere. This observation has been explained by a model in which S enters the oxide as an electron donor, thereby increasing the concentration of cations vacancies and interstitials [77]. A similar mechanism is suggested here to explain thicker Al_2O_3 scale at higher pS_2 or H_2S/H_2O volume ratio. S enters Al_2O_3 as electron donor and increases Al^{3+} vacancies and interstitials which in turn increase the Al^{3+} diffusivity.

However, Fe-25Cr-20Ni-1.5Al_2O_3 has lost its ability to form and retain protective Cr_2O_3 scale at $pO_2=1.18x10^{-22}$ and $pS_2=1.19x10^{-8}$ atm. Apparently the oxide formation is very slow, and the Fe^{3+} diffusion fast at relatively high pS_2. Both processes lead to massive sulfidation.

6.2.5 Effect of Temperature

The same gas mixture, $H_2/H_2O/H_2S/Ar$, was used for tests at 500°, 600° and 700°C. Therefore, the chemical potentials of oxygen and sulfur decrease with decreasing test temperature. Further, their rates of decrease determined by reaction constant are different for oxygen and sulfur. The oxygen potential falls faster than the sulfur potential. The same mixture becomes more sulfidizing at 500°C. In addition, the sulfidation rate is faster by several orders than the oxidation rate at a given temperature. The above two factors explain the breakaway (global) corrosion of Fe-25Cr-X and Fe-25Cr-20Ni-X alloys at 500°C and localized limited sulifidation at 600° and 700°C.

A decrease in temperature also shifts the thermodynamic boundaries in thermochemical stability toward lower values of chemical potentials. This shift in the thermodynamic boundaries, together with corresponding decreases in the chemical potentials of oxygen and sulfur in the experimental gas mixture at lower temperatures, does not change the position significantly of the experimental partial pressures of oxygen and sulfur with respect to the thermodynamic "CrS"/Cr_2O_3 boundary. Cr_2O_3 and Al_2O_3 are stable in the test

gas mixtures at all temperatures. FeS and NiS are also stable in these test gas mixtures and lead to scale breakdown at 500° and 600°C. Protective oxide scales become more and more difficult to form at lower temperature because of decreasing pO_2, and their useful life depends on the rate of formation and the diffusion rate of Fe^{3+}. However, our observations indicate no significant difference in the formation and breakdown process of protective scales at lower temperatures.

6.2.6 Effect of Preoxidation

Preoxidation is recommended as a method of delaying substrate degradation by sulfidation [4,40]. It is used under specific circumstances in industries but has certain limitations. To be effective the preformed oxide should form a barrier for the transport of reactants in oxygen-sulfur atmosphere. More time is required for Fe^{3+} to build up a critical concentration if the scales are thick and the diffusion paths are long.

Preformed Al_2O_3 scales on Fe-18Cr-6Al-1Hf at 1150°C are less protective than that formed at 950°C [3] because of scale cracking at higher temperatures. Localized sulfidation starts by the transformation of HfO_2 pegs to Hf-rich sulfides which are easy paths for S and cations diffusion [3].

We also observed delayed sulfidation of preformed oxide scale, and this delay depends on the scale thickness. Addition of reactive elements has not extended the delay in any significant way, suggesting that any improvement brought about by the additives is not sufficient to delay the sulfidation significantly.

6.2.7 Mechanical Property of Scales

Stresses are generated during scale formation. Pilling and Bedworth attempted to relate stress generation to volume change when a metal gets converted to oxide. In the early stages the epitaxial relation between the substrate and the oxide decides the growth stresses. Later volume change that occurs within the scale or at the interface introduces stresses. In addition stresses are induced in the scale due to thermal expansion mismatch between the scale and the substrate. To accommodate these stresses the scale fails when the strain reaches critical value. This is one process of stress relaxation. Frequent failure will lead to depletion of Cr or Al in the substrate and eventually to the formation of nonprotective scales. Several stress relaxation processes are operative at high temperatures. At higher temperatures creep of oxide and the substrate and recrystallization of oxide will lead to stress relief. Mechanical properties such as Young's modulus, fracture toughness and strain determine the protective behavior of the scale.

Scales are thin in the present investigation at 700°C and below. The Nanoindentor method was used to obtain representative values for Young's moduli of scales grown under different conditions. The purpose was to identify if there is any unique relationship between Young's modulus value and the improved protectiveness of the scale. The Young moduli of thermally grown Cr_2O_3 and Al_2O_3 are not comparable with that of single crystal oxides, Table 10 and Ref. 52. The Young modulus of a solid is an intrinsic property and depends essentially on interatomic bonding and chemistry. It does not depend on heat treatment and

secondary working. Porosity in sintered products can decrease the value of Young's modulus. The effect of porosity on Young's modulus is described by the semiempirical formulae [79]

$$E = E_o (1-p)^3 \tag{9}$$

and

$$E = E_o \exp(-bp) \tag{10}$$

where E_o is the modulus of the fully dense solid, p is the volume concentration of porosity and b is a constant with a approximate value of 3. According to Birchall et al [80] small pores reduce the values of Young's modulus while large pores could act as flaws initiating premature fracture. Although the Young moduli, E values in Table 10 may not represent the absolute values of E of scales, they may still represent in a consistent manner the variation of E with the conditions of scale growth. This variation is speculated to reflect the changes in the scale chemistry and porosity. Further work is necessary to make the use of Nanoindentor and the results therefrom more meaningful.

7.0 CONCLUSIONS AND RECOMMENDATIONS

It is possible to control and maintain protective Cr_2O_3 scales by metallurgical means on Fe-25Cr-20Ni which otherwise rapidly sulfidizes in coal derived atmospheres. Additions that bring about a remarkable improvement in sulfidation resistance at 500°-700°C are alumina dispersoids and silicon. Besides alumina dispersoids and silicon, other additions outside the group of so-called reactive elements need be identified: Nb is an example [42]. A major requirement to assure the protectiveness of thermally grown Cr_2O_3 on Fe-base alloys in sulfur bearing atmospheres appears to be that the presence and ingress of Fe in the scale must be negligible. Si seems to form a thin silica layer preventing Fe diffusion through scale and modify the scale defects beneficially. The presence of alumina dispersoids promotes Cr_2O_3 formation by modifying several factors in Eq. 1 and reduces the Fe presence and diffusion in the scale by a mechanism that may involve dissolution of Al_2O_3 and reprecipitation of Al^{3+}.

Addition of Si is equally effective in Fe-25Cr in improving the protectiveness of Cr_2O_3 scale. However, the improvement brought about by the incorporation of alumina dispersoids in Fe-25Cr is not significant. A combination of factors such as variation in the crystal structure, interdiffusion coefficients and presence of Ni are considered to be responsible for the observed difference in the corrosion behavior of oxide dispersion strengthened Fe-25Cr and Fe-25Cr-20Ni alloys. It is believed that the mechanism of improvement in corrosion resistance associated with the addition of Si and Al_2O_3 dispersoids is different. Minor addition of reactive elements and Pt has no major influence on the corrosion behavior of chromia forming Fe-25Cr and Fe-25Cr-20Ni at 0.3 and 1.0% levels.

Fe-25Cr-6Al exhibits the most corrosion resistance among the alloys studied. However, addition of reactive elements and Pt at concentration levels, 0.3 and 1.0% has little added effect. At 1.0% level local sulfidation at the intermetallics compounds containing the reactive element may actually be encouraged. Even the effectiveness of smaller concentrations which avoid segregation remains to be established at 700°C and below because the REE decreases considerably with temperature. The oxide scale formed is not always α-Al_2O_3 under conditions investigated here.

Preoxidation can be used to delay sulfidation, but does not lead to oxide scales with greater long term resistance to sulfidation in the presence of sulfur. Within the scope of this work neither ion implantation nor cold rolling has shown any positive effect on sulfidation resistance.

Additional fundamental work is required to identify additions similar to Si, Nb and Al_2O_3 and to understand their common characteristics such as their influence on activities and interdiffusion coefficients of substrate elements in the alloy and the oxide scale, and on the defects structure of oxide in the presence and absence of sulfur in the atmosphere and the mechanism of improvement. Any future alloy development phase needs to consider the effect of lower additions of Si and the mechanical properties of alloys with Si, Nb and Al_2O_3. Presence of Si at levels of 2 or 3% in ferritic and austenitic steels does pose a major welding and joining problem, and methods of joining and welding such steels need to be evolved.

REFERENCES

1. T.C. Tiearney and K. Natesan, Oxid. Met., 17 (1982) 1.

2. D.J. Baxter and K. Natesan, Oxid. Met., 24 (1985) 331.

3. G.M. Kim and G.H. Meier, Breakdown Mechanisms of Preformed Al_2O_3, Cr_2O_3 and SiO_2 Scales in $H_2/H_2O/H_2S$ Environments at 950°C, ORNL/Sub/83-43346/01, (1988).

4. R.A. Perkins, W.C. Coons and S.J. Vonk, Materials Problems in Fluidized-Bed Combustion and Coal Gasification Systems, EPRI CS-2452 (1982).

5. C. Wagner, Z. Electrochem., 63 (1959) 772.

6. C. Wagner, J. Electrochem. Soc., 99 (1952) 369.

7. V. Srinivasan, A Review of the Effects of Microalloying, Surface Treatment and Oxidation Conditions on the Formation and Breakdown of Protective Oxide Scales on Fossil Energy Materials, ORNL/Sub/86-95901C/01 (1989).

8. S. Mrowec, T. Walec, and R. Werber, Oxid. Met., 1 (1969) 93.

9. J.E. Croll and G.R. Wallwork, Oxid. Met., 4 (1972) 121.

10. A.S. Khanna and B. Gnanamoorthy, Oxid. Met., 23 (1985) 17.

11. J.C. Langevoort, T.Fransen and P.J. Gellings, Oxid. Met., 21 (1984) 271.

12. I. Kvernes, Oxid. Met., 6 (1973) 45.

13. D.R. Baer and M.D. Merz, Met. Trans., 11A (1980) 1973.

14. C.P. Jensen, D.F. Mitchell and M.J. Graham, Corros. Sci., 22 (1982) 1125.

15. C.S. Giggins and F.S. Pettit, Trans. AIME, 245 (1969) 2495.

16. H. Hindam and D.P. Whittle, Oxid. Met., 18 (1982) 245.

17. C. Wagner, Corros. Sci., 5 (1965) 751.

18. O. Kubaschewski and T. Hopkins, Oxidation of Metals and Alloys, 2nd Edition, Butterworth, London, UK (1965).

19. F.A. Golightly, F.H. Stott, and G.C. Wood, J. Electrochem. Soc., 126 (1979) 1035.

20. J. Stringer, Met. Rev., 11 (1966) 13.

21. D.P. Whittle and J. Stringer, Phil. Trans. Roy. Soc., London, Series A, 295 (1980) 309.

22. J.K. Tien and F.S. Pettit, Met. Trans., 3 (1972) 1587.

23. T.A. Ramanarayanan, M. Raghavan and R. Petkovic-Luton, Oxid. Met., 22 (1984) 83.

24. N. Patibandla, R. Ayer and T.A. Ramanarayanan in Corrosion & Particle Erosion at High Temperatures, eds. V. Srinivasan and K. Vedula, TMS, Warrendale, PA, (1989) pp. 585.

25. H. Pfeiffer, Werks Korros., 8 (1957) 574.

26. J.E. McDonald and J.G. Eberhart, Trans. AIME, 233 (1965) 512.

27. A.W. Funkenbusch, J.G. Smeggil and N.S. Bornstein, Met. Trans., A16 (1985) 1164.

28. J.L. Smialek, Met. Trans., A18 (1987) 164.

29. C.L. Briant and K.L. Luthra, Met. Trans., 19A (1988) 2099.

30. K. Przybylski, A.J. Garrett-Reed and G.J. Yurek, J. Electrochem. Soc., 135 (1988) 509.

31. K. Przybylski and G.J. Yurek, J. Electrochem. Soc., 135 (1988) 517.

32. M.J. Bennett and A.T. Tuson, AERE Rep. R-13309 (1988) Harewell Laboratory, Didcot, UK.

33. J. Stringer, B.A. Wilcox and R.I. Jaffee, Oxid. Met., 5 (1972) 11.

34. I.G. Wright, B.A. Wilcox and J. Stringer, Oxid. Met., 9 (1975) 275.

35. K.T. Jacob, D. Bhogeswara Rao and H.G. Nelson, Oxid. Met., 13 (1979) 25.

36. A. Rahmel, M. Schorr, A. Velasco-Tellez and A. Pelton, Oxid. Met., 27 (1987) 199.

37. G.J. Yurek, M.H. LaBranche and Y.K. Kim in High Temperature Corrosion in Energy Systems, ed. M.F. Rothman, TMS Warrendale, PA (1985) 295.

38. K. Natesan and M.B. Delaplane in Corrosion-Erosion Behavior of Materials, ed. K. Natesan, TMS, Warrendale, PA (1979), pp. 1.

39. K. Natesan in High Temperature Corrosion, ed. R.A. Rapp, NACE, Houston, TX (1983) pp. 336.

40. R.A. Perkins and S.J. Vonk, Materials Problems in Fluidized-Bed Combustion Systems, EPRI FP-1280 (1979).

41. D.J. Baxter and K. Natesan, Corros. Sci., 26 (1986) 153.

42. K. Natesan and J-H. Park, in Corrosion & Particle Erosion at High Temperatures, eds. V. Srinivasan and K. Vedula, TMS, Warrendale, PA (1989) 49.

43. F.H. Stott, F.M.F. Chong and C.A. Stirling in High Temperature Corrosion in Energy Systems, ed. M.R. Rothman, TMS, Warrendale, PA, (1985) 253.

44. T.T. Huang, R. Richter, Y.L. Chang and E. Pfender, Met. Trans., 16A (1985) 2051.

45. R. Stroosnijder, Ph.D. Thesis (1990) Delft University, The Delft, The Netherlands.

46. T.A. Ramanarayanan, R. Ayer, R. Petkovic-Luton and D.R. Leta, Oxid. Met., 29 (1988) 445.

47. D.R. Gaskell, Introduction to Metallurgical Thermodynamics, McGraw-Hill Book Co., New York, NY, 2nd edition (1981) pp. 170, 586.

48. B. Pieraggi, Oxid. Met., 27 (1987) 177.

49. M. Levy, P. Farrell and F. Pettit, Corrosion, 42 (1986) 708.

50. J.V. Cathcart, Operating Instructions for the Mechanical Properties Microprobe, HTML/ORNL (1988).

51. M.F. Doerner and W.D. Nix, J. Mater. Res. Soc., 1 (1986) 601.

52. J. Robertson and M.I. Manning, Mater. Sci. Tech., 6 (1990) 81.

53. D.R. Baer and J.T. Prater, J. Vac. Sci. Technol., 20 (1982) 1396.

54. P. Kofsted, High Temperature Corrosion, Elsevier Applied Science, New York, NY, (1988) pp. 391.

55. W.C. Hagel and A.U. Seybolt, J. Electrochem. Soc., 108 (1961) 1146.

56. L.C. Walters and R.E. Grace, J. Appl. Phy., 36 (1965) 2331.

57. K. Hoshiho and N.L. Peterson, J. Am. Ceram. Soc., 66 (1983) C202.

58. A. Atkinson and R.I. Taylor, Harewell Report, AERE-R11313 (1984).

59. W.C. Hagel, Corrosion, 21 (1965) 316.

60. C.S. Giggins and F.S. Pettit, J. Electrochem. Soc., 118 (1971) 1782.

61. F.S. Pettit, Trans. AIME, 239 (1967) 1296.

62. T.N. Rhys-Jones, H.J. Grabke and H. Kudielka, Corros. Sci., 27 (1987) 49.

63. R.J. Hussey, P. Papaiacovou, J. Shen, D.F. Mitchell and M.J. Graham in Corrosion & Erosion at High Temperatures, eds. V. Srinivasan and K. Vedula, TMS, Warrendale, PA, (1989) pp. 567.

64. G.M. Ecer and G.H. Meier, Oxid. Met., 13 (1979) 159.

65. G.M. Ecer, R.B. Singh and G.H. Meier, Oxid. Met., 18 (1982) 55.

66. C.S. Giggins and F.S. Pettit, Met. Trans., 2 (1971) 1071.

67. I.G. Wright, B.A. Wilcox and R.I. Jaffee, Oxid. Met., 9 (1975) 275.

68. J. Stringer, B.A. Wilcox and R.I. Jaffee, Oxid. Met., 5 (1972) 11.

69. M.M. El-Aiat and F.A. Kroger, J. Am. Ceram. Soc., 65 (1982) 280.

70. J.H. Park and K. Natesan, Transport Properties of Thermally Grown Cr_2O_3, ANL/FE-89/5 (1989.

71. T. Adachi and G.H. Meier, Oxid. Met., 27 (1987) 347.

72. G. Hobby and G.C. Wood, Oxid. Met., 1 (1969) 23.

73. T.T. Huang, B. Peterson, D.A. Shores and E. Pfeuder, Corros. Sci., 24 (1984) 167.

74. A.U. Seybolt, Trans. AIME, 242 (1968) 752.

75. D.R. Chang, R. Nemoto and J.B. Wagner, Met. Trans., 7A (1976) 803.

76. G. Romeo, H.S. Spacil and W.J. Pasko, J. Electrochem. Soc., 122 (1975) 1329.

77. S.C. Kung and V. Srinivasan, Oxid. Met., 33 (1990) 481.

78. R.C. McCune, W.T. Donlon and R.C. Ku, Commun. Am. Ceram. Soc., 69 (1986) C196.

79. R.W. Rice, in Treatise in Materials Science and Technolgy, Vol. 11, ed. R.K. MacCrone, Academic Press, New York, NY, (1977) pp. 200.

80. J.D. Birchall, A.J. Howard, and K. Kendall, Nature, 289 (1981) 388.

APPENDIX A

DISTRIBUTION LIST

DISTRIBUTION

AIR PRODUCTS AND CHEMICALS
P.O. Box 538
Allentown, PA 18105
S. W. Dean
S. C. Weiner

ALBERTA RESEARCH COUNCIL
Oil Sands Research Department
P.O. Box 8330
Postal Station F
Edmonton, Alberta
Canada T6H5X2
L. G. S. Gray

ALLISON GAS TURBINE DIVISION
P.O. Box 420
Indianapolis, IN 46206-0420
P. Khandelwal (Speed Code W-5)
R. A. Wenglarz (Speed Code W-16)

ARGONNE NATIONAL LABORATORY
9700 S. Cass Avenue
Argonne, IL 60439
K. Natesan

ARGONNE NATIONAL LABORATORY-WEST
P.O. Box 2528
Idaho Falls, ID 83403-2528
S. P. Henslee

AVCO RESEARCH LABORATORY
2385 Revere Beach Parkway
Everett, MA 02149
R. J. Pollina

BABCOCK & WILCOX
1562 Beeson St.
Alliance, OH 44601
T. I. Johnson
T. Modrak

BABCOCK & WILCOX
Domestic Fossil Operations
20 South Van Buren Avenue
Barberton, OH 44023
M. Gold

BABCOCK & WILCOX
Lynchburg Research Center
P.O. Box 11165
Lynchburg, VA 24506
H. Moeller

BATTELLE-COLUMBUS LABORATORIES
505 King Avenue
Columbus, OH 43201
V. K. Sethi
I. G. Wright

BRITISH COAL CORPORATION
Coal Research Establishment
Stoke Orchard, Cheltenham
Glochester, England GL52 4RZ
M. Arnold
C. Bower
A. Twigg

BRITISH GAS CORPORATION
Westfield Development Centre
Cardenden, Fife
Scotland KY5OHP
J. E. Scott

BROOKHAVEN NATIONAL LABORATORY
Department of Applied Science
Upton, Long Island, NY 11973
T. E. O'Hare

CANADA CENTER FOR MINERAL & ENERGY TECHNOLOGY
568 Booth Street
Ottawa, Ontario
Canada K1A OG1
R. Winston Revie
Mahi Sahoo

CASE WESTERN RESERVE UNIVERSITY
Department of Metallurgy & Materials Science
516 White Bldg., 10900 Euclid Avenue
Cleveland, OH 44106
G. Michal
K. M. Vedula

COMBUSTION ENGINEERING
911 W. Main Street
Chattanooga, TN 37402
D. A. Canonico

CONSOLIDATION COAL COMPANY
4000 Brownsville Road
Library, PA 15129
S. Harding

ELECTRIC POWER RESEARCH INSTITUTE
P.O. Box 10412
3412 Hillview Avenue
Palo Alto, CA 94303
W. T. Bakker
R. L. S. Chang
J. T. Stringer
R. H. Wolk

EUROPEAN COMMUNITIES JOINT RESEARCH CENTRE
Petten Establishment
P.O. Box 2
1755 ZG Petten
The Netherlands
M. Van de Voorde

FOSTER WHEELER DEVELOPMENT CORPORATION
Materials Technology Department
John Blizard Research Center
12 Peach Tree Hill Road
Livingston, NJ 07039
J. L. Blough

AS RESEARCH INSTITUTE
8600 West Bryn Mawr Avenue
Chicago, IL 60631
H. S. Meyer

GENERAL ELECTRIC COMPANY
1 River Road, Bldg. 55, Room 115
Schenectady, NY 12345
R. W. Haskell

IDAHO NATIONAL ENGINEERING LABORATORY
P. O. Box 1625
Idaho Falls, ID 83415
D. W. Keefer

LAWRENCE BERKELEY LABORATORY
University of California
Berkeley, CA 94720
A. V. Levy

LAWRENCE LIVERMORE LABORATORY
P.O. Box 808, L-325
Livermore, CA 94550
W. A. Steele

MOBIL RESEARCH & DEVELOPMENT CORPORATION
P. O. Box 1026
Princeton, NJ 08540
R. C. Searles

NATIONAL INSTITUTE OF STANDARDS AND TECHNOLOGY
Materials Building
Gaithersburg, MD 20899
S. J. Dapkunas

NATIONAL MATERIALS ADVISORY BOARD
National Research Council
2101 Constitution Avenue
Washington, DC 20418
K. M. Zwilsky

NEW ENERGY DEVELOPMENT ORGANIZATION
Sunshine 60 Bldg.
P.O. Box 1151
1-1, Higashi-Ikebukuro 3-chrome
Toshima-Ku, Tokyo, 170
Japan
S. Ueda

OAK RIDGE NATIONAL LABORATORY
P.O. Box 2008
Oak Ridge, TN
P. T. Carlson
J. H. DeVan
R. R. Judkins
J. L. Langford (8 copies)

RISOE NATIONAL LABORATORY
P.O. Box 49
DK-4000
Roskilde, Denmark
Aksel Olsen

SHELL DEVELOPMENT COMPANY
P. O. Box 1380
Houston, TX 77251-1380
L. W. R. Dicks

SOUTHWEST RESEARCH INSTITUTE
6620 Culebra Road
P.O. Drawer 28510
San Antonio, TX 78284
F. F. Lyle, Jr.

TENNESSEE VALLEY AUTHORITY
Energy Demonstration & Technology
MR 2N58A
Chattanooga, TN 37402-2801
C. M. Huang

TENNESSEE VALLEY AUTHORITY
1101 Market Street
MR 3N57A
Chattanooga, TN 37402
R. Q. Vincent

TEXAS EASTERN TRANSMISSION CORPORATION
P.O. Box 2521
Houston, TX 77252
D. H. France

THE MATERIALS PROPERTIES COUNCIL, INC.
United Engineering Center
345 E. Forty-Seventh Street
New York, NY 10017
M. Prager

THE TORRINGTON COMPANY
Advanced Technology Center
59 Field Street
Torrington, CT 06790
W. J. Chmura

UNITED ENGINEERS & CONSTRUCTORS
30 South 17th Street
P.O.Box 8223
Philadelphia, PA 19101
A. J. Karalis

UNIVERSITY OF CALIFORNIA AT BERKELEY
Department of Materials Science
and Mineral Engineering
Berkeley, CA 94720
E. R. Parker

UNIVERSITY OF CALIFORNIA AT BERKELEY
Department of Mechanical Engineering
Berkeley, CA 94720
J. A. C. Humphrey

UNIVERSITY OF TENNESSEE AT KNOXVILLE
Materials Science and Engineering
Department
Knoxville, TN 37996
C. D. Lundin

UNIVERSITY OF TENNESSEE SPACE
INSTITUTE
Tullahoma, TN 37388
J. W. Muehlhauser

WESTINGHOUSE ELECTRIC CORPORATION
Research and Development Center
1310 Beulah Road
Pittsburgh, PA 15235
S. C. Singhal

WESTINGHOUSE HANFORD COMPANY
P.O. Box 1970, W/A-65
Richland, WA 99352
R. N. Johnson

DOE
OAK RIDGE OPERATIONS OFFICE
P. O. Box 2001
Oak Ridge, TN 37831
Assistant Manager for Energy Research and
Development

DOE
OAK RIDGE OPERATIONS OFFICE
Oak Ridge National Laboratory
P. O. Box 2008
Building 4500N, MS 6269
Oak Ridge, TN 37831
E. E. Hoffman

DOE
OFFICE OF BASIC ENERGY SCIENCES
Materials Sciences Division
ER-131, GTN
Washington, DC 20545
J. B. Darby

DOE
OFFICE OF CONSERVATION AND
RENEWABLE ENERGY
Energy Conversion and Utilization
Technologies Division
CE-12, Forrestal Building
Washington, DC 20545
J. J. Eberhardt

DOE
OFFICE OF FOSSIL ENERGY
Washington, DC 20545
D. J. Beecy (FE-14)
J. P. Carr (FE-14)
F. M. Glaser (FE-14)
T. B. Simpson (FE-25)

DOE
MORGANTOWN ENERGY TECHNOLOGY
CENTER
P.O. Box 880
Morgantown, WV 26505
R. A. Bajura
R. C. Bedick
F. W. Crouse, Jr.
N. T. Holcombe
W. J. Huber
J. E. Notestein
J. S. Wilson

DOE
PITTSBURGH ENERGY TECHNOLOGY
CENTER
P.O. Box 10940
Pittsburgh, PA 15236
S. Akhtar
T. C. Rupel
R. Santore
T. M. Torkos